PRESSURE PREDICTION AND UNDERBALANCED DRILLING IN THE DEEPWATER NIGER DELTA

GOODWYNE, OLAR,KAMAL

PRESSURE PREDICTION AND UNDERBALANCED DRILLING IN THE DEEPWATER NIGER DELTA

By

Olar K. Goodwyne

This thesis was submitted in partial fulfillment of the requirements for the degree of Master of Science at the Department of Earth Sciences, Durham University, United Kingdom

November 2012

Abstract

The mechanisms that cause overpressure can be broadly classified into two categories: loading and unloading. This study looks at eight wells from the deepwater Niger Delta; the wells were evaluated with three aims in mind. The first aim was to determine shale pore pressure with the density log using the equivalent depth approach. The second aim, using depth profiles of density, velocity, resistivity, and vertical effective stress, and cross-plots, was to infer the overpressure mechanism. The third aim was to validate underbalanced drilling zones identified on the pressure–depth plot with indications observed on the drilling report, mudlog, and other post-drilling data. To discriminate clean shales intervals, a density–velocity transform based on Gardner's (1974) relationship and GR filters were applied to the well logs. Measured pore pressures, log data, temperature data, drilling data, and mudlog data, including the end-of-well-report, were analysed for selected wells. Based on pressure–depth plots, the top of overpressure in the wells lies in the range 500 – 1200 TVDml. The equivalent depth method using the density log, when properly calibrated with measured pore pressures, can give reliable pressure prediction results, especially in the shallow section at temperatures < 70°. However, in the deeper sections at temperatures >75°C, the equivalent depth method is unreliable. It was also noted that shale intervals may provide vertical permeability barriers and create pressure compartments in some of the wells. The predominant overpressuring mechanism in the shallow section, as evident from density and velocity reversals and, was found to be disequilibrium compaction. At greater depths (temperatures >75°C), a combination of disequilibrium compaction and unloading mechanisms appears to be responsible for overpressure in the wells. Evidence for unloading mechanisms includes formation temperatures of 80°C or greater, indications of smectite-to-illite conversion

on density–sonic cross-plots, rapid increases in mud weight that sometimes approached fracture gradient, and depressed density reversals relative to velocity reversals. Finally, intervals identified as being drilled underbalanced on pressure depth plots are consistent with drilling data, mudlog data, and information in the end-of-well reports. Specifically, increased gas (connection gas and background gas), hole washout, high torque, drilling break, and decreased D-exponent trend show strong association with zones of underbalanced drilling on pressure–depth plots.

TABLE OF CONTENTS

Contents

LIST OF FIGURES

LIST OF TABLES

DECLARATION

1. The material contained in this thesis has not been previously submitted for a degree in this or any other institution
2. This thesis is not based on joint research

STATEMENT OF COPYRIGHT

ACKNOWLEDGEMENTS

An enormous amount of gratitude is extended to my major supervisor Prof. Neil Goulty who made my coming to Durham University possible and helped secure a grant for my studies through GeoPOP 3. I would also like to thank Neil for all the suggestions and review sessions during my data analysis and thesis write-up. His suggestions and insight have proved to be very valuable and were used liberally throughout the project.

I would also like to thank Richard Swarbrick for suggesting the research idea and for taking time out of his busy schedule to brainstorm ideas and review some of my presentation. I would also like to thank my co-supervisor Dr Stuart Jones for his encouragement and support throughout my studies in Durham. This acknowledgement will be incomplete without thanking Alison Swarbrick for her support and all the delicious meals she provided.

I want to thank all the great staff at Ikon GeoPressure in Durham, in particular Dr Sam Green, Bitrus Pindar, and Patricia Kelly; and Folake Odeyemi (Sonar Nigeria) for their support with data mining and my initiation into RokDoc software. Also special thanks to Maggie Evans (Ikon Science, UK) for providing assistance with RokDoc licensing and installation.

Many thanks to my friend Alex Cicchino with whom I had very useful discussions; and learned the art of eating spaghetti, Ciao Alex! Special thanks also to all of my friends (too numerous to list) in the department of Earth Science at Durham University. Thanks for making my Durham days memorable most of the time.

Finally, this thesis is dedicated to my lovely family: my wife, Karen; my son, Sean; and my daughter, Yvonne. Thanks a bunch for your patience, support, understanding, and prayers. I love you all!

Above all, I just want to thank God Almighty for His Grace and Mercy that saw me through the study.

"Worthy are You, our Lord and our God, to receive glory and honor and power; for You created all things, and because of You they existed, and were created."

(Rev. 4:11 NASB)

CHAPTER 1

Introduction

1.1 Motivation for Research

The Niger Delta Basin is located in the Gulf of Guinea; it is the most significant petroleum province in Nigeria. The Niger Delta, with a total area covering 300,000 km^2 and sediment thickness up to 10 km (Kulke, 1995; Hospers, 1965; Kaplan et al., 1994; Tuttle et al., 1999) is one of the largest regressive deltas in the world. The deepwater Niger Delta is demarcated by Charcot fracture into southern and eastern lobes, majority of the wells used in this study are located in the eastern lobe. The average oil and condensate production, as at December 2010, reported by the Nigeria government agency NNPC, is 2.58 million barrels per day; and this number is expected to increase by about 55 % within the next few years. To increase the daily production from current level, as being proposed by NNPC, will require opening of new exploration frontiers for drilling; especially, the deep and ultra-deep water areas.

Drilling in deepwater is a tremendous logistic challenge and expensive. In addition to cost and logistics, overpressure within the surface is of great concern to all operators worldwide. Penetrating unanticipated overpressured strata or inadequate preparation can lead to serious environmental disaster and in some cases fatality. The potential impact of subsurface overpressure on the overall success or failure of a drilling campaign underscores the importance of this study in deepwater Niger Delta.

With regards to pore pressure in the Niger Delta, most studies are done in-house and are not in the public domain. However, in their study of offshore and onshore Niger Delta wells, Owolabi et al. (1990) applied the equivalent depth method using resistivity and sonic logs and

suggested that the main mechanism of overpressure is disequilibrium compaction. In another study, Opara & Onuoha (2009) used velocities obtained in 3D seismic data processing to conclude that a combination of mechanisms (i.e., disequilibrium compaction, gas generation, thermal expansion, and clay diagenesis) contribute to overpressure generation at great depths, in particular, where high pressures were observed. Likewise, Cobbold et al. (2009) attributed fluid overpressure, seepage forces and the rapid migration of fluid volume in the outer thrust belt of the Niger Delta to kerogen transformation and hydrocarbon generation in the Akata Formation, which is a chemical compaction process (Swarbrick et al., 2002).

The motivation for this study was based on observations by Ikon Geopressure of cases where traditional indicators of underbalanced drilling (i.e., cavings and increase background gas) were obscured in spite of evidence for underbalanced drilling (UBD) on pressure–depth plots. Thirty-six wells from the deepwater Niger Delta were initially screened, based on log quality, for inclusion in the study. Some of the wells were precluded from further analysis due to poor data and/or lack of well reports. Subsequently, pressure–depth plots were derived for selected wells by applying the equivalent depth method to density logs over carefully selected clean shale intervals. Also, logs and various cross-plots were used to infer possible mechanisms of overpressure. Finally, zones identified with UBD on pressure–depth plots were compared with corresponding intervals on drilling, mudlog and end-of -reports (EOWR) for corroboration or lack of it.

This research has shown that disequilibrium compaction is the dominant mechanism of overpressure generation in the shallow section, roughly corresponding to zones with temperature <70°C. Although the evidence requires further validation, intervals at greater depths where temperatures are >80°C show indications of smectite-to-illite (sm-ill) conversion, which can act

as an unloading mechanism of overpressure generation. Also, zones identified with UBD on pressure–depth plots were consistent with observations made on drilling and mudlog data.

1.2 Objectives

The main objectives of the study are:

1. Estimation of pore pressure using density logs by the equivalent depth method.
2. Identification of any evidence of sm-ill transformation, and whether it has contributed to overpressure.
3. Identification of UBD zones from pressure–depth plots with supporting evidence from drilling and mudlog data.

1.3 Data

The wells used in this study are from the deepwater area of the Niger Delta Basin in water depths ranging from ~600 m to < 2000 m. Two general types of data were used for this project: data acquired during drilling of a well, and data prepared or acquired after drilling of a well (i.e., after abandonment). The first data type includes wireline logs, logging while drilling (LWD) logs, wireline formation tester (WFT) results, mudlogs, and drilling logs. The second group of data includes EOWRs, comprising both drilling and geological reports. It should, however, be noted that complete sets of data were not available for some wells. For a well to be included in this study, at the minimum, it should have acceptable quality of wireline or LWD logs, pressure data, and corresponding EOWRs.

CHAPTER 2

Geology and Petroleum System

2.1 Geology

There are seven sedimentary basins in Nigeria: Anambra, Benin, Benue, Bida, Borno, Niger Delta, and Sokoto (Figure 2.1). However, the Niger Delta Basin is by far the most significant in terms of hydrocarbon production with active producing fields and ongoing exploration both onshore and offshore. The basin is located in the Gulf of Guinea and fed by the River Niger (Doust & Omatsola, 1990; Hooper et al., 2002). The Niger Delta is one of the largest regressive deltas in the world, covering an area of 300,000 km^2 with sediment volume of 500,000 km^3 and sediment thickness of up to 10 km (Kulke, 1995; Hospers, 1965; Kaplan et al., 1994; Tuttle et al., 1999).

In their World Energy Assessment of provinces, the US Geological Survey ranked the Niger Delta as the 12^{th} richest province in petroleum resource, based on 2.2% and 1.4% of world known oil and gas reserves, respectively (Tuttle et al., 1999). The current average production as reported by the Nigeria government agency, NNPC, is 2.58 million barrels per day. Cobbold et al. (2009) reported estimates of the region's ultimate recoverable hydrocarbons at 35 billion barrels of oil, 120 tcf of gas (Ekweozor & Daukoru, 1994), and 66 billion barrels of oil equivalent (Saugy & Eyer, 2003).

2.1.1 Regional tectonics and basin development

Several authors have discussed in detail the tectonics and basin development of the Gulf of Guinea region (e.g., Weber & Daukoru, 1975; Tuttle et al., 1999; Corredor et al., 2005). Here I give a broad overview of the regional tectonics and basin development of the Niger Delta.

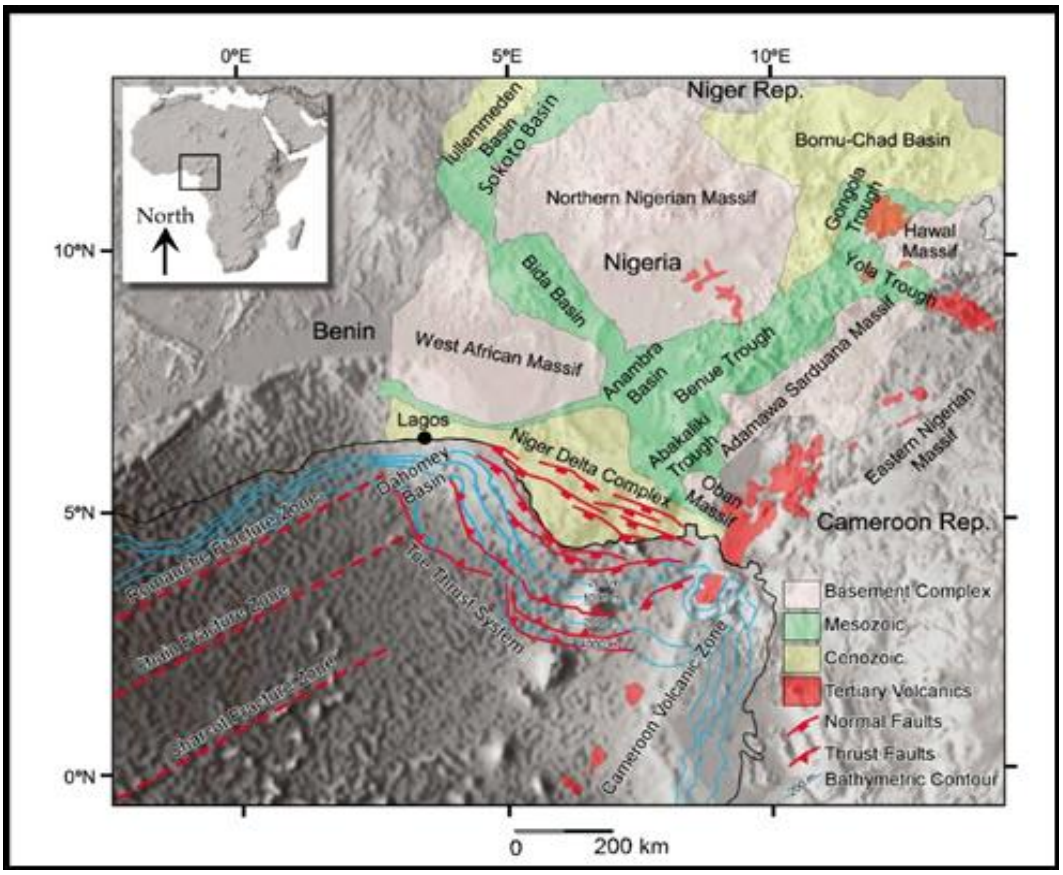

Figure 2.1. The sedimentary basins of Nigeria. The Niger Delta Basin is delineated by the Cameroon Volcanic Zone, the Dahomey Basin, and the 4000 m (13100 ft) bathymetric contour. After Corredor et al. (2005).

Development of the Niger Delta Basin started with the triple-junction rifting that separated Africa and South America, beginning in the Late Jurassic and lasting until the mid-

Cretaceous. The failed arm of the rifting system constitutes the Benue-Abakiliki Trough, which bounds the Niger Delta Basin to the north-east (Lehner & De Ruiter, 1977; Tuttle et al., 1999; Brownfield & Charpentier, 2006). The others arms, one striking westwards along the south-western coast of Nigeria and the other striking south-eastwards along the coast of Cameroon, developed into the passive continental margins of West Africa (Doust & Omatsola, 1990). Figure 2.2 shows the positions of the African and South American plates after the Cretaceous break-up. Within the region, post-rifting deformation occurred primarily by gravity tectonism, manifested in the form of shale mobility deformation (Tuttle et al., 1999). The deformation has been caused, firstly, by formation of shale diapirs within the overpressured Akata Formation and, secondly, by slope instability due to absence of basinward support for the Akata Formation (Figure 2.3). The complex structures that resulted include shale diapirs, roll-over anticlines, collapsed growth fault crests, and steeply dipping flank faults (Evamy et al., 1978; Xiao & Suppe, 1992; Tuttle et al., 1999). Deposition of the Benin Formation, in all of the depocentres, occurred after gravity tectonism.

Most workers in the Niger Delta Basin are in agreement that the Benue-Abakiliki Trough is the oldest pre-Tertiary sedimentary basin in Nigeria. Weber & Daukoru (1975) discussed some of the attributes associated with the three different phases of basin development.

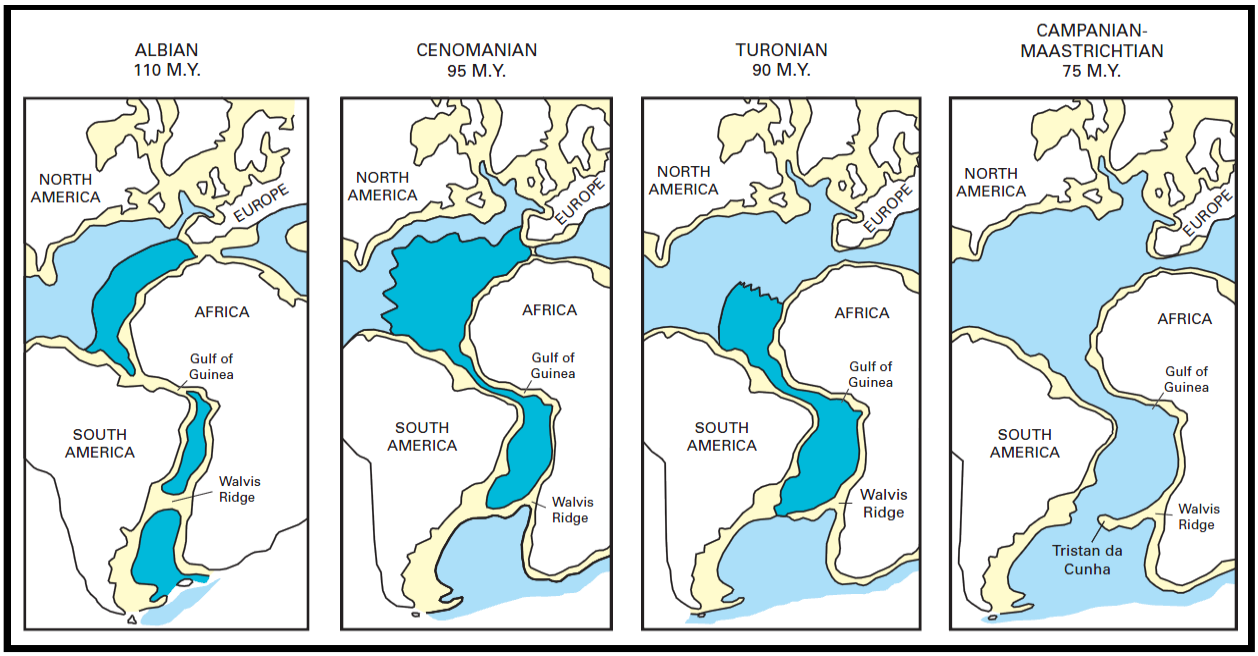

Figure 2.2. The Cretaceous break-up of Africa and South America. From Brownfield & Charpentier (2006).

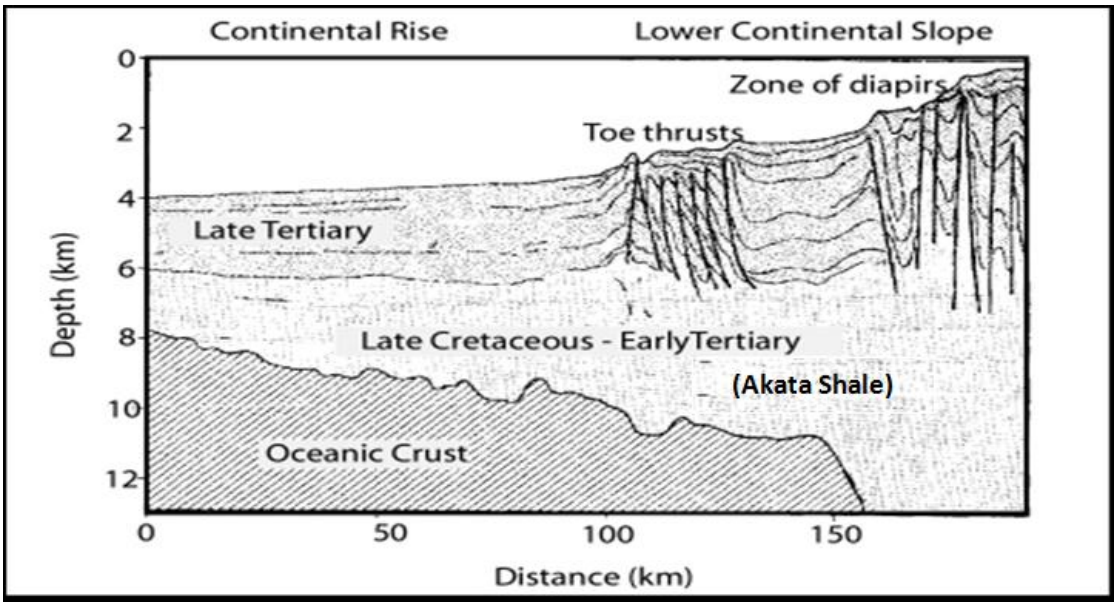

Figure 2.3. Schematic dip section of through the Niger Delta Basin in the direction SSW–NNE. From Tuttle et al. (1999).

It is well established that the Benue-Abakaliki Trough originated as a failed arm of the triple-junction rift system. In the mid-Aptian, the South Atlantic began to open up by crustal stretching and downwarping that reached the Gulf of Guinea (GOG) by the early Albian to form the Benue-Abakaliki trough in the northeast. By the beginning of the Albian, the Anambra and Ikpe platforms had already formed on either side of the Benue-Abakiliki Trough (Figure 2.4a). However, before the Benue-Abakaliki Trough began closing with accompanying crestal subduction, the trough was filled with over 3300 m of Albian to Coniacian sediments. Though uncorroborated by geophysical and stratigraphical evidence, it was suggested by Weber & Daukoru (1975) that closure of the trough is related to higher rates of seafloor spreading adjacent to northwest Africa relative to the South Atlantic.

The Benue-Abakiliki Trough was uplifted by Santonian-Campanian folding to form the Abakiliki High (Figure 2.4b), while the same fold downwarped the Anambra Platform to form the Anambra Basin (Weber & Daukoru, 1975). Within the same time interval, the Benin flank basement immediately to the west of the Anambra Basin was invaded by the sea for the first time. By some time from the Late Cretaceous to the Palaeocene, three sedimentary basins, the Anambra Basin, the Afikpo Syncline, and undeformed Ikong Trough, were already in existence. Development of the proto-delta of Cretaceous age was arrested by a major Palaeocene transgression that deposited the Imo Shale. The subsequent regressive phase formed the Eocene–Recent delta. The essential post-Palaeocene delta tectonic elements include the Anambra Basin, Abakiliki High, Afikpo Syncline, Ikang Trough and the contact between continental and oceanic crust. The tectonic events influenced the direction of clastic sediment supply and maximum sediment thickness. From the Eocene to the middle Miocene, clastic sediment was supplied to the Niger Delta complex from the Niger, Benue, and Cross rivers. Therefore, the rate of

deposition has been rapid (Weber & Daukoru, 1975), which has implications for overpressure generation within the basin. The merging of the Niger-Benue and Cross river delta systems after the middle Miocene masked the tectonic features created in the Late Cretaceous; from this time onwards the rate of delta spreading has been controlled mainly by erosion of newly uplifted hinterland and eustatic changes in sea level.

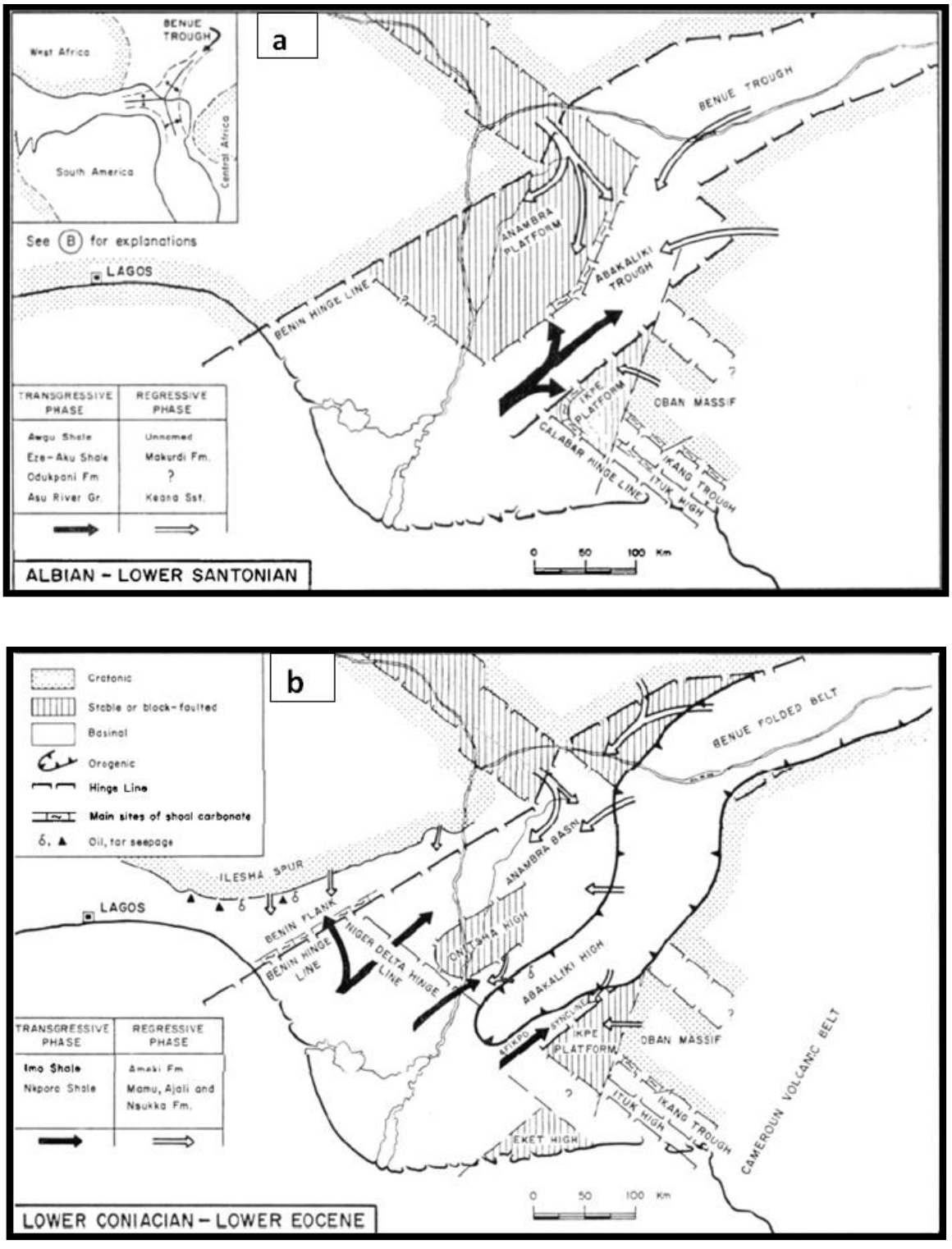

Figure 2.4. Early evolution of the Niger Delta Basin: (a) Albian–early Santonian; and (b) early Coniacian–early Eocene. From Weber & Daukoru (1975).

2.1.2 Basin structure

Discussions on the impact of tectonics on the overall basin structure and deformation within the sediments of the Niger Delta Basin are ongoing. Based mostly on seismic interpretation, several authors have described observations on the structural styles in the outer thrust belt of the basin (e.g., Haack et al., 2000; Hooper et al., 2002; Ajakaiye & Bally 2002a, b; Bilotti & Shaw, 2001; Corredor et al., 2005a, b; Higgins et al., 2007; Cobbold et al., 2009). Some of the general observations made by Cobbold et al. (2009) are:

1. Thrust wedges generally have small apical angles.
2. Fore-thrusts and back-thrusts with associated hanging wall anticlines are the predominant internal structures.
3. Planar fault surfaces within the Akata Formation are where detachment occurs.
4. Development of faults and folds generally occurs sequentially and progresses seawards.
5. Transfer zones parallel to oceanic transform faults demarcate homogeneous compressional domains in the western lobe.

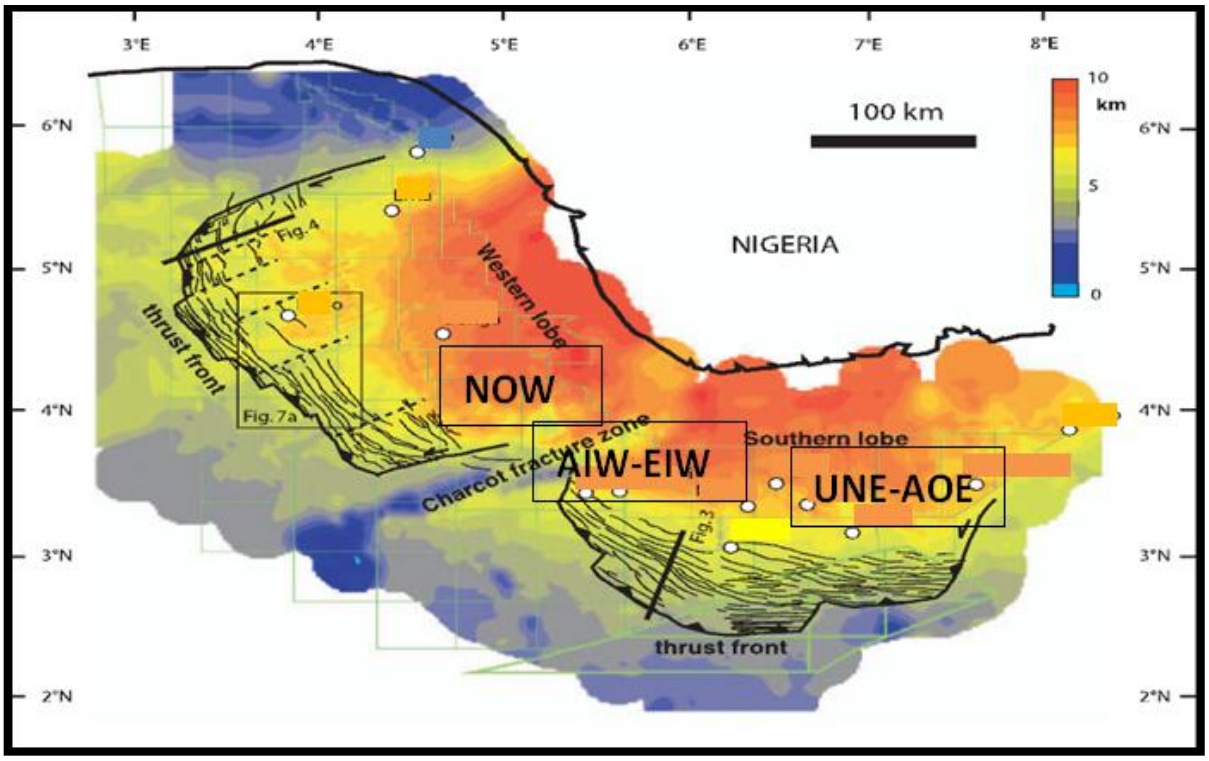

Figure 2.5. Western and southern sediment lobes in the offshore Niger Delta Basin, separated by shallow oceanic basement along the Charcot Fracture Zone. Also shown are the approximate locations of wells in NOW, AIW-NOW, UNE, and AOE fields. From Cobbold et al. (2009).

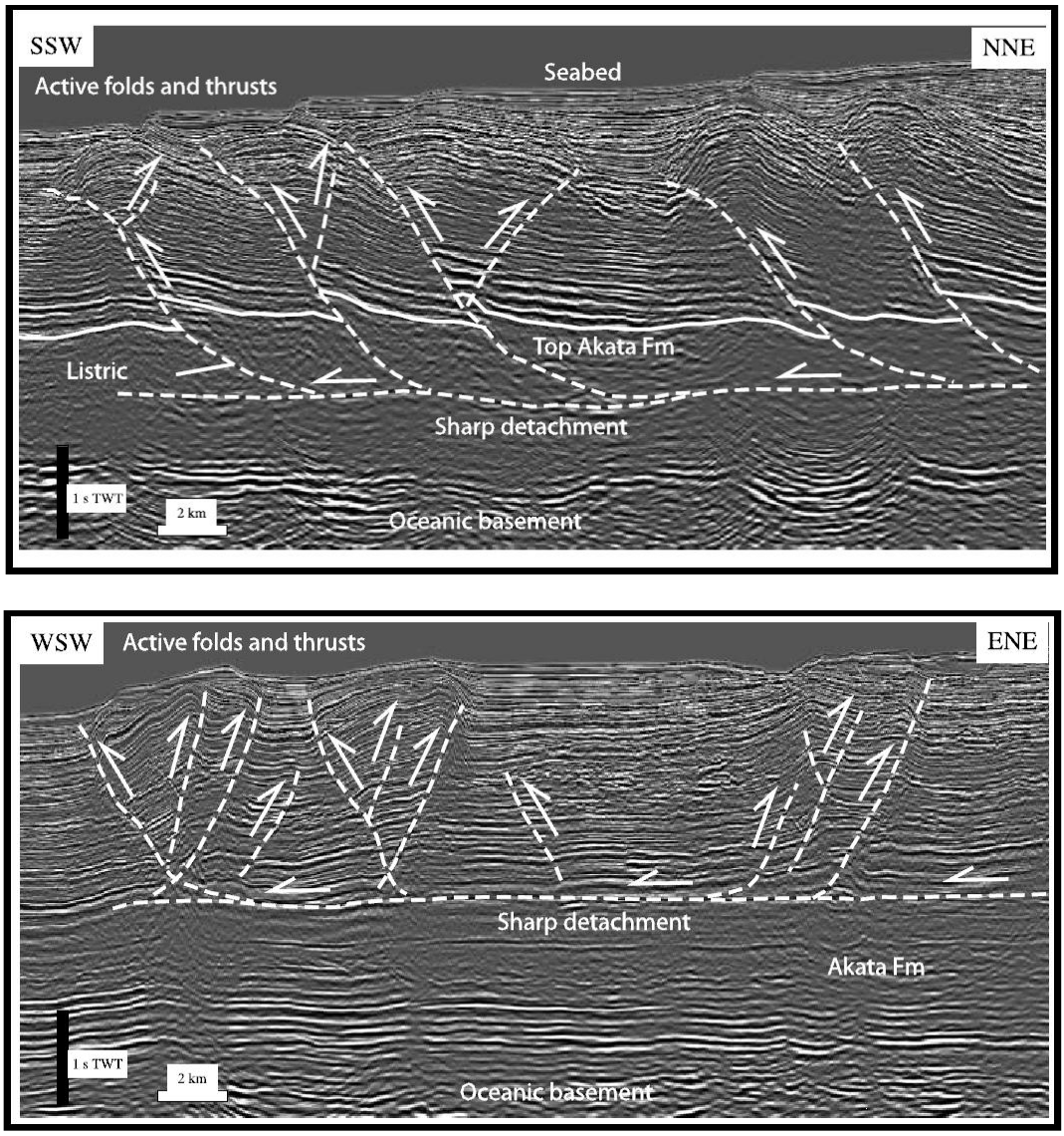

Figure 2.6. Seismic profiles. Top: outer thrust belt, southern lobe of Niger Delta, showing weak active folds and thrusts. Dashed lines are fault traces soling out in a sharp detachment within the Akata Formation. Solid line marks top of Akata Formation. Bottom: outer thrust belt, western lobe of Niger Delta, showing strong active folds and thrusts at the seabed. Dashed lines are fault traces, and a sharp detachment has been interpreted at the top of the Akata Formation. From Cobbold et al. (2009).

With regard to structural style, Corredor et al. (2005) and Cobbold et al. (2009) are in agreement on the role of detachment from the overpressured Akata Formation. In their study, Cobbold et al. (2009) compared physical models with the distribution and nature of overpressure in the Akata Formation. By comparing seismic structural profiles from southern and western lobes (Figure 2.6), they made the observations summarized in Table 2.1.

	Western lobe(WSW-ENE)	Southern Lobe (SSW-NNE)
Sea bed slope	• ~1 deg	• ~2.5 deg
Structure	• less evenly and closely spaced	• More evenly and closely spaced
Thrust	• more back-thrust than fore-thrust	• more fore-thrust than back-thrust
Detachment fault	• Near top of Akata Fm	• In middle of Akata Fm
Leading anticlines	• still active	• not currently active
Thrust faults	• listric over short interval	• listric over longer interval

Table 2.1. Summary comparison of structural characteristics of the western and southern lobes of the deep water Niger Delta according to Cobbold et al. (2009).

Both Corredor et al. (2005) and Cobbold et al. (2009) subdivided the basin into three broad tectonic domains, extensional, transitional/translational, and compressional, based on the

predominant structures. However, Corredor et al. (2005) examined high-resolution bathymetric images (Figure 2.7) in addition to seismic data, and included a mud-diapir zone, inner fold, and thrust belt in their subdivision (Figure 2.8). Table 2.2 summarizes the structural divisions and features of the different structural styles within the Niger Delta Basin, as discussed by Corredor et al. (2005).

Corredor et al. (2005)	
Extensional basin	• beneath continental shelf • Growth-normal-faults: dip towards the basin & counter-regional • rollovers and depocenters
Mud-diapir basin	• Beneath upper continental slope • Typical passive, active, and reactive mud diapirs (Morley and Guerin, 1996) • Shale ridge and massifs • Shale overhangs & vertical diapirs • Interdiapir depocenters
Inner fold & thrust belt	• Thrust faults lean basinward • Thrust faults usually imbricated • Detachment folds
Transitional detachment fold zone	• Beneath lower continental slope • Shows minor or no deformation • Detachment fold on thick Akata Fm.
Outer fold and thrust belt	• Thrust fault may lean basinward and towards hinterland • Deformation still active • Strong structural signature obvious on the bathymetry

Table 2.2. Summarized structure of the Niger Delta Basin based on predominant structural style. From Corredor et al. (2005).

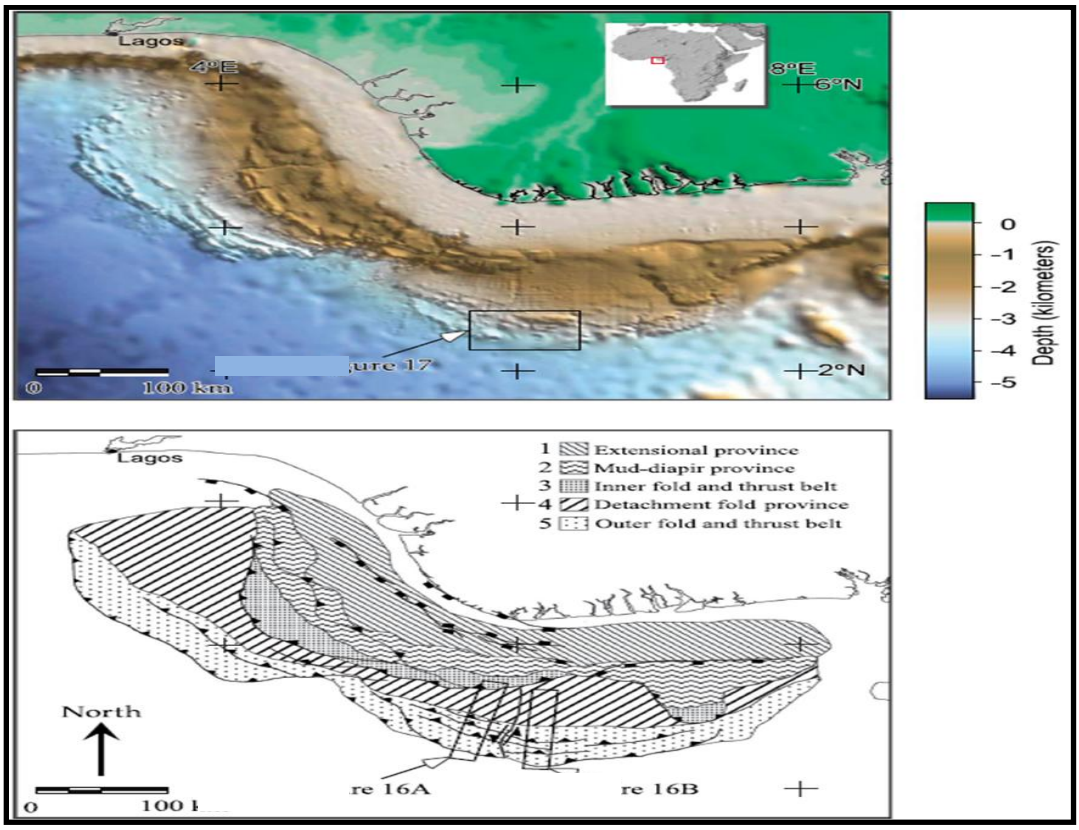

Figure 2.7. High-resolution bathymetric image of the Niger Delta showing the main structural domains. From Corredor et al. (2005).

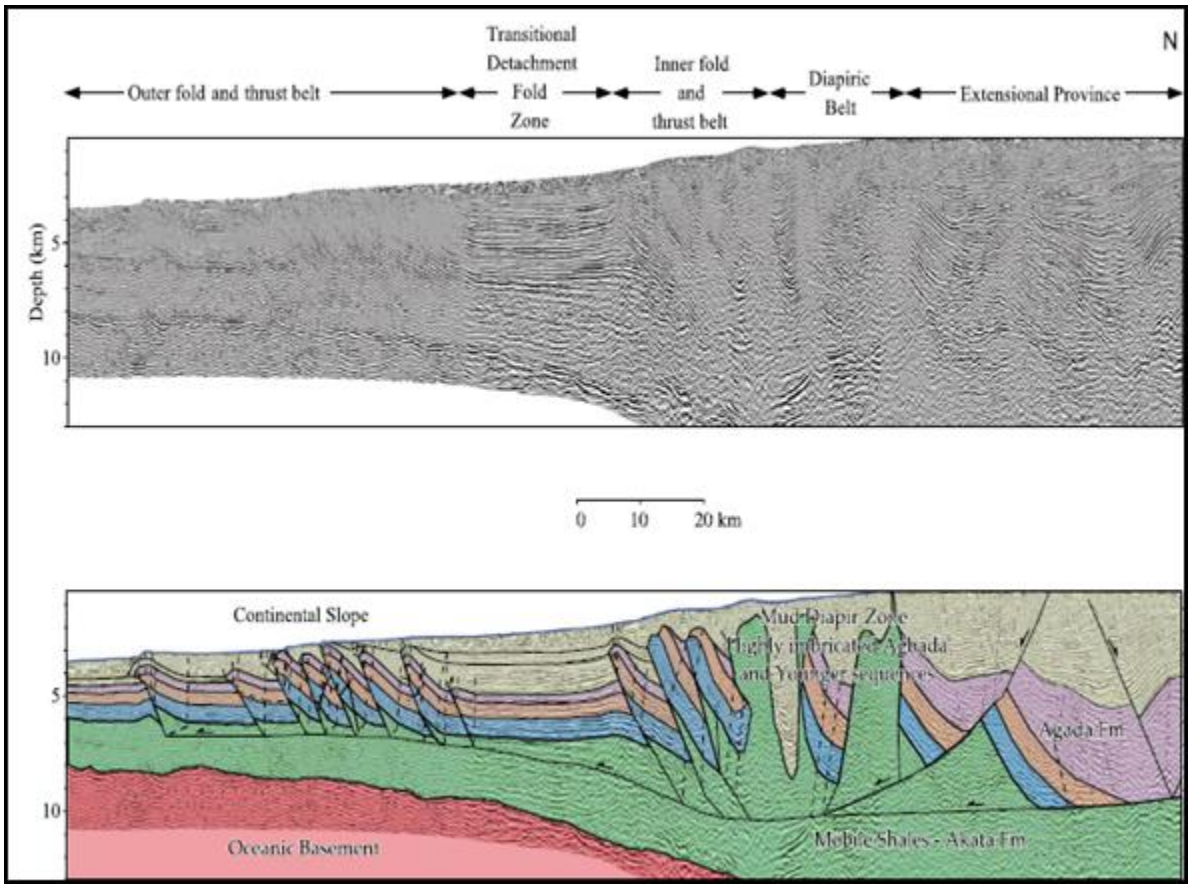

Figure 2.8. Uninterpreted and interpreted regional seismic profile across the Niger Delta showing the main structural features from the extensional province on the shelf to the toe thrust systems in the deep water. The inner and outer fold and thrust belts are separated by a zone of little or no deformation. From Corredor et al. (2005).

In short, the structure in the Niger Delta Basin is largely influenced by instability induced by overpressure, the ductility of the Akata Formation shale, and slope instability (Doust & Omatsola, 1990; Corredor et al., 2005; Cobbold et al., 2009). The predominant tectonics in the basin is related to extensional deformation in the sedimentary fill, clearly evident in the paralic Agbada Formation as extensional faulting. Structures related to compressional and wrench

movements are observable in the inner fold thrust belt, transitional fold zone, and the outer fold thrust belt of the deep water Niger Delta. The structure in the Akata Formation is obscure while the Benin Formation was deposited after cessation of most tectonic activity (Doust & Omatsola, 1990). The low density obtained from gravity modelling of Akata Formation may be indicative of presence of salt and/or undercompacted shales (Jacques et al., 2003 cited in Cobbold et al., 2009). However, the very low seismic velocities observed in Akata Formation suggests that salt is absent (Morgan, 2003 cited in Cobbold et al., 2009).

2.1.3 Stratigraphy and sedimentology

The Niger Delta is the world's largest regressive delta and comprises a series of offlap cycles of sediments (e.g., Doust & Omatsola, 1990; Kulke, 1996). The stratigraphy and sedimentology of the Niger Delta, like other major deltas, is a function of the rate of sediment supply and basin tectonics. Several workers (e.g., Short & Stauble, 1967; Weber & Daukoru, 1975; Doust & Omatsola, 1989) have extensively discussed the interplay of these two factors as it relates to the Niger Delta stratigraphy, sedimentology, and structure.

Three major depositional cycles have been documented in the Niger Delta Basin (Short & Stauble, 1967). Firstly, during the Early Cretaceous, a marine incursion covered the whole basin, and was terminated by weak folding in the Santonian. Secondly, the depositional cycle that created the proto-Niger delta during the Late Cretaceous terminated in a major Palaeocene marine transgression. The third depositional cycle has been ongoing since the Eocene, and is responsible for the southward growth of the main Niger Delta.

The Cenozoic strata in the Niger Delta area comprise three main formations (Figure 2.9). The base sequence, the Akata Formation, is up to 7000 m thick in the central part of the basin, and is a delta-front, deep marine deposit that mainly consists of a thick marine shale and clay with a rather silty base. It contains thin sand bodies of continental slope, channel-fill, and turbiditic origin. The shale forms diapirs offshore that are considered to be Palaeocene to Holocene in age (Doust & Omatsola, 1990). The Akata Formation is organic-rich and is generally accepted to be the main source rock in the Niger Delta area.

Overlying the Akata Formation is a paralic sequence of up to 3000 m thickness, the Agbada Formation, which comprises intercalated shallow marine fluvial sands, silts and clays. These are delta front, delta topset, fluvio-deltaic deposits, ranging in age from Eocene to Pleistocene, and contain both reservoir and caprocks (Doust & Omatsola, 1990). Though still quite controversial, Short & Stauble (1967), Frankl & Cordry (1967) and Lambert-Aikhionbare & Ibe (1984) have all suggested that the Agbada Formation may contain source rocks. The criteria for delineating the top and bottom of the Agbada Formation can be ambiguous and in practice vary from one company to another. Doust & Omatsola (1990) suggested the practice of picking the top on wireline logs as the base of fresh water invasion, and the bottom corresponding to the onset of hard overpressure during drilling. Using cuttings from wells, Doust & Omatsola (1990) pointed out that the Agbada Formation is sandier in the upper section than the lower section, may be consolidated to unconsolidated, and is generally poorly sorted with lignite streaks, shell fragments, and glauconite.

The topmost sequence of massive non-marine sand is the Benin Formation. In the central part of the basin, it has a maximum thickness of about 2100 m, and thins seawards to disappear near the shelf edge. The oldest sediments of the Benin Formation are thought to be Oligocene in

age, and generally lack fauna (Doust & Omatsola, 1990). As pointed out by Doust & Omatsola (1990), these alluvial, coastal plain deposits contain insignificant quantities of hydrocarbon, but are of great hydrogeological interest.

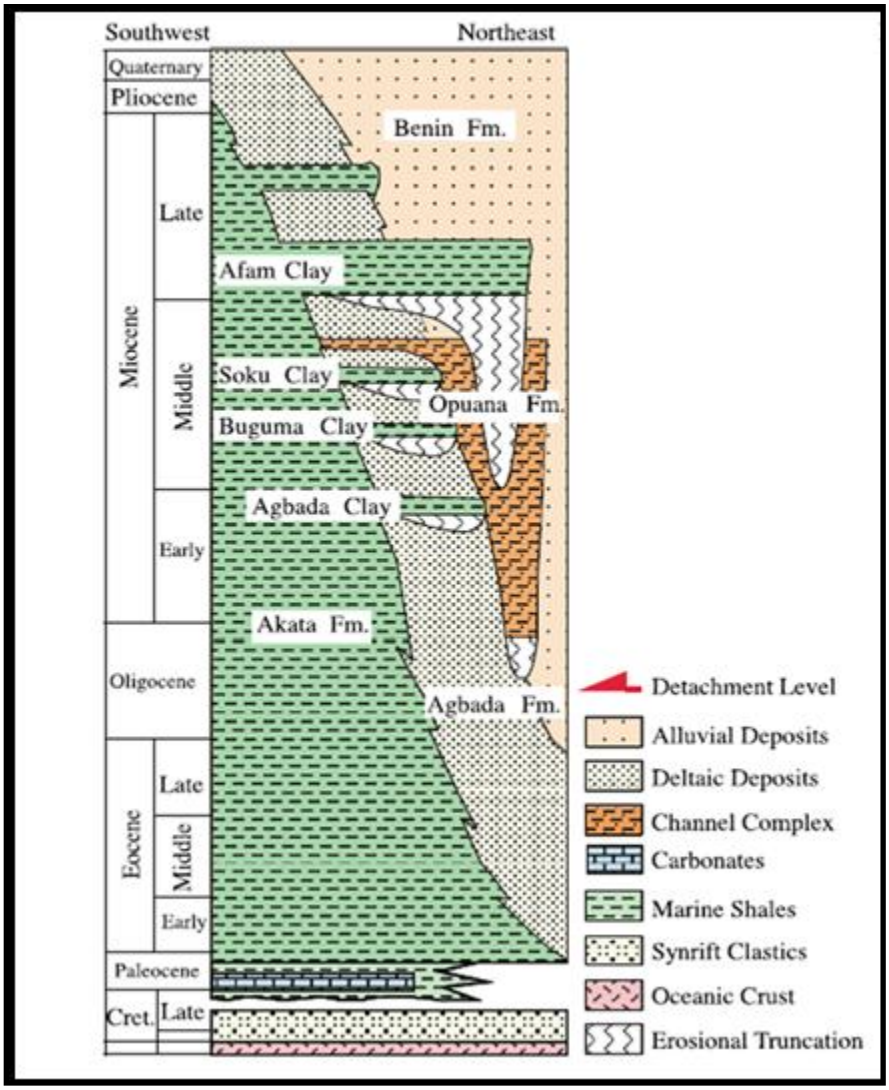

Figure 2.9. Schematic of the regional stratigraphy in the Niger Delta showing the main stratigraphic units in the outer fold and thrust belt. From Corredor et al. (2005).

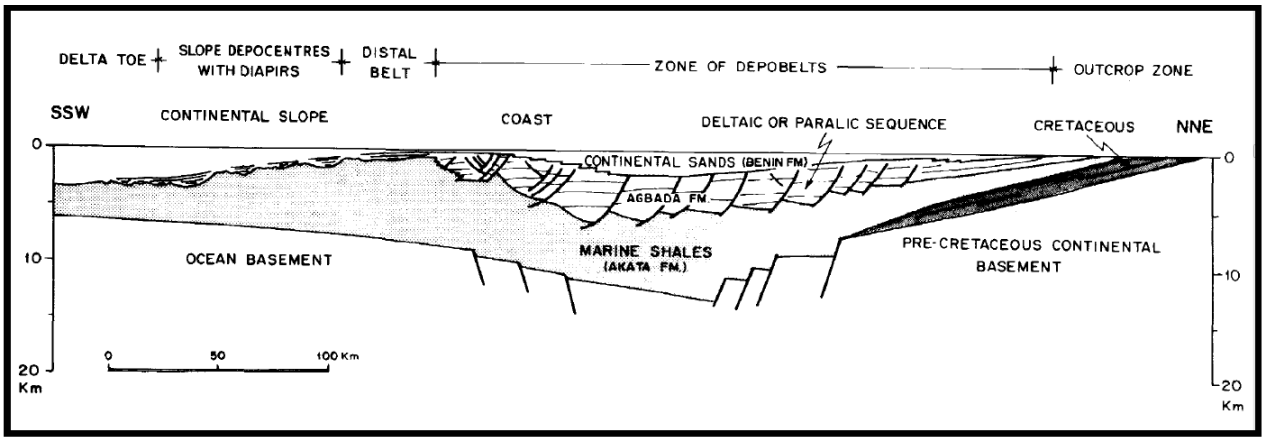

Figure 2.10. Schematic structural section through the axial portion of the Niger Delta showing the tripartite division of the Tertiary sequence in relation to the basement. From Doust & Omatsola (1990).

2.2 Petroleum system

There are two aspects to a petroleum system: firstly, the source rock and the characteristics of the hydrocarbons it contains; and, secondly, the timing of hydrocarbon generation, the development of traps, and lateral and vertical migration of hydrocarbons (e.g., Demaison & Huizinga, 1991; Haack et al., 2000). Tuttle at al. (1999) recognized one petroleum system in the Niger Delta, in the Tertiary strata. In contrast, Haack et al. (2000) identified three petroleum systems in Nigeria in the light of new geochemical, gravity and magnetic data, and structural analysis. What is presented here is a summary of the three systems based on Haack et al. (2000).

2.2.1 Lower Cretaceous (lacustrine) petroleum system

To support their position regarding the lacustrine petroleum system, Haack et al. (2000) reported that the source rock of Neocomian age encountered in the Ise-2 well in the western lobe of the Niger Delta, which is rich in the lacustrine alga *Botryococcus*, correlates to biodegraded oil seeps found in the northern flank of the Dahomey Embayment. Oil derived from the lacustrine Bucomazi source rock of Cretaceous age in the Lower Congo Basin shows geochemical finger prints similar to those of the source rock from Ise-2 well, and biodegraded oil seeps from the Dahomey Embayment. It should be pointed out, though, that Haack et al. (2000) cited mostly verbal communications as their sources. Figure 2.10 shows the approximate areal extent of this system. Geochemical data from Ise-2 indicates that this system may have source potential of up to 5.24 tonnes HC/m^2 rock, and this system may also possibly extend into the Benue Trough (Haack et al., 2000).

2.2.2 Upper Cretaceous-lower Palaeocene (marine) petroleum system

Evidence in support of this system draws heavily on the Epiya-1 well (Figure 2.11). Geochemical analysis of source rock from the Epiya-1 well indicates that it is rich in types II and II-III kerogen. Along the north-western margin of the delta, this same source rock is seen in marine Araromi, Awgu, and Imo shales. This same system is also thought to be the source rock for the Palaeogene reservoir of the Shango-1 well, according to Haack et al. (2000) who cited a personal communication with K.E. Peters in 1993.

Based on the Epiya-1 well, the source potential of this system is estimated at 10.5 tonnes HC/m^2 of rock. According to Haack et al. (2000), citing Demaison & Huizinga (1991), this

number is sufficient to provide hydrocarbon charge for a vertically drained basin. According to Haack et al. (2000), Dahl (1991) suggested that oil from this system has been found in the Anambra Basin and produced from the Seme Field. This system has been identified in outcrop along the eastern margin of the Niger Delta (Inyang et al., 1995), and has been penetrated also in the subsurface (Adakomola, 1992; in Haack et al., 2001). Unlike some other parts of Western Africa, no significant accumulation from this system is present in the Niger Delta region.

2.2.3 Tertiary (deltaic) petroleum system

Geochemical data have been used to differentiate the source rock for the Tertiary system into gas-prone or oil-prone. Using samples from Aroh-2 well, Haack et al. (2000) indicated that oil-prone and gas-prone source rocks occur on the up-thrown sides of normal faults, while the amount of source rock containing richer, oil-prone type II kerogen increases with depth. This oil-prone source rock has been found to be closely related to liquid hydrocarbons produced from the Niger Delta. To date, few or possible no wells in the Niger Delta have penetrated this oil-prone source rock due to its great depth. Information on the source rock trend within the delta has been inferred mainly by geochemical analysis of produced hydrocarbons. The estimated potential for this deltaic source rock is about 27 tonnes HC/m^2, although Haack et al. (2000) suggested that this estimate errs on the high side due to the contribution from the overlying gas-prone section.

Based on fossils found in the deeper and richer source rock in the Aroh-2 well, Haack et al. (2000) suggested the depositional environment to be outer neritic to bathyal. Oil and gas distribution across the delta is quite complex. The distribution complexity has been attributed to variation in source facies, and difference in maturity due to variations in geothermal gradient and

burial (Haack et al., 2000). Some workers have suggested that long-distance lateral migration of hydrocarbons across major faults is very unlikely in this system (Weber & Daukoru, 1975; Evamy et al., 1978; Damaison & Huizinga, 1991; Haack et al., 2000). This is because of extensive normal faulting, with the growth faults acting as migration pathways for hydrocarbons, thus making the delta a classic example of a vertically drained petroleum system (Weber & Dakoru, 1975; Evamy et. al., 1978; Demaison & Huizinga, 1991; Peters & Moldowan, 1993; Haack et. al., 2000). The traps in this system are mostly structural, though some large stratigraphic traps are present as well.

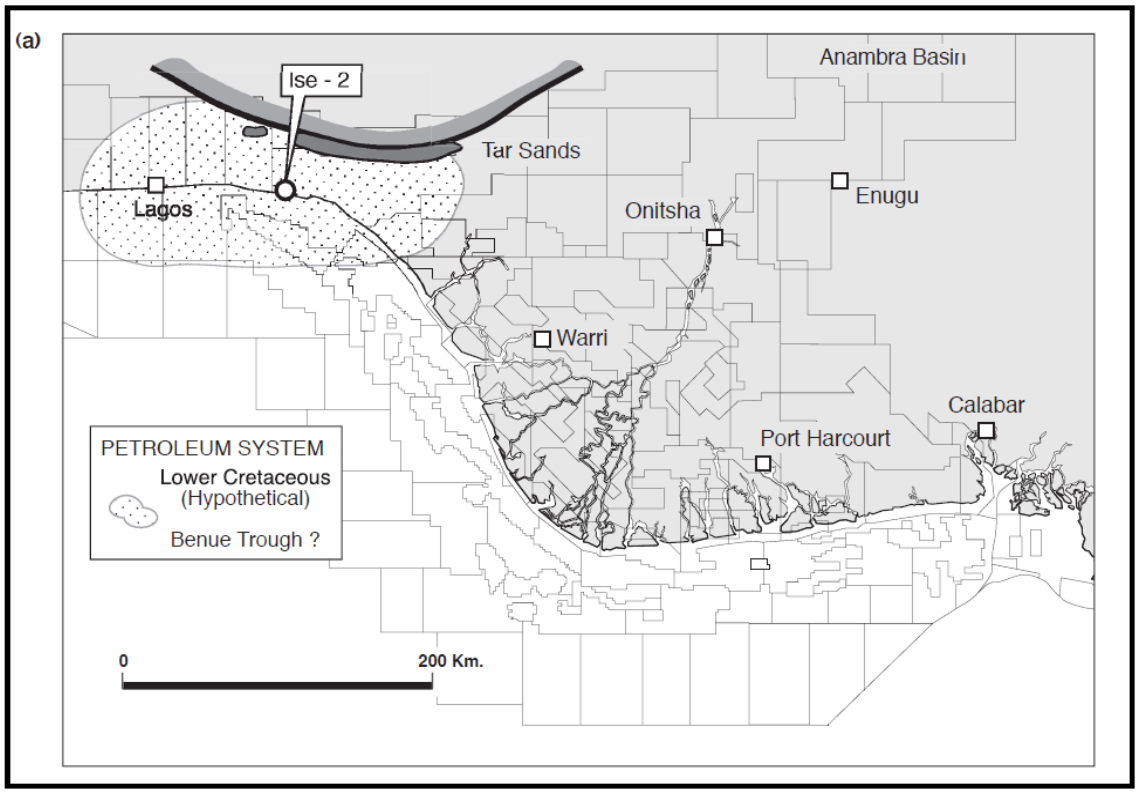

Figure 2.11. Map showing the Lower Cretaceous petroleum system and the location of the Nigerian tar sands on the northern flank of the Dahomey Embayment. From Haack et al. (2000).

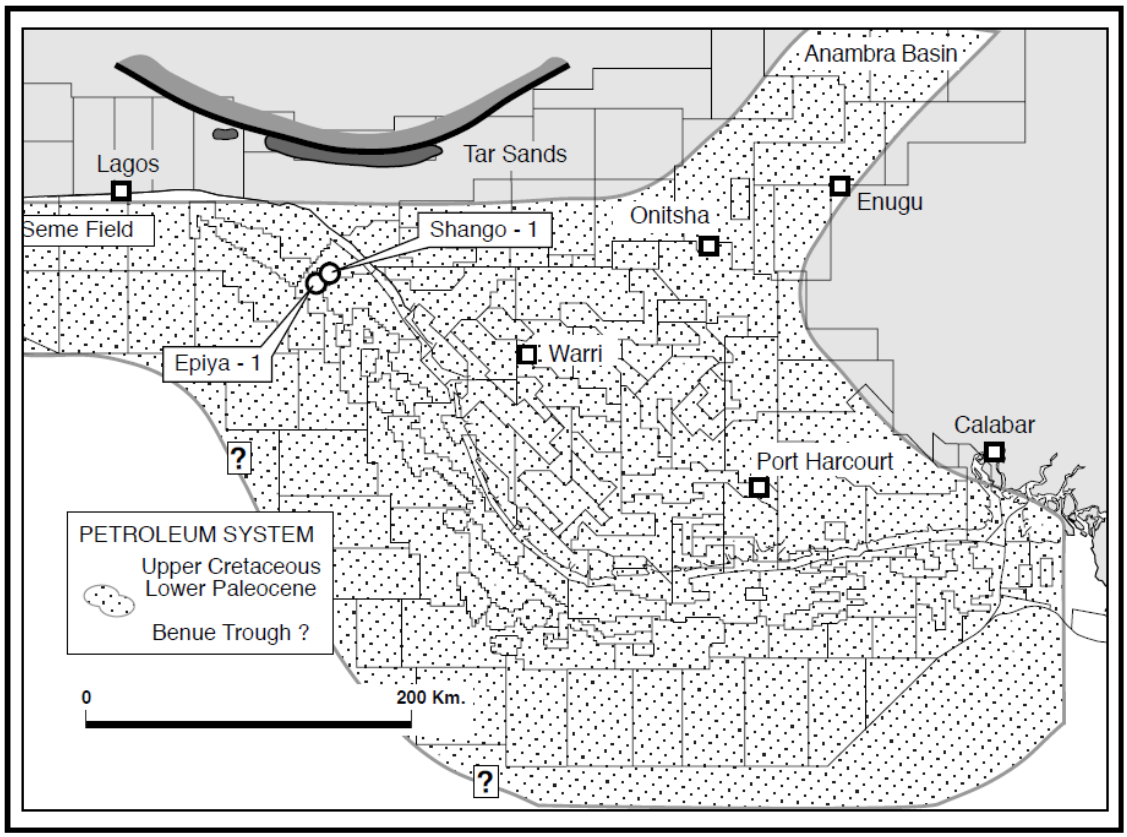

Figure 2.12. Map showing the Upper Cretaceous–lower Palaeocene petroleum system. From Haack et al. (2000).

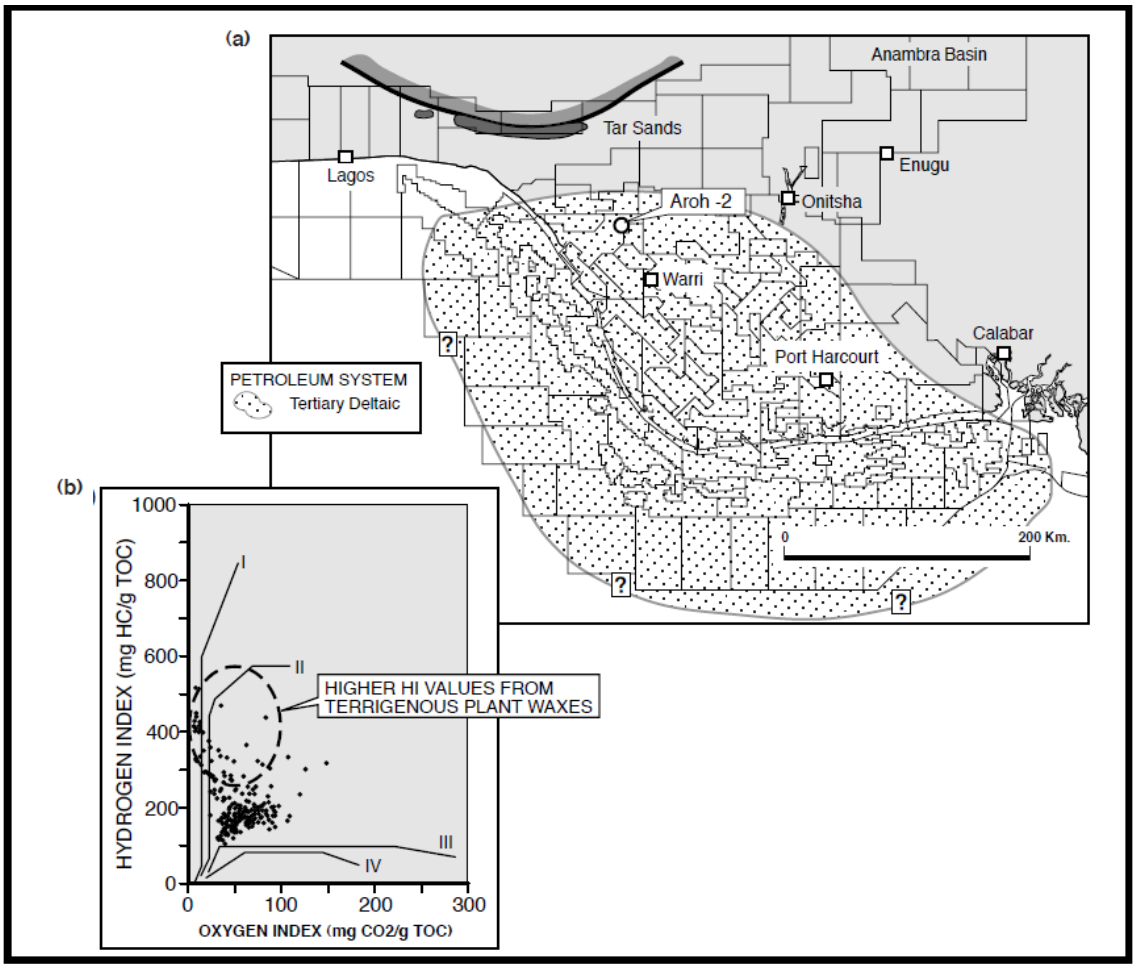

Figure 2.13. Map showing the Tertiary deltaic petroleum system. From Haack et al. (2000).

CHAPTER 3

Theoretical Background

This chapter provides background information pertaining to overpressure, underbalanced drilling and, to a lesser extent, drilling operations in general. Conscious effort is made to use definitions and explanations most widely accepted and in common usage among professionals within the oil and gas industry. The chapter begins with basic terminology commonly used by pore-pressure professionals (section 3.1). Section 3.2 is an overview of current understanding of mechanisms that generate overpressure in the subsurface. This is followed, in sections 3.3 examples of overpressure from around the world. Section 3.4 deals with aspects of overpressure in the subsurface, and commonly used overpressure estimation and detection methods are described in section 3.5.

3.1 Basic terminology

Figure 3.1 is used here to illustrate basic terminologies commonly used in subsurface pressure estimation and measurements.

Hydrostatic pressure

The hydrostatic pressure is the pressure exerted by static column of fluid at a reference depth. It is dependent on the density of the formation fluid, usually water or brine, and the true vertical height of the column of fluid. In reality, atmospheric pressure contributes to the hydrostatic

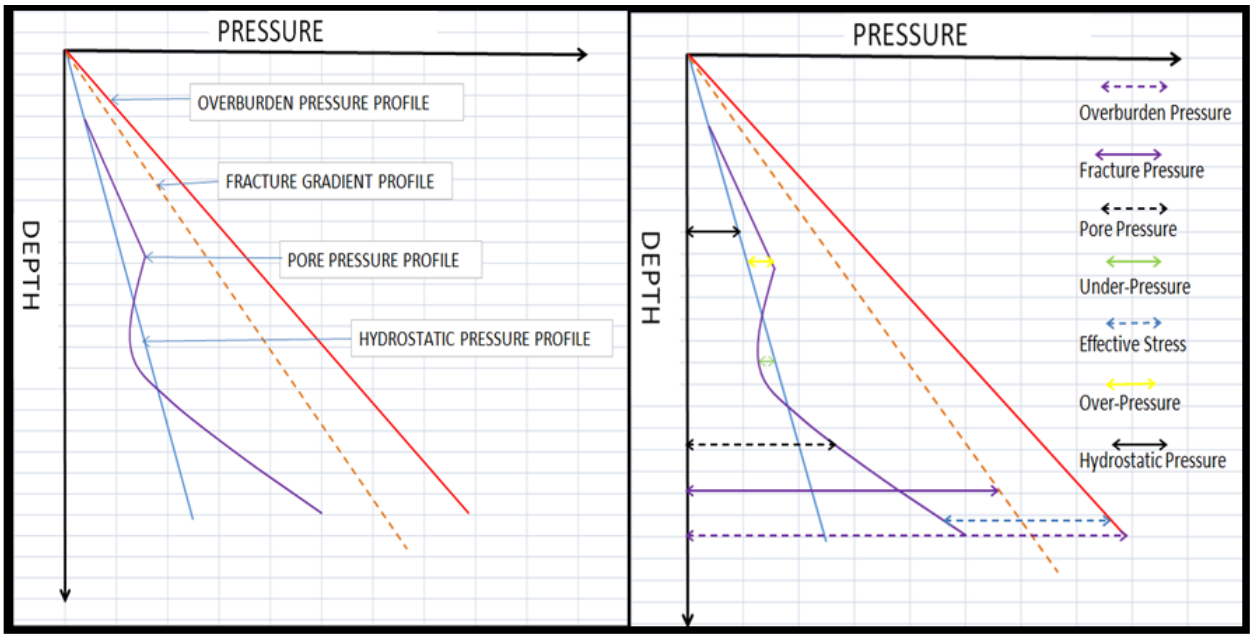

Figure 3.1. Schematic pressure–depth plot with illustration of typical terminologies used in pore pressure work.

pressure, but since its value is small, it is often neglected without introducing significant error. Hydrostatic pressure is thus calculated using equation 3.1:

$$P_h = \rho\, g\, H \qquad (3.1)$$

where P_h = hydrostatic pressure, ρ = average density of fluid, g = acceleration due to gravity, and H = vertical height of water column. It may also be expressed as the rate of change of hydrostatic pressure with depth, i.e., the hydrostatic pressure gradient as in equation 3.2:

$$dP_h / dH = \rho\, g \qquad (3.2)$$

For this project, a water density value of 1.025 g/cc (0.433 psi/ft) was used as the average formation water density.

Overburden pressure

The overburden pressure (OVB), also commonly referred to as overburden, lithostatic or vertical stress, is the pressure exerted at a particular depth by the weight of overlying sediments including the fluid it contains. In general, when density data are unavailable or unreliable, an overburden gradient of 1 psi/ft is often used as the default. But when data are available, a more realistic evaluation based on lithology and density coupled with knowledge of local geology is preferable. For OVB estimation in this project, the density at mudline varies over the range 1.45–1.75 g/cc. In contrast, bottom-hole densities vary over the range 2.5–2.85 g/cc. The low density values at mudline are based on the limited data available from the shallow sections of wells. Calculated OVB gradient values for this project range from 0.8 to 0.9 psi/ft. The greatest challenges with OVB evaluation are any large gaps in the data and extrapolation of density data from below in the shallow section of the well where density was not logged.

The overburden stress, S_v, is estimated by using the relationship:

$$S_v = \rho_b Z \tag{3.3}$$

where ρ_b = formation average bulk density and Z = vertical thickness of the overlying sediment. The bulk density is the density of the entire rock, that is, the matrix and the fluid within the pores. This relationship is expressed as:

$$\rho_b = \rho_m (1-\varphi) + \rho_f \varphi \tag{3.4}$$

where φ = porosity expressed as a fraction, ρ_f = formation fluid density, and ρ_m = formation matrix density.

Pore pressure

This is the pressure exerted by the fluid contained in the pore spaces of the rock, and also known as the formation pressure. Pore pressure can be estimated indirectly by comparing expected (normal) and actual density, neutron, resistivity, or sonic responses from wireline logs. However, direct measurements can only be obtained in permeable rocks with wireline formation testing (WFT) and sampling tools, e.g., XPT, MDT, RCI, RDT, and DST. Measurement of pressure in impermeable beds, such as mudrocks, can only be inferred through pressure measurements within adjacent permeable beds or from indirect indications such as mud weight, cavings, gas, or rate of penetration (ROP) during the drilling operation.

Normal hydrostatic formation pressure

When the pore pressure profile equates to the hydrostatic pressure profile (Figure 3.1), the pore pressure is referred to as normal formation pressure. Abnormal formation pressure refers to formation pressure that is higher (overpressure) or lower (underpressure) than hydrostatic pressure.

Overpressure

When the formation pressure, P_p, exceeds the hydrostatic pressure at the same depth, the formation is said to be overpressured, and the overpressure, *OP*, equals the excess pressure:

$$OP = P_p - P_h \tag{3.5}$$

During predrill planning, zones with overpressure must be identified and adequate preparations should be made to drill through such zones efficiently. To achieve such safe and efficient drilling requires meticulous predrill planning, drilling practice and procedure, and surveillance while drilling. When the mud-weight is not adequate while drilling through a zone, this is usually

manifested on the mudlog in the form of: increased background gas, excessive cavings arriving at the shale shaker, increased mud tank volume, increased bit torque, and overpull during trip.

Underpressure

A zone is underpressured if the formation pressure is less than hydrostatic pressure at the same depth. It may be caused by pressure depletion in reservoirs under production (Figure 3.2).

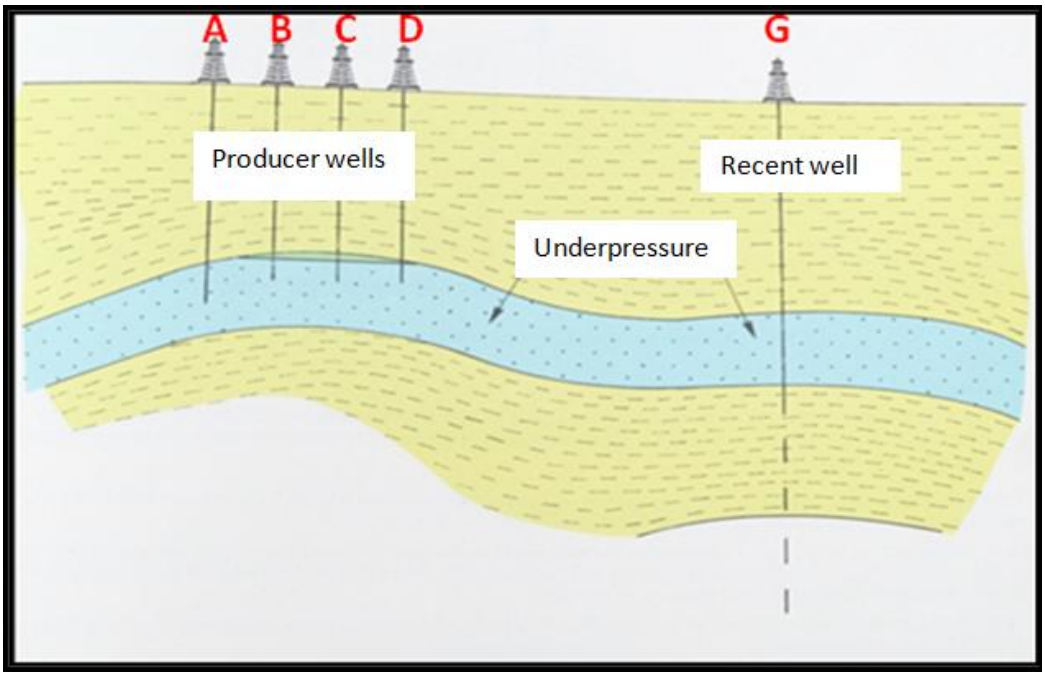

Figure 3.2. Example of underpressure due to reservoir depletion. Wells A, B, C, and D have been in production for some time, and without pressure maintenance (i.e., no injectors). New wells drilled into the same reservoir, such as well G, will be underpressured.

Vertical effective stress

The vertical effective stress, σ_v, is the difference between the overburden stress and the formation pressure. It cannot be measured directly, but it can be estimated using Terzaghi's equation:

$$\sigma_v = S_v - P_p \qquad (3.6)$$

Minimum horizontal stress

The brown dashed line in Figure 3.1 is the depth profile of the minimum horizontal stress, S_h, which is measured during a leak-off-test (LOT) below the casing shoe after drilling each section of hole (Mouchet & Mitchell, 1989). It is estimated as the minimum mud pressure required to hold open fractures in the formation. There is usually an interval of open hole of 3–5 m depth below the casing shoe in a compacted formation, and the LOT is run in this section of the hole to select a suitable mud weight for drilling the next section. The well is shut in and drilling mud is pumped into the well, with increasing pressure on the well bore. The pressure increase with time is monitored as shown in Figure 3.3. Point B is the fracture pressure, i.e., the pressure at which mud invades the formation – hence the drop in pressure. The leak-off pressure (LOP) obtained during an LOT indicates the maximum mud weight that can safely be used for drilling the next section of hole without tensile failure in the formation.

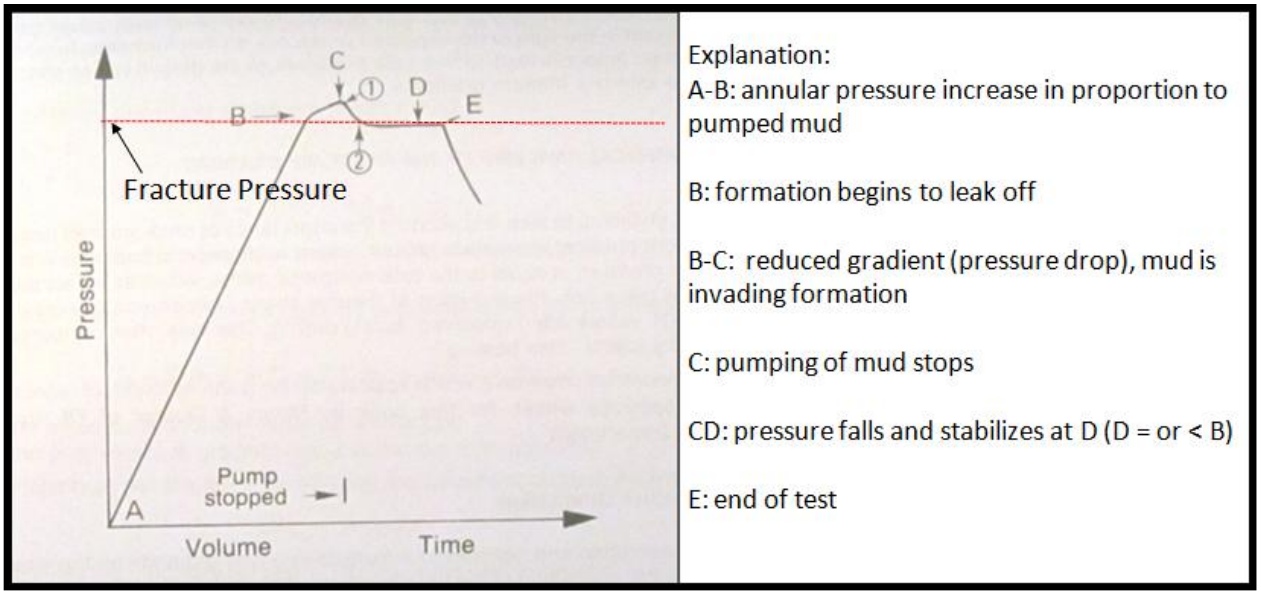

Figure 3.3. Example of LOT pressure–time profile. After Mouchet & Mitchell (1989).

A similar test to the LOT is the formation integrity test (FIT). The procedure and purpose is similar to the LOT, except that during the FIT the mud weight or pressure is increased to a predetermined value, without causing the formation to leak off, or fracture.

There are empirical methods suggested in the literature on how to estimate the minimum horizontal stress. In their survey of drilling engineers working for major operating companies, Yoshida et al. (1996) concluded that the methods due to Matthews & Kelly (1967), Eaton (1975), and Daines (1982) are the most popular, of which Eaton's method and then the method of Matthews and Kelly (1967) are the most widely used. In a similar study of deepwater Niger Delta wells, Ajienka et al. (2009) concluded that the method due to Matthews & Kelly (1967) is the most reliable method for fracture gradient estimation.

Maximum horizontal stress

The maximum horizontal stress, S_H, also cannot be measured directly during the drilling of a well, although it can be inferred from borehole breakouts seen on image logs or caliper logs, provided the caliper has four arms or more. In a tectonically active basin, knowledge of S_H is highly desirable in order to accurately determine the mean stress, and hence obtain a better estimate of pore pressure in tectonically active settings through estimating mean effective stress from porosity logs (Goulty, 2004). Several methods have been reported in the literature for estimation of S_H. For example, Bolas & Hermanrud (2002) reported methods using anelastic strain recovery, fracturing of intervals between packers, and calculations based on LOTs. A complete review is outside the scope of current study.

Supercharging

Supercharging is usually manifested as a very high pressure value in a dataset of WFT measurements. It is liable to occur in low permeability or tight zones, where drilling mud has been forced into the formation during drilling.

3.2 Overpressure generating mechanisms

In one of the earliest studies in the Gulf of Mexico (GOM), Dickinson (1953) described overpressure as incomplete dewatering. The term disequilibrium compaction, or compaction disequilibrium, has since been coined for Dickinson's mechanism, which is still thought to be the most common mechanism of overpressure generation in young, rapidly buried sequences of mud-rich sediment at depths down to ~2 km. Diverse additional mechanisms of overpressure generation have since been suggested, both for the GOM and for other basins around the world. Notwithstanding all the current debate on the magnitude of the various mechanisms, a driller should be aware that the additive contributions from the various mechanisms can make the difference between a successful and a catastrophic drilling operation.

Current thoughts on overpressure generation mechanisms can be classified into two main categories: firstly, loading mechanisms, which are related to stress; and secondly, fluid expansion mechanisms (Swarbrick et al., 2002). Another cause of overpressure in hydrocarbon accumulations is hydrocarbon buoyancy.

3.2.1 Loading mechanisms

If pore fluid cannot escape fast enough to stay in hydrostatic equilibrium as increasing compressive stress is applied, overpressure is generated. Increasing overburden stress as sediment is buried can cause overpressure by disequilibrium compaction. The other loading mechanism that may generate overpressure is increasing tectonic stress, which acts in the horizontal plane assuming that the vertical stress is a principal stress.

Disequilibrium compaction

This mechanism of overpressure generation is most common in Neogene and Quaternary basins with rapid sedimentation rates and low permeability sediment. In older basins, due to the transient nature of pressure, overpressure can only be preserved in thick, low permeability rocks, because excess pressure dissipates with time (Swarbrick & Osborne, 1998; 2002). During deposition in young basins, the weight of overlying sediment compacts and expels fluid from underlying, previously deposited sediments. However, if pore fluid is not expelled rapidly enough for the pore pressure to remain hydrostatic, the overburden becomes increasingly supported by the pore fluid, causing increased pore fluid pressure. In these circumstances, the sediment has higher porosity (lesser compaction) than it otherwise would have had at the same depth or interval. Using examples from Jurassic shales offshore mid-Norway and Miocene shales in the Lower Kutai Basin, Goulty et al. (2012) contend that disequilibrium compaction is only effective to depths where the temperature reaches ~100°C, below which chemical compaction takes place, largely independent of effective stress.

In such a system, with no lateral drainage, the velocity of expelled fluid relative to the matrix is governed by Darcy's equation:

$$V = -(k \rho_f g/\mu)\, d(OP)/dz \quad (3.7)$$

where k = sediment permeability, μ = viscosity of pore water; and $d(OP)/dz$ = overpressure gradient.

Tectonic compressive stress

This mechanism is similar to the process responsible for generating overpressure by disequilibrium compaction, but in this case the loading is by additional horizontal compressive stress caused by tectonics. Examples are found in geologically younger regions of the Earth's crust, e.g., Rocky Mountains, USA; mountain chains in Indonesia (Agip manual, 1980).

3.2.2 Unloading mechanisms

Unloading refers to a decrease in effective stress, either by a reduction in confining stress or by an increase in pore pressure. Confining stress is reduced by exhumation, and if fluid escape is restricted, overpressure may result. Other unloading mechanisms may be categorized as fluid expansion mechanisms, where the rock matrix restricts expansion of incoming fluid or an internal increase in fluid volume. Examples in this category include hydrocarbon generation, the cracking of oil and bitumen to gas, clay diagenesis, and aquathermal expansion (e.g., Bowers, 1995; Swarbrick & Osborne, 1998; Swarbrick et al., 2002).

Hydrocarbon generation (kerogen maturation)

The kinetics of this reaction is highly dependent on time and temperature (Swarbrick et al., 1998, 2002). Kerogen maturation contributes to overpressure by creation of lower density fluid from higher density kerogen. Unless sufficient fluid is expelled, the porosity and will not be consistent with the expected amount of compaction at a given depth. Conversion of kerogen to lighter

hydrocarbon is expected to occur at depths of 2–4 km and temperatures of 70–120°C (Tissot et al., 1987).

For example, the action of bacterial at shallow depth on organic material can produce biogenic methane. If such methane is generated within a closed system, it will increase the pore pressure. If the presence of such methane at shallow depth is not anticipated when drilling, the result can be catastrophic, especially in offshore drilling where blow-out preventers (BOPs) are absent when drilling the shallow section. High resolution seismic data can reveal shallow gas hazards predrill (Mouchet & Mitchell, 1989).

Cracking of oil and bitumen to gas

Another process related to hydrocarbon generation that is highly dependent on depth and temperature is thermochemical cracking. This involves the transforming of a heavier product to a lighter one, and transformation reaches a maximum at ~100°C (e.g., Mouchet & Mitchell, 1989). Barker (1990) suggested that conversion of oil/bitumen to gas occurs at depths of 3.0–3.5 km and temperatures of 90–150°C.

Clay diagenesis

Water is released during smectite dehydration and by the transformation of smectite to illite. Smectite dehydration occurs with release of water in pulses (Power, 1969; Burst, 1969). According to Swarbrick et al. (1998; 2002), the amount of water generated from the process is minimal and cannot generate significant overpressure. Furthermore, Colton-Bradley (1987) noted that overpressure slows the dehydration process.

However, Lahann (2002) and Lahann & Swarbrick (2011) have argued that sm-ill transformation involves ‘framework weakening’, by which they mean that the illitized mudrock

compacts to a lower porosity for a given effective stress state. Thus the mudrock tends to compact on sm-ill transformation, provided excess pore water can be expelled. Where expulsion of water is inhibited by low permeability, overpressure can develop. Water is also released during transformation of kaolinite to illite (Bjørlykke, 1998), and presumably can contribute to overpressure as for sm-ill transformation (Lahann & Swarbrick, 2011).

Conversion of smectite to illite requires the presence of potassium and may commence at temperatures of 65–70°C (Freed & Peacor, 1989). Bredehoeft et al. (1988), in Swarbrick el al. (2002) observed no change in the smectite–illite ratio in overpressured strata in the Caspian Sea Basin, at 6 km depth and a temperature of 96°C. This observation may be due to absence and/or low concentration of potassium.

Aquathermal expansion

Barker (1972) suggested that thermal expansion of pore water causes increase in pore pressure. The concept is based on the fact that water expands when heated, and if this happens in a closed system it will generate additional pressure. A major weakness with aquathermal expansion as a cause of overpressure is that it requires a system with a near-perfect seal to be effective, a condition that is near to impossible (Daines, 1982; Luo & Vasseur, 1992). Other objections include the association between temperature increase and reduced viscosity, and hence increased ease of fluid expulsion, and the fact that transitions into hard overpressure show evidence of some permeability (Mouchet & Mitchell, 1989).

Other mechanisms

There are other mechanisms of overpressure generation, generally considered to be of secondary importance: osmosis, hydraulic head, and density contrast.

Osmosis is due to large differences in formation salinity, causing fluid to flow across a semi-permeable membrane layer from a region of low concentration to high concentration. If the separating layers are not a semi-permeable membrane, or if they are fractured, osmotic flow will not occur. It is believed that the contribution from this process is minimal, and at most of local importance.

Hydraulic head contributes to overpressure where water-bearing porous rock, encased by impermeable rock, crops out at a higher altitude than the rig site.

Where an interval is hydrocarbon-bearing, the pore pressure is higher due to the buoyancy effect of oil and/or gas. Because gas density is less than oil density; for the same column height, buoyancy overpressure due to gas is higher than that for oil.

3.3 Worldwide examples of overpressure

Overpressure, though more common in young sedimentary basins, has been reported in virtually all sedimentary basins worldwide (Figure 3.4) and can occur in all lithologic types and formations of all ages. For example, cases of overpressure have been reported in the GOM, USA (e.g., Dickinson, 1930; Mello & Karner, 1996; Bowers, 2001); Wyoming Basin, USA (Evers et al., 1983); Niger Delta, onshore (Onuoha et al., 2009); Niger Delta, offshore (Swarbrick et al., 2011); Baram Delta, Brunei (Tingay et al., 2008); Taranaki Basin, New Zealand (Webster et al., 2010); Central Graben, UK North Sea (Daniel, 2000); and the Kutai Basin Indonesia (Ramdhan & Goulty, 2010). Due to lack of data and drilling activity, not much is known regarding overpressure in the Greenland and Antarctica areas (Mouchet and Mitchell, 1989).

Prior to drilling operations, it is pertinent to recognize the various overpressure mechanisms within the system. For example, Daniel (2001), Bowers (2001) and Katahara (2003) all suggested that overpressure calculation should take into account the mechanism of overpressure and this should inform the choice and/or modification of method.

Examples of basins where disequilibrium compaction is the predominant mechanism of overpressure include the US Gulf Coast (Dickinson, 1953; Pennebaker, 1968) and the Baram Basin (Tingay et al., 2009). Goulty (2012) noted that although the most commonly cited cause of overpressure is disequilibrium compaction, it is only a plausible explanation of overpressure down to depths of 2–4 km. At greater depths, mudrocks are in the chemical compaction regime where porosity generally decreases independently of effective stress, in association with ongoing chemical compaction.

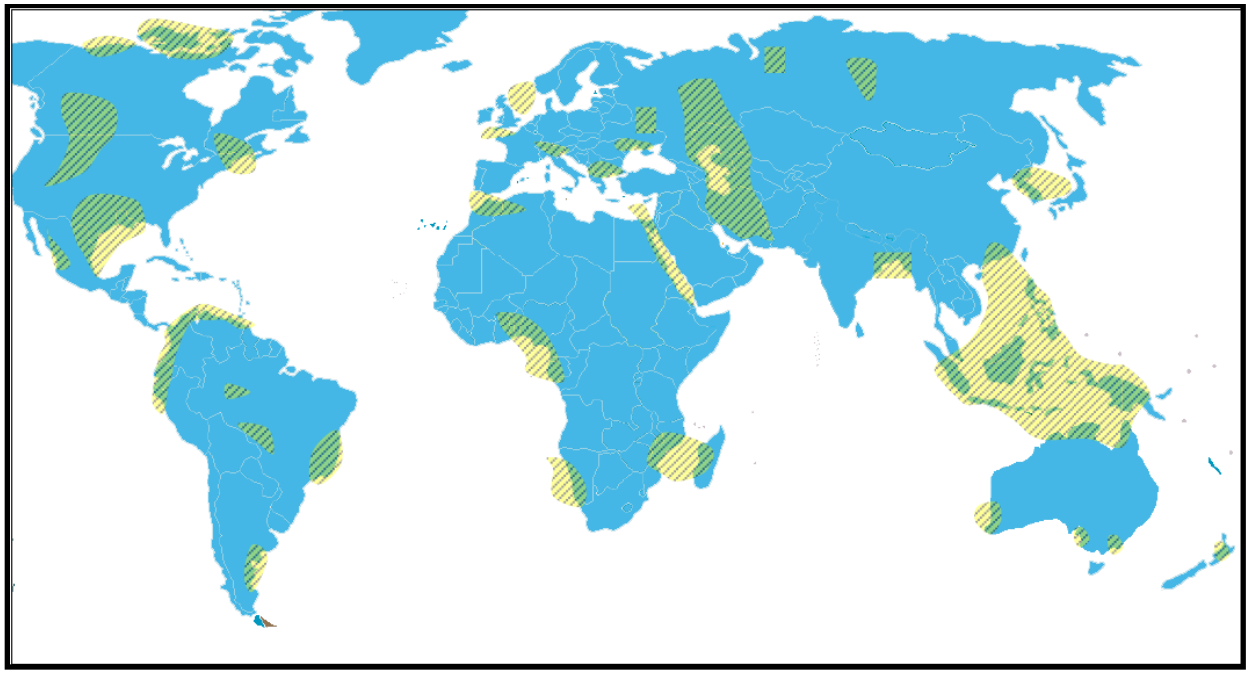

Figure 3.4. Map showing basins where overpressure has been reported. From Ramdhan et al. (2011).

3.4 Overpressure characteristics

As described in Section 3.2, the main mechanisms responsible for overpressure can be divided into two categories: loading by burial or tectonic compressive stress, leading to overpressure generation by disequilibrium compaction; and unloading processes that reduce the effective stress acting on the sediment, such as clay mineral transformations, gas generation, and lateral transfer (Swarbrick et al., 2002; Lahann & Swarbrick, 2011). The two categories of overpressure-generating mechanisms cause different characteristic trends in wireline logs and cross-plots. This section is a review of the common plots that can be used to infer whether overpressure is caused by loading and/or unloading mechanisms.

During burial, compaction of sediment proceeds rapidly at first, with decreasing porosity and increasing resistivity, density, and sonic velocity. As depth increases, the rate of compaction reduces. The "normal compaction trend" for any porosity log means the compaction trend when the pore pressure is hydrostatic and may be influenced by clay mineral transformations in addition to mechanical compaction processes (e.g., Dutta, 1987 cited in Bowers, 2001; Lahann, 1998). If a deviation from the normal compaction trend towards higher porosity occurs, that is an indication of undercompaction (Figure 3.5). There may also be apparent deviations from the normal compaction trend due to differences in lithology

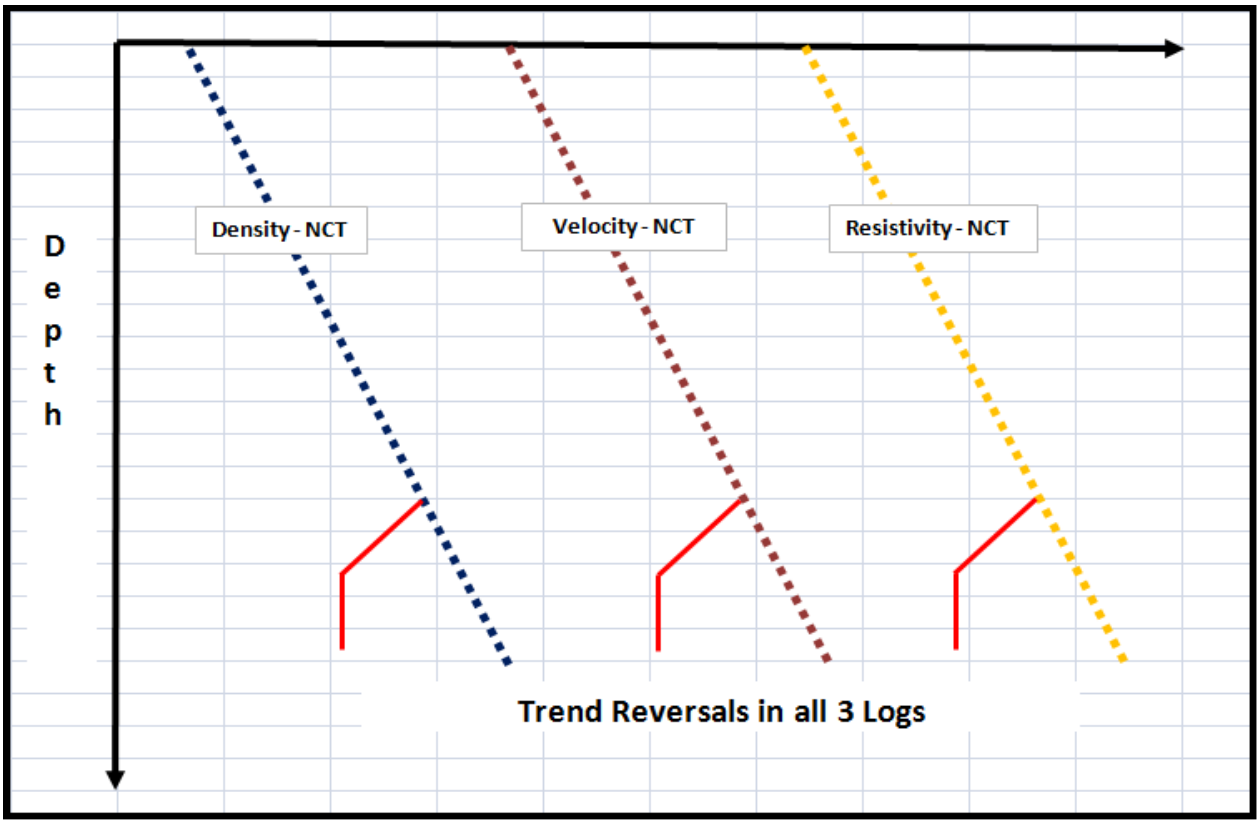

Figure 3.5. Schematic of density, velocity and resistivity vs. depth showing trend reversal.

In the case of unloading, overpressure is created as a result of fluid expansion or reduction of porosity. The pore pressure can increase at a much faster rate than the overburden, leading to decrease in effective stress as depth increases which commonly manifests as velocity reversal (Bowers, 2001). Katahara (2003) noted that, in unloading, significant decrease in sediment velocity is typically associated with large decrease in effective stress, but density is insensitive. In other words, unloading causes little or no change in density, whereas there is a significant reversal in velocity, and also in resistivity.

Bowers (1995, 2001), Katahara (2003) and Ramdhan & Goulty (2010) have used similar plots of depth against porosity, density, sonic velocity, and resistivity to infer the presence of

overpressure due to unloading. In Figure 3.6, both velocity and resistivity show obvious reversals, but minor or no change is noticeable on the density plot. This observation has been attributed by Bowers & Katsube (2002) to the nature and behaviour of storage and connecting pores of mudrock under the influence of stress. They pointed out that connecting pores have low aspect ratios and are mechanically flexible, whereas storage pores have higher aspect ratios and are relatively stiff (Figure 3.7). Sediment porosity is overwhelmingly in the form of storage pores, so the behaviour of storage pores dominates the bulk density log response. Opening of connecting pores has negligible influence on the bulk density, but does affect the sonic and electrical properties. It therefore follows that in fluid expansion or unloading, the density log response will be absent or minimal, while the sonic and resistivity logs should show significant responses.

Four useful plots for diagnosing overpressure and its causes are given below.

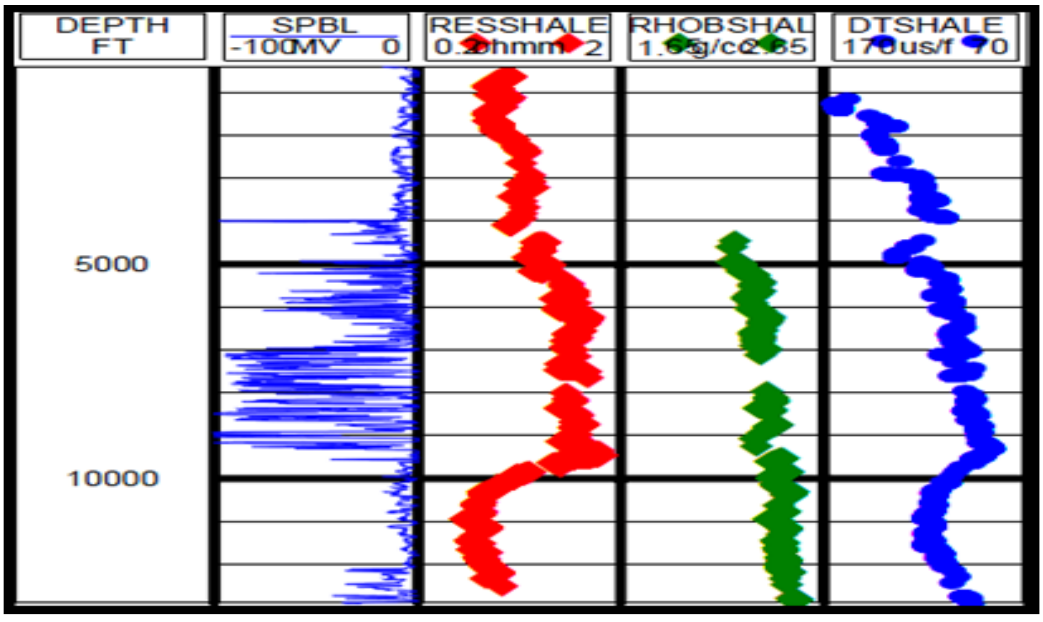

Figure 3.6. Example of reversals in resistivity (red) and sonic (blue) in a thick mudrock succession, but no reversal in density (green). After Katahara (2003).

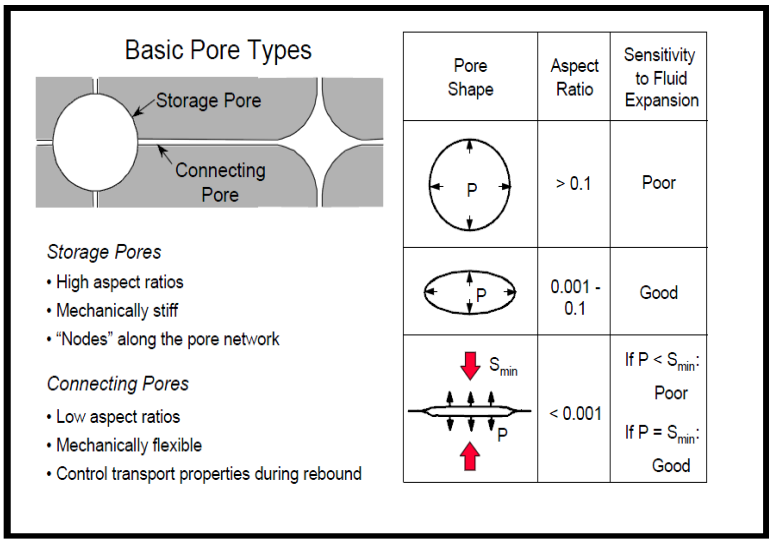

Figure 3.7. Model used to explain observed reversal in velocity and resistivity but no reversal in density when unloading is present. During unloading, high aspect ratio pores will not recover but low aspect ratio pores will recover and show as low velocity and resistivity. After Bowers & Katsube (2001).

Vertical effective stress–depth

As noted by Bowers (1995, 1998, 2001), Alberty et al. (2003) and Katahara (2003, 2006), a decrease in σ_v with depth is an indication of unloading. In contrast, Bowers (1995) pointed out that disequilibrium compaction does not cause σ_v to decrease with depth, nor does it cause a reversal in the sonic log, for example.

Sonic velocity–vertical effective stress

Borrowing from soil science terminology, Bowers generated a "virgin" curve from GoM data. This is a curve depicting sonic velocity, V_p, as a function of σ_v for a normal or undercompacted

formation. It implies that at great depth, when the rock is fully compacted, V_p approaches the sonic velocity in the rock matrix. However, if the mudrock is unloaded, V_p follows a higher trend for given values of σ_v and plots above the virgin curve (Figure 3.8). In other words, not all of the porosity lost or density increase that occurred during loading is recoverable when sediment is unloaded. Lahann (2001) used a similar plot to distinguish between loaded and unloaded intervals (Figure 3.9). It has also been pointed out (e.g., Bowers, 1995; Katahara, 2003, 2006) that the unloading curve is not a single fixed curve above the virgin curve. In fact, its position above the virgin curve depends on the maximum effective stress experienced by the mudrock.

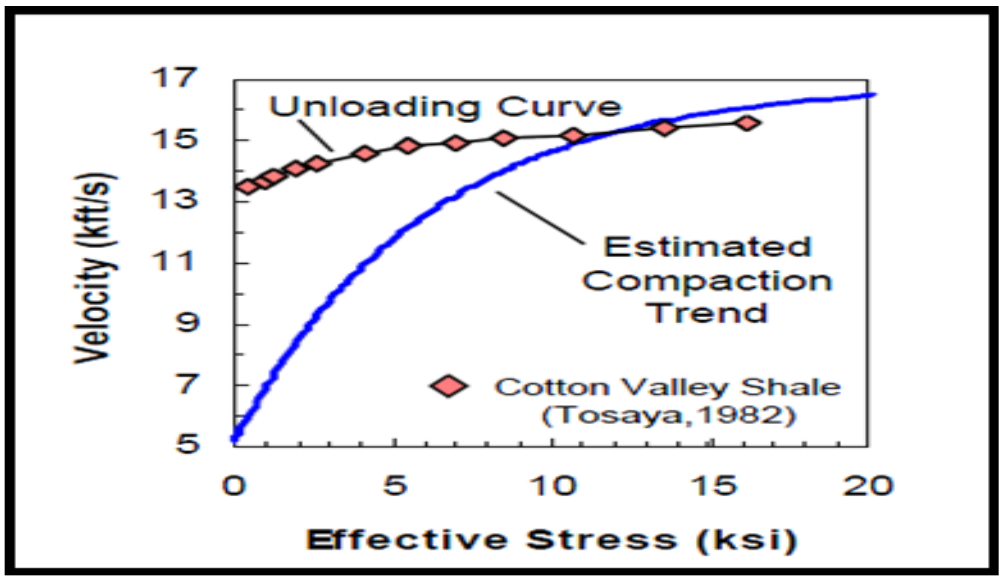

Figure 3.8. Plot of sonic velocity against vertical effective stress showing shale compaction and unloading trends. From Bowers (2001).

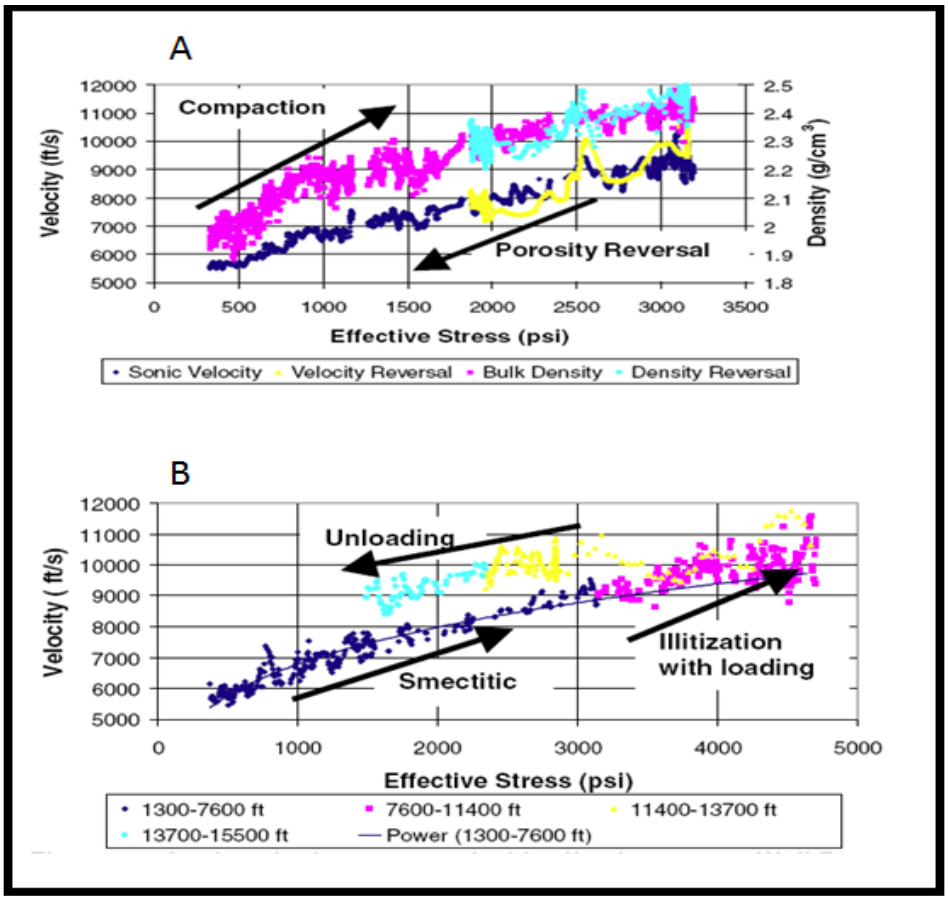

Figure 3.9. Plots of velocity against vertical effective stress for two wells, A and B, with density also plotted against vertical effective stress for well A. Well A has no unloaded interval; well B has an interval with unloading. Note that there are reversals in effective stress in both wells, but in well B the deeper section that is unloaded has a different trend from the shallow section. In well A, velocity tracks a single trend in both shallow and deep sections. From Lahann (2001).

Density–vertical effective stress

Lahann (2001) inferred sm-ill conversion with unloading by cross-plotting density and vertical effective stress. Figure 3.10 shows that intervals with smectite, and illitized shales (with loading) show a trend of increasing density with VES (a proxy for depth). Whereas, illitized shales with unloading shows VES reversal with constant or slight increase in density.

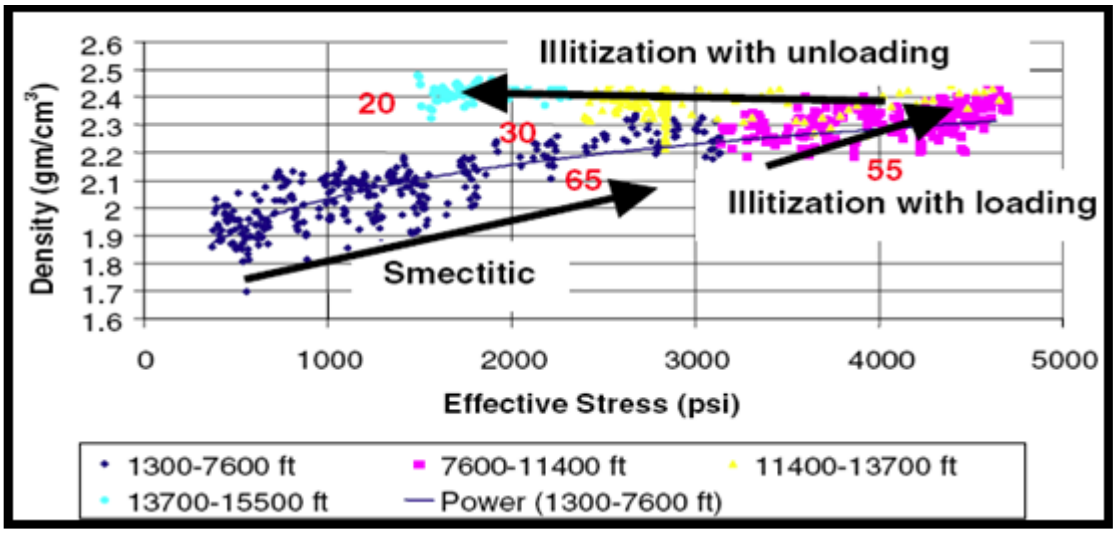

Figure 3.10. Plot of density against vertical effective stress showing shale responses during illitization in loading and unloading zones. The red figures are the expandability of I-S layers, in per cent, determined from XRD analysis. From Lahann (2001).

Rho – p-Sonic

The cross-plot of density against sonic velocity or transit time has been used to identify smectite to illite transformation in a system (e.g., Bowers, 1995, 1998, 2001, 2002; Lahann, 2001; Alberty & McLean, 2003; Katahara, 2003, 2006). The basic idea here is that smectite-rich shale plots on the green line and as the illite fraction increases the trend moves onto the red line (Figure 3.11).

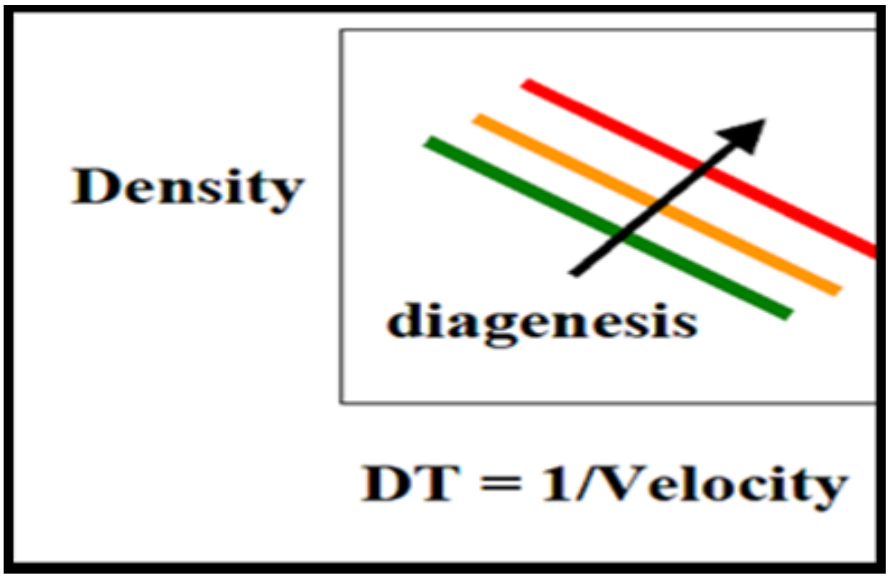

Figures 3.11. Density–sonic cross-plot. As the illite fraction increases at the expense of the smectite fraction, the compaction trend moves to higher density for fixed sonic transit time, or higher sonic transit time for fixed density. From Katahara (2003).

3.5 Overpressure estimation methods

This section deals with aspects of three methods used in overpressure estimation: firstly, the quantitative methods of pore pressure estimation, especially the equivalent depth method, Eaton's (1975) method, and Bowers' (1995) method; direct measurements of pore pressure using wireline formation testing tools (WFT), e.g., MDT, RCI, RDT, and XFT; and thirdly, methods used during drilling operations to detect overpressure, e.g., ROP, gas, cuttings/cavings, drag and torque, and drilling exponent, *D*.

Quantitative methods of pressure estimation from wireline logs require the establishment of a normal compaction trend (NCT) for each log type as an input in the workflow. The NCT should be established in the cleanest possible shale intervals. Shale pressure prediction is based

on the assumption that shale pressure is at equilibrium with pressure in the adjoining sand interval, an assumption that is not always true. What follows in the next couple of paragraphs is the theoretical bases for using NCTs in pore pressure prediction or estimation.

Sediment compaction is a function of mean effective stress and differential stress (Goulty, 2004), but traditional methods have generally been applied on the assumption that porosity is a function of vertical effective stress. The establishment of a NCT for any log type that is sensitive to porosity is based on the expectation of linear, exponential, logarithmic, or power-law functional relationship in the mudrock as a function of depth. For example, NCTs may be determined for density, sonic velocity or transit time, and resistivity as functions of depth.

An effort should be made to pick the cleanest shales for analysis by using, for example, the gamma-ray log response with one or more thresholds. (Matthews, 2004) cautioned against being excessively aggressive in choosing clean shale, and thereby limiting data density. Ramdhan & Goulty (2010, 2011) preferred to use neutron and density logs in combination to identify clean shales, with NPHI – DPHI >18% as their cut-off threshold. In this study, Gardner's (1974) shale–sand line crossplot and carefully selected threshold values for the gamma-log response, in API, have been used to select clean shale intervals. Bowers (2001) indicated that Gardner's shale line works well for shale density greater than 2.1 g/cc, but will generally overestimate shale density close to mudline. He therefore suggested a lower bound shale line to be used in conjunction with Gardner's upper bound trend. Gardner's shale-line velocity–density relationship is

$$V_p = (\rho_b/0.23)^4 \qquad (3.9)$$

where V_p is the velocity in ft/s and the units of bulk density are g/cc. With the same units for velocity and density, Bowers (2001) suggested a lower bound for sonic velocity in shale:

$$V_p = 4790 + 2953\,(\rho_b - 1.3)^{3.57} \qquad (3.10)$$

NCT from porosity logs

The NCT can be established by using either the linear or exponential form of Athy's (1930) equation:

$$\varphi = \varphi_o - cz \qquad \text{Athy's linear form} \qquad (3.11)$$

$$\varphi = \varphi_o \exp(-cz) \qquad \text{Athy's exponential form} \qquad (3.12)$$

where φ_o = initial surface porosity (%), c = compaction constant (m^{-1}), φ = porosity (%); and z = depth in (m).

Issler (1991) noted that the exponential form of the equation is the most commonly used; however, he has successfully used the linear form in more compacted areas of Beaufort-Mackenzie Basin of Northern Canada. According to Issler neither of the equations fits perfectly over his entire data range whenever overpressure is present. He therefore recommended a modified form of the equation over certain depth intervals. Dutta (2000) modified Athy's (1930) equation to the form:

$$\varphi = \varphi_o \exp(-k\sigma) \qquad (3.13)$$

where k = coefficient related to bulk density of sediment and density of pore water, and σ = effective stress.

There are other similar transforms for porosity computation that can be plotted against depth or effective stress. Depending on the log type available, a few of the commonly cited transforms in literature for NCT computation is presented below.

NCT from sonic (Δt) log

Where the sonic transit log is available, Ramdhan & Goulty (2011) used:

$$\Delta t = (\Delta t_0 - \Delta t_m) \exp(- b\, z) + \Delta t_m \qquad (3.14)$$

where Δt = transit time; Δt_o = initial surface transit time; Δt_m = matrix transit time; b = compaction constant (m^{-1}); and z = depth in (m)

NCT from resistivity log

$$R = R_o \exp(b\, z) \qquad (3.15)$$

where R = resistivity; R_o = initial surface resistivity; b = compaction constant (m^{-1}); and z = depth in (m) (Ikon's RokDoc training manual).

NCT from density log

The NCT can be constructed from density by applying Athy's (1930) or by first using transforms shown in equation 3.17 to convert density to porosity and applying applicable equation.

$$\varphi = (\rho_m - \rho_b)/(\rho_m - \rho_f) \qquad (3.16)$$

where φ = porosity (fraction); ρ_m = matrix density; ρ_b = bulk density; and ρ_f = fluid density (m).

The limitations of the NCT-based approach to the prediction of formation pressure have been pointed out by many. For example, the NCT does not adequately account for: lateral

transfer, shallow overpressure or choice of curve in shallow sections of hole (Swarbrick, 2001); variation of shale mineralogy (Swarbrick, 2001; Alberty & Mclean, 2003); the need to use the three mean principal stresses (Swarbrick, 2001; Alberty & Mclean, 2003; Goulty, 2004); fluid expansion contribution to overpressure (Osborne & Swarbrick, 1997; Swarbrick et al., 1998 in Swarbrick, 2001); and chemical compaction at depths >2–4 km (Goulty et al., 2012).

3.5.1 Overpressure estimation from wireline logs

For quantitative evaluation of pressure, the most common methods are equivalent depth, Eaton (1975), and Bowers (1995). The ultimate choice will depend on the pressure analysts and/or asset team preference and experience. The types of data needed for each method are listed in Table 3.1.

		Methods			
		Eaton	Equivalent Depth Method	Bowers	D-xc
Data	Interval Velocity (seismic)	Yes	Yes	Yes	
	Sonic (DT)	Yes	Yes	Yes	
	Resistivity	Yes			
	Conductivity	Yes			
	Density/Porosity		Yes		
	ROP_normarlized	Yes	Yes		Yes

Calibration Types	
Data	Quality
RFT, MDT,RCI, FMT, etc.	HIGH
DST	MODERATE
Kick	Low

Table 3.1. Data types that can be usedfor the different estimation methods.

Equivalent depth method

This is based on the assumption that every point on a log has an equivalent point on the NCT. In the example of Figure 3.12, the log response at 700 ft depth is the same as at 400 ft depth, where the pore pressure is hydrostatic, so the vertical effective stress is also assumed to be the same at those two depths, and hence the pore pressure may be estimated provided that the vertical stress due to the weight of the overburden can be calculated from density information.

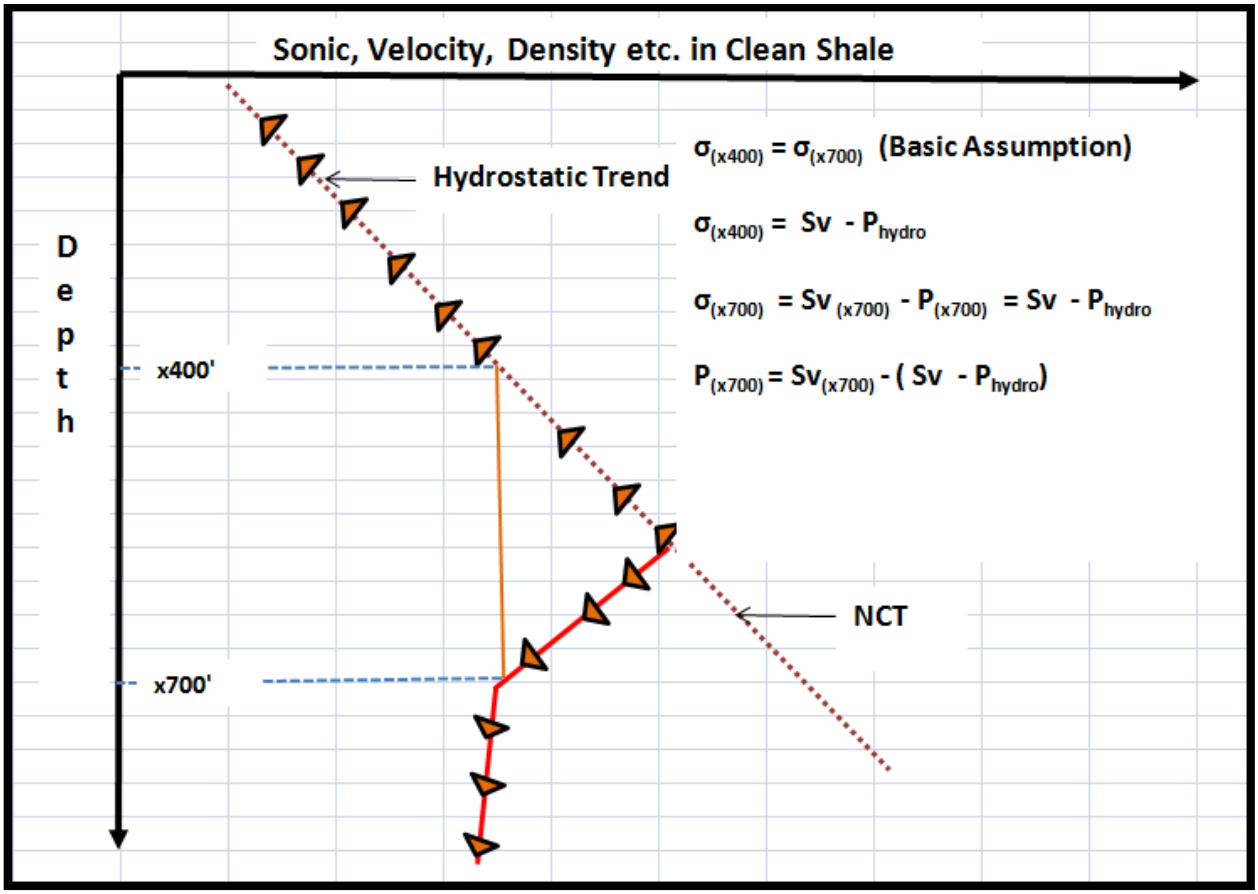

Figure 3.12. Illustration of the equivalent depth method for pore pressure estimation.

Bowers (2001) pointed out that, where mechanisms other than disequilibrium compaction are present (i.e., unloading mechanisms), the equivalent depth method under-predicts pressure.

Bowers (2001) gave some insight on how to determine when equivalent depth will not work for pressure prediction:

- By picking and cross plotting clean shale within the normal trend and the reversal trend, if all points plot on the same trend, the equivalent depth will work .
- In situations where all three logs (density, V_p, and resistivity) shows reversal, Bowers suggests picking similar points from each reversal and projecting them vertically until they cross the log at a shallower depth. If projected depths come out similar, the equivalent depth will work; but if the depth from density is deeper, the equivalent depth method will not work.

Eaton's Method

This is an empirically determined method based on data from the GOM. Eaton's method is based on the relationship that pressure is related to the difference between overburden and, the product of effective stress (from normal pressure zone) and ratio of log value inside reversal and log value on projected normal trend. Yoshida et al. (1996) in their survey, of mostly drilling engineers in the GOM, concluded that: The major operating companies still rely on the use of offset wells and history in combination with seismic for pore pressure work. Though the most commonly cited prediction methods are Hottman and Johnson (1969), Eaton (1975) and the Equivalent Depth method. However, Eaton's method, at times with modification of exponent, is the most commonly used for pressure prediction. Some commonly used forms of Eaton's equation are listed below.

Eaton's method from sonic log

$$P_p = S_v - [(S_v - P_h) \times (\Delta t_{norm} / \Delta t_{obs})^3] \quad (3.17)$$

where P_p = pore pressure; S_v = vertical stress; P_h = hydrostatic pressure;

Δt_{norm} = sonic velocity on normal trend; and Δt_{obs} = sonic velocity observed.

Alternatively,

$$P_p = S_v - [(S_v - P_h) \times (V_{p\,obs} / V_{p\,norm})^3] \quad (3.18)$$

where $V_{p\,obs}$ = velocity observed; and $V_{p\,norm}$ = velocity on normal trend.

Eaton's method from resistivity log

$$P_p = S_v - [(S_v - P_h) \times (R_{obs}/R_{norm})^3] \quad (3.19)$$

R_{obs} = Resistivity observed; R_{norm} = Resistivity in normal trend

Eaton's Method from DX or DXC Exponent

$$P_p = S_v - [(S_v - P_h) \times (DX_{obs}/Dx_{norm})^3] \quad (3.20)$$

Dx_{obs} = Dx observed; Dx_{norm} = Dx in normal trend

Bowers' method

Bowers (1995) accounts for shortcomings related to predicting pore pressure when unloading is involved in overpressure generation. To obtain what he termed the 'virgin curve' (NCT), data from GOM were empirically fitted to equation 3.21. And an unloading curve was also empirically determined to give equation 3.22. In Bowers (2001), he provided steps and

theoretical background on how to determine maximum past sonic velocity, in ft/s (V_{max}) and maximum past density, in g/cc (ρ_{max}) which were not presented in his 1995 paper.

(Bowers, 1995; 2001) suggested Equation 3.23, by combining equations 3.21 & 3.22, to account for pressure contributions from disequilibrium compaction and fluid expansion, by subtracting effective stress calculated from velocity from overburden to obtain pore pressure.

$$V = 5000 + A\,\sigma^{B} \qquad (3.21)$$

where V_p = velocity (ft/s), σ = effective stress (psi), A & B = obtained from regional velocity – effective stress calibration of offset wells.

$$V_p = 5000 + A\,[\sigma_{max}\,(\sigma/\sigma_{max})^{(1/u)}]^{B} \qquad (3.22)$$

$$\sigma = \sigma_{max}\,[1/\sigma_{max}(V_p - 5000/A)^{(1/B)}]^{U}; \qquad (3.23)$$

where U = clastic – plastic coefficient of mudstone.

3.5.2 Wireline formation testers

When measurements are taken by following strict and standard operating procedures this group of tools provides the most accurate and direct means of pressure measurement in the subsurface. Depending on the service provider, WFT tools in this category include Repeat Formation Tester (RFT), Reservoir Description Tool (RDT), Reservoir Characterization Instrument (RCI), Modular Dynamic Tester (MDT), and PressureXpress-HT Tool (XPT). Apart from the much older generation Formation Interval Tester (FIT), most of these tools are still very much in use today in oil fields around the world. Regardless of the service provider or tool, the operating principles are quite similar (Figure 3.13).

1. The tool is lowered in hole until zone of interest identified from correlation logs (GR, resistivity, and density-neutron) is reached.
2. A rubber packer is activated and forced against the wellbore until a seal is achieved, essentially isolating the probe inlet from the mud pressure, and estimating pretest mud hydrostatic pressure in the process.
3. The pretest chambers are than activated; the tool draws a small volume (~10 cc) of fluid from the formation causing pressure drop in the flow line.
4. The reservoir produces an equal amount of fluid to replace fluid drawn by the tool.
5. When the mass transfer in step 4 above is completed, formation pressure will equilibrate with the tool flowline pressure; hence measurement of static formation pressure can be accomplished.
6. The probe in step 2 is retracted at the end of the test and the mud hydrostatic pressure is measured again.

Depending on operational requirement these group of tools are capable of measuring downhole pressure and sampling of formation fluids. The newer tools downhole fluid analyzers (XFA) are capable of performing downhole fluid analysis. Table 3.2 shows some of the measurement specification for the different tools.

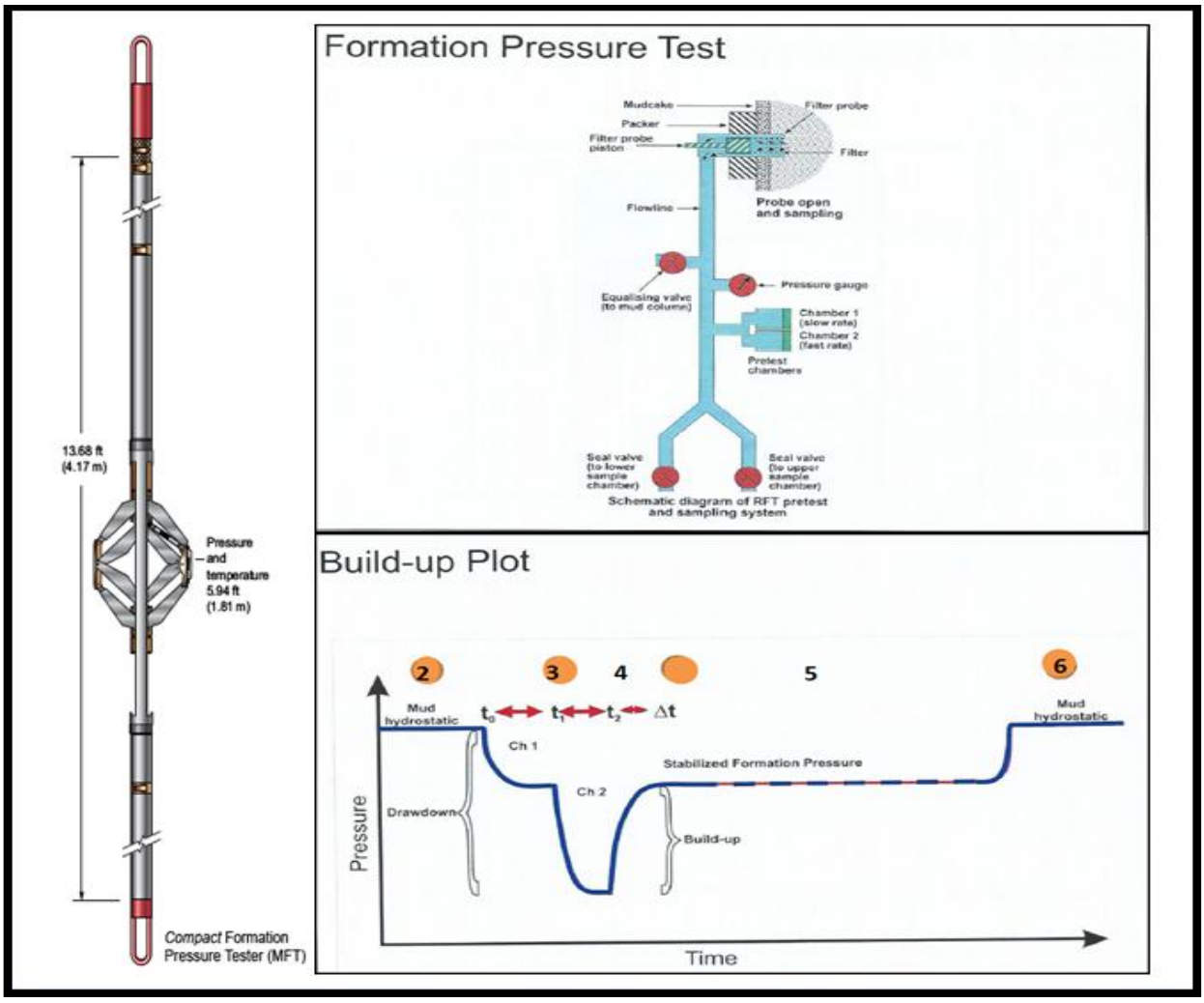

Figure 3.13. Schematic of typical WFT tool and pressure test profile.

Company		Schlumberger		Weatherford	Baker Atlas		Halliburton
Tool		RFT/MDT	XPT	MFT	FMT/RCI	RCX	SFT/RDT
Pressure Rating		20-25 Kpsi	20 Kpsi(138Mpa)	12.5 - 15 Kpsi	27 Kpsi(172.4Mpa)		20 Kpsi
Temperature Rating		350 -392 degF	450 degF (232 degC) 14 h	257 degF	375°F(191°C)		350 degF
Tool Diameter	Max	5"	4.0625" (10.32 cm)	3.5"	4.88"(124mm)		
	Min	4.75	3.75" (9.53 cm)	2.4"			
Hole Diameter	Max	no limit	15.4"(39.12 cm)	14"	24"(609.6 mm)		18"
	Min	5 5/8"	4.75"(12.07 cm)	3.86"	5.625"(142.9 mm)		6"
Strain Guage	Resolution	0.1- 0.2 psi					
	Accuracy	10 -20 psi		15 psi			
	Repeatability						
Quartz Guage	Resolution	0.01psi	0.01psi(29 pa/s)				0.01psi
	Accuracy	2-4 psi + 0.012% of reading	±0.02% of full scale + 0.01% of reading	3.2 psi + 0.01%			1psi + 0.01% of Reading
	Repeatability						1psi
Pretest Volume		0.005 gal				56cc to unlimited	0.1 - 100 cc
Depth of Investigation			0.45" (1.14 cm)				
Chamber Options		1 gal 2.75 gal 6 gal					1 - 5 gal
H2 S Rated		Yes YES			Yes		

Table 3.2 – Showing the tools specifications and operating conditions. (Obtained from respective companies website).

Table 3.2. Showing the tools specifications and operating conditions. Information from respective companies website.

3.5.3 Detection methods during drilling

Rate of penetration (ROP)

ROP is an indication of how fast the bit drills through an interval. The expectation is that, if drilling parameters are kept constant, ROP should decrease with depth due to increased compaction of rock with depth. Therefore, increased ROP or any deviation from increasing trend could potentially be due to undercompaction which is typically associated with overpressure. However, because parameters such as weight on bit (WOB), revolutions per minute (RPM), hydraulics, and mud weight are hardly ever kept constant, ROP may increase or decrease independent of the sediment compaction state. When available, normalized ROP used in conjunction with other indicators is a more accurate means of inferring undercompaction during drilling. Examples of normalized ROP including the D-exponent are discussed later in the section.

Gas shows

Progressive increase in trip gas (TG), background gas (BG), and connection gas (CG) are all pointers to a likely UBD situation and should be investigated before drilling progresses. In most cases it will require circulating out the gas by circulating bottom up (CBU) and increasing mud weight. While on bottom drilling, the equivalent circulation density (ECD) is typically high enough to balance the pore pressure and the gas produced from formation. When circulation is stopped, the equivalent static density (ESD) is typically lower than the ECD. If the ESD is lower than pore pressure, both liberated and produced gas enters the mud and will show as increased TG, BG, and CG. If the situation is not arrested, with each pipe connection; CG dilutes the mud further causing further drop in mud weight and progressively higher CG is recorded.

Cavings and cuttings

The type, shape, size, and quantity of carvings/cuttings may be indicative of overpressure or UBD. In particular splintery, curved and large quantity of cuttings are typical in UBD situations (Figure 3.14). Cavings can also be produced due to bedding plane instability but these generally have distinct shape (i.e. blocky) and appears to be "man made", this occur more at connection (ESD < PP) and, increasing MW typically worsens the situation. Information on nature of cavings and cuttings obtained from mudlog, drilling data, and end-of-well-report (EOWR) is used in corroboration with other data to infer UBD.

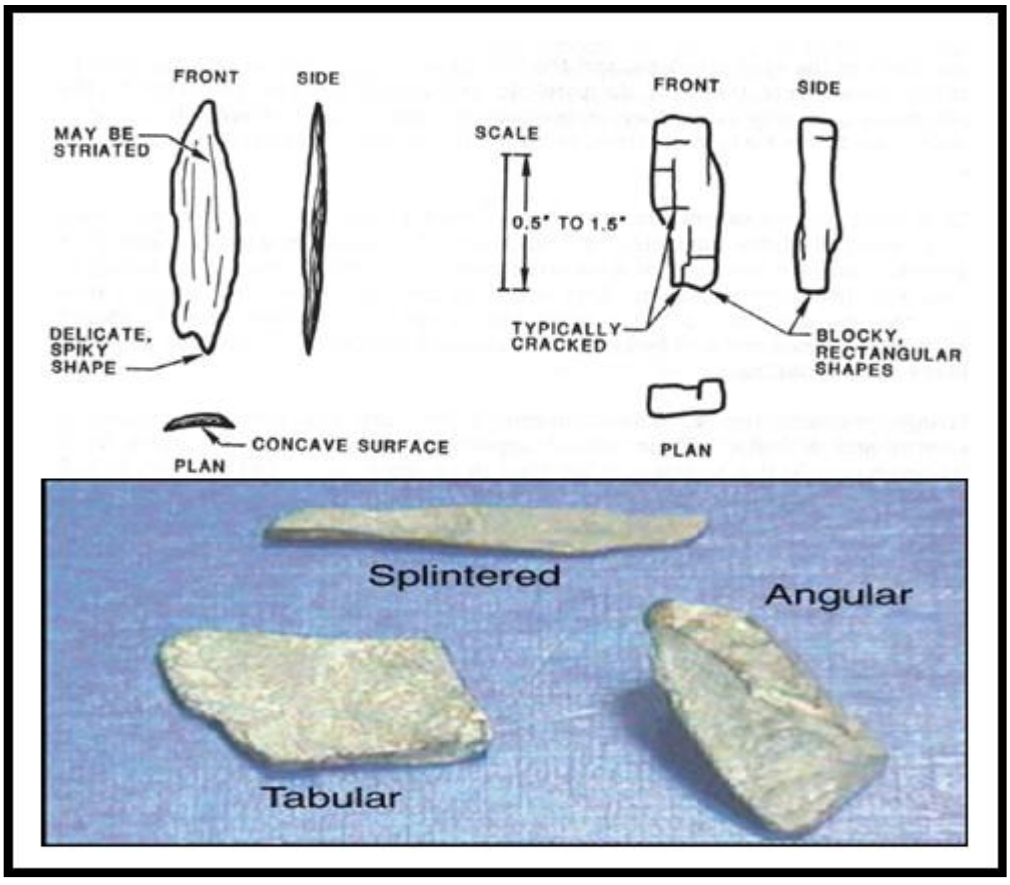

Figure 3.14. Typical cuttings character seen in underbalanced situation; blocky cuttings are in general, not indicative of UBD.

Torque

The torque should increase with depth due to contact between drill string and wellbore. In the underbalanced situation, the hole will "flow" into the bore leading to increased string-to-wall contact and consequently increased torque. Bit balling, BHA configuration, hole deviation, and instability that is unrelated to formation pressure may also cause increase in torque. Modern drilling rigs and mudlogging units now have the capability to differentiate between downhole and surface torque. Balling up may be indicative of a pressure transition zone and is typically characterized by a steady torque reading.

Mud weight (MW)

With constant mud weight going in hole, if MW(out) is lower than MW(in) this is a typical indication that the well may be flowing and the well is underbalanced.

Overpull and Drag

Overpull may be noticed on the hookload while pulling out of hole (POOH) or picking up off-bottom, in which case the hookload reads higher than the free weight of string. Drag refers to difficulty in getting back on bottom freely, and some value of WOB may be shown when in fact the bit is not on bottom. Both overpull and drag are caused by hole pinching or cutting debris downhole, which may not always be due to underbalanced drilling.

Examples of normalization to ROP

Forgotson (1969) suggested direct use of drilling rate (ROP) to predict geopressure, basically equating increase ROP to geopressure (Fertl & Timko, 1971). It is now known, as pointed out earlier, that hole size, WOB, RPM, mud weight, and bit (type, wear, and hydraulics) may cause

increased or decreased ROP. To eliminate the effect of hole conditions and drilling parameters, ROP data must be normalized.

The D-exponent (Dx) was developed by Jordan and Shirley (1966), according to the equation:

$$Dx = [\log (R/60N)] / \log (12W/10^6B); \text{ or} \quad (3.24)$$

$$R/N = a\,(W/B)^d \quad (3.25)$$

where R = drilling rate (ft/hr), N = rotary speed (RPM), W = weight on bit (pounds), B = bit diameter (inches), a = lithology constant, and d = compaction exponent.

Dx is dimensionless and sensitive to differential pressure, hence can be used to adjust the mud weight as drilling progresses. In general, Dx is expected to increase with depth if lithology is constant and pore pressure is hydrostatic, but decrease in overpressured zones (Figure 3.15). However, Dx is not corrected for mud weight; increased mud weight during drilling generally decreases ROP but increases Dx, making the interpretation difficult in such situations.

The corrected D-exponent (Dxc) is similar to Dx in principle, but with normalization for mud weight. However, bit (type & wear), hydraulics, lithology, and compaction are not corrected (Agip in-house manual, 1980).

Some points to bear in mind when using Dxc for pressure detection are the following: (1) use only trends in shale; (2) trends will typically change with bit and hole size changes; (3) do not use in sections with controlled drilling or sliding; (4) trend more reliable when drilling with roller cone bits; (5) use in conjunction with other indicators; and (6) deviation from normal trend is indicative of transition zone.

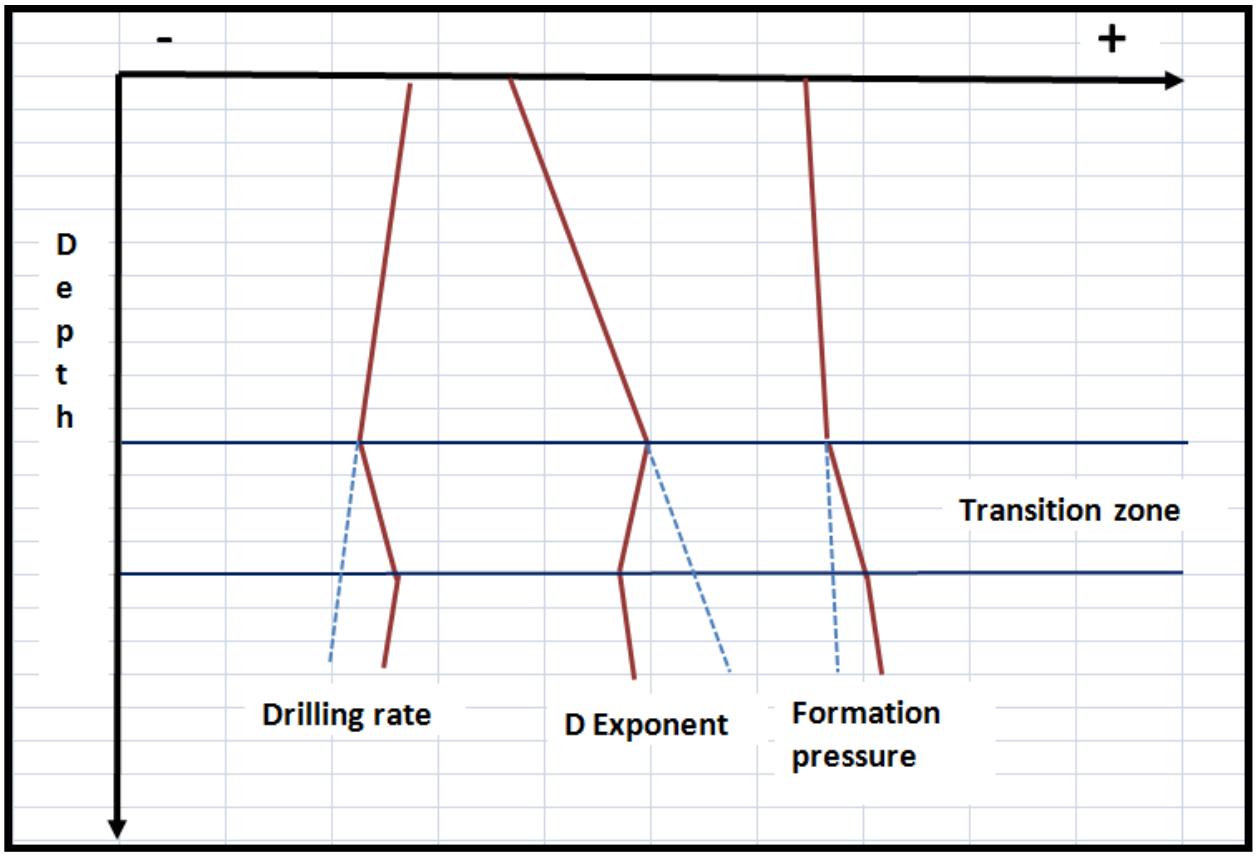

Figure 3.15. Idealized responses of drilling rate, Dx, and formation pressure with depth.

CHAPTER 4

Research Methodology

The wells used in this study are from the deepwater area of the Niger Delta Basin in water depths ranging from ~600 m to < 2000 m. In general, water depth < 200 m is typically considered shallow water, while depths from 200 m up to < 2000 m are considered to be deep water, and depths >2000 m are considered to be ultra-deep water.

Two general types of data were used for this project: data acquired during drilling of a well, and data prepared or acquired after drilling of a well (i.e., after abandonment). The first data type includes wireline logs, logging while drilling (LWD) logs, wireline formation tester (WFT) results, mudlogs, and drilling logs. The second group of data includes end-of-well reports (EOWRs), comprising both drilling and geological reports. It should, however, be noted that complete sets of data were not available for some wells. What follows is a review and examples of how the different datasets were used in this study. For a well to be included in this study, at the minimum, it should have acceptable quality of wireline or LWD logs, pressure data, and corresponding EOWRs.

4.1 Data acquired during drilling

4.1.1 Wireline and LWD logs

A sample of a typical wireline log suite from the study area is shown in Figure 4.1. Before using the wireline and LWD logs, they were quality checked for the accuracy of the log heading, logger's remarks, depth discrepancies, correct scaling, spikes and gaps, cycle skipping in sonic

logs, and consistency of log curves over repeat sections and with offset wells. Logs that do not meet the QC standard were excluded from the study.

As a preliminary discrimination step in identifying clean shale, a cross-plot of shale velocity against density was used to determine the shale trend for each well, assuming that the trend should follow a Gardner-type relationship (Gardner et al., 1974). The API value on the GR log for the shale baseline was picked by visual inspection of the GR log, and then applied as a cut-off. Where feasible, a resistivity filter was also applied for further discrimination of 'clean' shale. The GR cut-off value for shale varies from well to well over the range 65–95 API. Several authors (e.g., Mathews, 2004; Katahara, 2008) have pointed out that use of the GR alone to discriminate shale can be very misleading, especially in radioactive sands; other thresholds/discriminators should be applied in addition to the GR API value. In the following paragraphs, the different plots generated from wireline and LWD logs are described. The generated data are required input to enable proper evaluation and estimation of subsurface pressures from shale.

Shale volume

The volume fraction of shale, V_{sh}, is generated from the GR log through Ikon Science's RokDoc software using the standard equation:

$$V_{sh} = (GR_{log} - GR_{sd})/(GR_{sh} - GR_{sd}) \quad (4.1)$$

where GR_{log} is the log response, GR_{sh} is the log value in clean shale, and GR_{sd} is the log value in clean sand. The V_{sh} output is also used as additional filter in picking clean shale during NCT generation, and for pore pressure estimation using the equivalent depth method. An example of a V_{sh} plot is shown in track 5 of Figure 4.1.

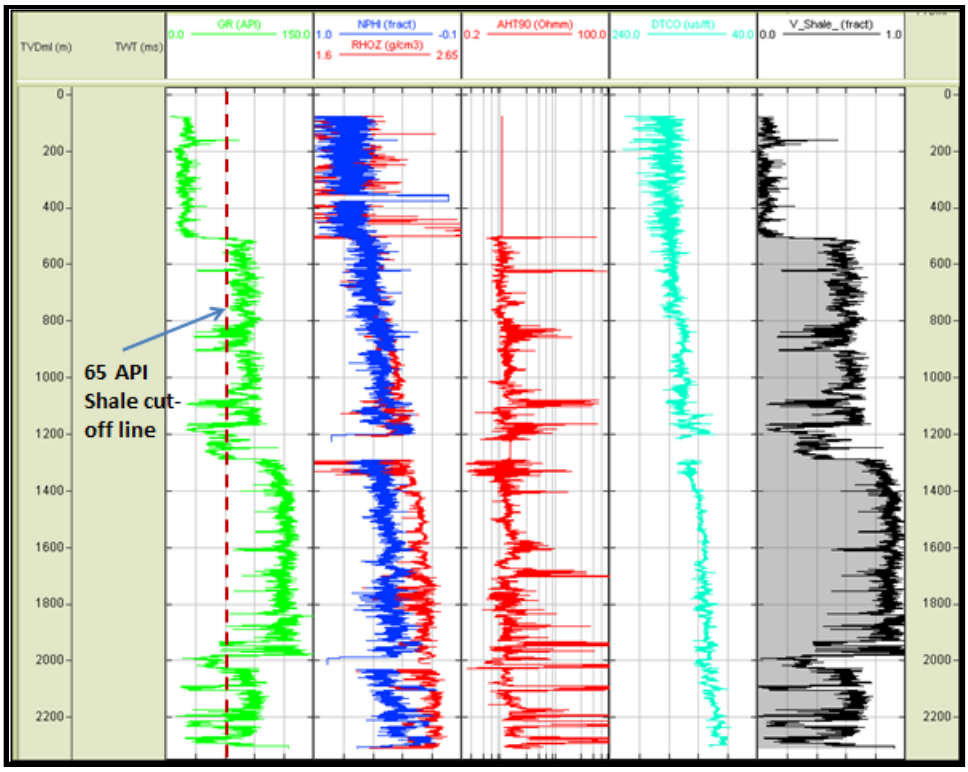

Figure 4.1. Example wireline log from a deep water Niger Delta well. Track 1 shows the natural gamma ray (GR) log, track 2 the density and neutron logs, track 3 is the deep resistivity, track 4 the sonic log, and track 5 shows the shale volume fraction.

Overburden stress

Estimation of the overburden stress (OVB) as a function of depth is typically required for predrill well planning. The estimates are also used in the determination of overburden gradient and in Terzaghi's equation relating vertical effective stress and pore pressure.

When the pore pressure becomes equal to or greater than the OVB, i.e., when the weight of the overburden is supported by pore fluid, the rock will fracture and the fractures will be approximately horizontal. As pore pressure increases, tensile and/or shear failure may occur (Secor, 1965 cited in Grauls & Cassignol, 1993). Tensile failure occurs under the conditions

$P_p > S_3 + T$ and $S_1 - S_3 \leq 4T$ (4.2)

where T is the tensile strength of the formation and S_1 and S_3 are the maximum and minimum principal compressive stresses, respectively. But if tensile failure has already occurred in the formation, the condition for the reopening and propagation is governed by the relationship

$P_p > S_3$ with $T \approx 0$ (4.3)

In order for the pore pressure to reach, or exceed, the OVB, the orientation of S_3 must be vertical.

Figure 4.2 is an example of OVB estimation from one of the wells in the study area. The OVB is calculated from bulk density log using cumulative summation of the sediment weight for each depth interval.

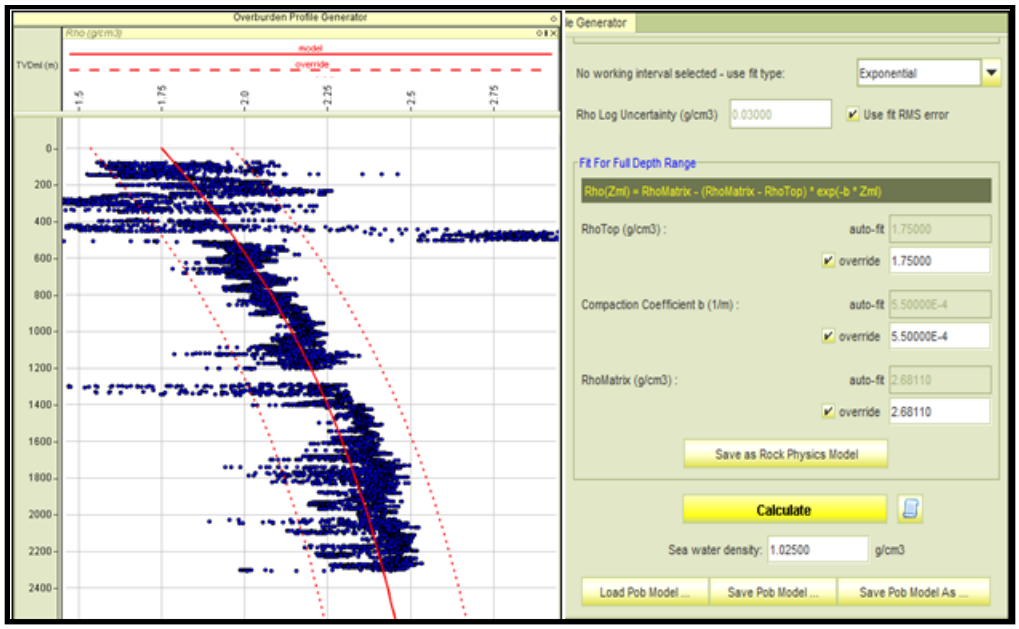

Figure 4.2. Sample OVB generated from the density log.

The shallow sections, from mudline to about 800 m, in most of the wells in this study do not have density logs due to lack of interest by operators and the lack of availability of a suitable tool for the shallowest (large hole) part of the section. In such cases, determination of seafloor density was based on experience, knowledge of the sedimentation rate, mudlog data, and a trial-

and-error approach. Based on Monte Carlo simulation, Mathews (2004) suggested that the impact of density variation on OVB calculations is generally small due to the weighted average nature of the estimation method. However, he noted that the impact of inappropriate shallow density modelling can be quite significant. Although the OVB in this project was calculated with the aid of Ikon Science's RokDoc software, the principle is the same as when the OVB is calculated manually. Table 4.1 is a sample of manually estimated OVB.

MD(m)	TVDkb(m)	TVDss(m)	TVDSS(ft)	Interval Tickness (ft)	g/cc	psi/ft	Interv-OVB	Cum-OVB	Gradient psi/ft
0		0	0				214.56	214.56	0.000426
1435	1434.999	1408.779	4621.922	4621.922	1.024	0.443392	2049.323	2263.883	0.489814
1970.002	1970.001	1943.781	6377.157	1755.235	2.09	0.90497	1588.435	3852.318	0.604081
2259.578	2259.559	2233.339	7327.139	949.9819	2.008	0.869464	825.9751	4678.293	0.638488
2368.642	2368.563	2342.343	7684.759	357.6203	2.09	0.90497	323.6357	5001.929	0.650889
2537.145	2536.745	2510.525	8236.53	551.7715	2.18	0.94394	520.8392	5522.768	0.670521
2567.251	2566.786	2540.566	8335.089	98.55851	2.105	0.911465	89.83263	5612.6	0.67337
2625.228	2624.679	2598.459	8525.024	189.9354	2.17	0.93961	178.4652	5791.066	0.679302
2751.47	2750.842	2724.622	8938.94	413.9156	2.17	0.93961	388.9192	6179.985	0.691355
3143.777	3141.809	3115.589	10221.62	1282.685	2.303	0.997199	1279.092	7459.077	0.729735
3166.354	3164.329	3138.109	10295.51	73.88362	2.263	0.979879	72.397	7531.474	0.73153

Table 4.1. Sample manually calculated OVB using density log.

Normal compaction trend (NCT)

An example of an estimated NCT in the study area is shown in Figure 4.3. Because the NCT is a required input for pressure prediction using the equivalent depth method and Eaton's method, it must be as accurate as possible. The major challenges in constructing NCTs for wells in this study are estimation of the trend in the shallow sections of wells where density logs are not

available, and onset of overpressure in the shallow section of a well, making it difficult to establish the NCT even in the shallow section.

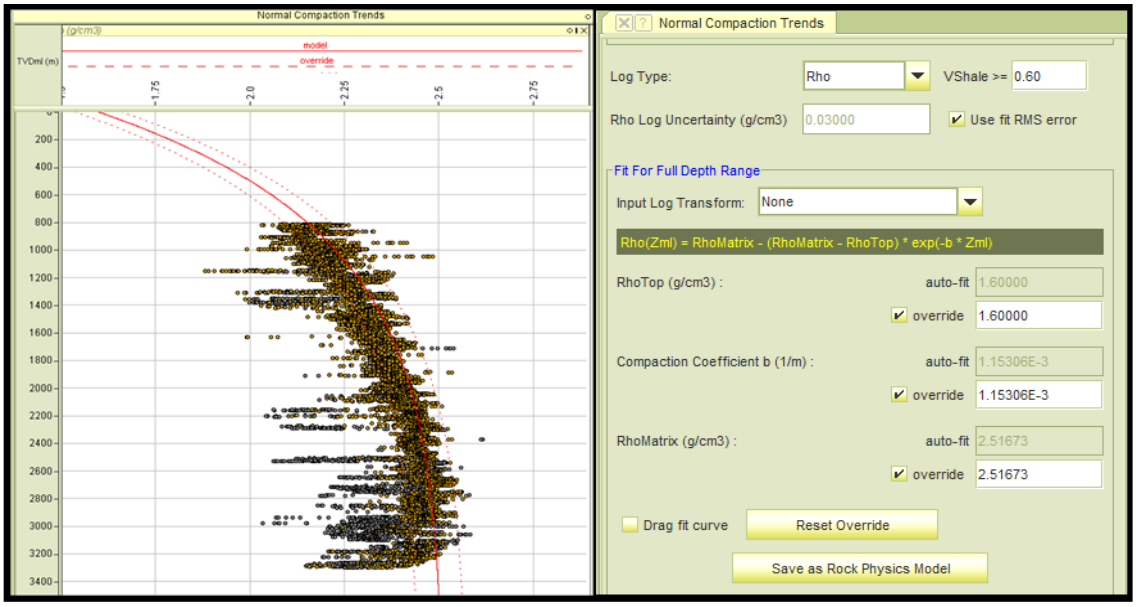

Figure 4.3. Sample NCT construction from a well in the study area.

Eaton (1975) has suggested that the NCT should be constructed using experience and every relevant available data. On the other hand, Matthews (2004) noted that most of the uncertainty associated with pore pressure prediction is related to the correct choice of NCT, citing an example for a resistivity log. Because limited velocity logs were available and are generally of low quality, the NCTs were mainly constructed using density logs.

4.1.2 Wireline formation tester data

Pressure data from WFT were provided by the operating companies, and depending on service provider comprise mainly: Reservoir Description Tool (RDT), Reservoir Characterization Instrument (RCI), and Modular Dynamic Tester (MDT).

Before using or accepting pressure data for use in this study, the following quality control procedures were followed:

1. Pressure data classified as 'GOOD' in the REMARK column were used – otherwise the data were discarded.
2. Tool measurements of mud hydrostatic pressure before and after a pipe change were compared, and should be reasonably close (< 1.5psi), depending on the tool type and its specified accuracy.
3. Pressure–depth data were plotted and compared with GR, resistivity, density and neutron logs; data points outside clean sands, within very thin or tight sand, and off depth were rejected.
4. Excessively low pressure values (likely due to depletion) or excessively high pressure values (likely due to supercharging) were rejected.
5. When available, DST or PVT data were used for validation.

Pressure data that have passed the QC process were then plotted against depth for further analysis. The resulting pressure–depth plot was used to:

- Identify zones of underbalanced drilling (UBD) by comparing the WFT pressure data and shale predicted pressure with mud weight used while drilling.
- Identify and quantify the magnitude of overpressure.
- Calculate effective stress by subtracting measured formation pressure from the OVB.
- Analyse cross-plots to identify any contribution of unloading to overpressure.

4.1.3 Temperature

The vast majority of temperature data used in this study are WFT measurements, and to a limited extent BHT measurements from wireline and LWD logs. When only BHTs from logs are available, linear extrapolation is used to estimate temperature for deeper interval. Some operators in the Niger Delta area have shown, based on regressed BHTs from logs with DST temperatures, that a 10% addition to the logged BHT is comparable to DST temperature measurements for the same interval (Operator's report, 2006).

Most of the temperature data are from measurements with MDT tools. MDT temperature may not represent the true formation temperature because of time required for formation temperature to stabilize after mud circulation. For more accurate formation temperature measurement, some operators are now using permanent downhole sensors to monitor reservoir properties including temperature over extended periods of time – months and years.

Nwachukwu & Chukwura (1986), Avovobo (1978) and Doust & Omatsola (1990) have all pointed out that the geothermal gradient in the Niger Delta varies and depends on where one is within the lithostratigraphic sequence. For example, the geothermal gradient for the Benin Formation is estimated at 1.3 to 1.8 deg C/100m, for the Agbada Formation at 2.7 deg C/100m, and for the Akata Formation at 5.5 deg C/100m. The variation of geothermal gradient is related to differences in sand–shale volume and hence thermal conductivity (Doust & Omatsola, 1990). The approach taken in this project is to use average temperature data calculated from wells within the same field. Temperature measurements and estimates have been used mainly to infer possible smectite-to-illite transformation, hydrocarbon generation, and cracking of oil to gas, i.e., to investigate whether unloading is contributing to overpressure.

4.1.4 Deviation survey

Deviation surveys were either acquired during drilling from LWD and MWD tools, or with a gyro survey after drilling each hole section. The main quality control checks were to ensure that the survey method is consistent with the default software (RokDoc) setting, and surface and bottom hole coordinates are accurate. The surveys are critical for use in calculation of TVD, interval true thickness, and the well path.

4.1.5 Mud log and drilling log

Information taken from the mud log and the drilling log was used to corroborate indications of UBD seen on pressure–depth plots. Such information includes rate of penetration (ROP), gas shows, cavings and cuttings, torque, mud weight, overpull and drag, and the corrected D-exponent, as described in section 3.5.3.

Tops and markers

Formation tops and marker horizons were provided by different operators in the Niger Delta. Difficulties with using the tops arose because the companies use in-house nomenclatures that are not transferable to other operators, and the criteria for picking tops varies from one company to another. Hence the tops used are specific to the individual well, or group of wells.

4.2 Data acquired after drilling

The end-of-well report (EOWR) provides a detailed summary of well operations from predrill to abandonment or completion. Relevant information in the form of plots, charts, graphs, and text were used to verify and clarify observations made on the pressure–depth plot.

4.3 Interpretation

The interpretation stage requires putting together all the information and observations from various wells in a cohesive and meaningful way. For this project, data interpretation involves, firstly, identifying the presence of overpressure and possible contributory mechanisms. This was done by evaluating compaction trends from density logs, and generating pressure–depth plots using the equivalent depth method. In addition, effective stress–depth plots using RokDoc software were generated after evaluation of sonic, density, and resistivity logs, the velocity–density cross-plot; the density–sonic transit time cross-plot, and the temperature gradient for the respective wells. Secondly, zones of UBD were identified by comparing WFT and shale-predicted pressures with the mud weight profile. Thirdly, evidence was sought from mud logs, EOWRs, and drilling data that are indicative of UBD within the zones of interest.

CHAPTER 5

Results of Shale Pressure Prediction and Underbalanced Drilling – Examples from AIW-EIW and NOW Wells

Thirty-six wells located in water depths ranging from 800 m to 2000 m were screened for this study. Most of the wells are located east of the Charcot Fracture Zone in the Southern Lobe of the deep water Niger Delta Basin (Figure 5.1). Wells selected for the study are spread across eight different fields and four operating companies. In AIW-EIW and NOW fields, six wells located in water depths from 1500 m to 2000 m and within 80 km of the Charcot Fracture Zone were screened for inclusion in the study. Specifically, well logs were quality checked for completeness of data, minimal or absence of spikes and gaps on logs, depth accuracy, accurate

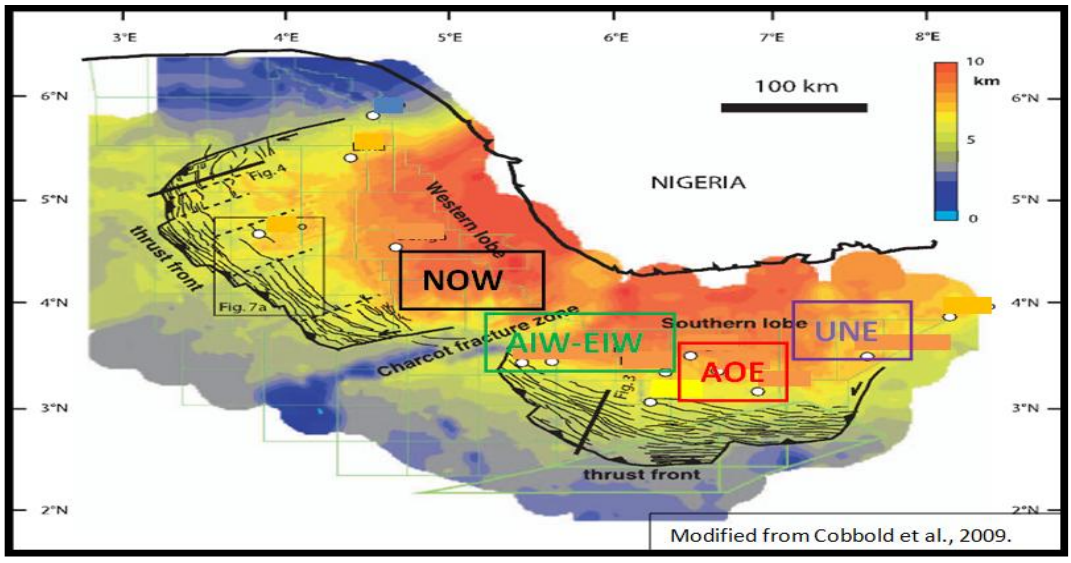

Figure 5.1. Map of Western and Southern sedimentary lobes in the offshore Niger Delta Basin, separated by the Charcot Fracture Zone. Approximate locations of NOW, AIW-EIW, AOE, and UNE fields are shown.

surveys and pressure data, and availability of mudlog and end-of-well reports. On average, 3–4 wells per field were analysed, depending on the availability and quality of well data.

Results for wells AIW-1 and 2, EIW-1, and NOW-1 and 2 are presented in this chapter. In chapter 6, results for UNE -4, UNE- 5, AOE-1, and AOE-4G1 are presented. The aims in this chapter are (1) to present the results of pore pressure prediction from density using the equivalent depth method; (2) report indications of the presence or absence of unloading as a contributory mechanism to overpressure development; and (3) identify zones with UBD, i.e., intervals drilled with lower mud weight than measured or estimated pore pressure gradients. The chapter begins with geological background information on the AIW-EIW and NOW fields in section 5.1. The data analysis is described in section 5.2, and the results wells identified with UBD from pressure–depth plots are presented in section 5.3.

5.1 Geological setting

5.1.1 Structural setting

The structural setting of the individual fields is sparingly discussed due to limited relevant data and/or lack of seismic interpretation from the operators. Based on regional data, there are three main structural provinces in the Niger Delta: from onshore (NE) to offshore (SW) the provinces are extensional, diapir, and toe thrust (Corredor et al., 2005) (Figure 5.2). Most deep water discoveries in Nigeria are in the inner thrust belt. Three discoveries that are not part of this study, Etan, Ikija, and Bobo, have recently been reported in the outer thrust belt.

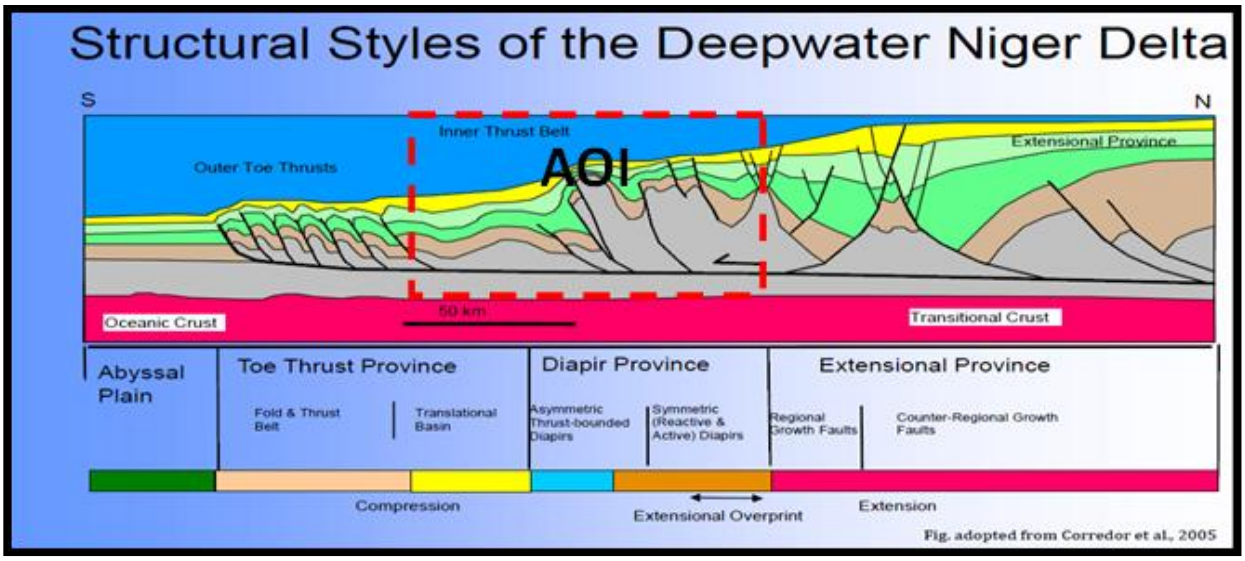

Figure 5.2. Structural styles of the deep water Niger Delta Basin showing the main provinces. Wells in this study are mainly in the diapir province and translational basin.

The wells in this study are located mainly in the inner thrust belt which comprises the mud diapir province and the translational basin of the deep water Niger Delta (Figure 5.2). Specifically, these are characterized by dome-shaped collapsed-crest structures and back-to-back faulting that may be antithetic or synthetic. In these areas, it is common to find pairs of faults with each fault dipping towards the crest, forming a collapse structure at the crest as compensation for overburden extension (Doust & Omatsola, 1990). Also common within the study area are blocks of northerly dipping strata that are bounded by closely spaced seaward dipping faults (Doust & Omatsola, 1990).

5.1.2 Chronostratigraphy

In the absence of high resolution palaeontological and core data, the chronostratigraphic intervals in the Niger Delta are quite difficult to place. For most wells in this project, the

chronostratigraphic tops were not provided and palaeontological data were not included. For example, the tops of the middle Miocene in wells AIW-1 & AIW-2 were given at 950 m true vertical depth below mudline (TVDml) and 1750 m TVDml, respectively. The tops provided for AIW wells were those used by a specific operator. There are no indications that the criteria used in establishing the tops are standardized or universal in the Niger Delta area. For wells the NOW field, a different operator from the AIW-EIW field, tops for standard chronostratigraphic nomenclature were not provided. The reason for the apparent inconsistency in naming of tops is due to the fact that the fields are operated by different companies with different in-house naming systems and different criteria for picking tops.

The chronostratigraphic tops for AIW-EIW wells are shown in Figure 5.3. Based on the available tops, intervals are thinner, sandier, and siltier southwards.

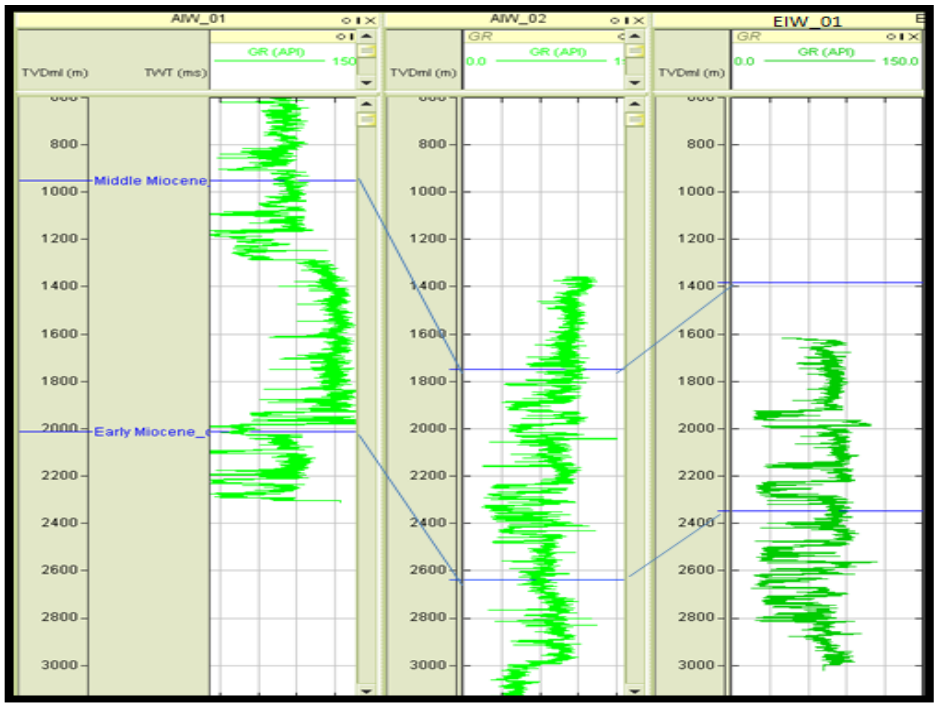

Figure 5.3. Stratigraphic tops example for wells AIW-1, AIW-2 and EIW-1.

5.2. Results of analysis for AIW-EIW and NOW wells

5.2.1 OVB

The OVB is generated from the density log (RHOB) using Ikon Science's RokDoc software. The software uses the following equation to generate the OVB:

$$\rho = \rho_m - (\rho_m - \rho_0) \exp(-bz) \quad (5.1)$$

where ρ is the density at depth z below mudline, ρ_m is formation matrix density, ρ_0 is density at mudline (seabed), and b is the compaction coefficient. Users have the option of constraining the top and bottom density, ρ_0 and ρ_m, and adjusting b until a suitable trend that fits the data is obtained.

Figures 5.4 and 5.5 show examples of OVBs generated for the AIW-EIW Field (three wells) and the NOW Field (two wells). Except where stated otherwise, all depth measurements are TVDml and pressures are in pounds per square inch (psi) - these choices are a matter of convenience and preference based on available data. The generated OVB is used as a proxy for maximum principal stress, and in the estimation of vertical effective stress.

The top and bottom densities observed in each well, even from the same field, show some variation. To generate the OVB for the AIW-EIW Field (three wells), a top density of 1.75 g/cc and a bottom density of 2.68 g/cc were used, whereas in the NOW Field (two wells) a top density of 1.8 g/cc and bottom density of 2.53 g/cc worked quite satisfactorily (Table 5.1). Both of these fields are within 80 km of the Charcot Fracture Zone, and the densities used to constrain the OVB are within the ranges used by other studies within the Niger Delta (e.g., GPT/Sonar Nigeria limited, personal communication). Overall, based on calculations using logged densities, the

overburden gradient ranges from 0.80 to 0.96 psi/ft. The leak-off pressure (LOP) data used are those acquired by operators during LOTs in compacted mudrocks. The pressure values obtained from this operation are used as a proxy for the minimum principal stress.

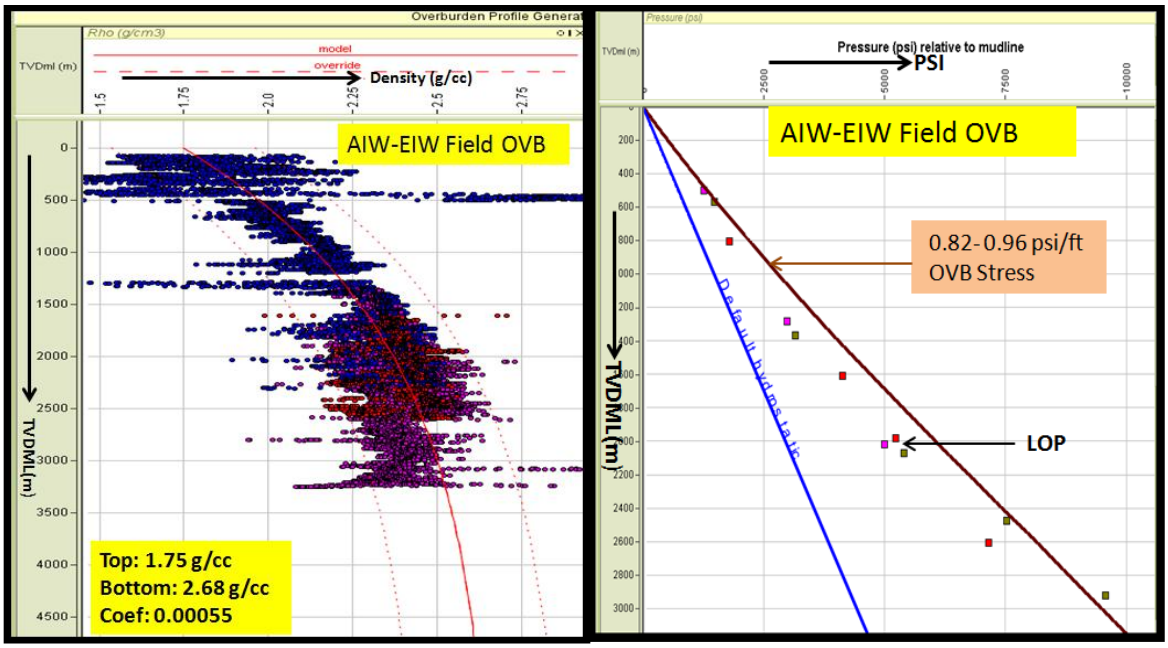

Figure 5.4. Left: Density profile generated for wells AIW-1, AIW-2 and EIW-1. Right: OVB stress profile for the same wells calculated from the density profile.

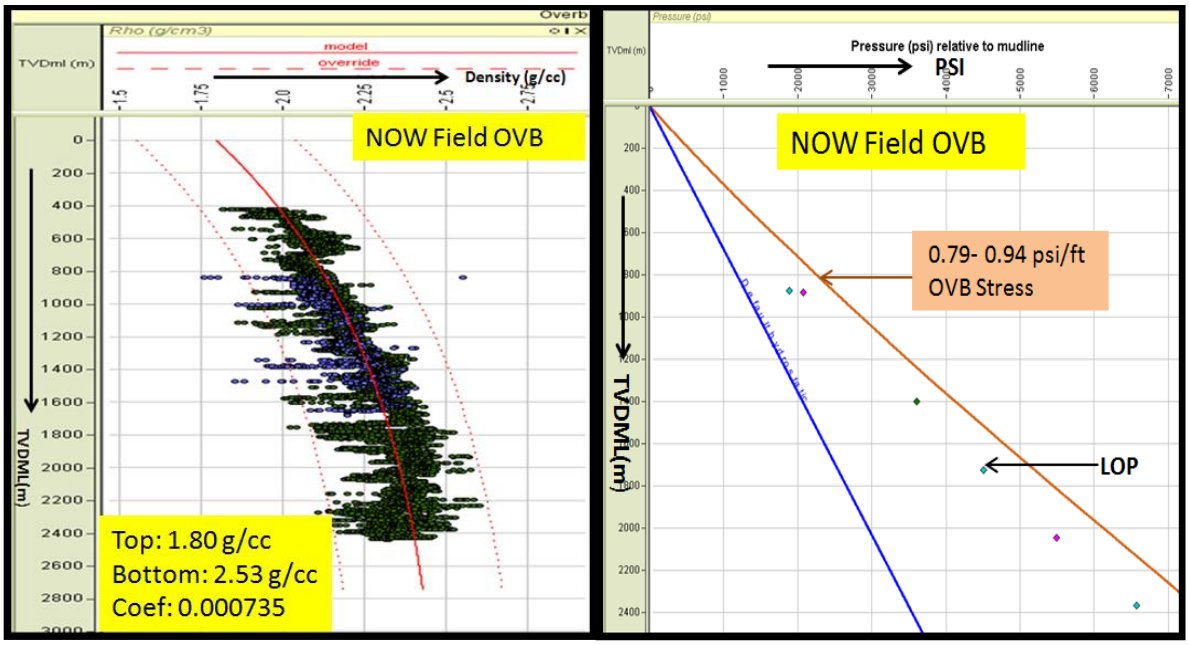

Figure 5.5. Left: Density profile generated for wells NOW-1 and NOW-2. Right: OVB stress profile for the same wells calculated from the density profile.

5.2.2 NCT

An NCT was generated for shales in each well with RokDoc using equation 5.1. Shales were selected using Gardner's velocity- density relationship (equation 3.9) as the first step (Figure 5.6). A GR cut-off value in the range 65–75 API was then applied as additional filter. A final constraint of $V_{sh} \geq 60\%$ (equation 4.1) was also applied, and the data points removed are greyed out zones in Figure 5.7.

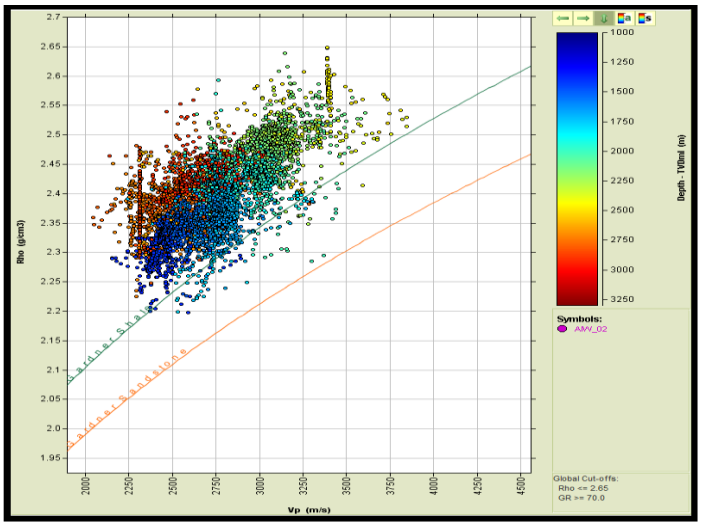

Figure 5.6. Gardner's plot of density against sonic velocity filtered with GR threshold of ≥65 API to pick data points from cleanest shales. The green line on the plot is the shale-bounding curve.

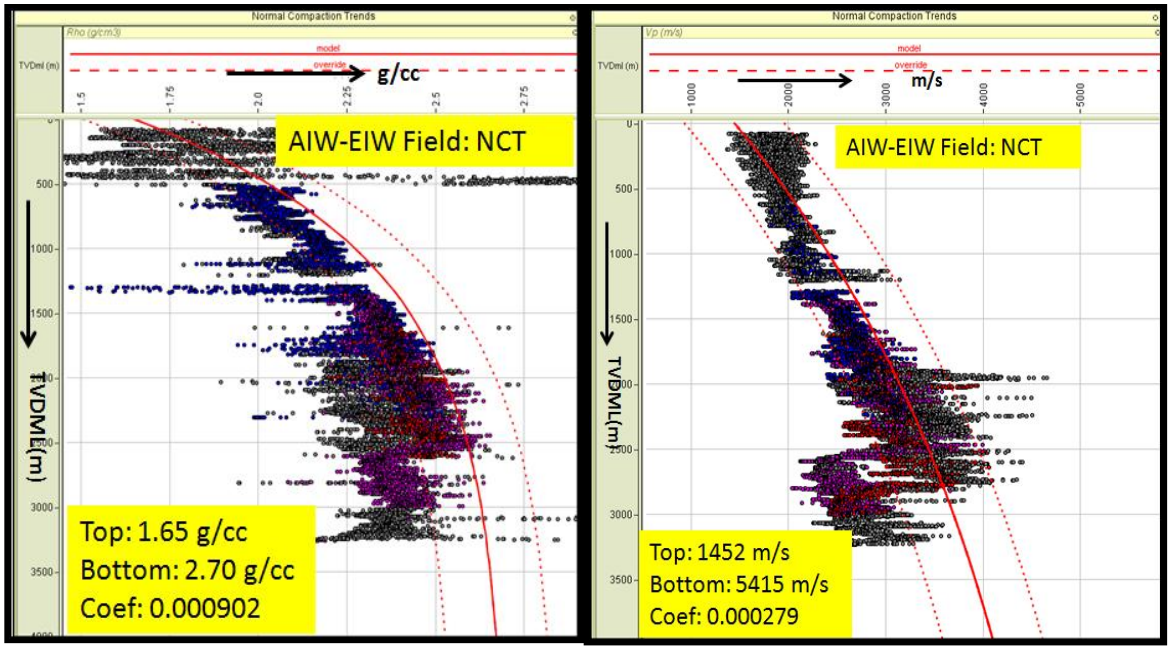

Figure 5.7. Left: Density-generated NCT for wells AIW-1, AIW-2 and EIW-1. Right: Velocity-generated NCT for same wells.

In this example (Figure 5.7), where there is sufficient quality data to use both density and velocity logs for NCT construction, velocity is included for comparison only. Within the study area, the NCT was derived mainly using the density log because velocity logs were either absent or of low quality in majority of the wells. Two main challenges with NCT construction in this study were the lack of log data at shallow depths, and the top of overpressure in most of the wells is very shallow. In such cases, experience and knowledge of local geology was used to constrain log data at mudline. This situation is not peculiar to the Niger Delta area. Overpressure at or close to mudline have been reported by others. Based on regional and high-resolution 3D seismic velocity and rock models, Banic et al. (no date) reported the onset of overpressure at seafloor in an un-named deep water basin offshore West Africa. Also, Bowers (2002) reported that in the deepwater Gulf of Mexico, overpressure can start within a few hundred feet of the seafloor.

In AIW-EIW wells, the NCTs from both density and velocity show that the undercompaction starts at about 500 m below mudline or even shallower. Well AIW-1 does not have density or velocity data below 2500 m, so it is impossible to say whether a reversal would have been found below at greater depth in this well. The first reversal occurs just below 2500 m and another at ~2800 m which is quite conspicuous, especially on the velocity log (Figure 5.7).

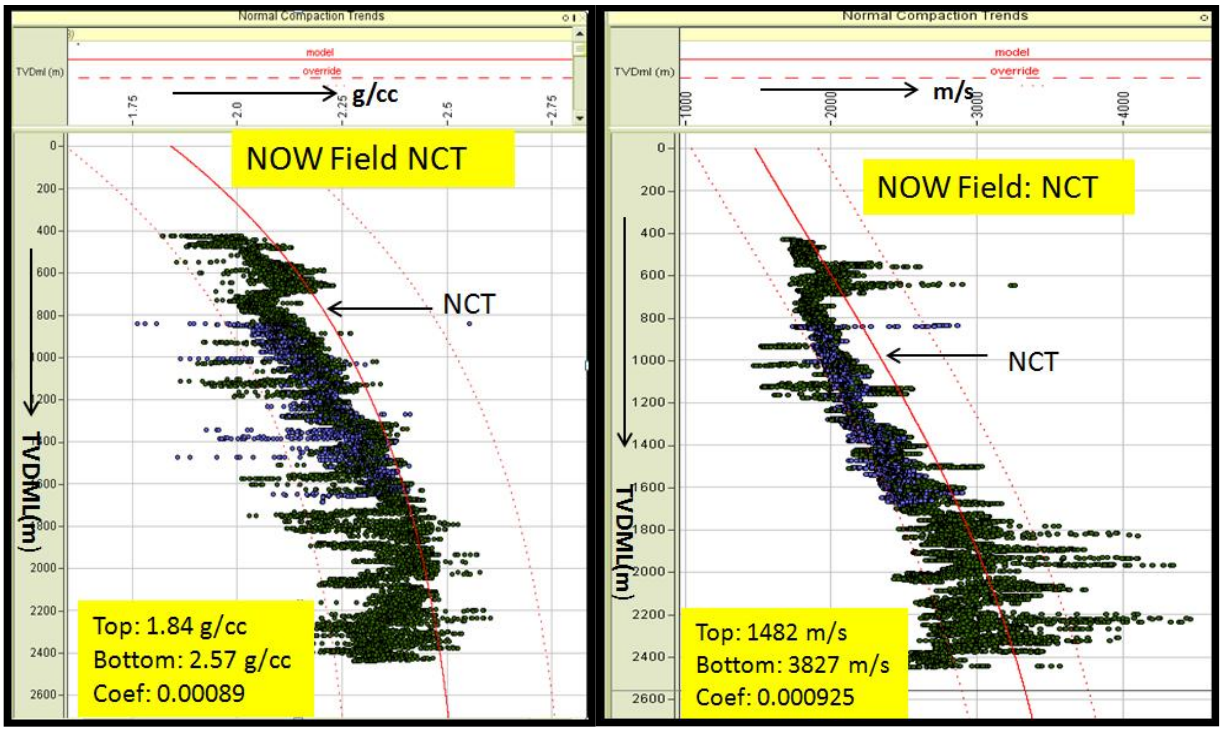

Figure 5.8. Left: Density-generated NCT for wells NOW-1 and NOW-2. Right: Velocity-generated NCT for same wells.

In the two wells from the NOW field, the NCTs are similar to those for the AIW-EIW fields (Figure 5.7). The sediments are normally compacted, or close to normally compacted, down to ~ 400 m below mudline. There is an increase in velocity around 1800 m that does not correlate with any significant change in the density trend. There is a reversal on the density log at at ~2200 m and also on the velocity log at ~2400 m.

Standard chronostratigraphic tops were not available for any of the NOW wells, so it is quite challenging to compare intervals between these two wells; hence references are made relative to mudline for comparison. It should also be noted that well NOW-2 has data only from about 800 m to 1600 m. However, the log data in NOW-2 do match quite well with NOW-1 where data is available for both wells.

5.2.3 Plots generated from log data

Results from wireline logs recorded in the AIW-EIW and NOW wells are presented in this section. The density, velocity, and resistivity logs were quality checked and discriminated for clean shale, as discussed in section 4.1. The logs were then plotted for examination of trends. The rationale for the use of cross-plots in pressure analysis has been discussed in section 3.4. Bowers (1995, 2001), Lahann (2001), Alberty et al. (2003) and Katahara (2003, 2006) have written extensively on the subject, especially for the US Gulf Coast and GOM. Using examples from AIW-EIW and NOW fields, results from two categories of cross-plot are presented here: firstly, those that are used to infer whether unloading, in general, has contributed to overpressure and, secondly, those that are used to infer whether, specifically, smectite-to-illite transformation has occurred in the system.

Depth profiles for density, velocity and resistivity

Figures 5.9 to 5.12 are the depth profiles of density, velocity and resistivity for wells AIW-1, AIW-2, EIW-1 and NOW-1, plotted individually. The idea is to check whether reversals have occurred at the same depth in all of the log types, or just in some, both to look for and also to choose appropriate pore pressure prediction methods (Bowers, 1995, 2001; Lahann, 2001; Katahara, 2003, 2006).

In the AIW-1 well there is no obvious reversal on any of the logs (Figure 5.9). In the AIW-2 well the logs followed a normal trend down to 2400 m, i.e., top of reversal (Figure 5.10). There is a very marked reversal on the density, velocity, and resistivity logs around the interval 2500–2600 m.

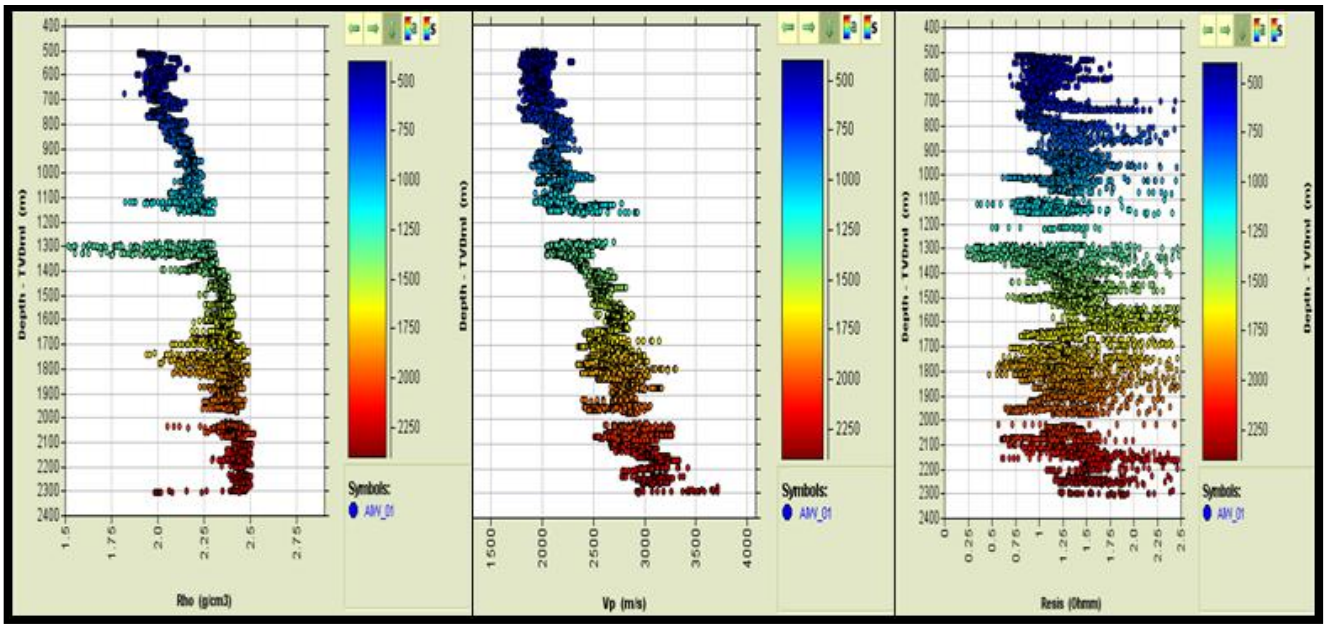

Figure 5.9. AIW-1 well depth plots of density, sonic velocity and resistivity.

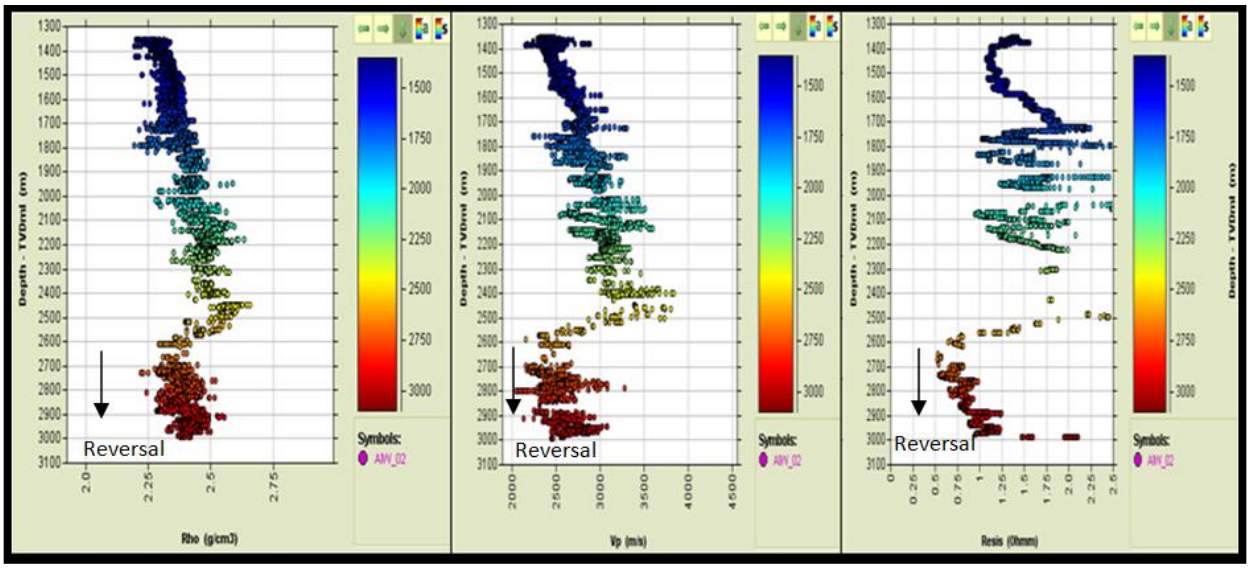

Figure 5.10. AIW-2 well depth plots of density, sonic velocity and resistivity.

In the EIW-1 well, the logs follow a normal trend down to ~2500 m (Figure 5.11). There are reversals on the velocity and resistivity logs at 2800 m; the density log in this well was only

run above 2600 m. In the NOW-1 well, a conspicuous reversal is seen on the velocity log at ~2000 m. The reversal is not as conspicuous on the density log and a resistivity log is not available for this well (Figure 5.12). It should be noted that the GR log, used as filter, in this well did not log beyond 2050 m and consequently limits the maximum depth seen in Figure 5.21.

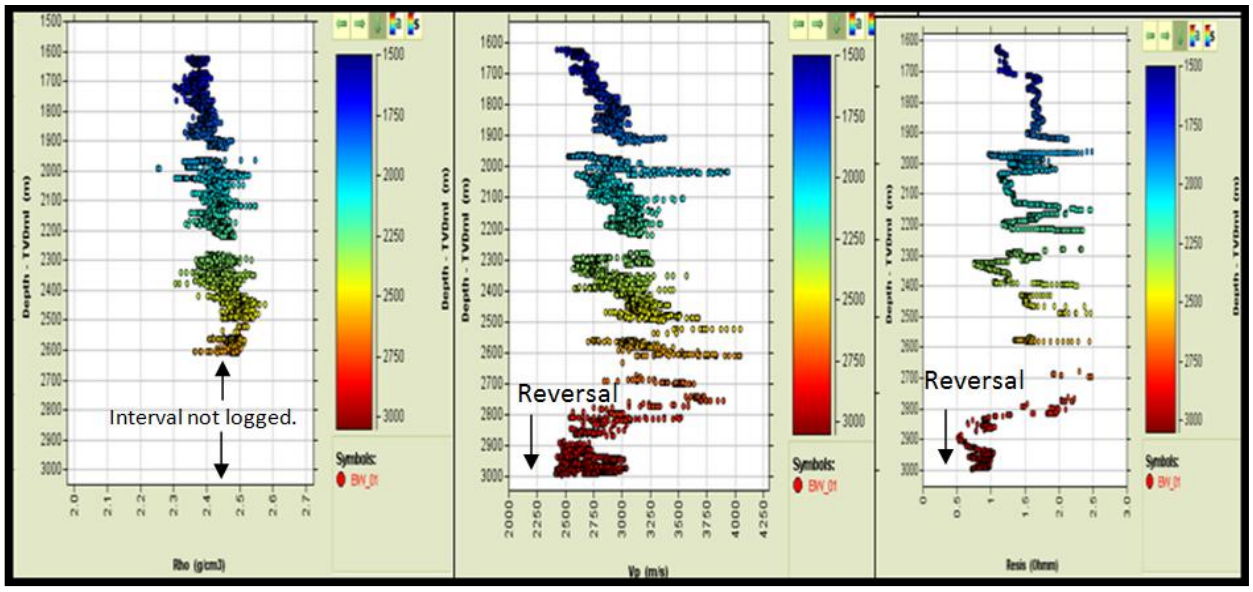

Figure 5.11. EIW-1 well depth plots of density, sonic velocity and resistivity.

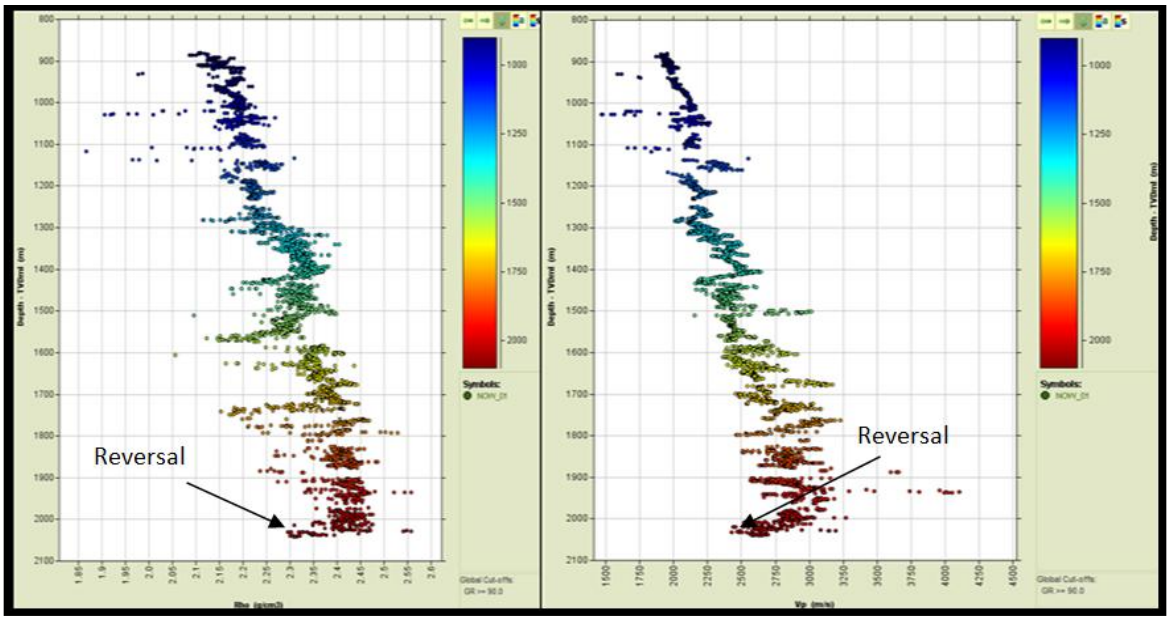

Figure 5.12. NOW-1 well depth plots of density and sonic velocity.

Vertical effective stress (VES)

Measured formation pressure from MDT, RFT, or RCI tools and calculated overburden (OVB) were processed with the Ikon Science RokDoc software to generate depth plots of VES. The software interpolates between pressure measurements to give a continuous VES profile. The generated VES profiles were checked for any apparent bad data, and the final results are shown in Figures 5.13 and 5.14. The gaps in the trends are sand intervals that have been filtered out since only shale intervals are of interest. As noted by Bowers (1995, 1998, 2001), Alberty et al. (2003) and Katahara (2003, 2006), a decrease in σ_v with depth is an indication of unloading. In contrast, Bowers (1995) pointed out that disequilibrium compaction does not cause σ_v to decrease with depth, nor does it cause a reversal in the sonic log, for example.

The shallowest VES decrease is in well AIW-1 between 2025 m and 2125 m. In well AIW-2, there is a VES reversal is noted between 2080 m and 2180 m, and in well EIW-1 there is a reversal between depths of 2300 m and 2405 m.

The plots of NOW-1 and NOW-2 are more straightforward (Figure 5.14). There is a minor disruption in trend at 1600–1620 m, which does not amount to a reversal, and a marked reversal starting at 1980 m that continues to the deepest pore pressure measurement at ~2040 m. Otherwise, the general trend is increasing VES with depth in both wells. Are these reversals due to unloading? The answer will be explored in chapter 8 with the use of additional cross-plots.

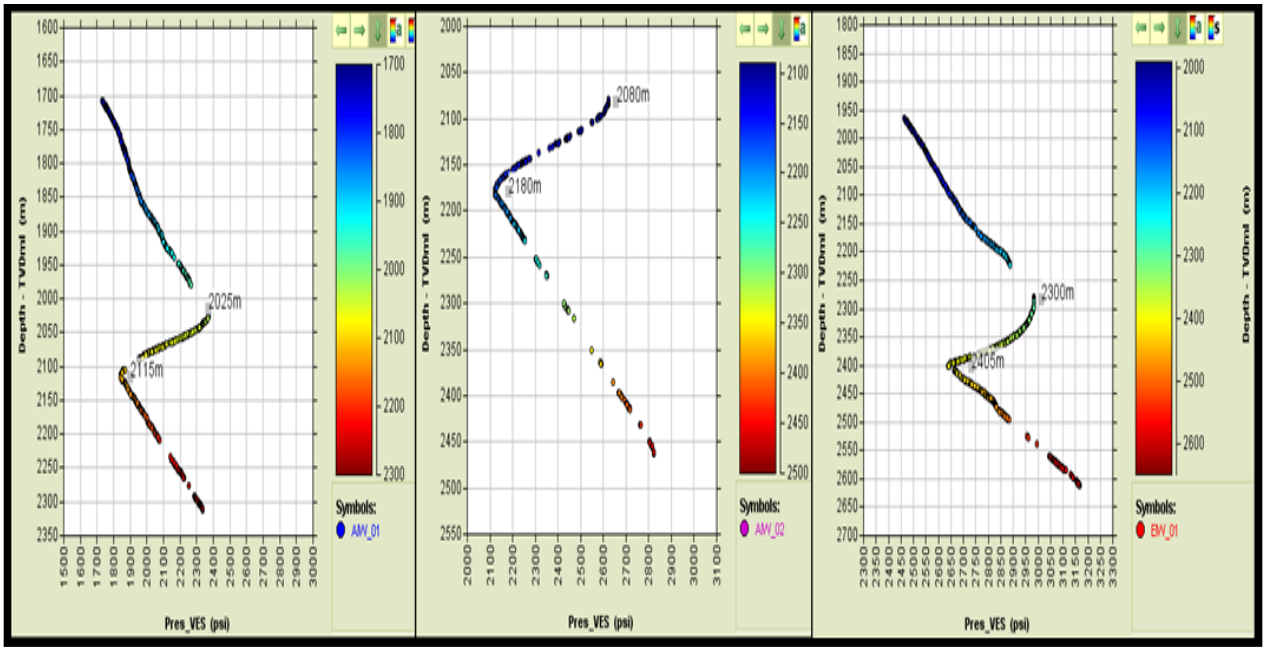

Figure 5.13. Depth plots of VES showing intervals with VES reversals in AIW-1 (left), AIW-2 (middle) and EIW-1 (right).

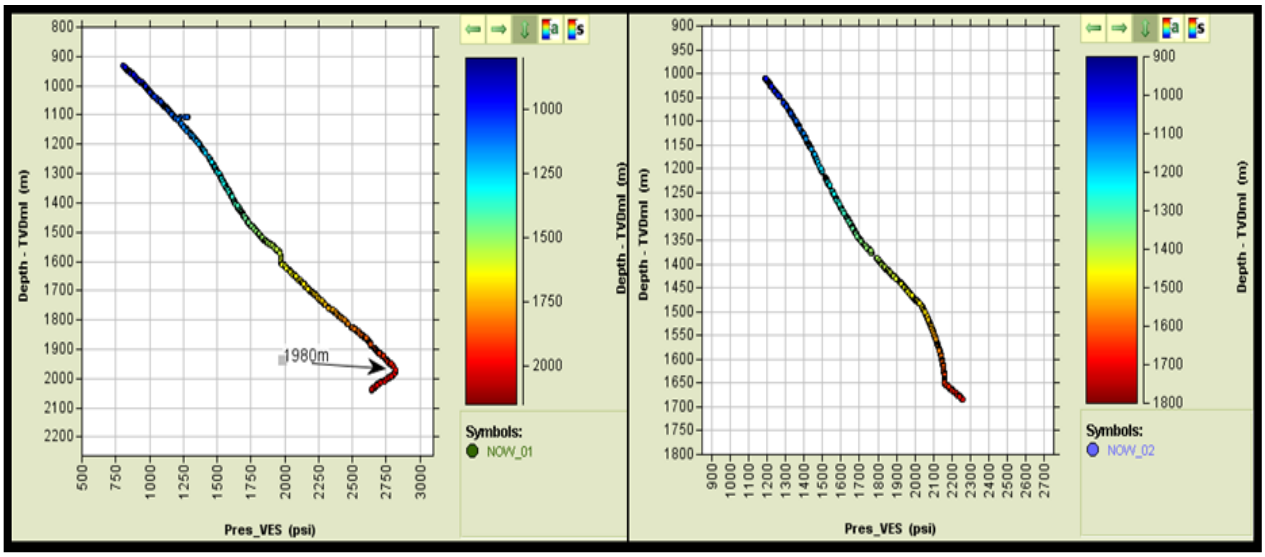

Figure 5.14. Depth plots of VES showing intervals with reversals in wells NOW-1(left) and NOW-2 (right).

Velocity–VES cross-plots

Figures 5.15–5.19 are cross-plots of sonic velocity against VES for the AIW-1, AIW-2, EIW-1, NOW-1 and NOW-2 wells. Before cross-plotting, both velocity and VES data were quality checked as previously discussed in section 4-1. It should be noted that these plots are limited by the depth of the VES depth profile which terminates at the deepest pore pressure measurement. This cross-plot has been used by Bowers (1995) and Lahann (200l), amongst others, to infer whether unloading is present in shales. The NCT for sonic velocity shows rising velocity as VES increases, asymptotically approaching rock matrix velocity as porosity approaches zero. If the mudrock is unloaded (VES reduction), an unloading curve is followed with a faster sonic velocity for a given value of VES function. In other words, not all of the porosity lost or density increase that occurred during loading is recoverable when sediment is unloaded, because unloading causes a poroelastic response in the mudrock. As has pointed out by, for example,

Bowers (1995) and Katahara (2003, 2006), the unloading curve is not a single fixed curve above the virgin curve. The unloading curve for a particular bed is fixed by the maximum value of VES that it has experienced.

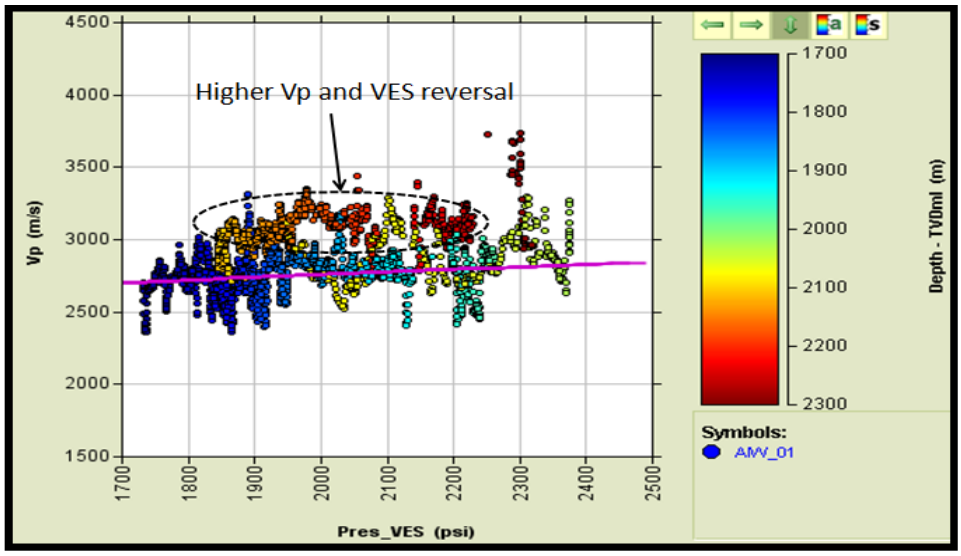

Figure 5.15. Cross-plot of velocity against VES for AIW-1.

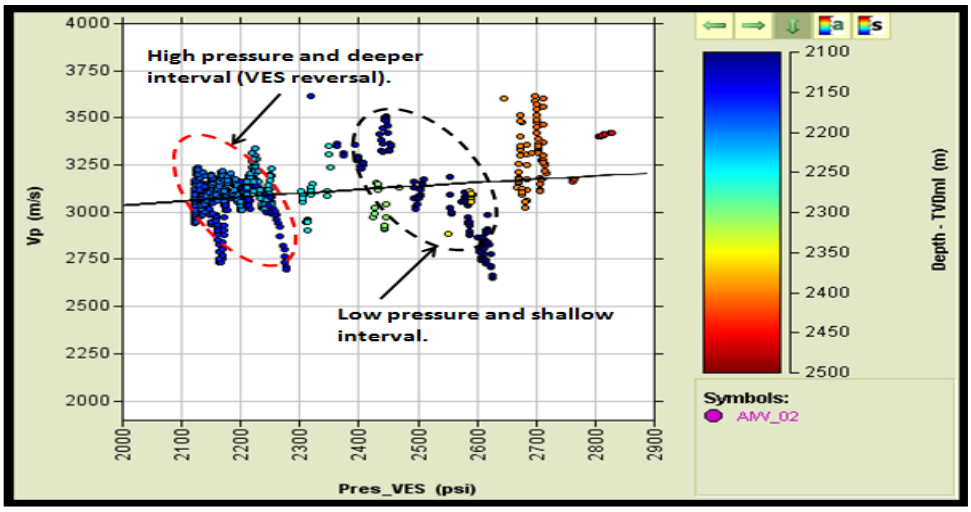

Figure 5.16. Cross-plot of velocity against VES for AIW-2.

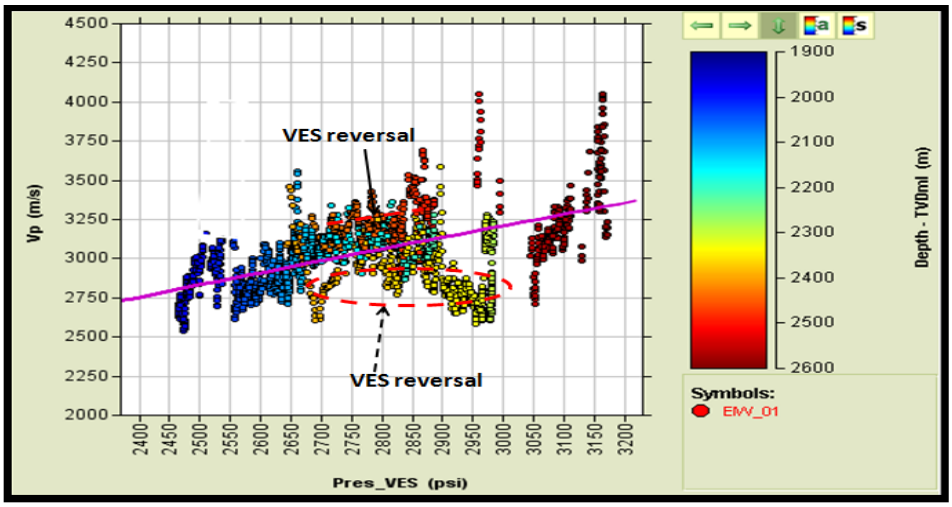

Figure 5.17. Cross-plot of velocity against VES for EIW-1.

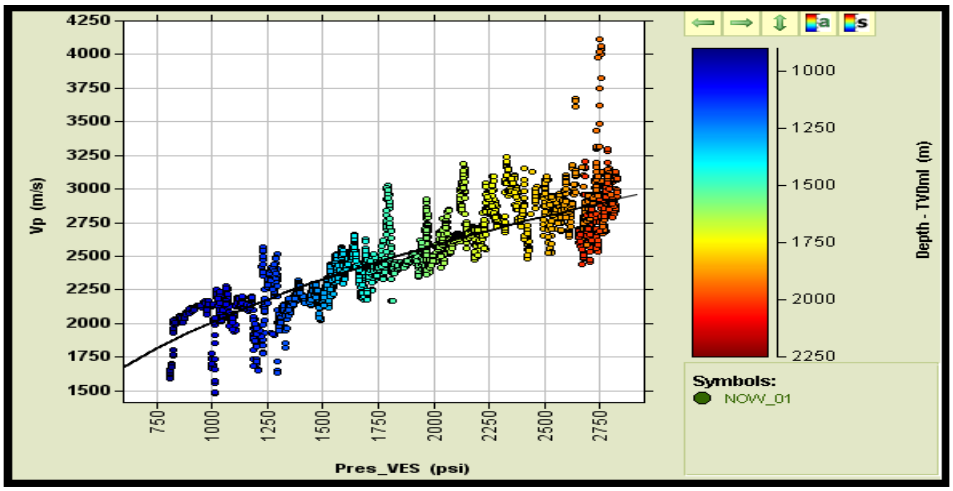

Figure 5.18. Cross-plots of velocity against VES for NOW-1.

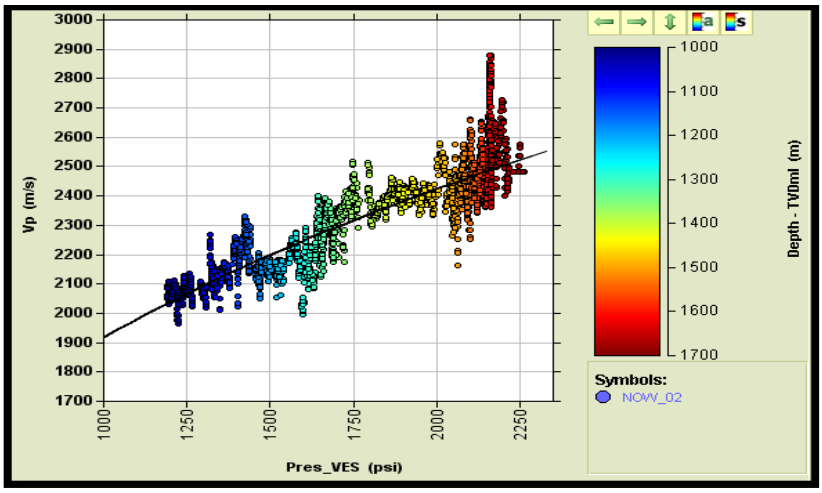

Figure 5.19. Cross-plot of velocity against VES for NOW-2.

Figure 5.15 for the AIW-1 well shows two trends, a lower trend with a best-fit line in purple and an upper trend corresponding to the reversal in the VES depth profile (Figure 5.13, left). The lower trend corresponds to increasing values of VES down to the reversal at 2015 m depth. The data points on the upper trend (warm colours) correspond first to decreasing VES and then increasing VES, as indicated by the colour-coded depth scale. It is not clear whether these points fit a single unloading curve.

Figure 5.16 for the AIW-2 well plot is quite problematic in the sense that VES data available were scanty and limited mostly to the shallower section of well. However, it is quite apparent from the plot that intervals between 2200 m – 2250 m is overpressured and shows significant VES reversal.

In the EIW-1well (Figure 5.17), the general trend from the shallow section down to ~ 2300 m shows velocity increasing with VES. The first interval with VES reversal begins at ~ 2300 m and the velocity values are generally lower than seen in the main trend. The cross-plots for wells NOW-1 and NOW-2 are less complex than those for the AIW-EIW wells (Figures 5.18

and 5.19). A general trend of increasing velocity with VES is seen on these plots, with a single trend from shallower to deeper intervals. Note that the NOW-2 plot is limited to ~1700 m depth, corresponding to the deepest measurement of pore pressure available for VES calculation.

Density–VES cross-plots

These cross-plots provide additional means of identifying illitic shale with or without unloading. Before cross plotting the data, both density and velocity data were quality checked as previously discussed in section 4.1. Two trends are recognizable on the density–VES plot for the AIW-1 well (Figure 5.20). First, is a lower general trend that starts from shallow section to 1950 m. In the second trend, the VES reversal begins at ~2050 m and density values are slightly higher than average density seen in the general trend. Although, the interval from 2050 – 2300 m shows overall VES reversal, however, VES value increases from 2050 – 2300 m. The plot for well AIW-2 (Figure 5.21) is quite problematic because the available VES data were scanty and limited mostly to the shallower section of well. However, the interval between 2200 m and 2250 m is overpressured (lower VES) and a VES reversal is seen within the interval.

In well EIW-1, density increases with VES down to 2200 m depth (Figure 5.22). The first VES reversal is seen at 2300 m, with density values initially below the trend in the shallow section. Notice that reversal seen on the velocity log at 2800 m cannot be correlated with this plot because the density log stops at 2600 m.

The cross-plots for the NOW wells in Figures 5.23 and 5.24 are less complex than the cross- plots for the AIW-EIW wells. The general trend here is an increase in density with increase in VES over the whole depth interval. Due to the limited pressure measurements, the maximum depths represented on the plots are limited to 2050 m and ~1700 m for NOW-1 and NOW-2, respectively (Figure 5.14).

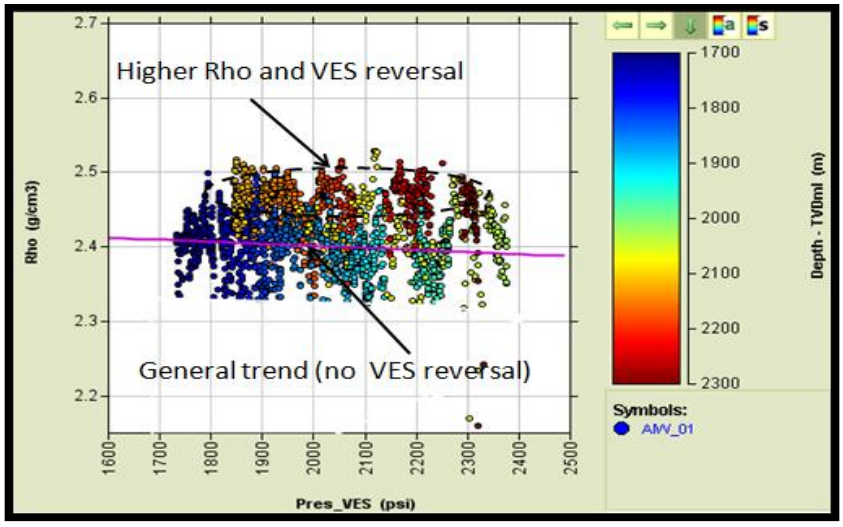

Figure 5.20. Cross-plot of density against VES for AIW-1.

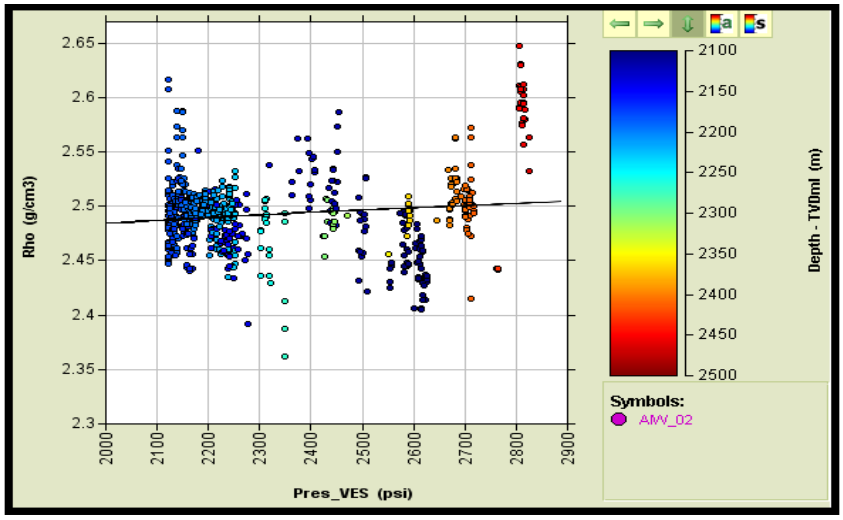

Figure 5.21. Cross-plot of density against VES for AIW-2.

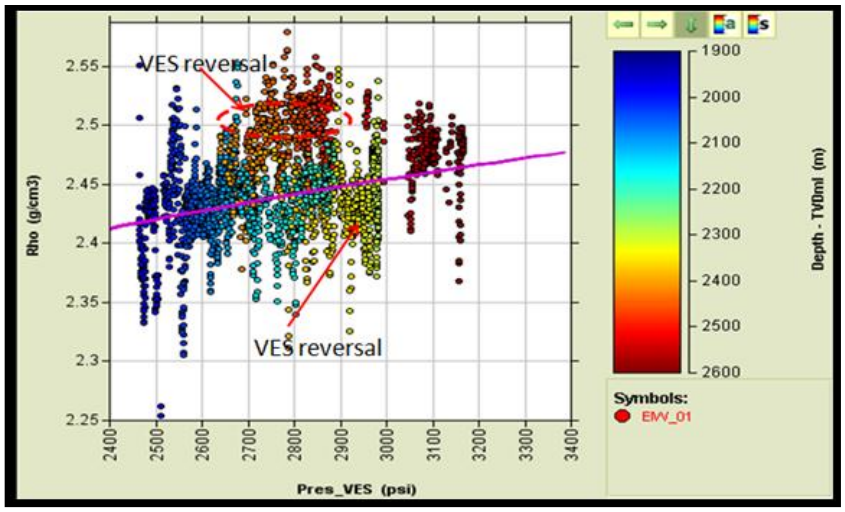

Figure 5.22. Cross-plot of density against VES for EIW-1.

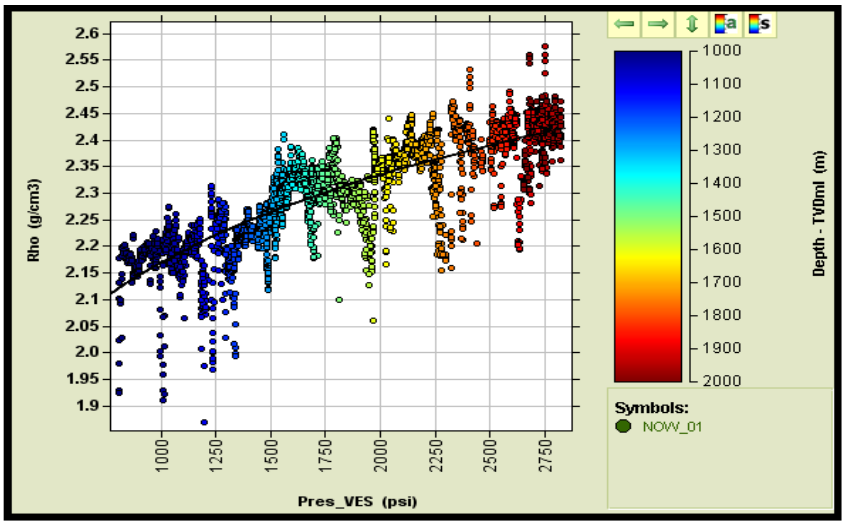

Figure 5.23. Cross-plot of density against VES for NOW-1.

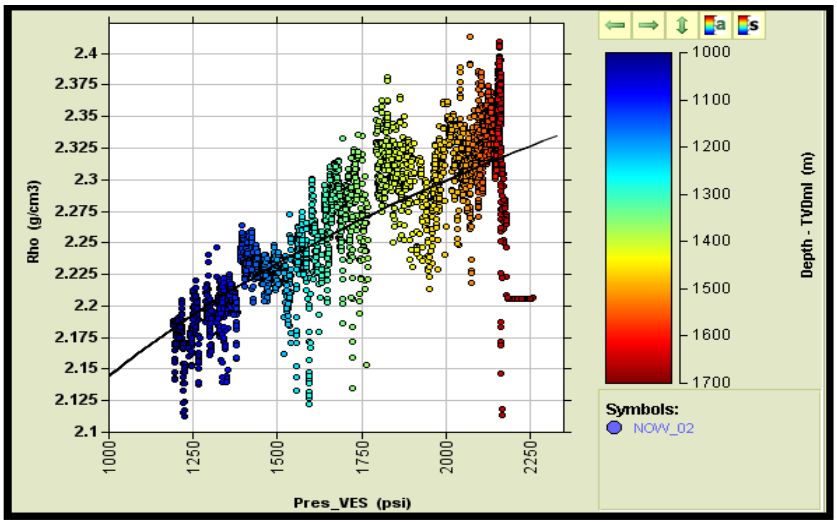

Figure 5.24. Cross-plot of density against VES for NOW-2.

Velocity–density cross-plots

Figures 5.25–5.27 show velocity–density cross-plots for wells AIW-1, AIW-2 and EIW-1. The plots have been used to identify the presence of illitization with loading and illitization with unloading (e.g., Lahann, 2001). Velocity and density data were discriminated for clean shale and then cross plotted using IKON Science software (RokDoc).

In Figure 5.25 (AIW-1) the general trend is an increase in velocity with density down to about 1500 m.

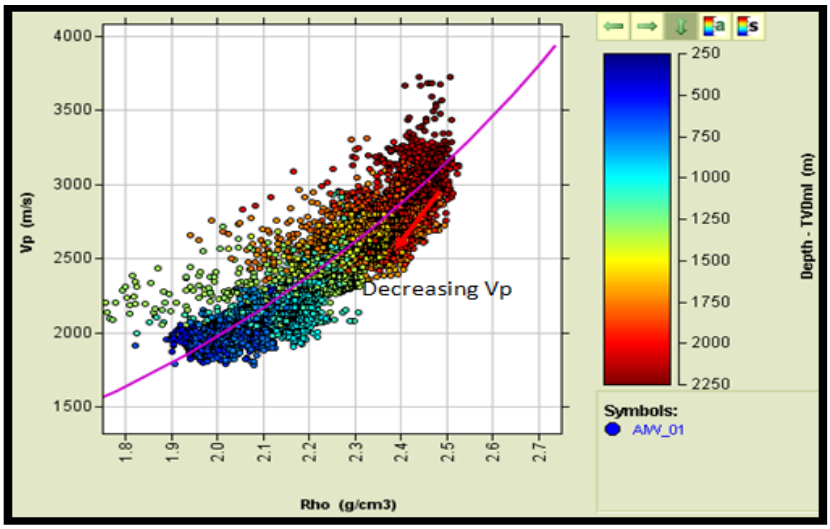

Figure 5.25. Cross-plot of velocity against density for AIW-1.

In the plot of AIW-2 well (Figure 5.26), a fairly linear relationship is seen from shallow depth till about 2250 m. However, from 3000 m to 3250 m there is a large drop in velocity relative to density, as may be seen in Figure 5.10, where both logs show strong reversals.

For well EIW-1, velocity increases with density for most of the intervals (Figure 5.27). However, there is considerable drop of velocity for interval around 2300 m, this is also evident in Figure 5.10. For wells NOW-1 and NOW-2, velocity generally increases with density (Figures 5.28 and 5.29).

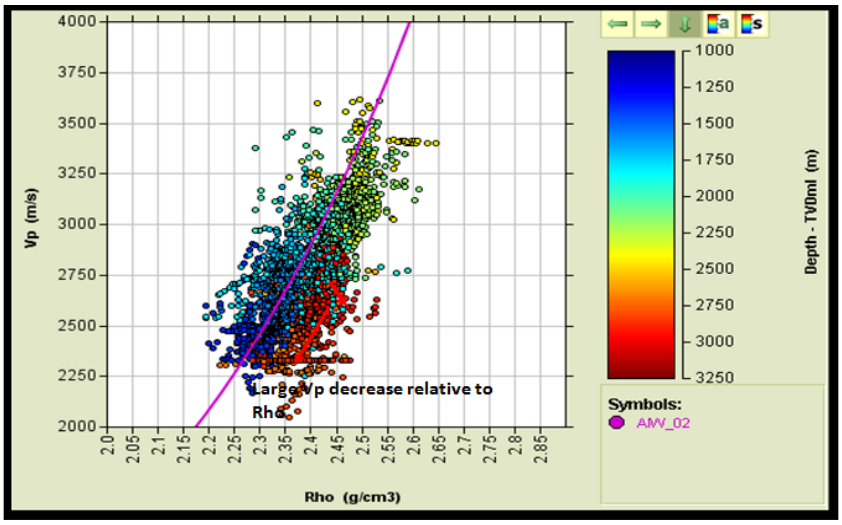

Figure 5.26. Cross-plot of velocity against density for AIW-2.

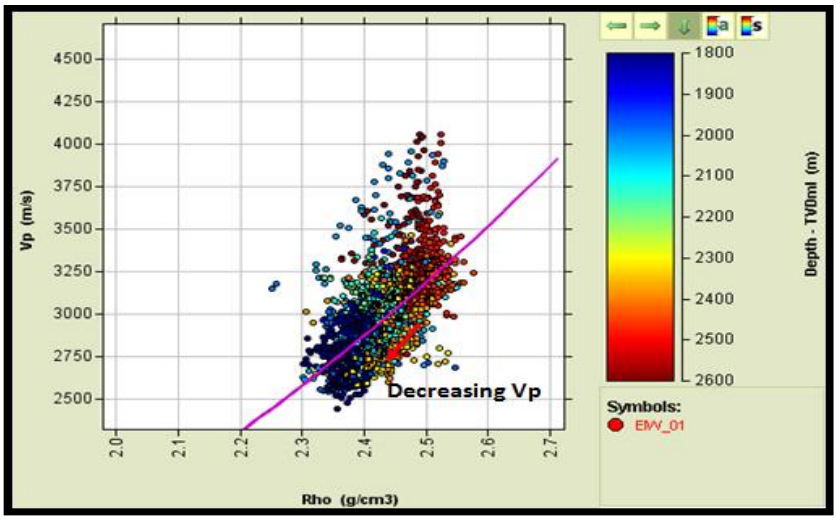

Figure 5.27. Cross-plot of velocity against density for EIW-1.

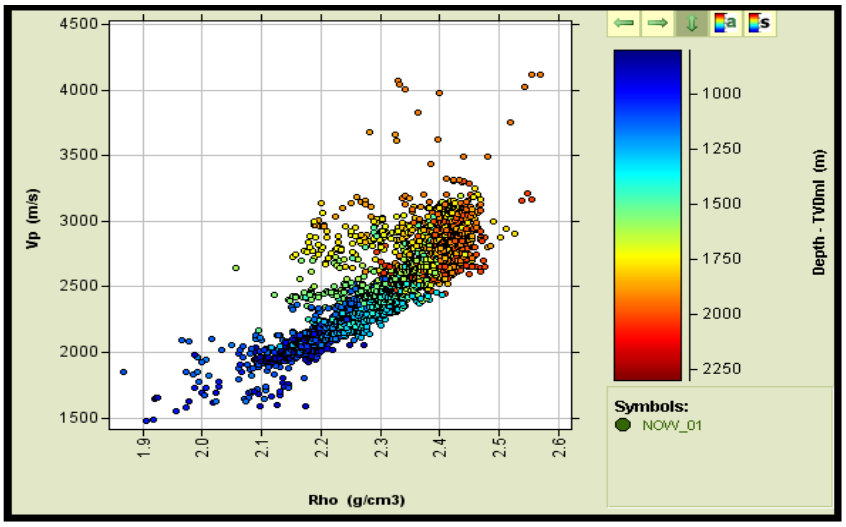

Figure 5.28. Cross-plot of velocity against density for NOW-1.

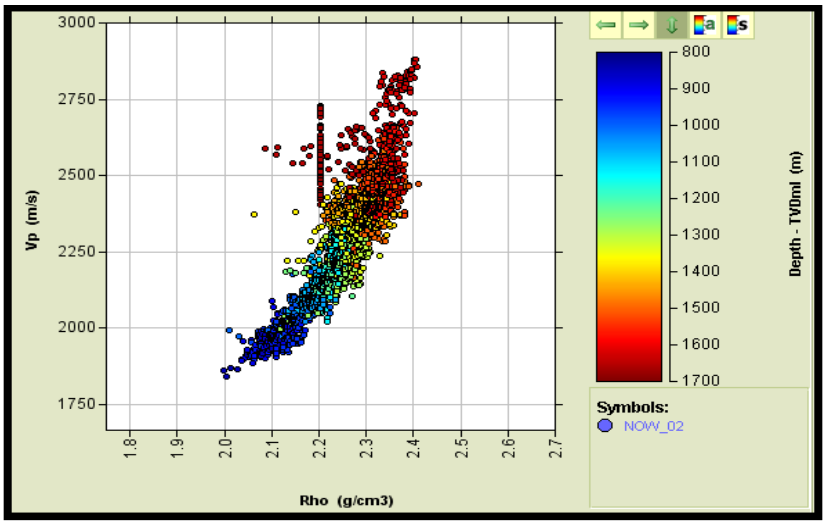

Figure 5.29. Cross-plot of velocity against density for NOW-2.

Density–sonic transit time cross-plots

Similar to velocity – density, cross-plots of density against sonic transit time have been used to identify smectite-to-illite transformation in wells (e.g., Bowers, 1995, 1998, 2001, 2002; Lahann, 2001; Alberty & McLean, 2003; Katahara, 2003, 2006). The basic idea is that smectite-rich

mudrocks plot on the smectite line (blue line) in Figure 5.30, and as illite content increases, the points will move up and to the right towards the illite-rich line (red line). The transformation is temperature-dependent and requires a potassium-rich system. For example, Mouchet & Mitchell (1989) have suggested that this reaction can proceed at a lower temperature if sufficient supply of potassium ions is available, though they did not specify the minimum concentration required.

In Figure 5.30 for well AIW-1, it is apparent that the shallower intervals align with the smectite-rich line, but in the deeper section the data points shifts toward the illite-rich line. In well AIW-2 (Figure 5.31), there is an obvious shift of data from shallow intervals towards the illite-rich line in the deeper interval. In well EIW-1 (Figure 5.32), most of the data plot between the lines for smectite-rich and illite-rich mudrocks, with a trend that parallels the smectitic and illitic trends.

In wells NOW-1 and NOW-2, a subtle shift from the smectitic trend for the shallower interval towards the illitic trend is noticeable (Figures 5.33 and 5.34).

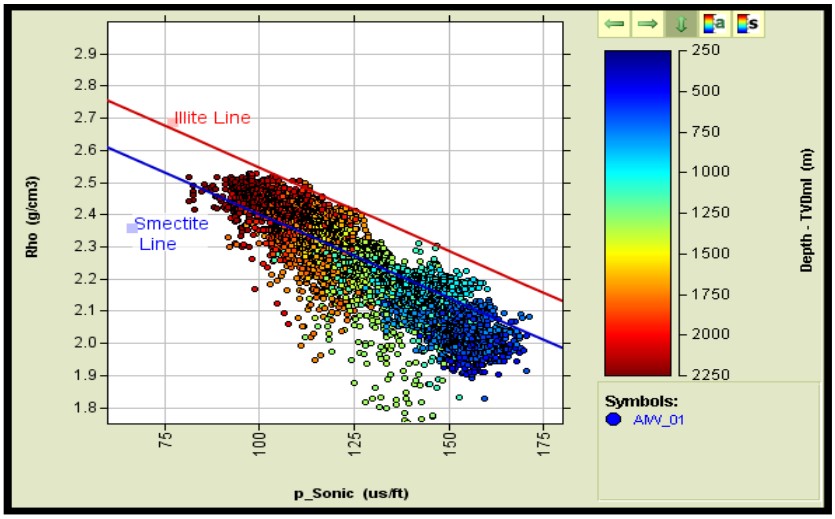

Figure 5.30. Cross-plot of density against sonic transit time for AIW-1.

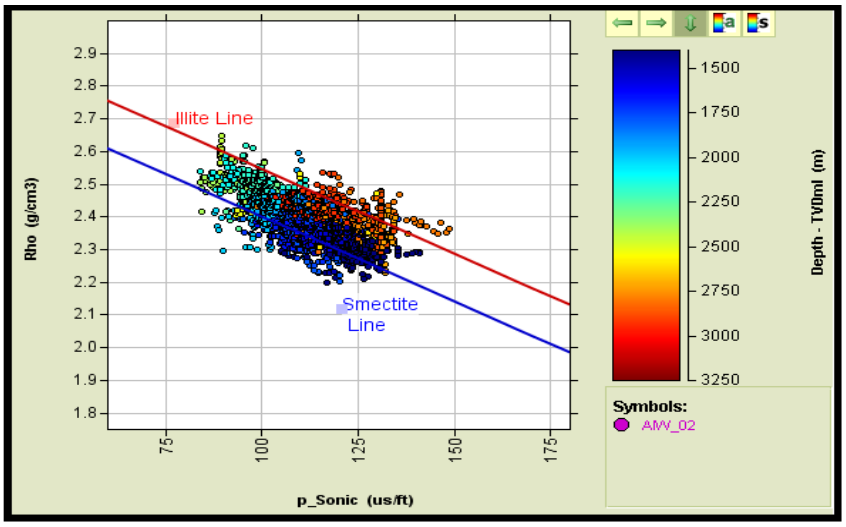

Figure 5.31. Crossplot of density against sonic transit time for AIW-2.

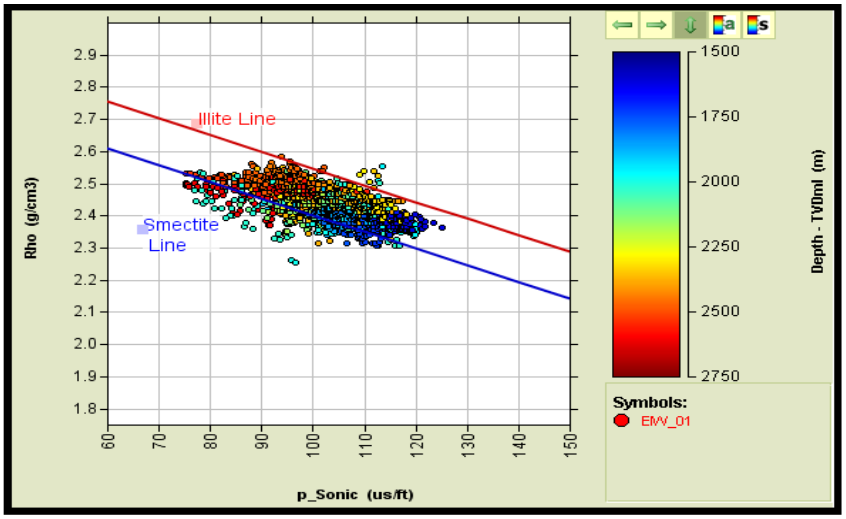

Figure 5.32. Cross-plot of density against sonic transit time for EIW-1.

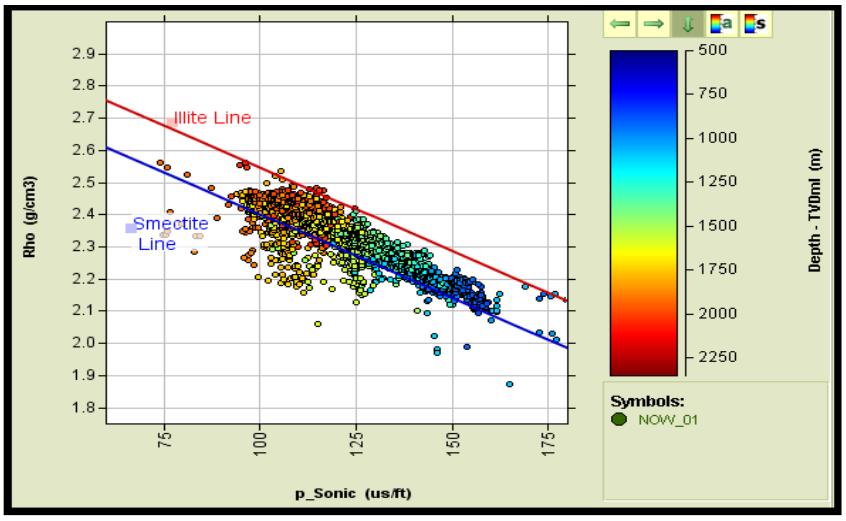

Figure 5.33. Cross-plot of density against sonic transit time for NOW-1.

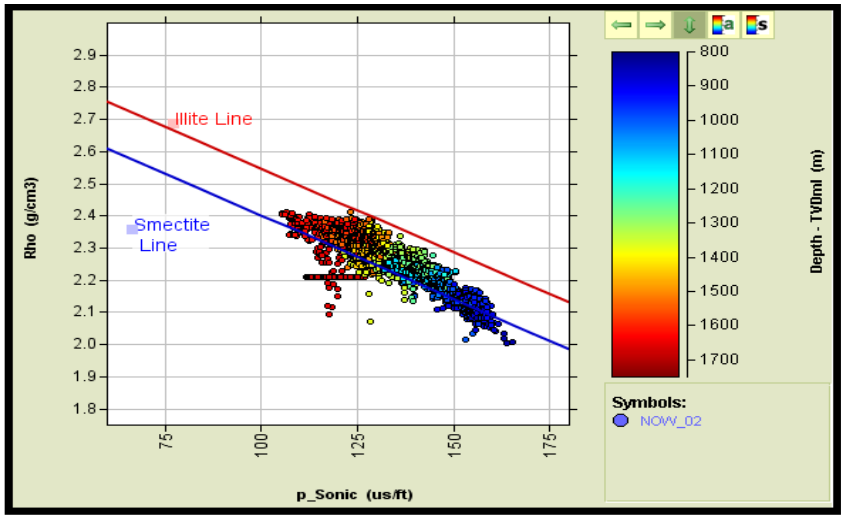

Figure 5.34. Crossplot of density against sonic transit time for NOW-2.

Temperature data

Tables 5.1 and 5.2 show temperature gradient estimates for AIW-EIW and NOW wells. Temperatures from MDT tool were provided by the operator. Apparently poor temperature data, that were subjectively judged to be too low or too high by comparison with the general trend,

were discarded. For ten AIW-EIW wells, the average temperature gradient is 2.92 deg C /100 m. For three NOW wells, the average temperature gradient is 3.58 deg C /100 m.

Wells	Depth m (TVDml) Top	Bottom	Temp deg C Top	Bottom	Grad deg C /100m
AIW-5	2418.625	3073.628	78.89	102.73	3.639677942
AIW-6	1643.527	2818.193	76.4	102.77	2.244894069
AIW-7	2157.429	2912.562	82.33	100.44	2.39825348
AIW-8	2535.927	3269.876	84.5	107.77	3.170518917
AIW-9	2276.856	2910.84	79.94	100	3.164117706
AIW-10	1850.063	2602.517	73.05	96.56	3.124444883
AIW-11	1880.598	2814.404	72.78	103.33	3.271555317
AIW-12	1988.25	2542.203	80.05	94.55	2.617552174
AIW-13	706.1393	2299.28	38.83	88.38	3.110208401
AIW-14	1939.537	2508.184	81	94.83	2.432088492
					2.917331138

Average temp gradient for 10 wells in AIW field.

Table 5.1. MDT temperature data obtained from 10 AIW wells.

Wells	Depth m (TVDml) Top	Bottom	Temp deg C Top	Bottom	Grad deg C /100m
NOW-1	931.5511	2238.058	34.2	84.05	3.81551751
NOW-2	1007.334	2743.718	41.23	96.76	3.198024143
NOW-3	736.9759	1984.858	33.89	80.3	3.7191026
					3.577548084

Average temp gradient for 3 wells in NOW field.

Table 5.2. MDT temperature data obtained from three NOW wells.

5.3 Pore pressure prediction by the equivalent depth method

Figures 5.35 and 5.36 show the results of pore pressure prediction in shales for the AIW-1 and NOW-1 wells using the equivalent depth method. As a preliminary step, the NCTs of Figures 5.7 and 5.8 were created using clean shale intervals.

From the respective NCT, a predicted pressure profile was then generated with the RokDoc software using the equivalent depth method. The generated pressure profile was further constrained with measured pore pressures.

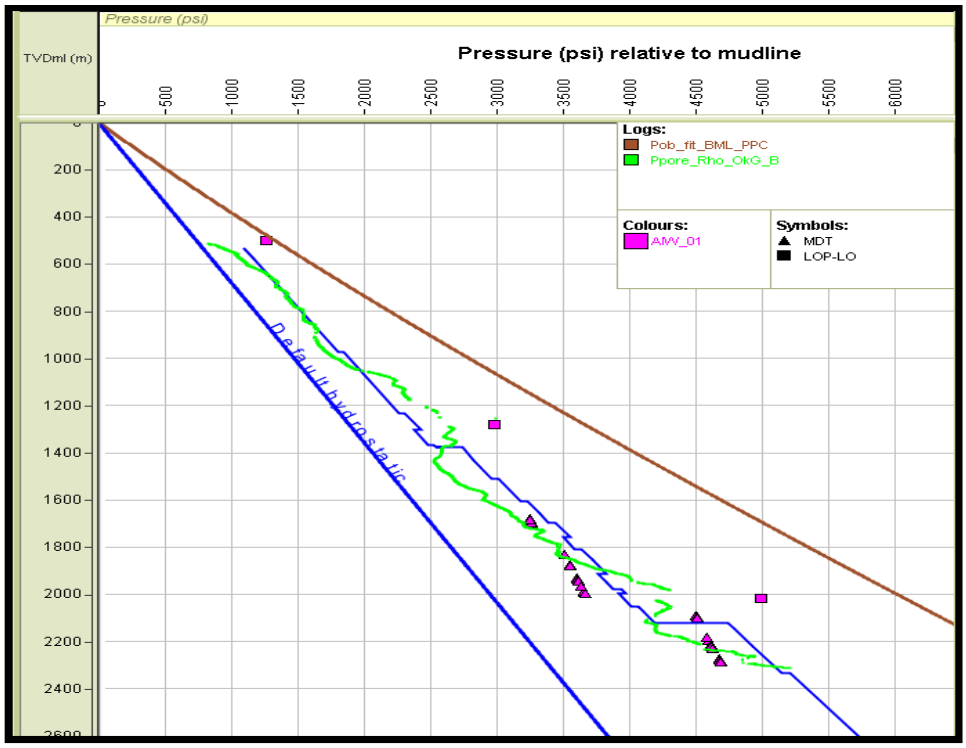

Figure 5.35. Predicted (green) and measured (triangles) pore pressures for AIW-1. The mud weight is shown in blue.

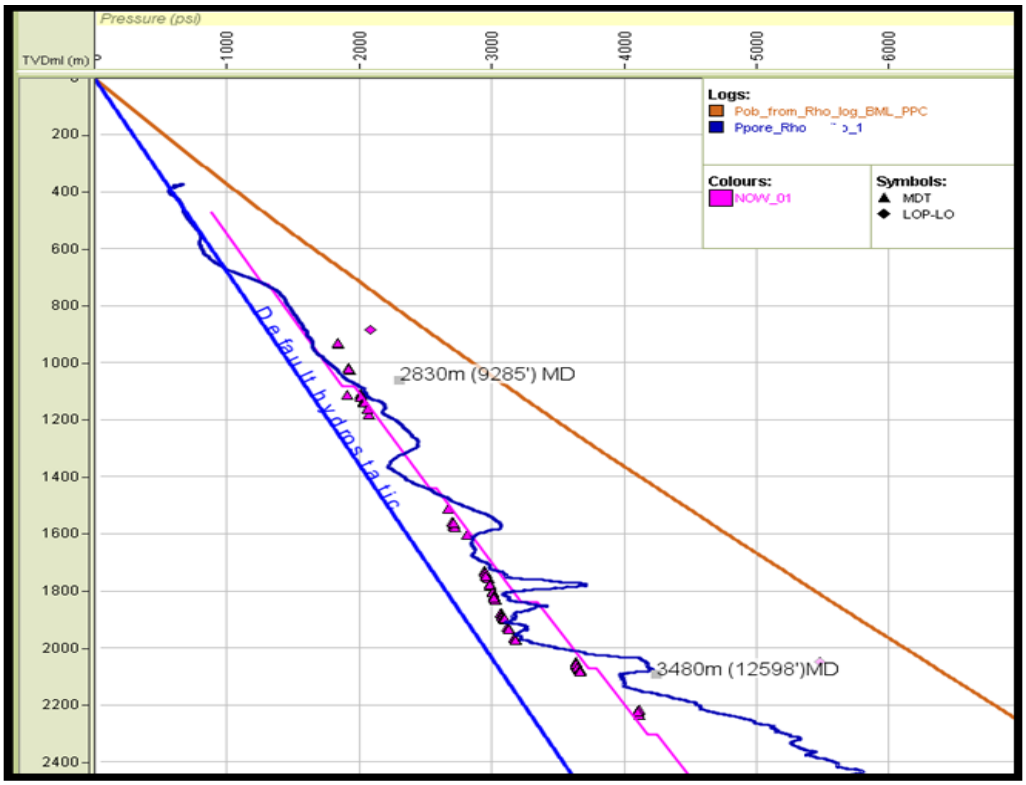

Figure 5.36. Predicted (dark blue) and measured (triangles) pore pressures for NOW-1. The mud weight is shown in pink.

5.4 UBD zones in wells AIW-1 and NOW-1

By comparing predicted pore pressures with measured pore pressures and mud weight in Figures 5.35 and 5.36, it was then possible to identify zones that were drilled underbalanced. Well AIW-1 had two zones from 1055 m to 1370 m and from 1905 m to 2105 m (Figure 5.37) that are indicative of underbalanced drilling and/or poor lithology discrimination; otherwise, predicted pressure matches well history quite well up to 2200m TVDML. In well NOW-1, predicted shale pressure is successful to about 2000m, beyond this depth underbalanced drilling is suggested; underbalanced drilling effect seen from 910 m to 1400 m is attributed to lithology effect. (Figure 5.38). Detailed results of observed mudlog and drilling signatures seen in the UBD zones are

discussed in chapter 7; underbalanced drilling is invoked only if drilling and mud log data support indications of UBD

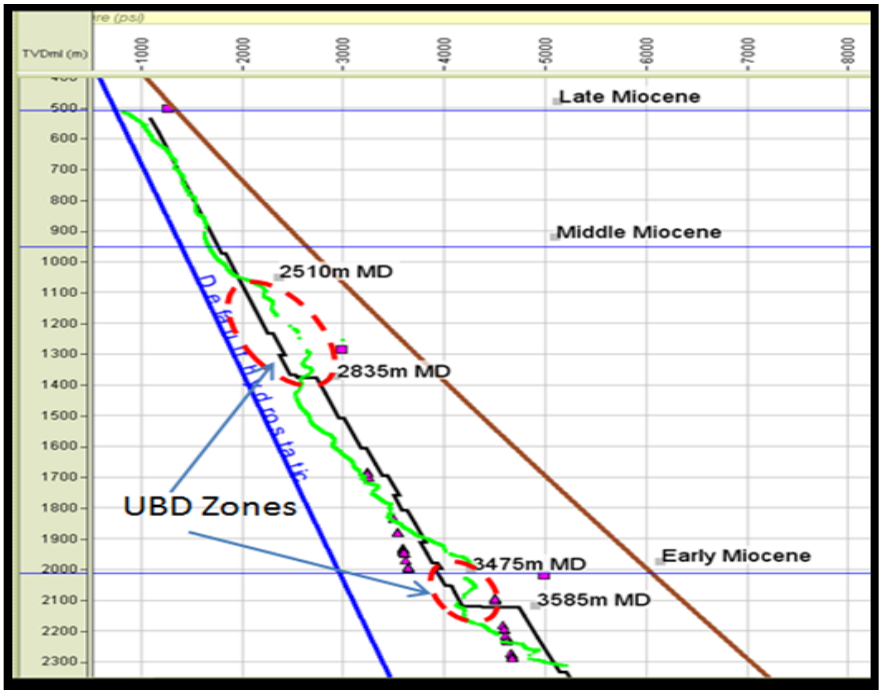

Figure 5.37. UBD zones identified in AIW-1.

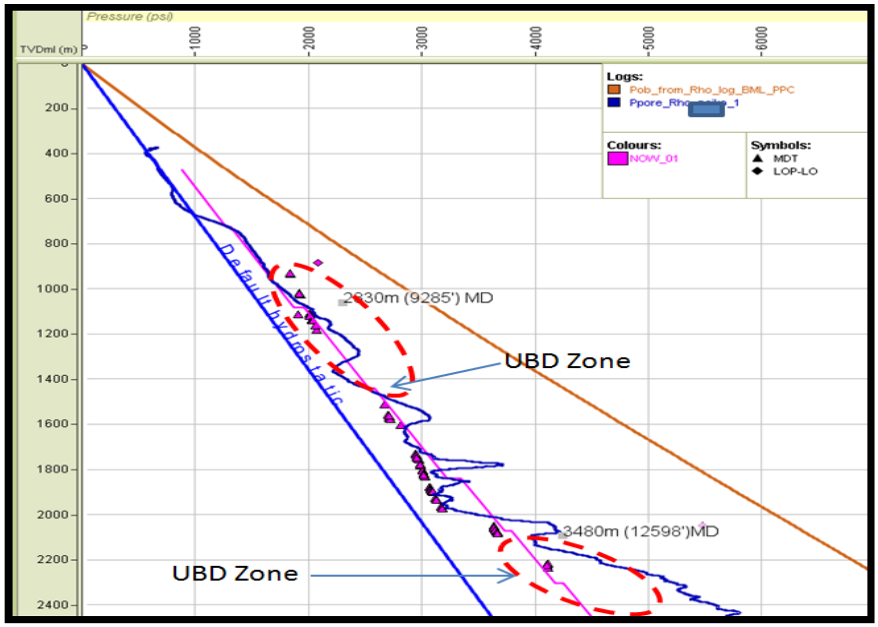

Figure 5.38. UBD zones identified in NOW-1.

Chapter 6

Results of Shale Pressure Prediction and Underbalanced Drilling – Examples from UNE-AOE Wells

Nine wells were screened in UNE and AOE fields as potential candidates for inclusion in this study, from three different operating companies. Both UNE and AOE fields are located to the east of Charcot Fracture Zone (Figure 6.1) in water depths ranging from 500 m to 1500 m. After editing and checking the wireline logs, seven wells were selected and evaluated for pore pressure and UBD. Two of the wells analysed, UNE-5 and AOE-4G1, were noted to have zones drilled underbalanced.

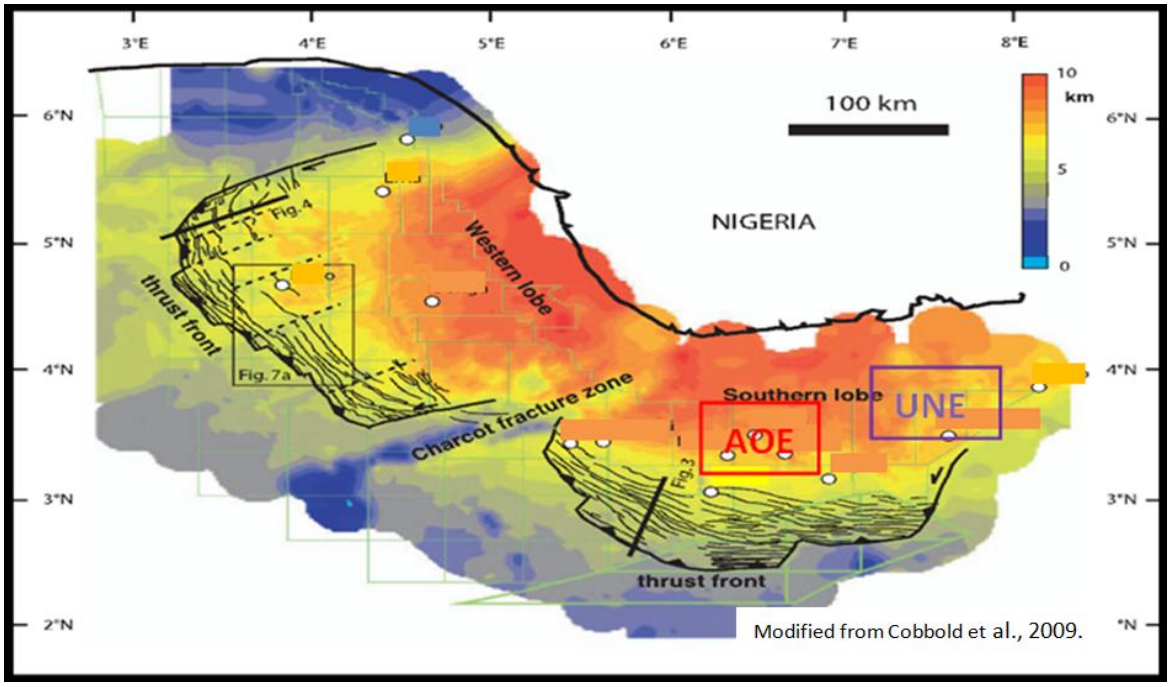

Figure 6.1. Map of Western and Southern sedimentary lobes in the offshore Niger Delta Basin showing the approximate locations of wells in UNE and AOE fields.

The aims in this chapter are to present results of (1) shale pore pressure prediction from density using equivalent depth method; (2) report indications of the presence or absence of unloading as a contributory mechanism to overpressure development; and (3) identify zones with UBD, i.e., intervals drilled with lower mud weight than measured or estimated pore pressure gradients. This chapter begins with geological background information on the UNE and AOE fields in section 6.1. The data analysis is described in section 6.2, and the results wells identified with UBD from pressure–depth plots are presented in section 6.3.

6.1 Geological setting

The structural setting of the individual fields is sparingly discussed due to the lack of relevant data and any seismic interpretation from the operators. The wells in this study are located mainly in the inner thrust belt which comprises the mud diapir province and translational basin of deep water Niger Delta (Figure 5.2), as described in section 5.1.1.

In the absence of high resolution palaeontology and core data, the chronostratigrahic intervals in the Niger Delta are quite difficult to place, as described in section 5.1.2. Formation tops have not necessarily been picked consistently, even for wells in the same field. For example, in UNE-4 and UNE-5, the top of the upper Miocene was picked at 711 m and 531m, while for the middle Miocene the tops were picked at 2286 m and 1523 m, respectively, and the top of the lower Miocene in UNE-5 was picked at 2470 m. All depths are TVDml. In AOE-1, tops of late, middle and early Miocene were picked at 2020 m, 3320 m, and 3925 m (MD), respectively. Based on the tops shown in Figure 6.2a, the middle to late Miocene intervals thin from UNE-4 to UNE-5. Since no tops were provided for AOE-4G1, a similar comparison cannot be made for

AOE wells. However, the early to middle Miocene interval in well AOE-1 is much thinner than in the UNE wells.

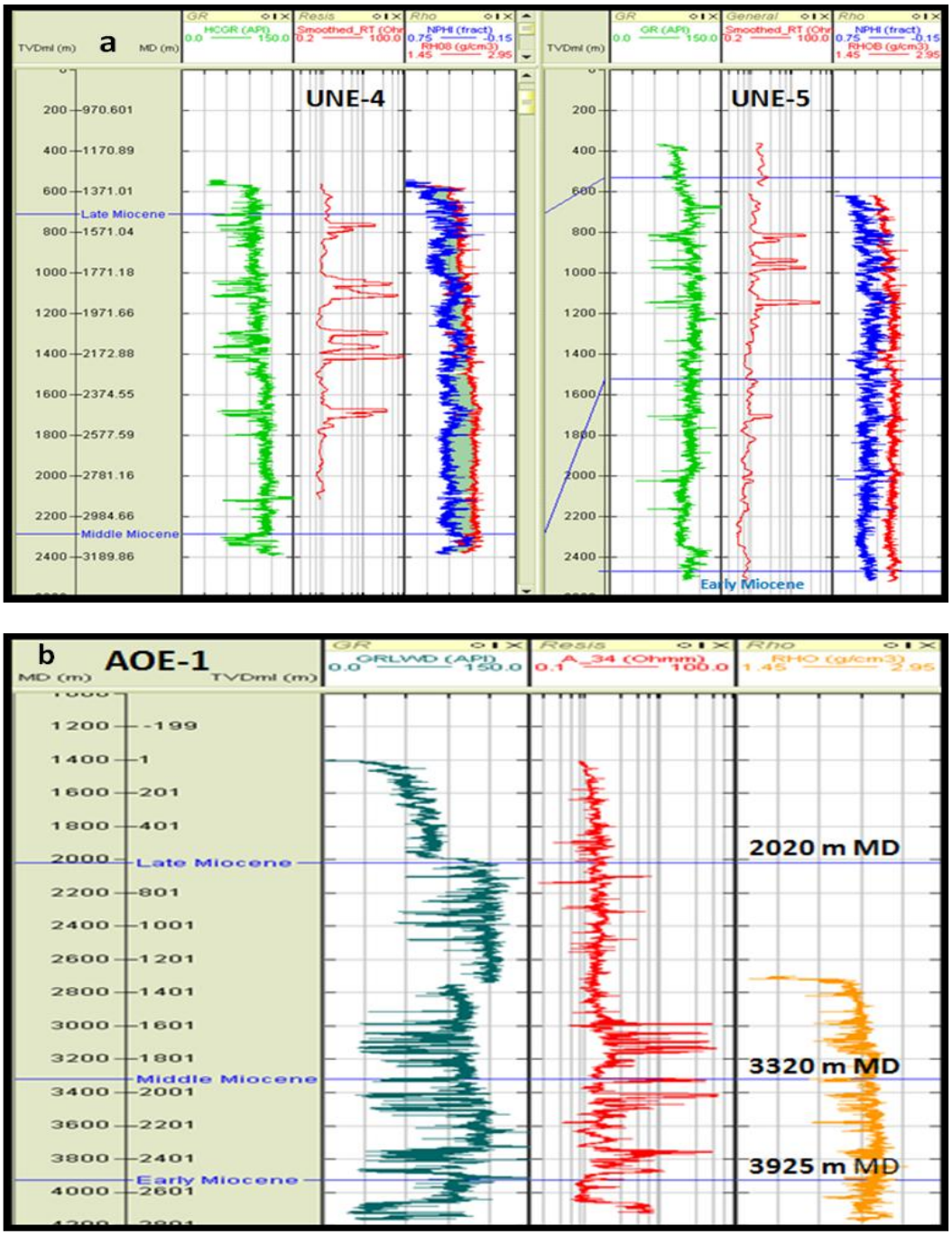

Figure 6.2. Chronostratigraphic tops for (a) UNE-4 and 5, and (b) AOE-1.

6.2. Results of analysis from UNE and AOE fields

6.2.1 OVB

The OVB is generated from the density log (RHOB) using Ikon Science's RokDoc software, as described in section 5.2.1. Figures 6.3–6.6 show examples of the OVB generated for UNE and AOE wells. Except where stated otherwise, all depths are referenced true vertical depths below mudline (TVDml) and pressures are in pounds per square inch (psi); these choices are mainly a matter of convenience.

The top and bottom densities observed in each well, even from the same field, show some variation. In general, relative to AIW-EIW and NOW fields, density log data for wells in this area are of poor quality. This in part has affected the density value used to constrain the top densities in particular. However, experience, judgment, and knowledge of sediment compaction at shallow depths have been use to constrain the data. To generate a composite OVB for UNE-4 and UNE-5 would be unsatisfactory because density values in the deeper section in both wells were very different, so results of OVBs for individual wells are provided for UNE and AOE wells (Table 6.1). Overall, based on calculations from logged densities, the overburden gradient for the two wells ranges from 0.80 to 0.96 psi/ft. The leak-off pressure (LOP) data used are those acquired by operators during LOTs in compacted mudrocks. The pressure values obtained from this operation are used as a proxy for the minimum principal stress.

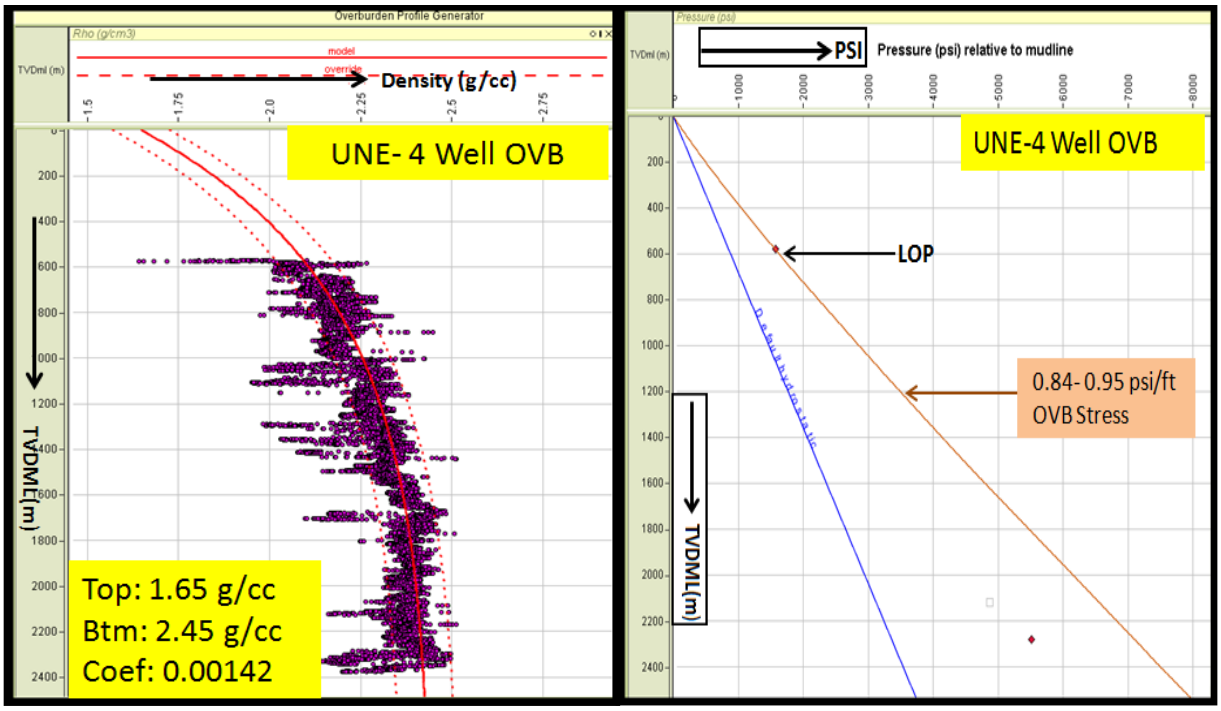

Figure 6.3. Left: Density profile generated for well UNE-4. Right: OVB stress profile for the same well calculated from the density profile.

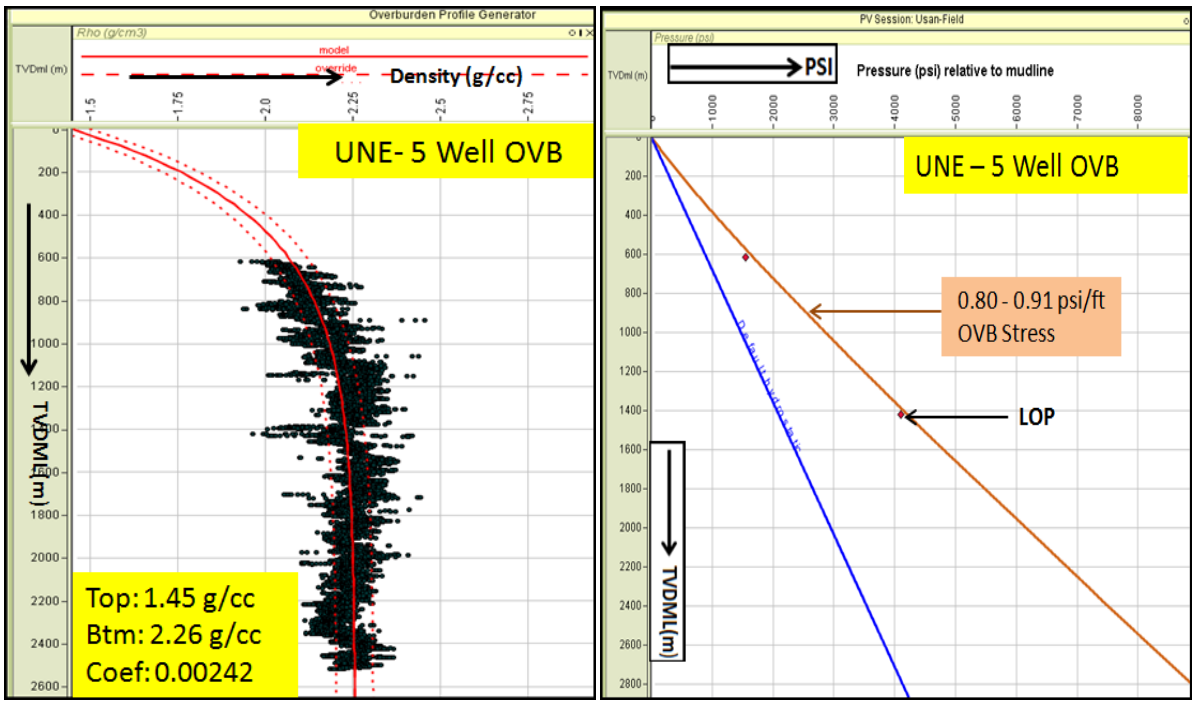

Figure 6.4. Left: Density profile generated for well UNE-5. Right: OVB stress profile for the same well calculated from the density profile.

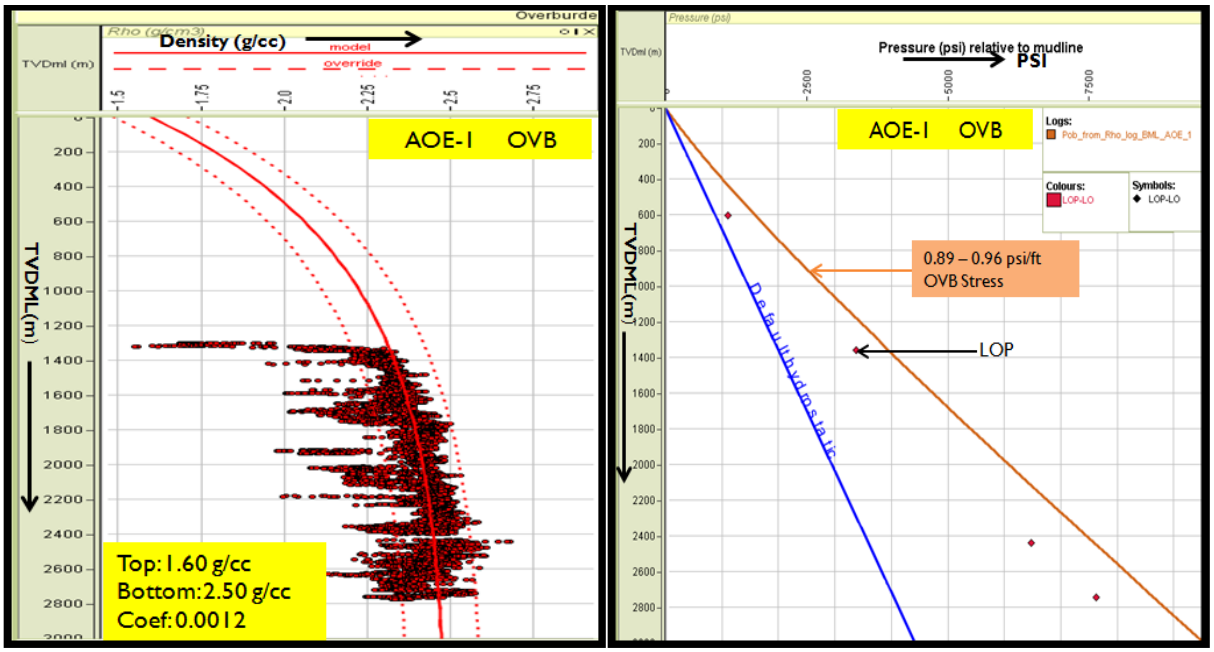

Figure 6.5. Left: Density profile generated for well AOE-1. Right: OVB stress profile for the same well calculated from the density profile.

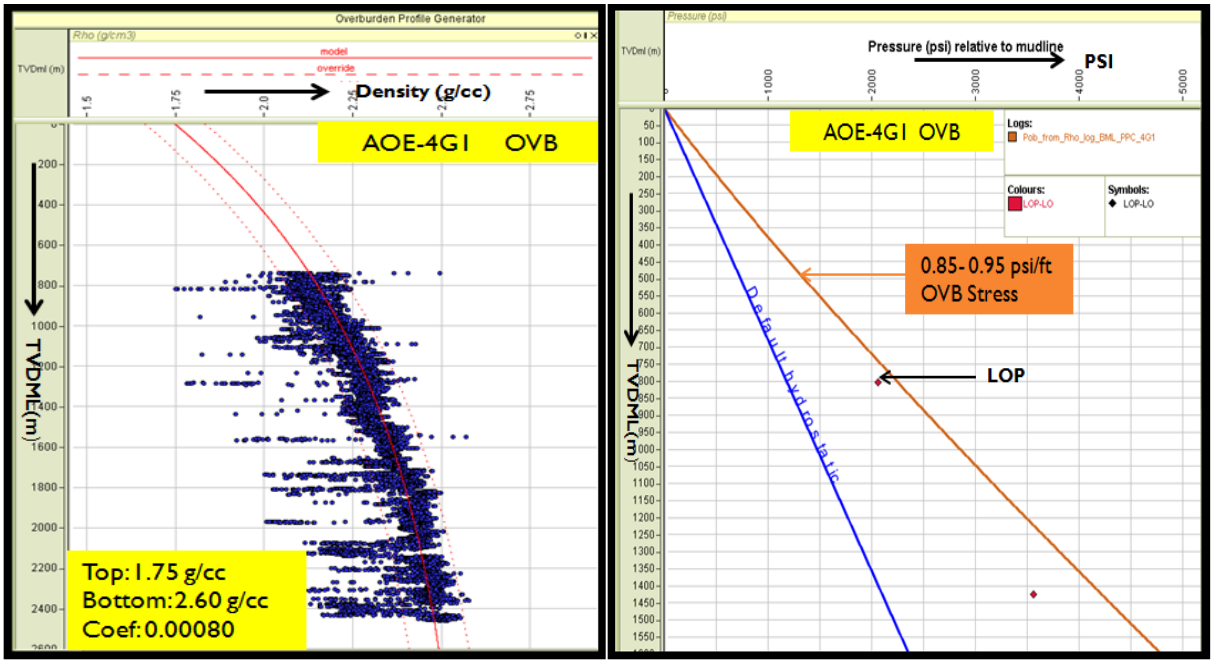

Figure 6.6. Left: Density profile generated for well AOE-4G1. Right: OVB stress profile for the same well calculated from the density profile.

Field	Well	Top Density (g/cc)	Bottom Density (g/cc)	Coefficient
UNE	UNE-4	1.65	2.45	1.42×10^{-3}
	UNE-5	1.45	2.26	2.24×10^{-3}
AOE	AOE-1	1.60	2.50	1.3×10^{-3}
	AOE-4G1	1.75	2.60	8.0×10^{-4}

Table 6.1. Top and bottom densities and coefficients used for density profiles in UNE and AOE wells.

6.2.2 NCT

An NCT was generated for shales in each well with RokDoc using equation 5.1. Shales were selected using Gardner's velocity-density relationship (see equation 3.9) as the first step (Figure 5.6). A GR cut-off value in the range 80–90 API was then applied for further filtering. A final constraint of $V_{sh} \geq 65\%$ (see equation 4.1) was also applied, and the data points removed are greyed out zones in Figure 5.7. The greyed-out zones in the NCT plots are the sand intervals that were filtered out (Figures 6.8 and 6.9).

Two main challenges with NCT construction on this study were the lack of data at shallow depths, and the top of overpressure in most of the wells is very shallow. In such cases, experience and knowledge of local geology was used to constrain density at mudline. This situation is not peculiar to the Niger Delta area. Overpressure at or close to mudline have been reported by others. Based on regional and high-resolution 3D seismic velocity and rock models, Banic et al. (no date) reported the onset of overpressure at seafloor in an un-named deep water

basin offshore West Africa. Also, Bowers (2002) reported that in the deepwater Gulf of Mexico, overpressure can start within a few hundred feet of the seafloor.

In wells UNE-4 and UNE-5, the NCTs for density show that undercompaction begins at about 600 m to 900 m below mudline (Figure 6.8). In AOE-1 and AOE-4G1, the top of undercompaction is hard to place due to limited density data. However, judging from the NCT in AOE-1 and AOE-4G1, undercompaction begins at 1100 m and 1200 m respectively.

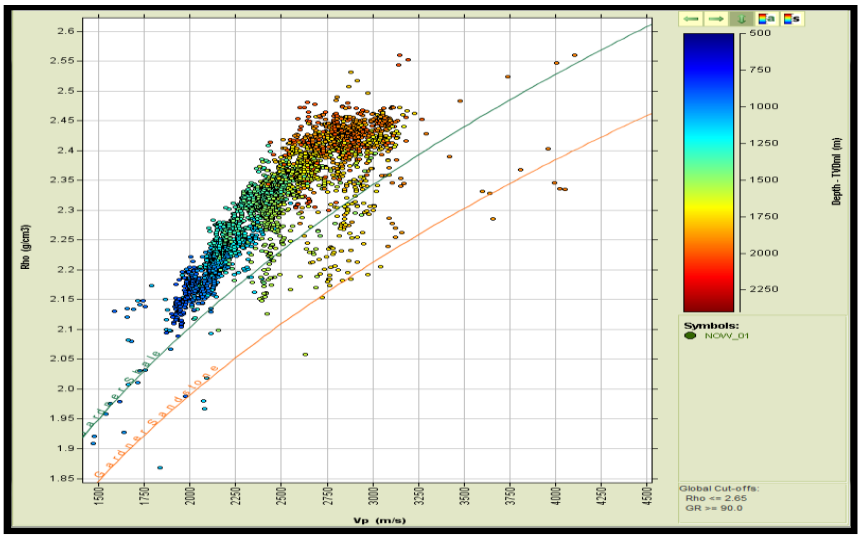

Figure 6.7. An example of Gardner's plot of density against velocity filtered with a GR threshold value of 90 API to pick data points from cleanest shales. The green line on the plot is the shale-bounding curve.

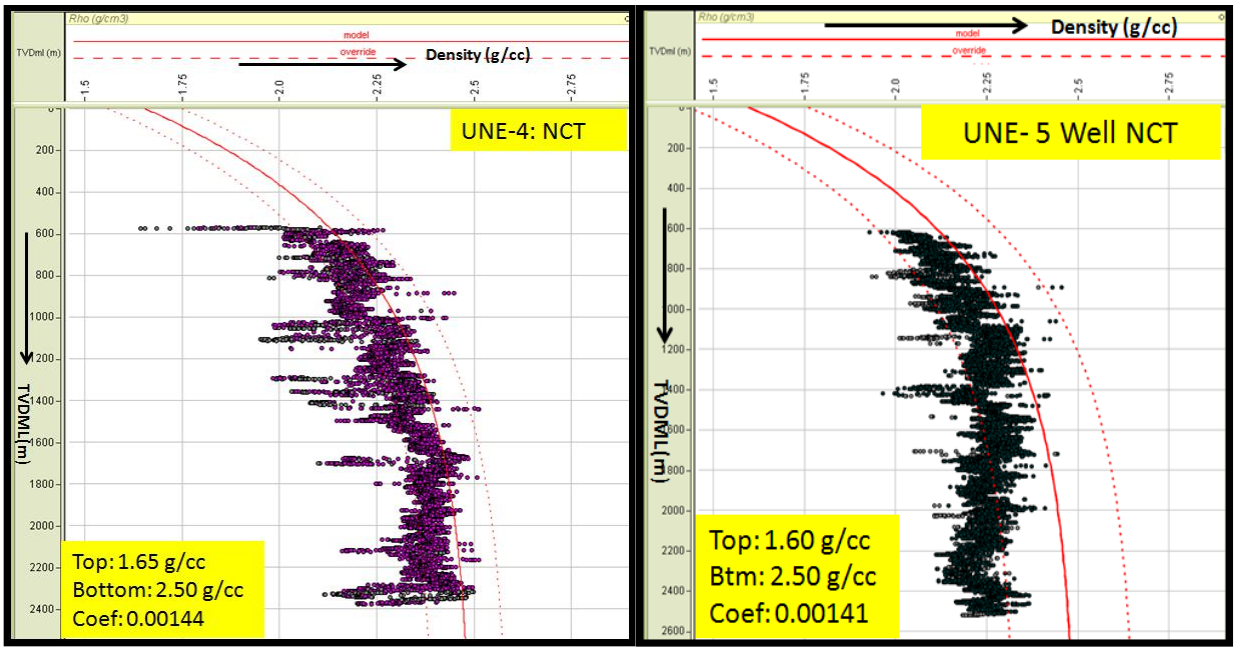

Figure 6.8. Left: Density-generated NCT for well UNE-4. Right: Density-generated NCT for well UNE-5.

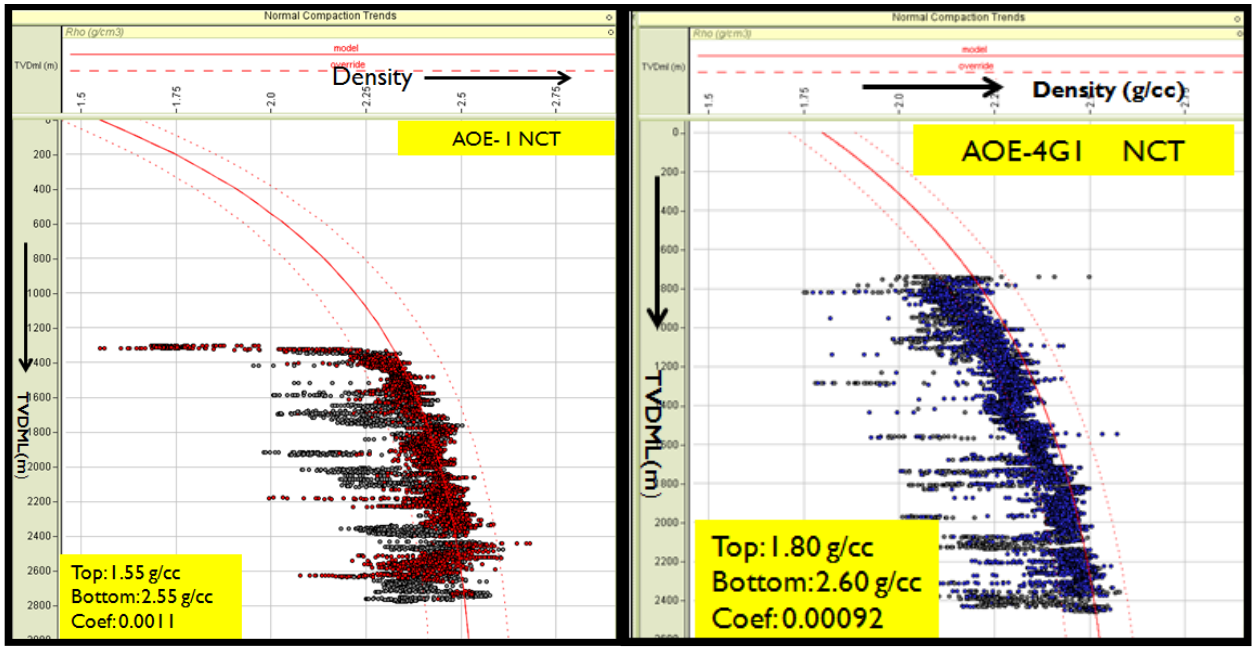

Figure 6.9. Left: Density-generated NCT for well AOE-1. Right: Density-generated NCT for well AOE- 4G1.

6.2.3 Plots generated from log data

Results from wireline logs recorded in the UNE and AOE wells are presented in this section. The density, velocity, and resistivity logs were quality checked and discriminated for clean shale, as discussed in section 4.1. The logs were then plotted for examination of trends. The rationale for the use of cross-plots in pressure analysis has been discussed in section 3.5. Using examples from the UNE and AOE fields, results from two categories of cross-plot are presented here: firstly, those that are used to infer whether unloading, in general, has contributed to overpressure and, secondly, those that are used to infer whether, specifically, smectite-to-illite transformation has occurred in the system.

Depth profiles for density, velocity and resistivity

Figures 6.10–6.13 are the depth profiles of density, velocity and resistivity for wells UNE-4, UNE-5, AOE-1 and AOE–4G1, plotted individually. The idea is to check whether reversals have occurred at the same depth in all of the log types, or just in some, both to look for and also to choose appropriate pore pressure prediction methods (Bowers, 1995, 2001; Lahann, 2001; Katahara, 2003, 2006).

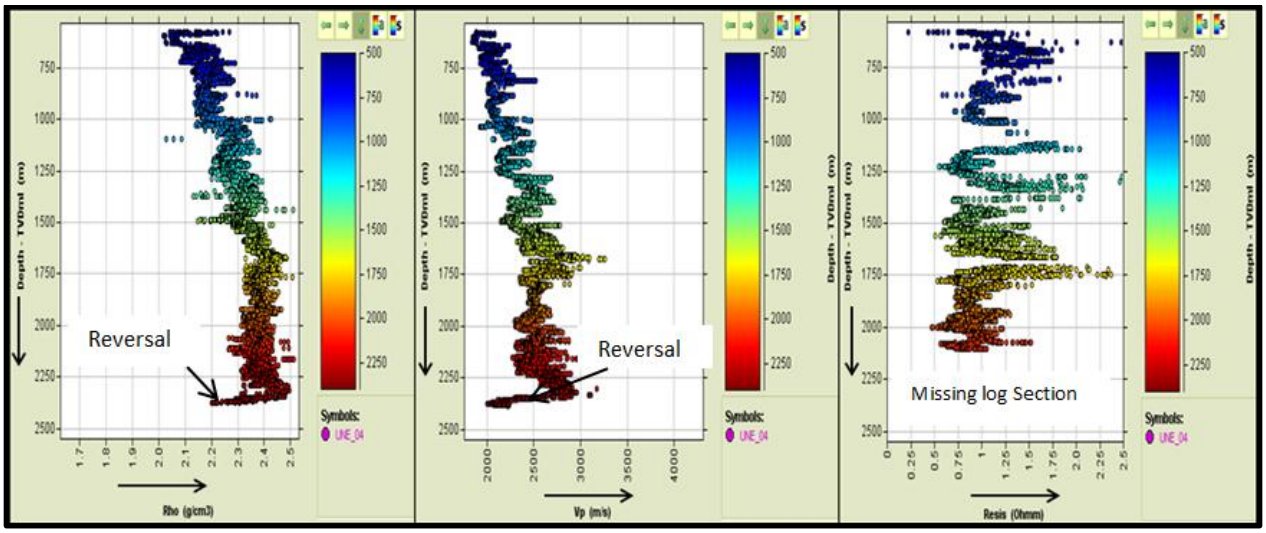

Figure 6.10. UNE-4 well depth plots of density, sonic velocity and resistivity.

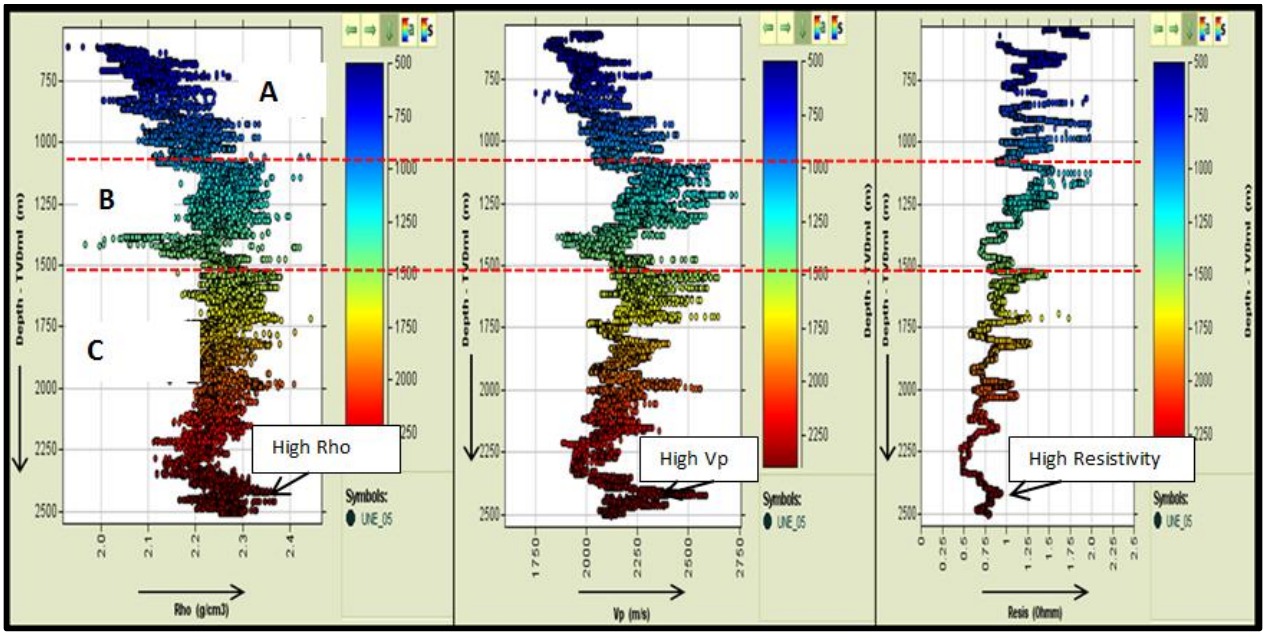

Figure 6.11. UNE-5 well depth plots of density, sonic velocity and resistivity. Labels A, B, and C are used to highlight intervals of trend changes.

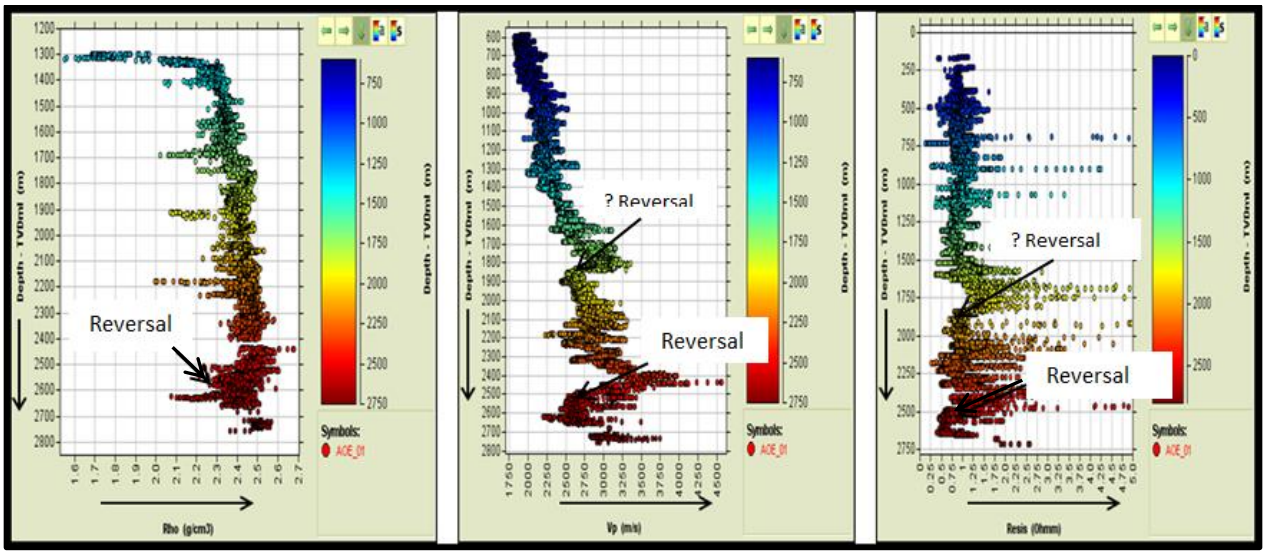

Figure 6.12. AOE-1 well depth plots of density, sonic velocity and resistivity.

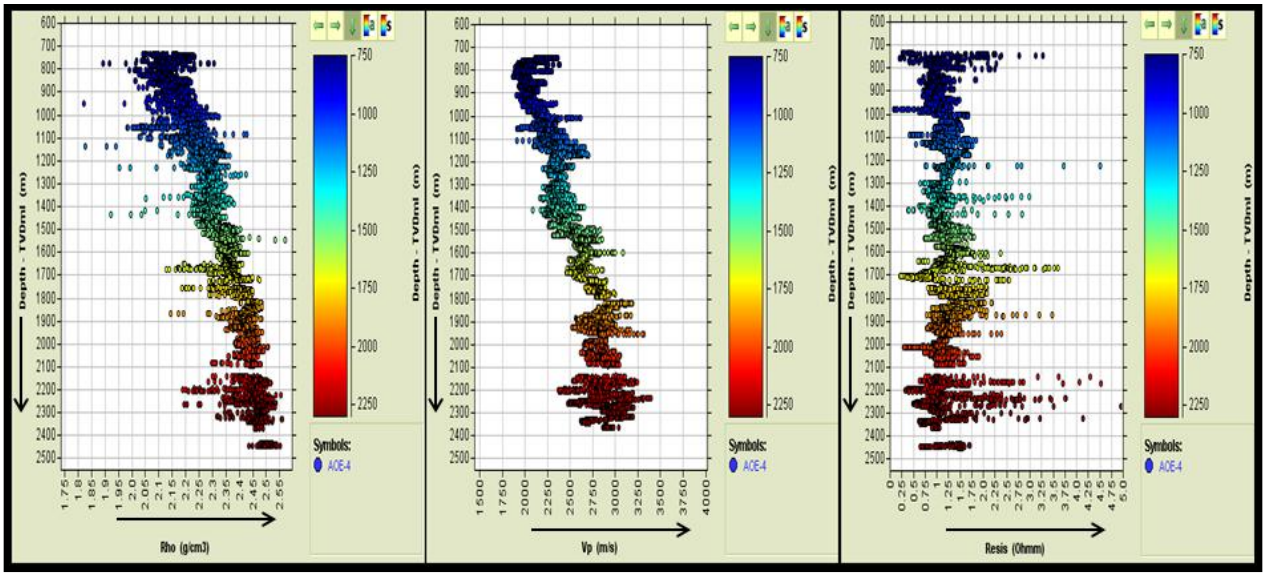

Figure 6.13. AOE-4G1 well depth plots of density, sonic velocity and resistivity.

In well UNE-4 (Figure 6.10), the general trend is increasing density and velocity with depth until ~2350 m, where reversals are seen on both logs. The resistivity log in this well does not reach 2350 m depth. In well UNE-5 (Figure 6.11); velocity, density and resistivity logs have normal trends down to ~1100 m. Three general observations are made regarding log trends

below that depth. First, between 1100 m and 1500 m there is a clear reversal on the sonic and resistivity logs, and there is no density increase over the same interval. Secondly, there is also a decreasing trend from 1500 m to ~2300 m, observable on all three logs. And finally, between 2350 m and 2500 m is a zone with higher density, velocity and resistivity.

In well AOE-1, a reversal at 1800 m is seen on the velocity and resistivity logs at 2500 m (Figure 6.12), and there is a reversal on all the logs at 2500 m. The latter reversal most likely results from a change in lithology because, as previously discussed, the density log is insensitive to unloading because storage pores do not expand significantly during unloading. In the AOE-4G1 well, the general trend follows a normal trend and no apparent reversal is noticeable (Figure 6.13).

Vertical effective stress (VES)

Measured formation pressure from MDT, RFT, or RCI tools and calculated overburden (OVB) were processed with the Ikon Science RokDoc software to generate depth plots of VES. The software interpolates between pressure measurements to give a continuous VES profile. The generated VES profiles were checked for any apparent bad data, and the final results are shown in Figures 6.14 and 6.15. The gaps in the trends are sand intervals that have been filtered out since only shale intervals are of interest.

In the UNE-4 well, a VES reversal is seen from ~1830 m to 2100 m (Figure 6.14); below this depth pressure data were unavailable. In UNE-5, small reversals are seen at 700–800 m, 1700–1710 m, and 1900–2100 m (Figure 6.14). The VES from 1150 m to 1700 m remains approximately constant. The plot shows data to a maximum depth of ~2190 m, where the deepest measurement of pore pressure was taken.

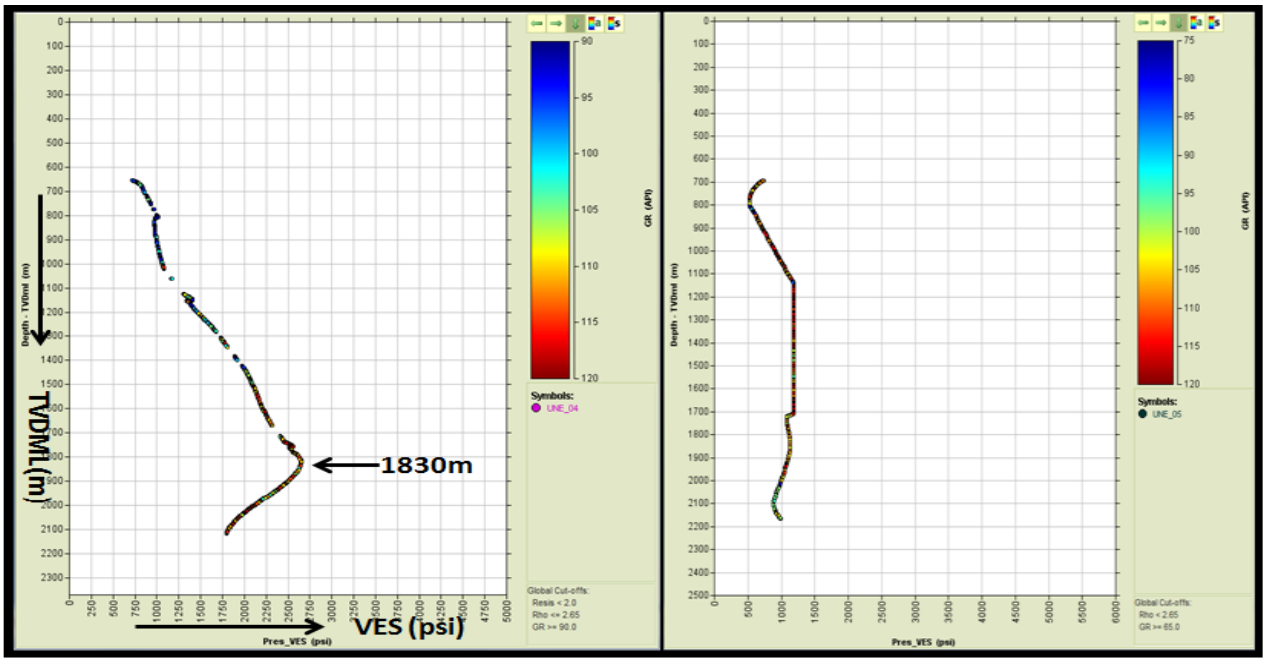

Figure 6.14. Depth plots of VES for well UNE-4 (left) and UNE-5 (right).

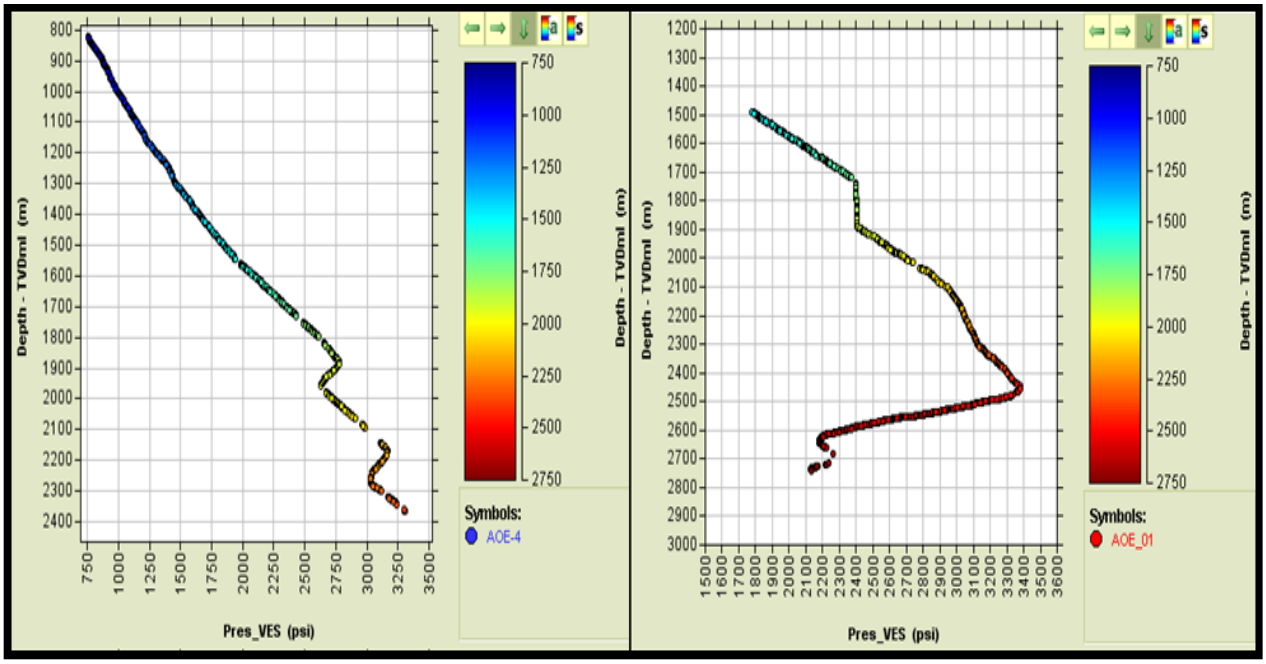

Figure 6.15. Depth plots of VES for well AOE-4G1 (left) and AOE-1 (right).

In well AOE-4G1, small reversals are seen at 1890–1970 m and 2180–2280 m (Figure 6.15). In well AOE-1, there is a plateau in VES at 1720–1900 m and a strong reversal below 2450 m (Figure 6.15). Are these reversals due to unloading? The answer will be explored in chapter 8 with the use of additional cross-plots.

Velocity–VES cross-plots

Figures 6.16–6.19 are cross-plots of sonic velocity against VES for wells UNE-4, UNE-5, AOE-1. The plot for the UNE-4 well (Figure 6.16) shows a single trend through the shallow and deep intervals. Velocity increases with increasing VES down to ~1830 m. At greater depths, VES reverses, yet the data appear to track the trend of the shallow data down to ~2100 m, although there is an upward kick in velocity for the deepest data points which may, or may not, be significant. The UNE-5 well plot (Figure 6.17) is quite similar to UNE-4 in that there are reversals in VES at depth, and the data points in the reversals fall on the same trend as the shallower data.

There is quite a lot of scatter in the velocity–VES cross-plot for well AOE-1 (Figure 6.18). Nevertheless, it appears possible that the data are scattered around a single trend, even though there are several intervals where data points cluster above or below the average trend, both at shallower levels and within the VES reversal. The trend in well AOE-4G1 is a straightforward increase in velocity (Figure 6.19), which is expected considering the overall increase in VES with depth evident on Figure 6.15.

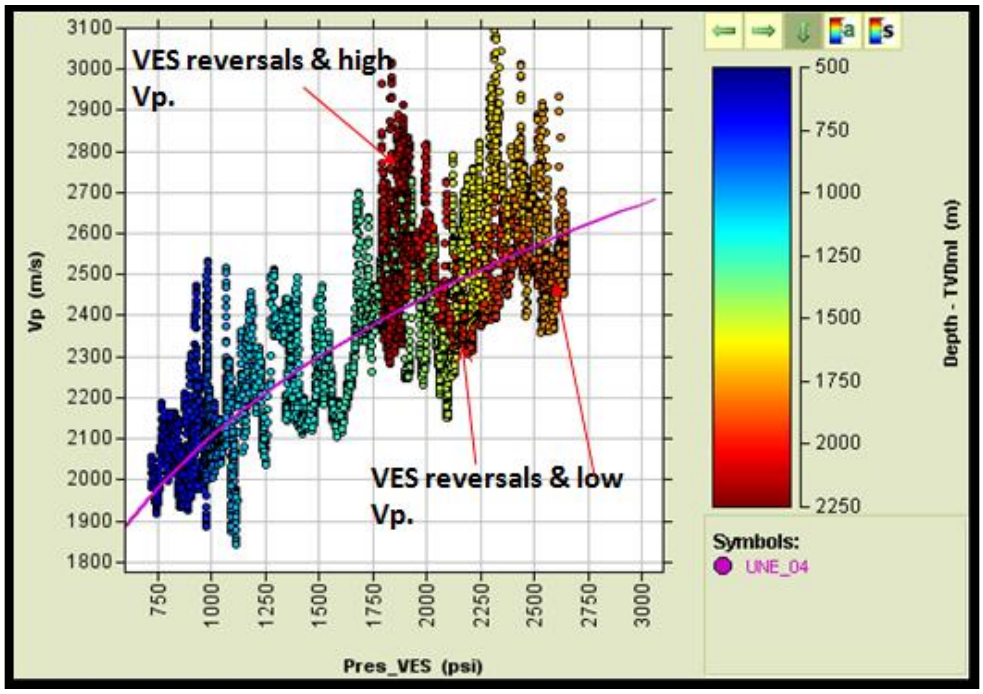

Figure 6.16. Cross-plot of velocity against VES for UNE-4.

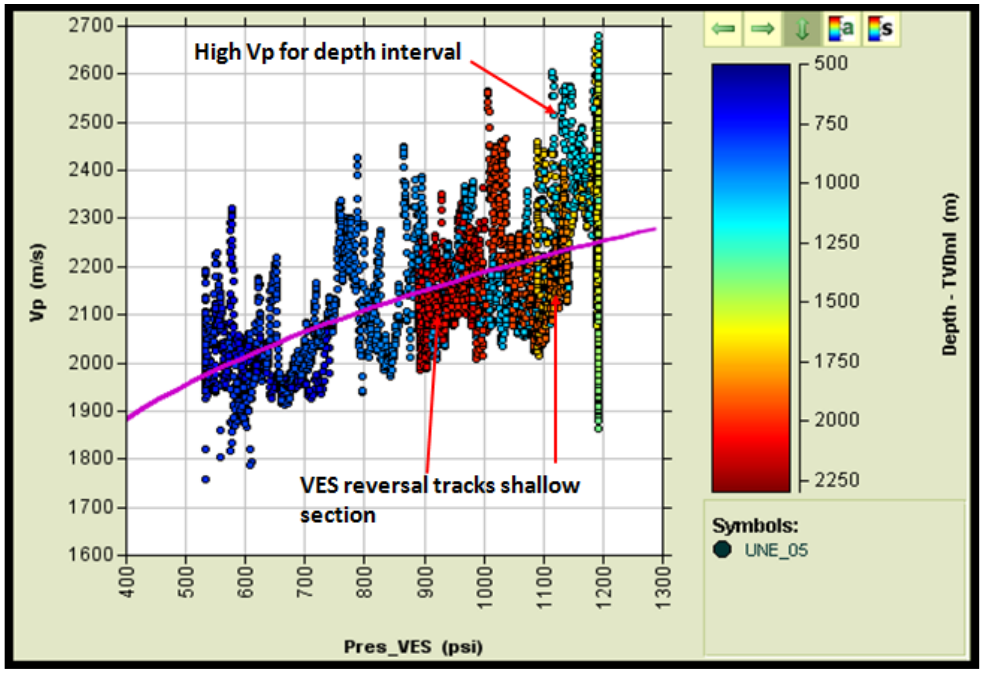

Figure 6.17. Cross-plot of velocity against VES for UNE-5.

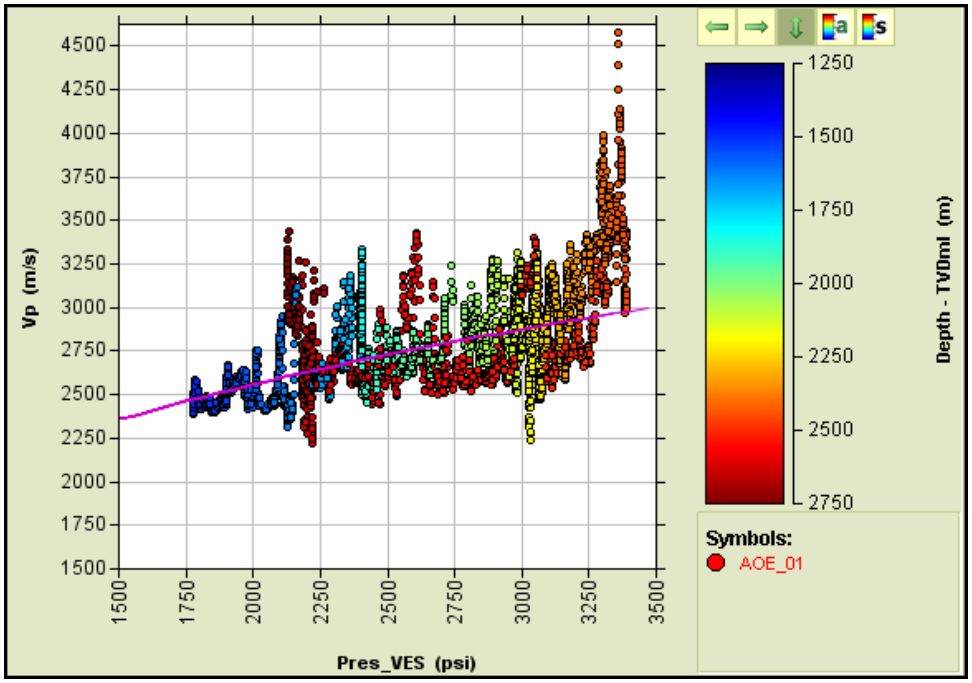

Figure 6.18. Cross-plot of velocity against VES for AOE-1.

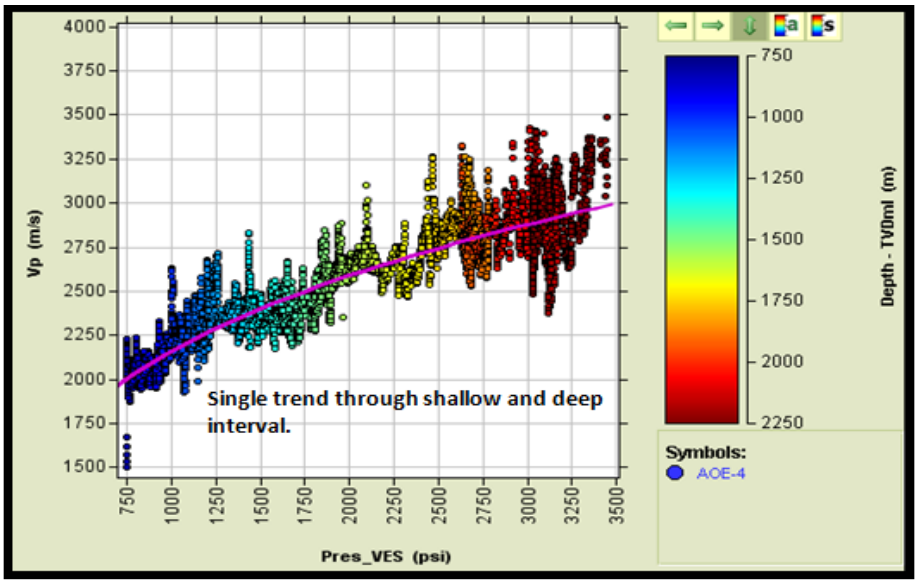

Figure 6.19. Cross-plot of velocity against VES for AOE-4G1.

Density–VES cross-plots

The density–VES trend in well UNE-4 (Figure 6.20) is quite similar to the trend seen in the velocity–VES plot. The interval 500–1750 m shows a general trend of increasing density with VES. Reversal of VES begins at 1830 m with density values that track the shallower interval until a depth of 2000 m, below which the density fluctuates around an approximately constant-value trend. In well UNE-5 (Figure 6.21), density increases with VES from 500 m to 1250 m. Reversal in VES starts at 1600 m with an almost constant density value.

The plot for well AOE-1 (Figure 6.22) generally shows that density increases with VES. In the VES reversal, below 2450 m, the average density value is slightly greater than the shallower trend, but the difference may not be significant. In well AOE-4G1, density increases with VES from shallow to deeper intervals (Figure 6.23), which is expected considering the overall increase in VES with depth evident on Figure 6.15.

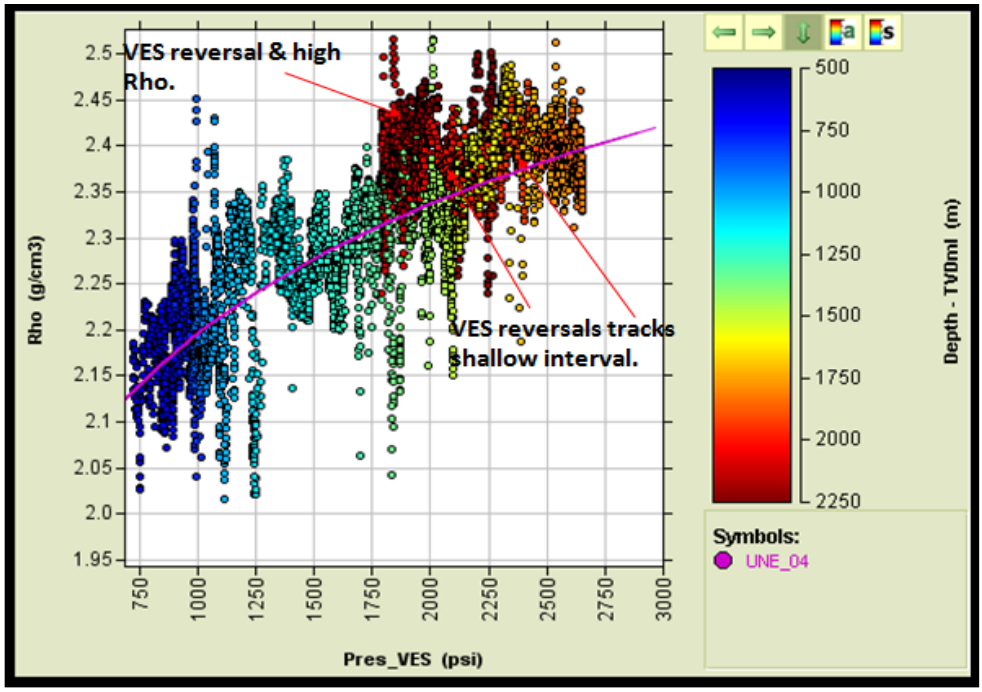

Figure 6.20. Cross-plot of density against VES for UNE-4.

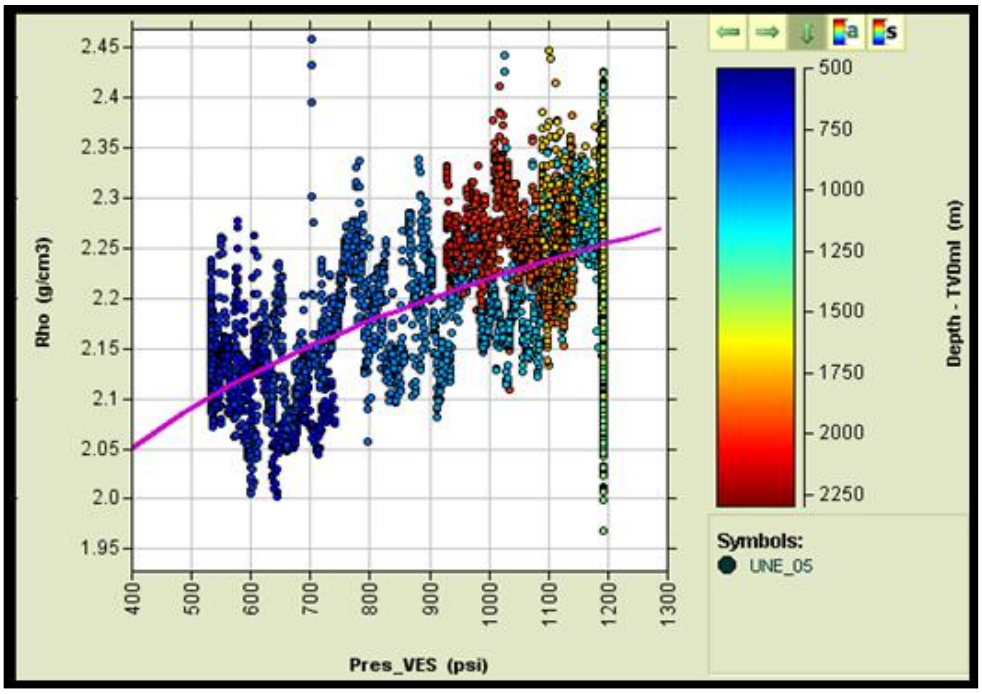

Figure 6.21. Cross-plot of density against VES for UNE-5.

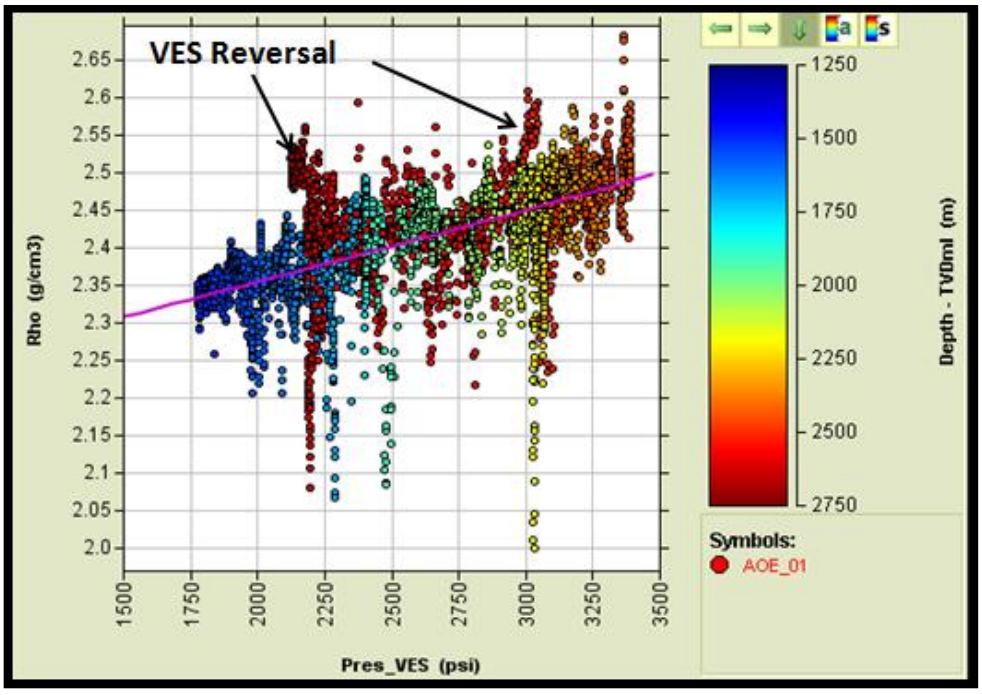

Figure 6.22. Cross-plot of density against VES for AOE-1.

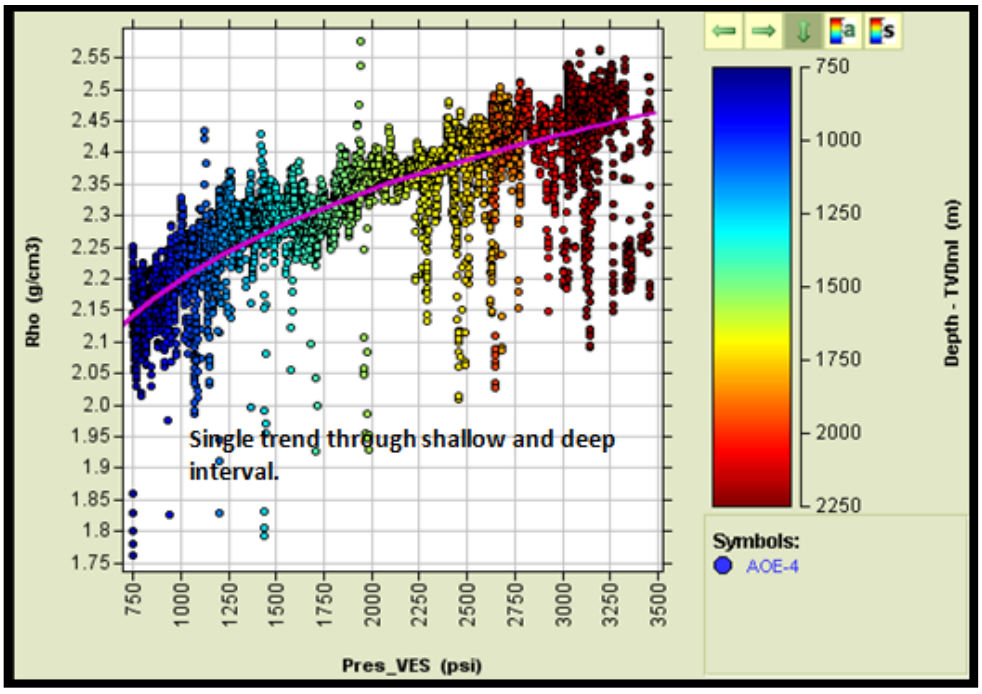

Figure 6.23. Cross-plot of density against VES for AOE-4G1.

Velocity–density cross-plots

Figures 6.24–6.27 show velocity–density cross-plots for wells UNE-4, UNE-5, AOE-1, and AOE-4G1. In well UNE-4 (Figure 6.24), the general trend is an increase in velocity with density from 500 m to 1700 m, and the gradient of the trend steepens with depth. The second trend for data points below 1750 m lies slightly to the right of the main trend.

In well UNE-5 (Figure 6.25), there is a trend of velocity increasing with density through the shallow interval from 500 m to 1300 m. The second trend for data from depths below ~1500 m lies to the right of the shallow trend: density values are higher for a given velocity, and velocity values are lower for a given density.

In well AOE-1 well (Figure 6.26), the shallow trend in the interval 1250–1800 m is similar to that in wells UNE-4 and UNE-5. The trend of the deeper points below ~2000 m depth

is more scattered, and overall is not significantly different from the shallow trend. In well AOE-4G1 (Figure 6.27), the shallow data again have the same trend, and the deeper data below ~2200 m are suggestive of the same deeper trend as the UNE-4 and UNE-5 wells.

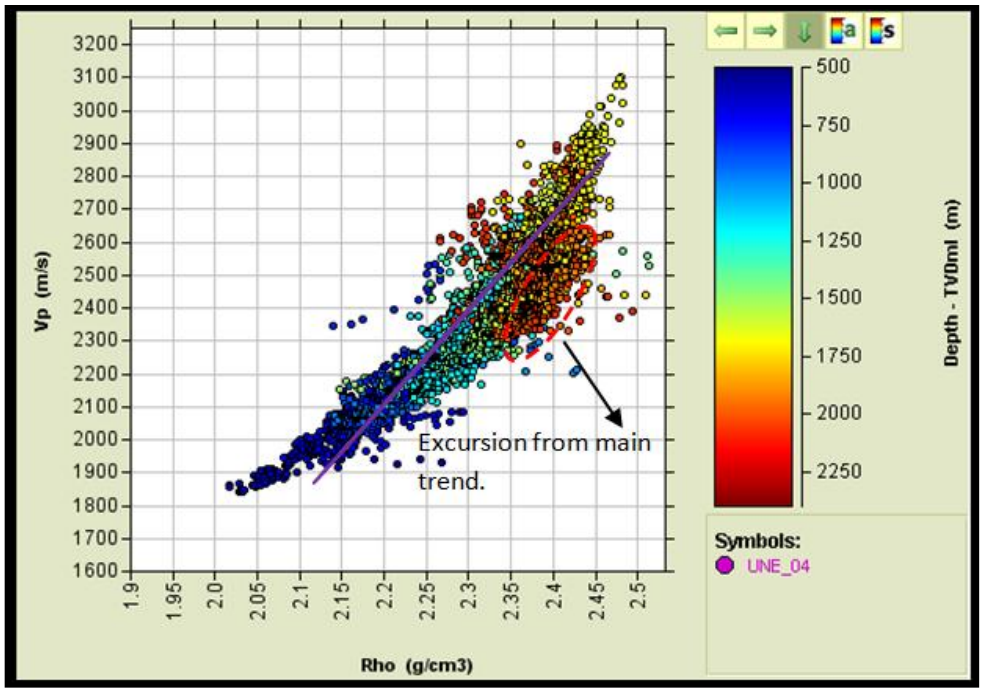

Figure 6.24. Cross-plot of velocity against density for UNE-4.

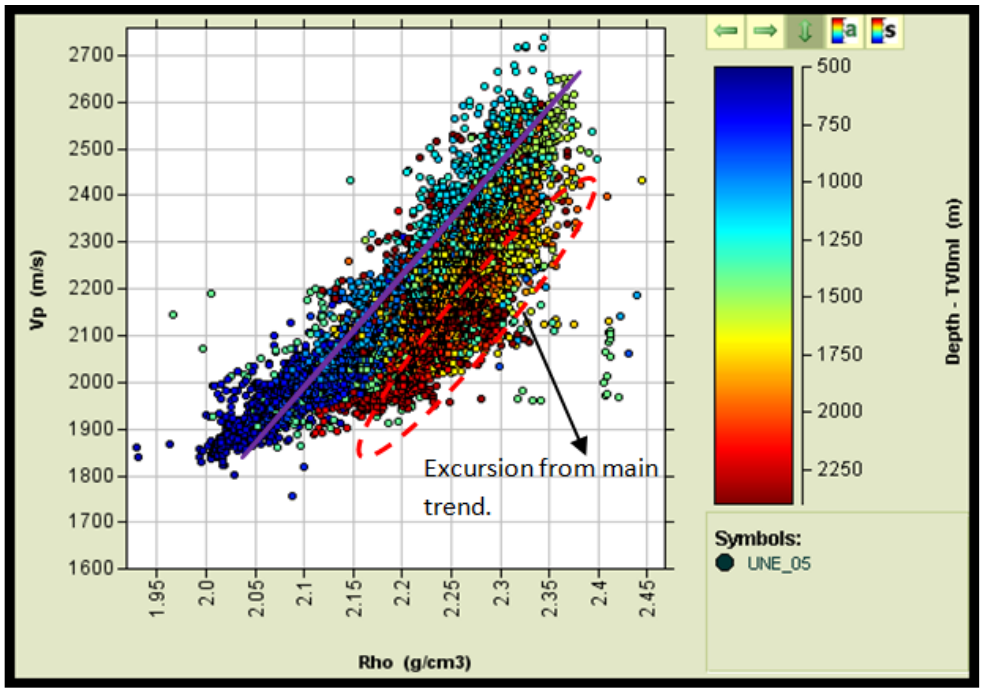

Figure 6.25. Cross-plot of velocity against density for UNE-5.

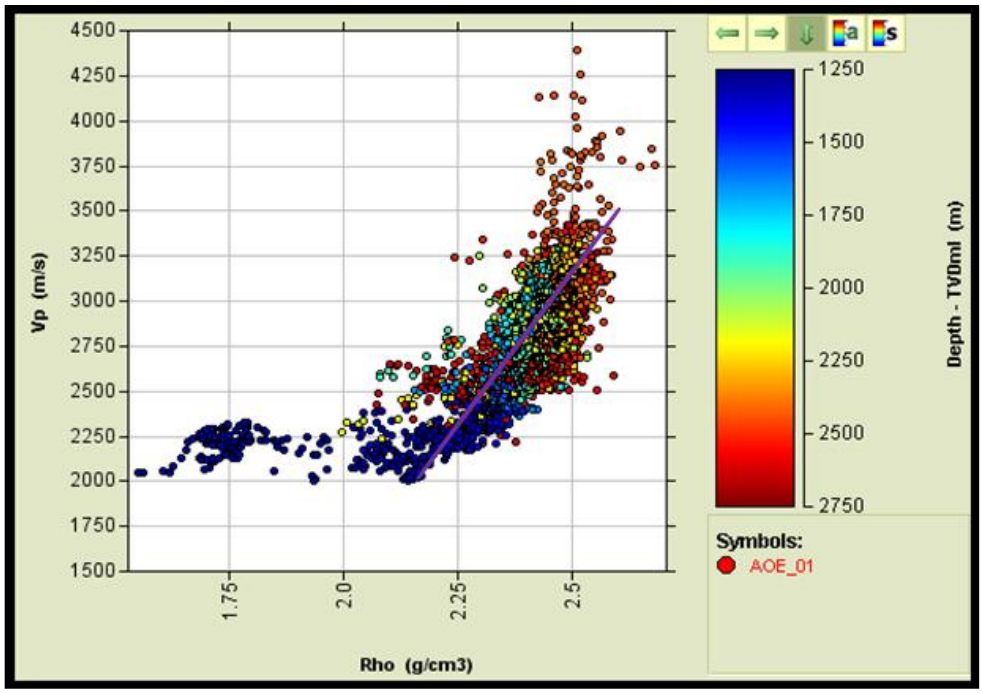

Figure 6.26. Cross-plot of velocity against density for AOE-1.

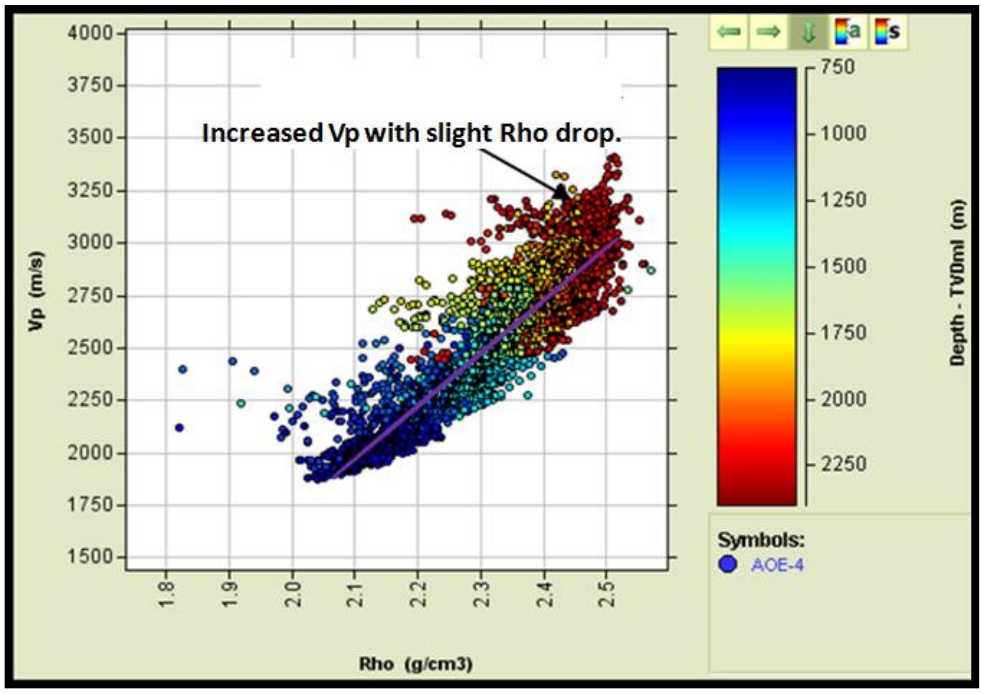

Figure 6.27. Cross-plot of velocity against density for AOE-4G1.

Density–sonic transit time cross-plots

The overall trends in Figures 6.28–6.31 are, of course, similar to those seen in Figures 6.24–6.27, given that the sonic transit time is the reciprocal of velocity and the axes have been switched. This plot was introduced by Dutta (2002) to show compaction trends of smectite-rich and illite-rich shales in the GoM. It can be seen here that as depth increases, points generally shift from the smectite-rich line towards the illite-rich line.

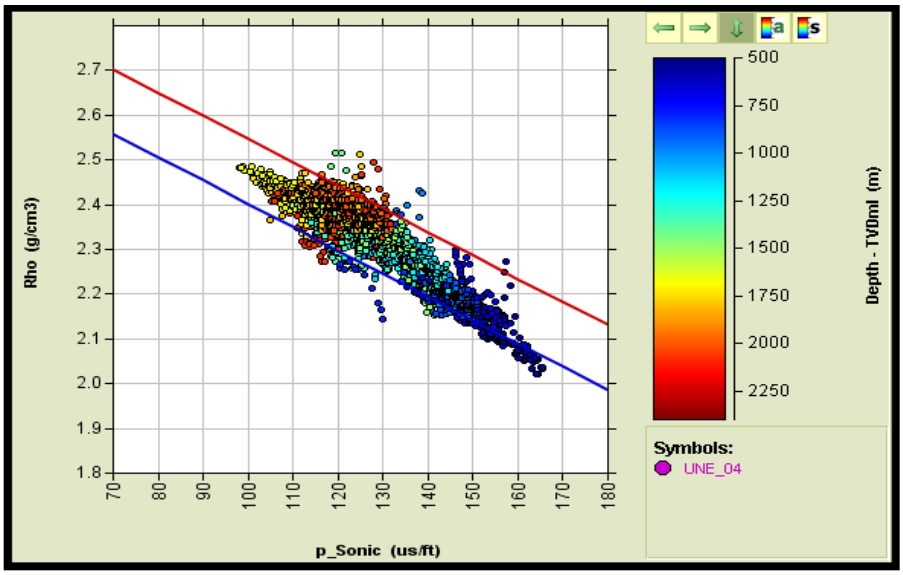

Figure 6.28. Cross-plot of density against sonic transit time for UNE-04 well.

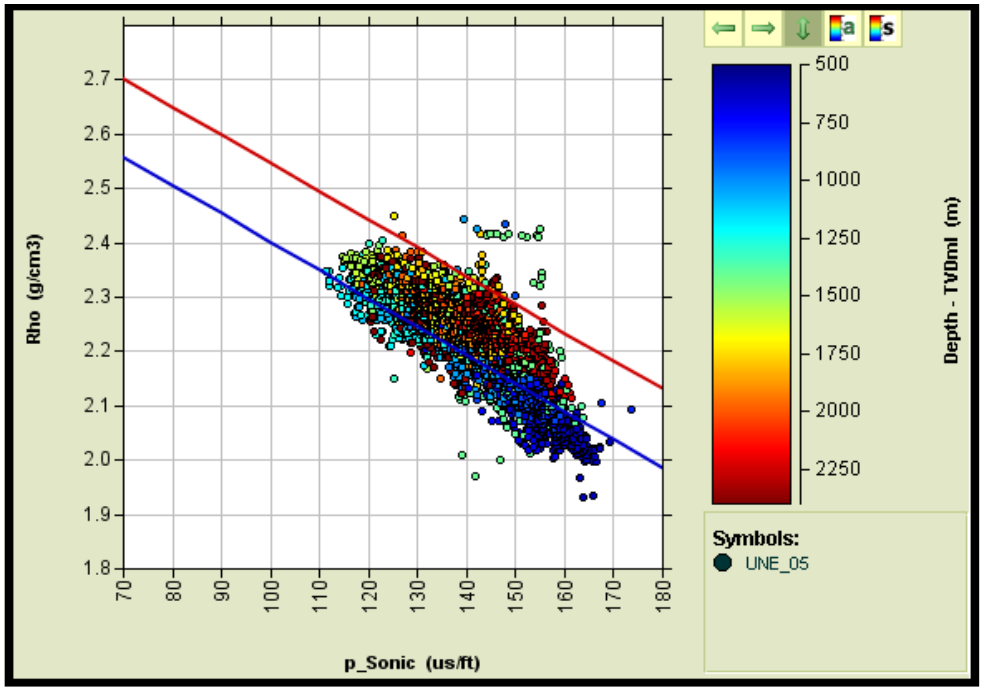

Figure 6.29. Cross-plot of density against sonic transit time for UNE-05 well.

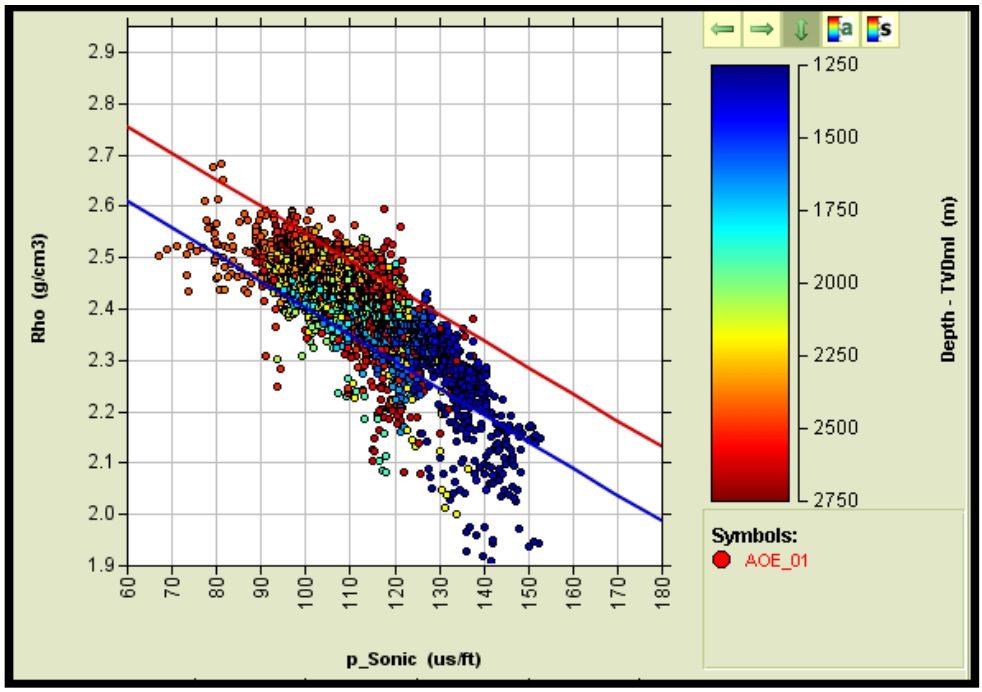

Figure 6.30. Cross-plot of density against sonic transit time for AOE-01 well.

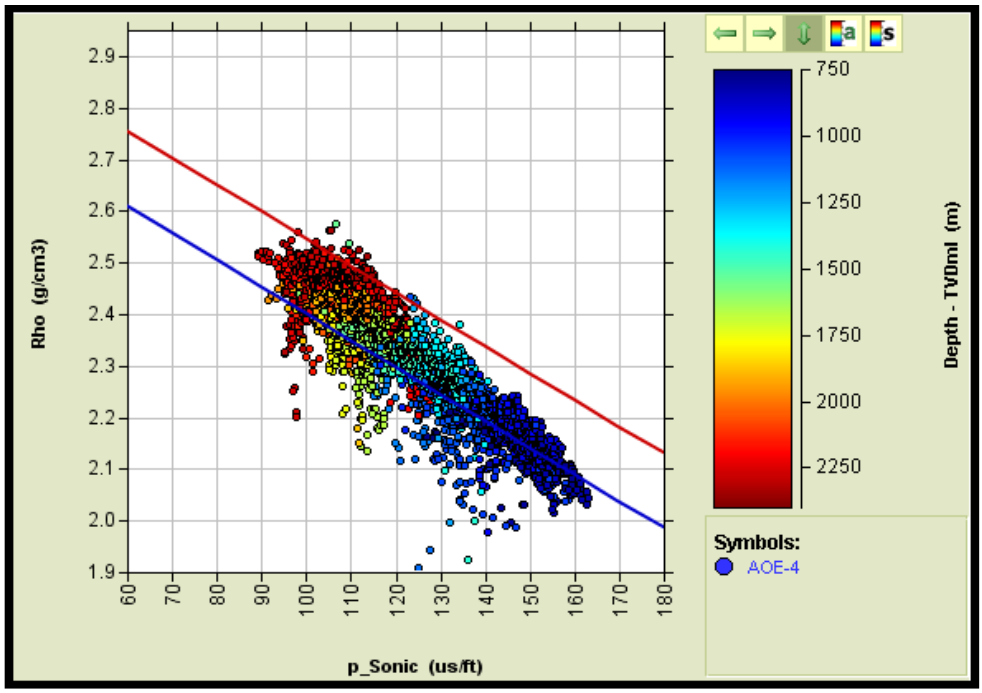

Figure 6.31. Cross-plot of density against sonic transit time for AOE-4 well.

Temperature data

Tables 6.2 and 6.3 show temperature gradient estimates for UNE and AOE wells. Temperatures from the MDT tool were provided by the operators. Apparently poor temperature data, that were subjectively judged to be too low or too high by comparison with the general trend, were discarded. For eight UNE wells, the average temperature gradient is 3.77 deg C /100 m (Table 6.2). For 10 AOE wells, the average temperature gradient is 3.56 deg C /100 m (Table 6.3).

Wells	Depth m (TVDml)		Temp deg C		Grad deg C /100m
	Top	Bottom	Top	Bottom	
UNE-1	1455.115	1889.221	65	85.6	4.745392376
UNE-2	900.5011	1844.311	41.3	84.1	4.534810302
UNE-3	992.3404	2087.478	54.6	92.6	3.469884692
UNE-4	628.3787	2275.689	38.7	101.7	3.824417036
UNE-5	721.041	2196.489	44.1	96	3.517574706
UNE-6	634.8009	1554.017	39.4	71.9	3.535622276
UNE-7	611.7671	1516.148	36.5	66.8	3.350357039
UNE-8	907.8316	1755.124	52.3	79.3	3.186622102
					3.770585066

Average temperature gradient for 8 wells.

Table 6.2. MDT temperature data obtained from eight UNE wells.

Wells	Depth m (TVDml) Top	Bottom	Temp deg C Top	Bottom	Grad deg C /100m
AOE-1	1516.843	2776.307	60	114	4.287537919
AOE-3T1	1391.001	2240.499	51.4	96.4	5.297240302
AOE-5G1	1636.553	2028.243	66.6	87	5.208209192
AOE-6	1443.88	1913.245	70.1	81.5	2.428815632
AOE-7T1	1366.65	2449.233	67.4	102.7	3.260721337
AOE-9	1208.7	2349.898	61.5	93.1	2.769018391
AOE-10	1626.459	2055.26	68.6	78.8	2.378721447
AOE-11	1364.477	1720.968	61.1	74.4	3.730809139
AOE-24	1501.177	1662.461	68.2	72.8	2.852095534
AOE-25	1561.762	2152.556	64.2	84.1	3.368349271
					3.558151816

Average temp grad for 10 wells in AOE field

Table 6.3. MDT temperature data obtained from 10 AOE wells.

6.3 Pore pressure prediction by the equivalent depth method

Figures 6.32 and 6.33 show the results of pore pressure prediction in shales for the UNE and AOE wells using the equivalent depth method. The generated pressure profile was further constrained with measured pore pressures.

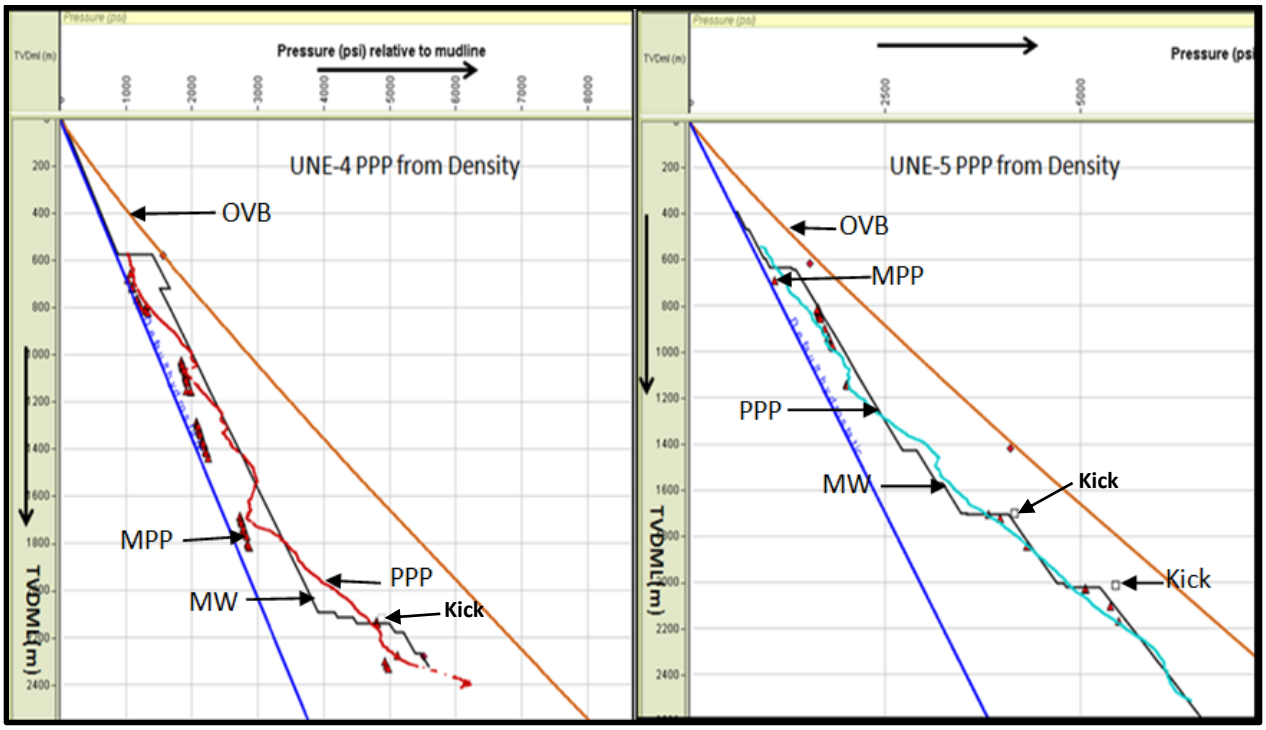

Figure 6.32. Left: Predicted (red) and measured (triangles) pore pressures for well UNE-4. Right: Predicted (cyan) and measured (triangles) pore pressures for well UNE-5. Mud weight in black.

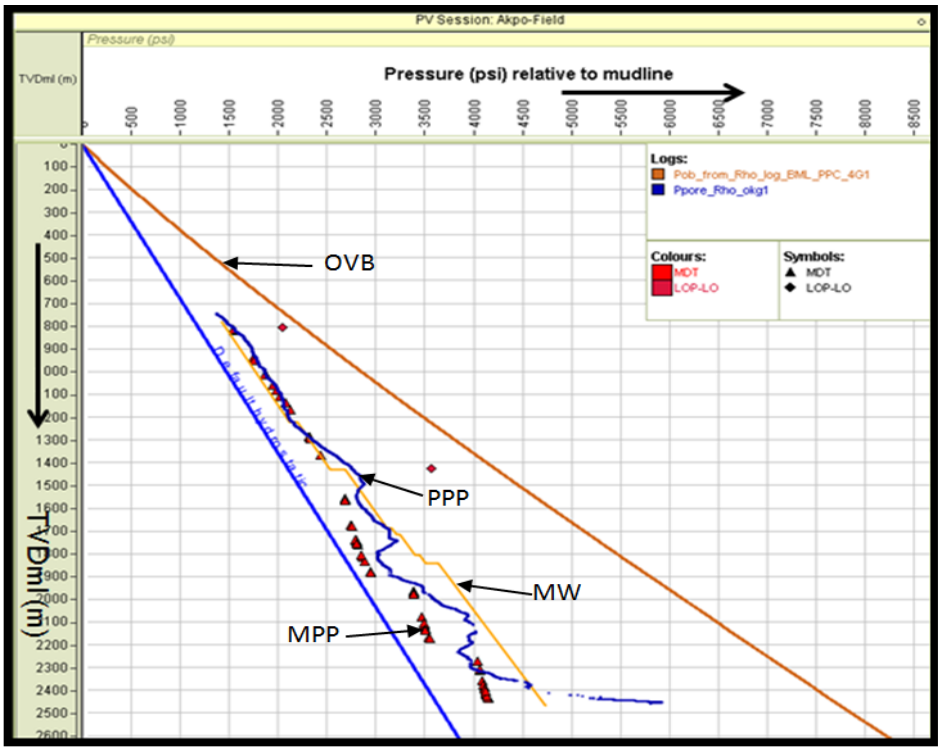

Figure 6.33. Predicted (blue) and measured (triangles) pore pressures for AOE-4G1. The mud weight is shown in orange.

6.4 UBD zones in wells UNE-05 and AOE-4G1

Figures 6.34 and 6.35 show the measured and predicted pore pressures in wells UNE-5 and AOE-4G1, respectively, and the mud weight used to drill each section of each well. In well UNE-05, a zone of UBD is apparent from 1330 m to ~2000 m, and in AOE-4G1 there is a zone of UBD from 750 m to 1300 m. Detailed results of observed mudlog and drilling signatures seen in the UBD zones are discussed in chapter 7. In addition to observed differences between predicted and measured pore pressure and MW; underbalanced drilling is invoked only if zones are corroborated with drilling parameters and mud log data.

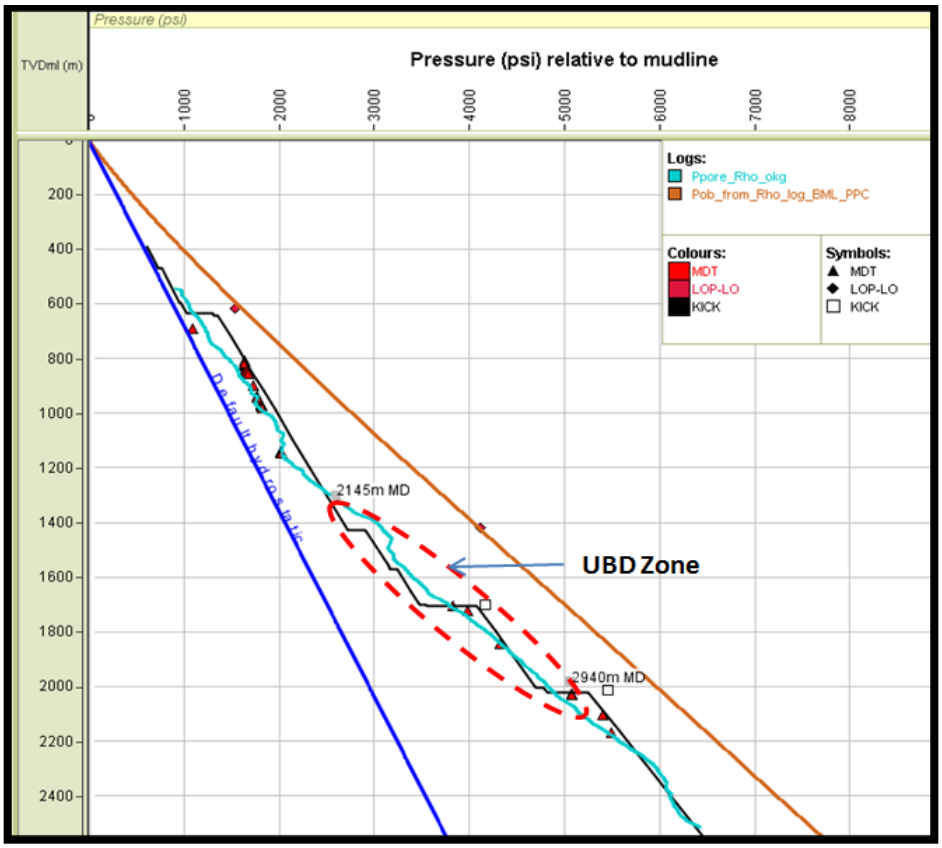

Figure 6.34. UBD zones identified in UNE-5.

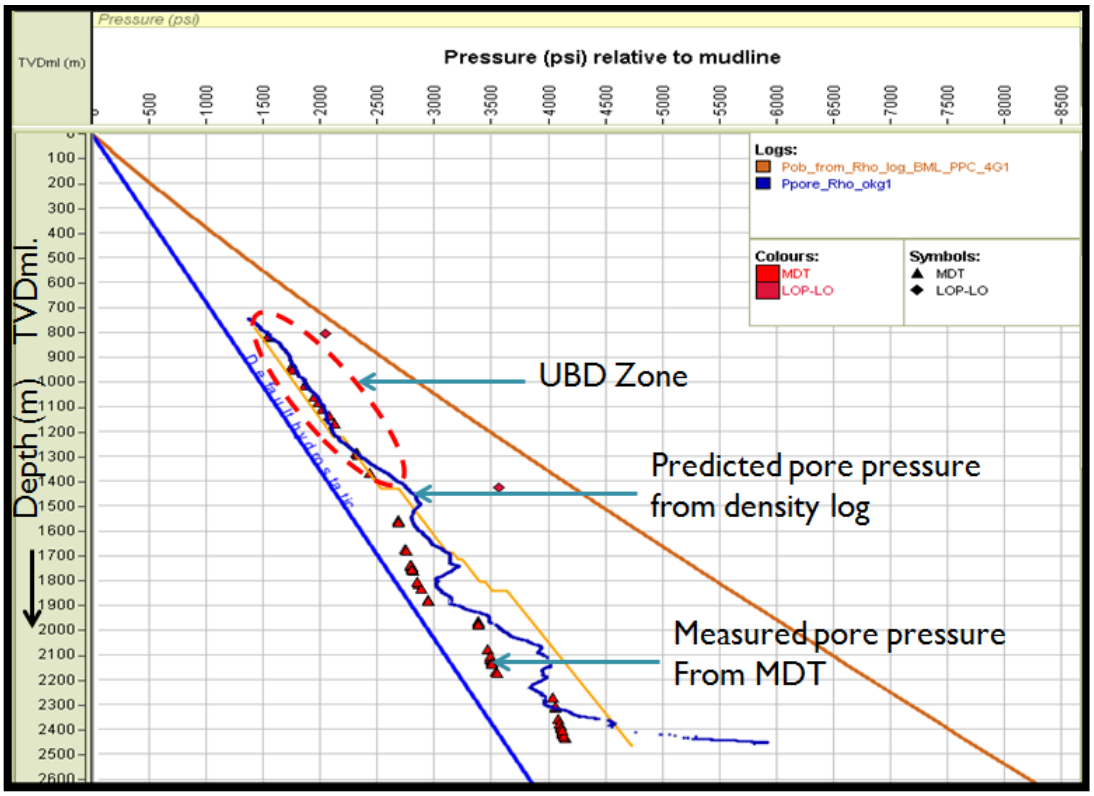

Figure 6.35. UBD zones identified in AOG-4G1.

Chapter 7

Drilling Evidence of UBD in AIW-1, NOW-1, AOE-4G1 and UNE-5 Wells

The UBD zones identified from pore pressure estimation in shales, as described in sections 5.4 and 6.4, are compared in this chapter with indications of UBD from drilling, mudlogs, and EOWRs. Only those wells identified with UBD zones in section 5.4 (i.e., AIW-1 and NOW-1) and section 6.4 (i.e., AOE-4G1 and UNE-5) are covered. The wells are dealt with successively in the four sections of this chapter. Each section begins with a general description of the UBD zone or zones identified from the pressure–depth plot by comparing measured pore pressures and mud weight with pore pressures predicted in shales from the density log, using the equivalent depth method. Then, depending on availability, UBD zones are checked against mudlog, drilling, and well reports for corroboration. Specifically, the caliper log, TG, CG, ROP, Dxc, torque, and sample descriptions on the mudlog are checked over the UBD zones on the pressure–depth plots.

7.1 AIW-1 well

Well AIW-1 is the only one of the three wells analysed in the AIW-EIW field that has UBD identified on the pressure–depth plot (Figure 7.1). Due to the absence of measured pore pressures, inference of UBD in the top section of hole is based on the predicted pore pressure exceeding MW. However, in the lower UBD zone, UBD identification is based on comparison of MW with measured and predicted pore pressures, both of which are greater than MW. Two zones of UBD were identified, over the intervals 2510–2880 m and 3475–3585 m. All depths in

this chapter are measured depths. For evidence of UBD from drilling and mudlog data, delineated zones are compared with the caliper log, ROP, Dxc, TG, and torque data. Below is a presentation of results from selected intervals to illustrate the relationship between UBD identified on the pressure–depth plot and drilling data.

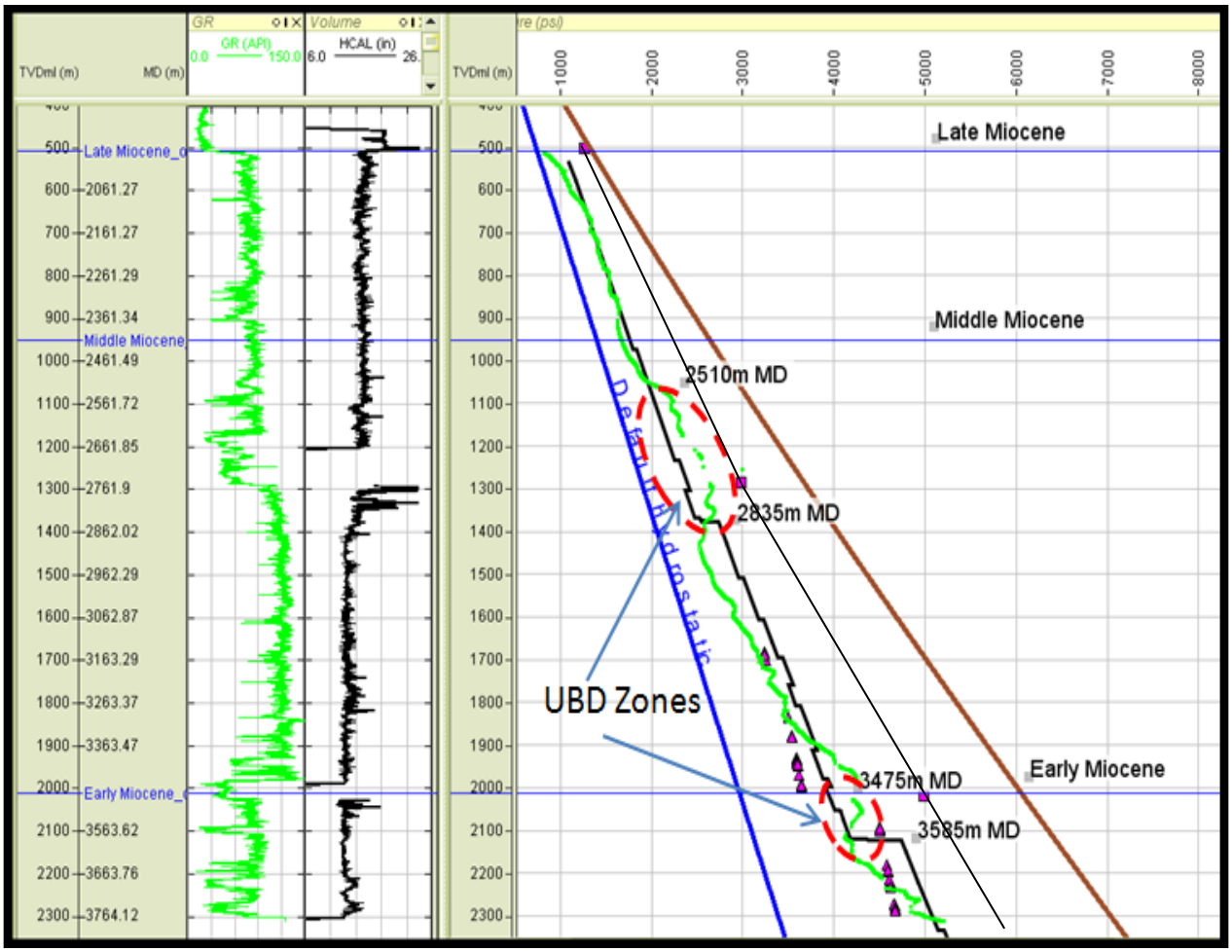

Figure 7.1. GR and caliper logs (left panel) and pressure–depth plot (right panel) with UBD zones identified at 2510–2835 m and 3475–3585 m in well AIW-1.

Interval 2470–2580 m

Comparison of the caliper log and bit size (BS) shows two zones of greater washout in the sand-shale beds below 2500 m and 2540 m (red circles in Figure 7.2). The ROP trend is quite erratic within this interval and it is difficult to establish a clear trend. Except for the drilling breaks at 2510 m and 2534 m, the other drilling breaks seen on the plot appear to correlate with lithology change. The Dxc shows a decreasing trend with depth down to the shale at the bottom of the interval. The TG started out low at the top of the interval and progressively increases, peaking in the sand interval, and then decreases but remains higher than at the top of the interval. Although

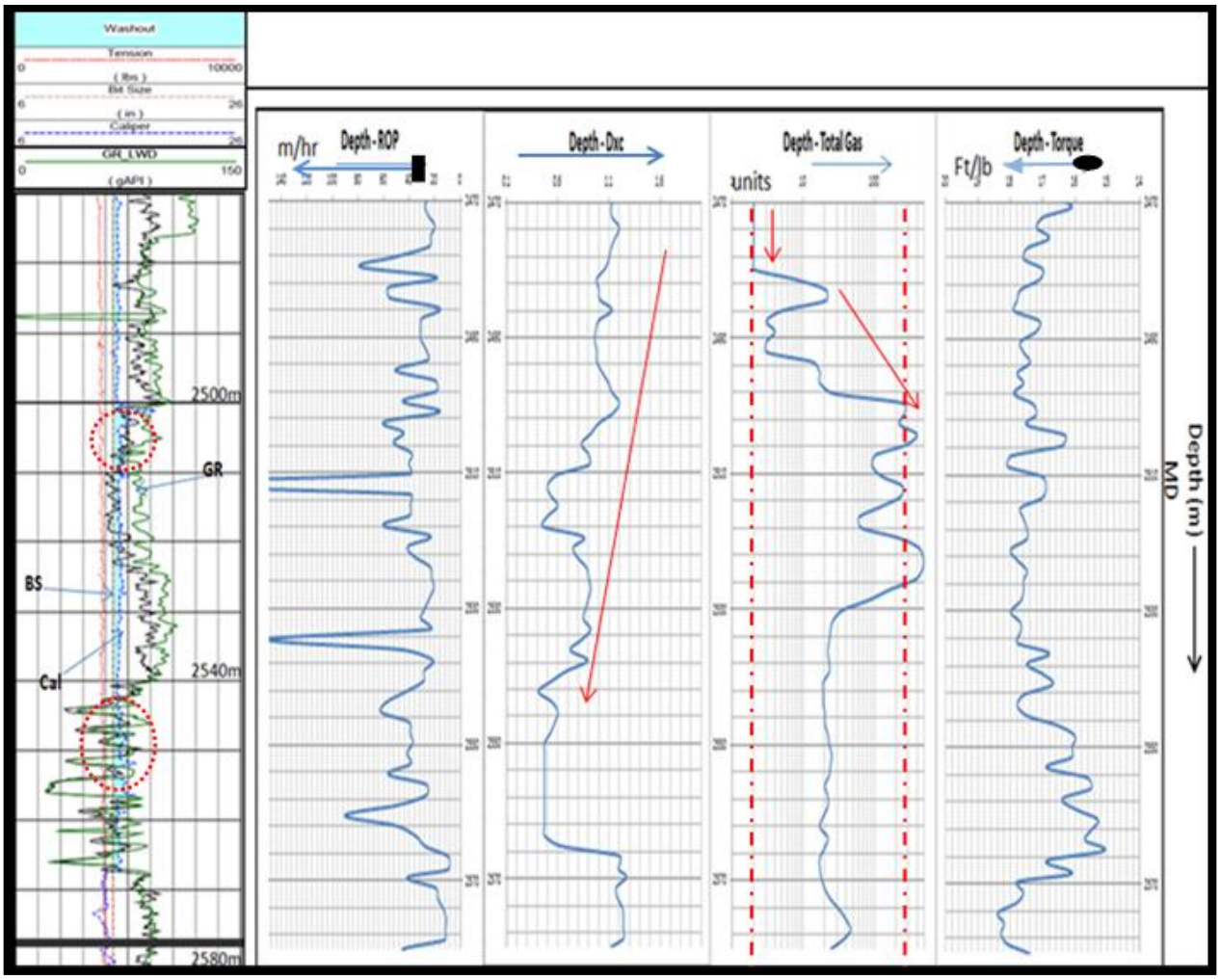

Figure 7.2. Drilling logs from AIW-1 for the interval 2470–2580 m. Track 1: BS, caliper and GR logs showing washout zone at 2470–2570 m. Tracks 2–5: ROP, Dxc, TG and torque logs.

the torque in this interval is somewhat erratic, it shows an increase from the top of interval down to about 2530 m, and then decreases until the top of the shale at the bottom of the interval.

Interval 2750–2860 m

The top section of this interval shows severe hole washout (Figure 7.3). It is worth noting that the 13-3/8” casing shoe was set at about 2746 m and this in part may account for the severity of the hole washout in the section. In general, this interval has greater washout than the previous interval of 2470–2580 m. Several drilling breaks are seen on the ROP plot that do not correspond to lithology change. The trend seen on the Dxc plot is a decrease with depth, whereas the TG started out increasing with depth but flattens out from about 2770 m before increasing again at about 2810 m. The torque trend is similar to TG plot: it shows slight increase with depth for most of the interval before it started decreasing from about 2810 m.

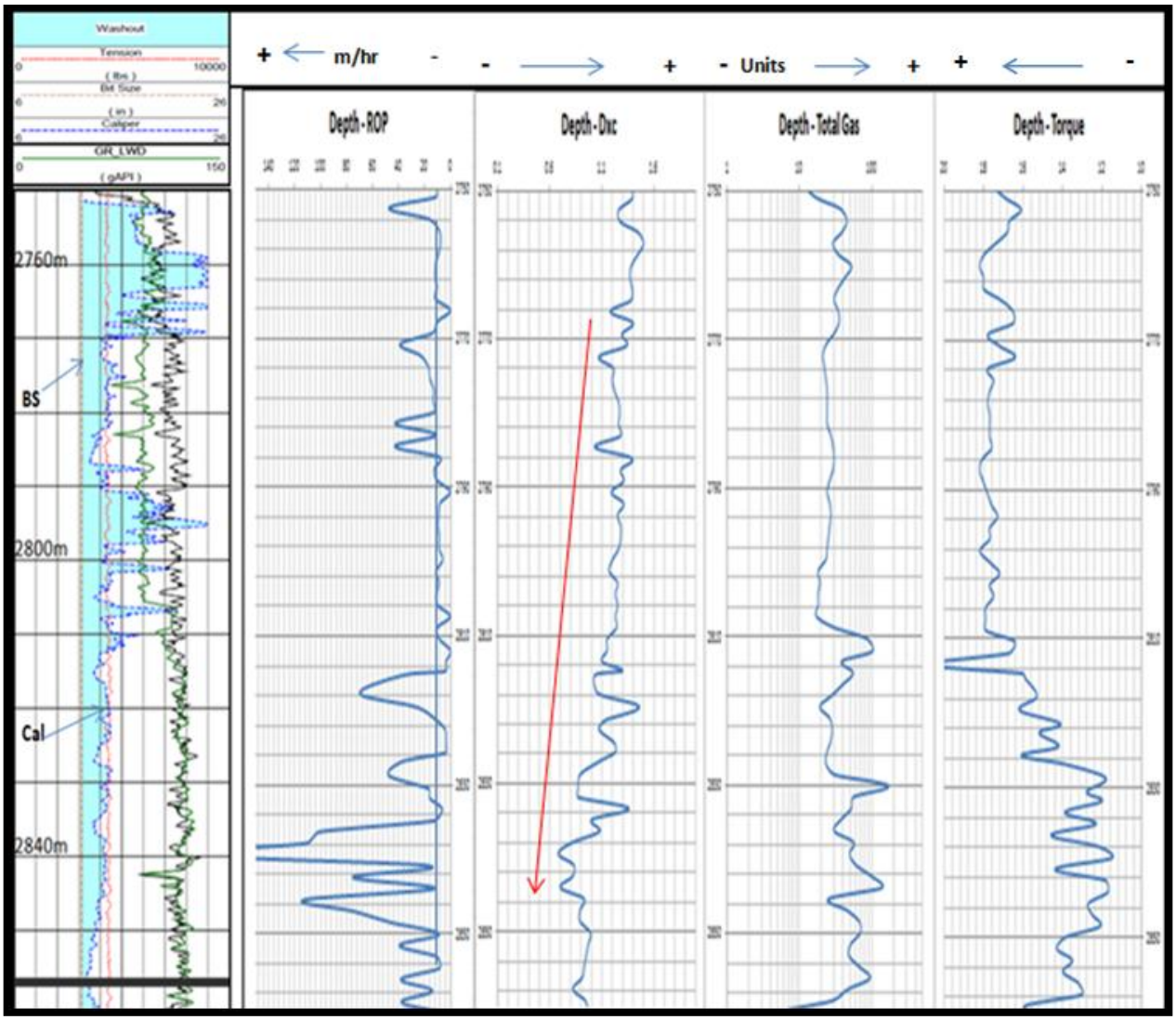

Figure 7.3. Drilling logs from AIW-1 for the interval 2750–2860 m. Track 1: BS, caliper and GR logs showing washout zone over the whole interval. Tracks 2–5: ROP, Dc, TG, and torque logs.

Interval 3480–3580 m

Although this interval is the lower UBD zone identified in Figure 7.1, it has minor hole washout relative to the previous sections shown (Figure 7.4). The general trend observed on the ROP and TG is increase with depth; maximum ROP is seen in the shale interval at 3510–3550 m, and a similar trend is seen in TG with a peak between 3530 m and 3542m. Likewise, the Dxc shows a

declining trend down to 3510 m and then stays fairly constant all the way to the bottom of the interval. The torque trend decreases overall from the top to the bottom of the interval.

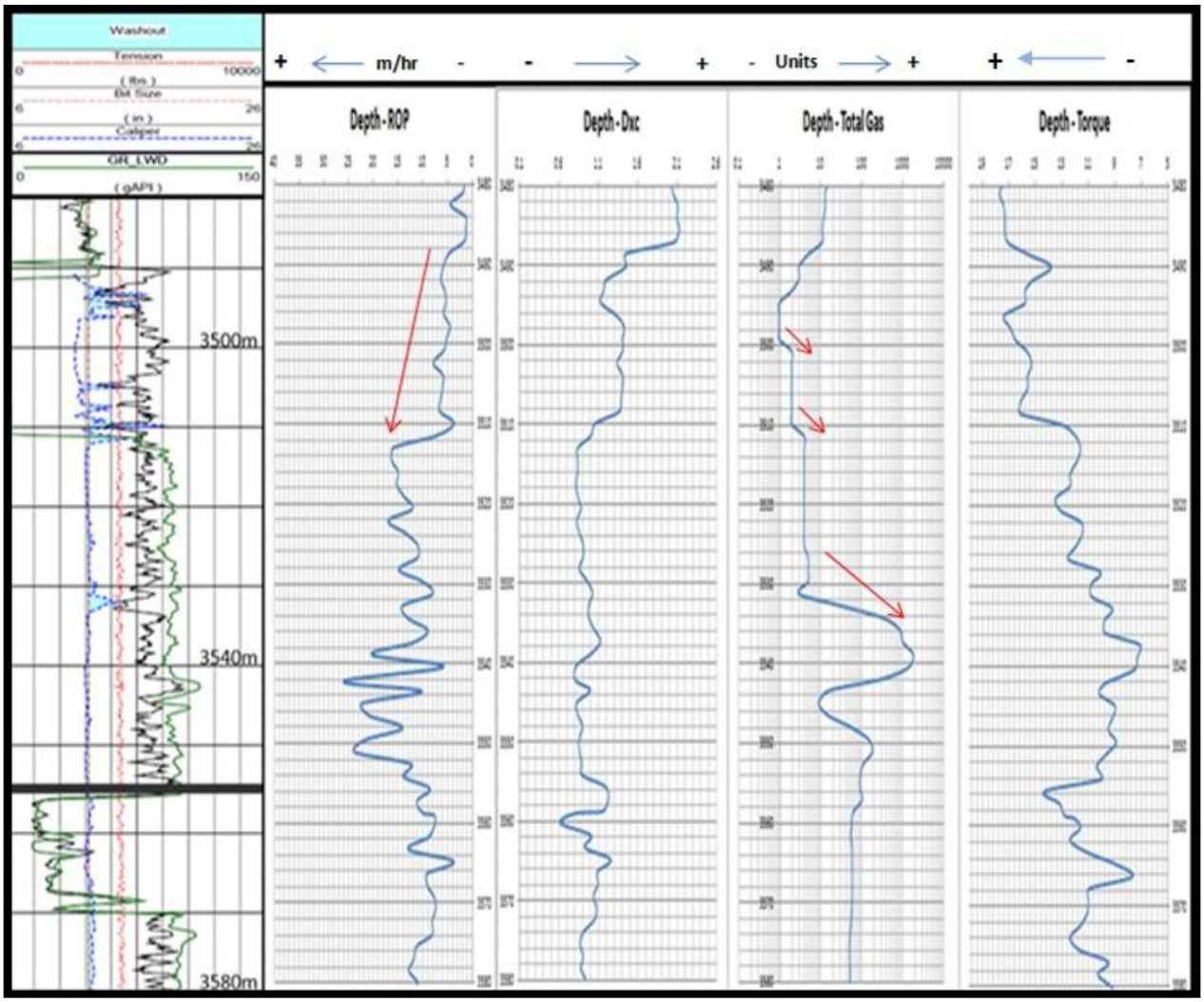

Figure 7.4. Drilling logs from AIW-1 for the interval 3480–3580 m. Track 1: BS, caliper and GR logs. Tracks 2–5: ROP, Dxc, TG, and torque logs.

7.2 NOW-1 well

Two UBD zones have been identified from the pressure–depth plot for the NOW-1 well at 2621–3002 m and 3810–4257 m (Figures 7.5 and 7.6). The corresponding intervals on the caliper, ROP, TG and torque logs have been examined for complementary evidence of UBD. Results from selected intervals are presented to illustrate the relationship between identified UBD zones and drilling data.

In the upper UBD zone measured and/or predicted pore pressure is higher than MW for most part, therefore UBD is invoked here. Similarly, in the lower UBD zone the single measurement and is the predicted pore pressure are greater than MW – UBD is also invoked here.

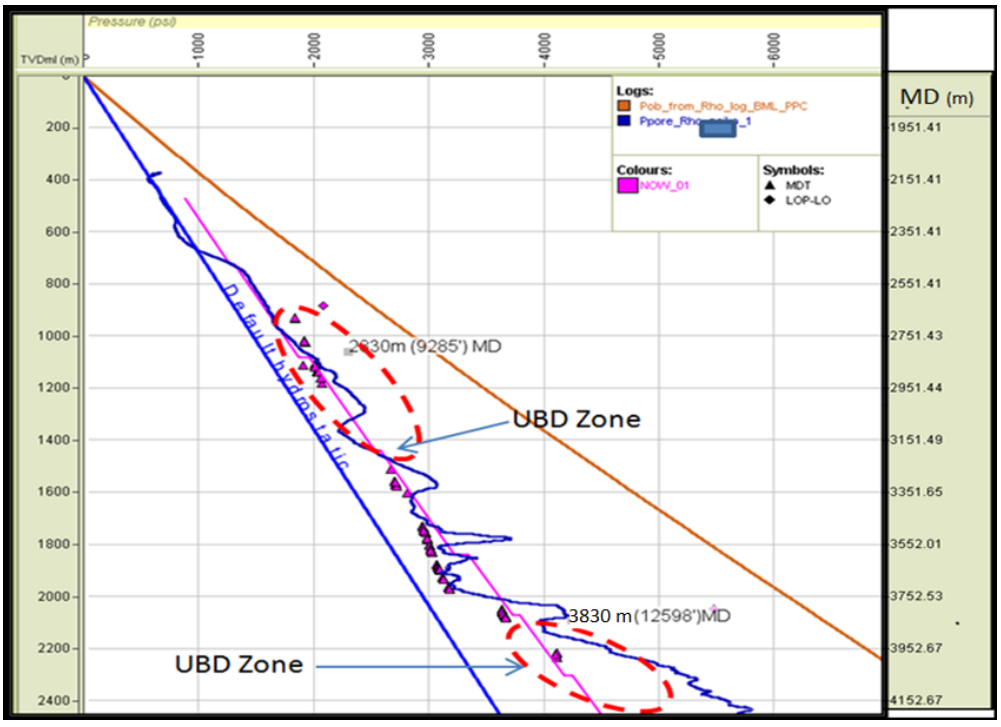

Figure 7.5. Pressure–depth plot for well NOW-1 with UBD zones identified at measured depths of 2621–3002 m and 3810 m to TD.

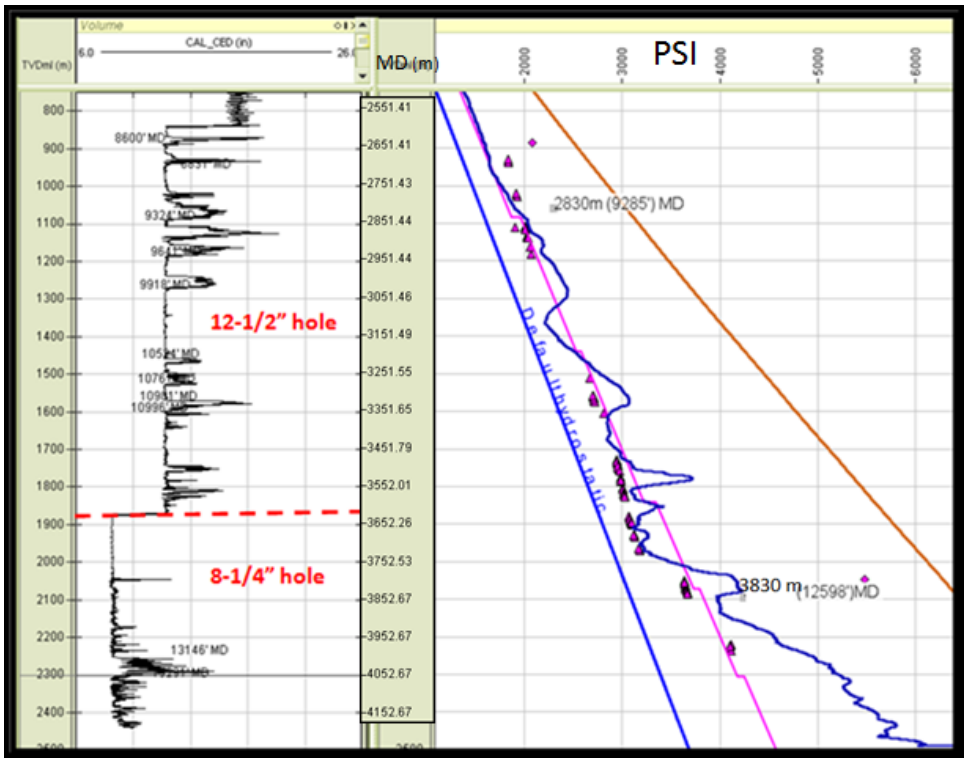

Figure 7.6. Well NOW-1 caliper log (left panel) and pressure–depth plot (right panel).

Interval 2499–2621 m

Figure 7.7 is a wellsite geological log in the 17" hole for this interval. The lithology is predominately shale, and was drilled with a mud weight of 9.0–9.1 ppg (1.08–1.09 g/cc). Torque increased from 3000 to 4000 kft lb from top to bottom of the interval. The average TG of 1.5% stays fairly constant for the whole section.

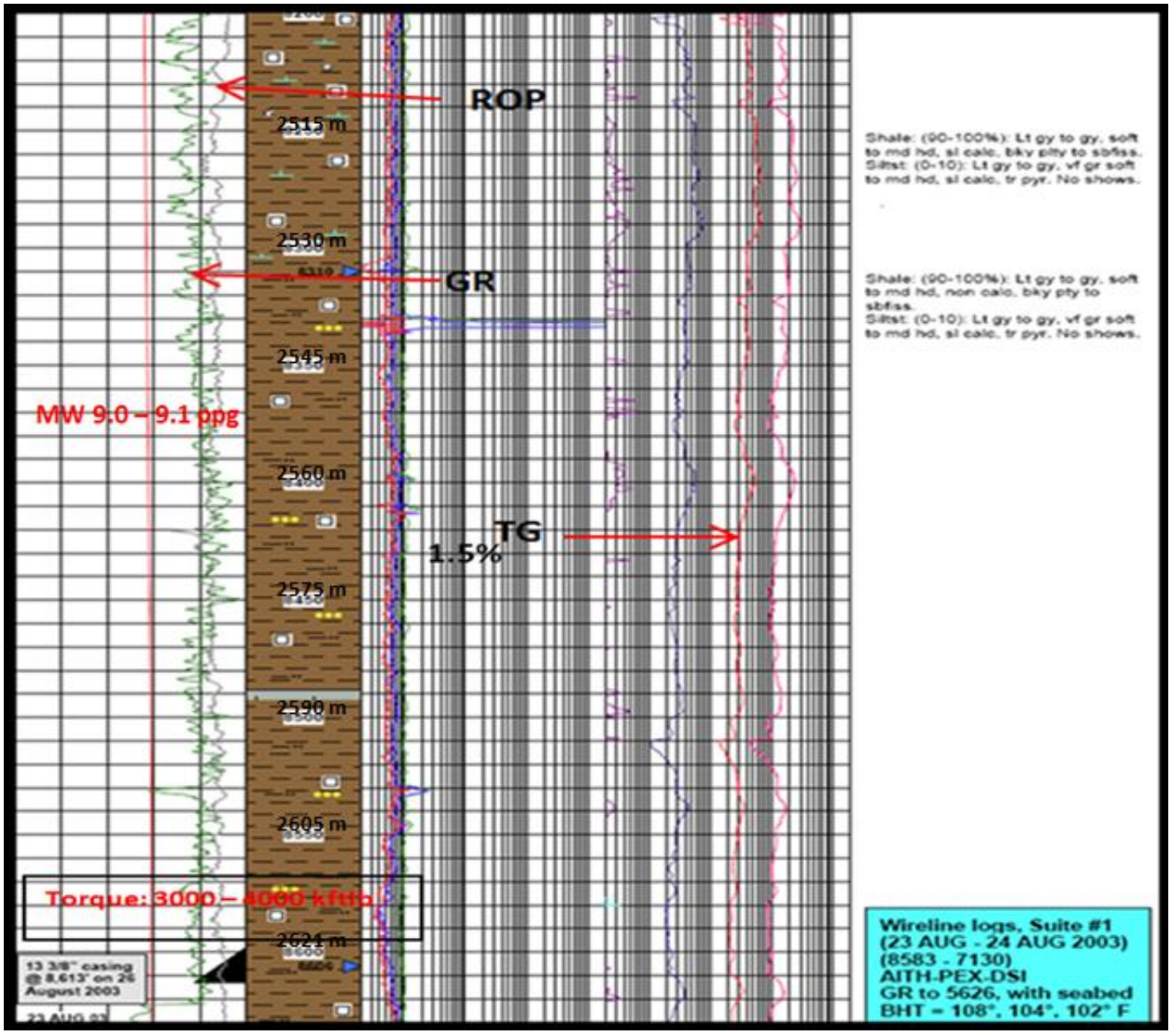

Figure 7.7. Wellsite geological log in the 17" hole section for the interval 2499–2621 m.

Interval 2621–2896 m

With the exception of the sand beds between 2685 m and 2690 m, the interval is predominately shale (Figure 7.8). Relative to the previous interval, immediately above, torque decreased in this section to 2000 kft lb. Though mud weight was increased to 9.3 ppg (1.11g/cc) in the section, the TG increased to 5% in the shale sections and peaked at 40% in the sands. TG character within the interval 2758–2896 m, though subtle, shows an increasing trend from top to bottom of the

interval (Figure 7.9). TG increased with depth in the shale section, reaching a maximum in the sand interval. At the final depth of 3798 m in the 12-1/4” hole section, torque increased to 8000 kft lb and mud weight was raised to 9.6 ppg (1.15 g/cc).

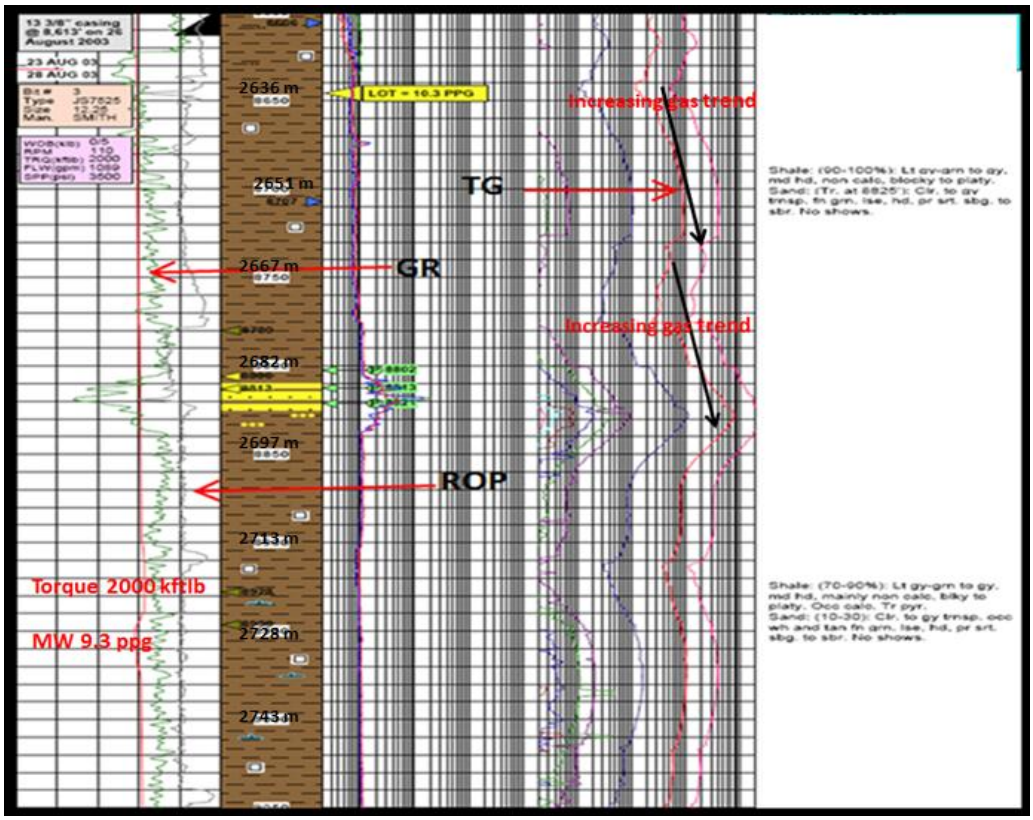

Figure 7.8. Wellsite geological log in 12-1/4” hole section for the interval 2621–2758 m.

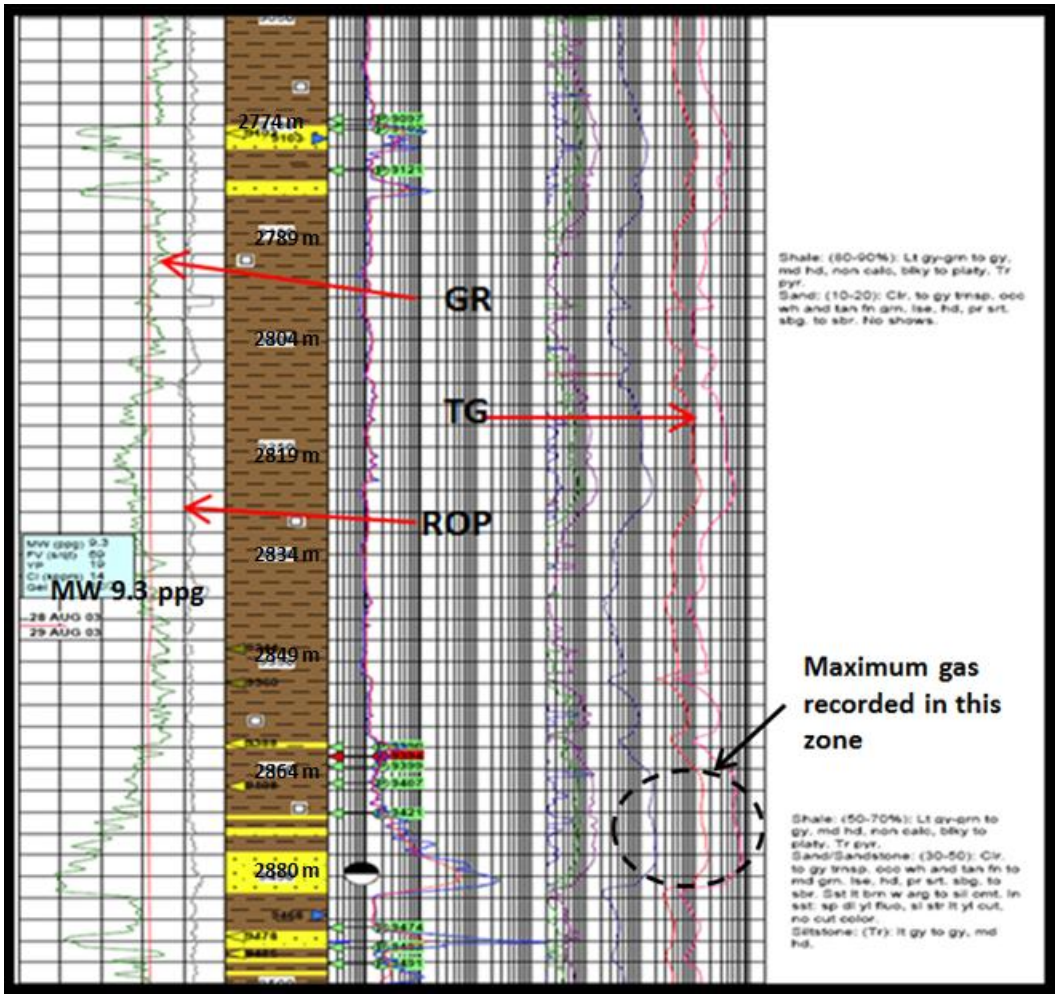

Figure 7.9. Wellsite geological log in 12-1/4" hole section for the interval 2758–2896 m.

Interval 3810–4257 m

The caliper log in the 8-1/2" hole, in general, shows indications of hole washout. A more severe washout is seen between 4008 m and 4054 m (Figure 7.10). Also, the bottom section of the hole has more severe washout than the upper section of hole (Figure 7.10). What now follows are results of gas and other drilling indicators for sections within this interval.

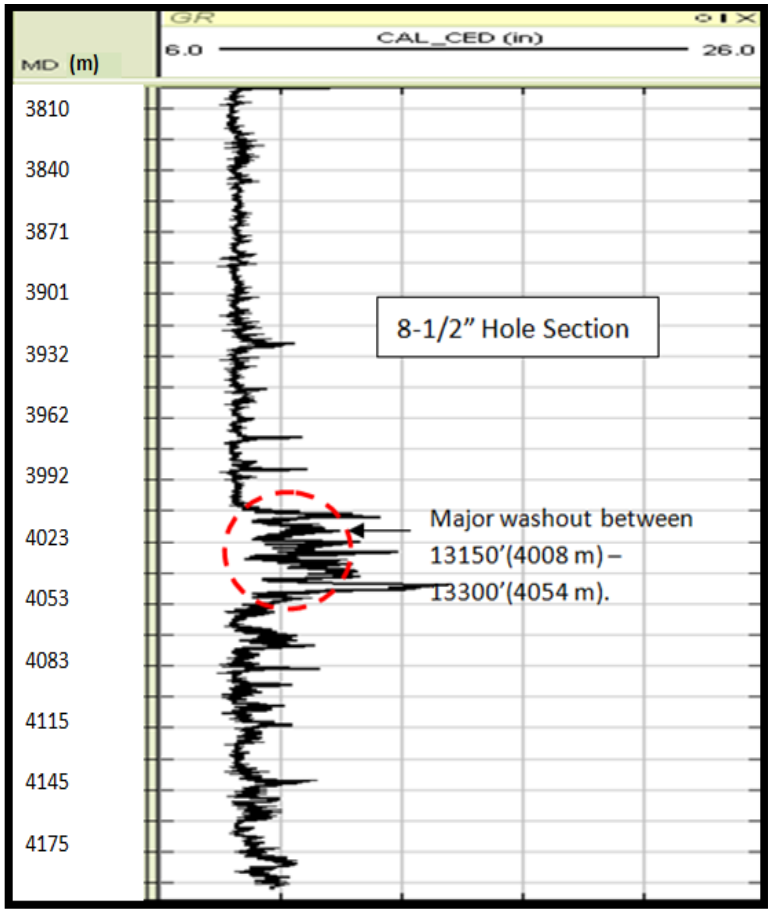

Figure 7.10. Caliper log in the 8-1/2" hole interval 3810–4275 m. There is a major washout between 4008 m and 4054 m.

Figures 7.11 and 7.12 are the wellsite geological logs for the intervals 3810–3932 m and 3932–4069 m, showing associated gas and drilling data profiles. The TG value is elevated, especially within the sand at the top of the section (Figure 7.12), and there is an increasing gas trend observed in the shale section between 3856 m and 3886 m. The BG for this section was 0.24% with pipe connection gas (PCG) of 0.56% at 4033 m MD. The majority of the section was

drilled with a mud weight of 9.7 ppg (1.16 g/cc) until 4063 m, where it was increased to 9.8 ppg (1.17 g/cc). A maximum torque of 8000 kft lb was recorded in the interval.

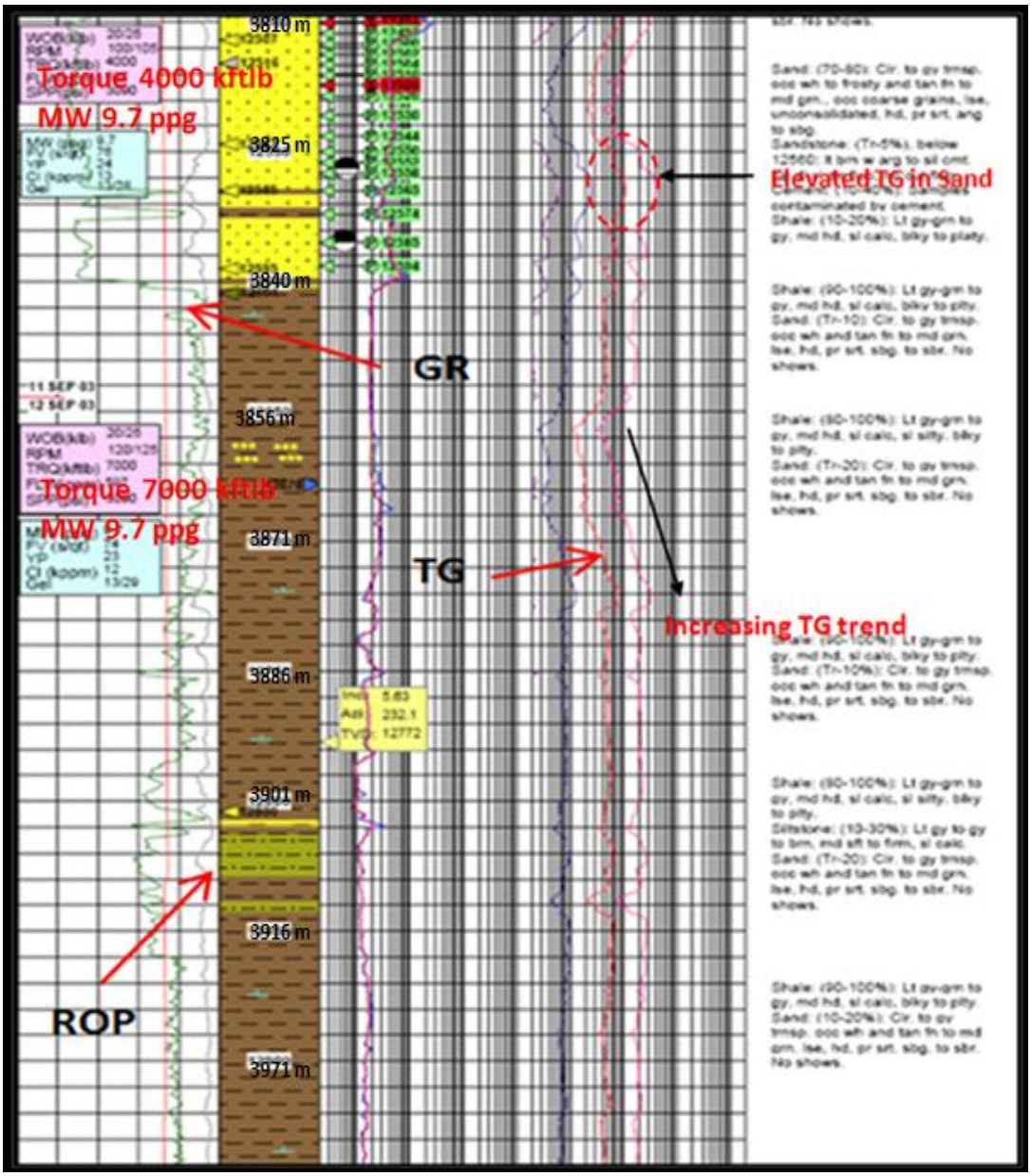

Figure 7.11. Wellsite geological log in 8-1/2" hole section for the interval 3810–3932 m.

The interval 4069–4257 m is a continuation of the 8-1/2" hole section. With the increased mud weight of 9.8 ppg (1.17 g/cc), BG (0.14%) and PCG (0.40%) decreased in the shale

between 4069 m and 4115 m (Figure 7.13). Below 4115 m, a progressive increase of PCG was observed with maximum of 2.38% at 4198 m. Likewise, maximum BG of 2.05% was recorded at

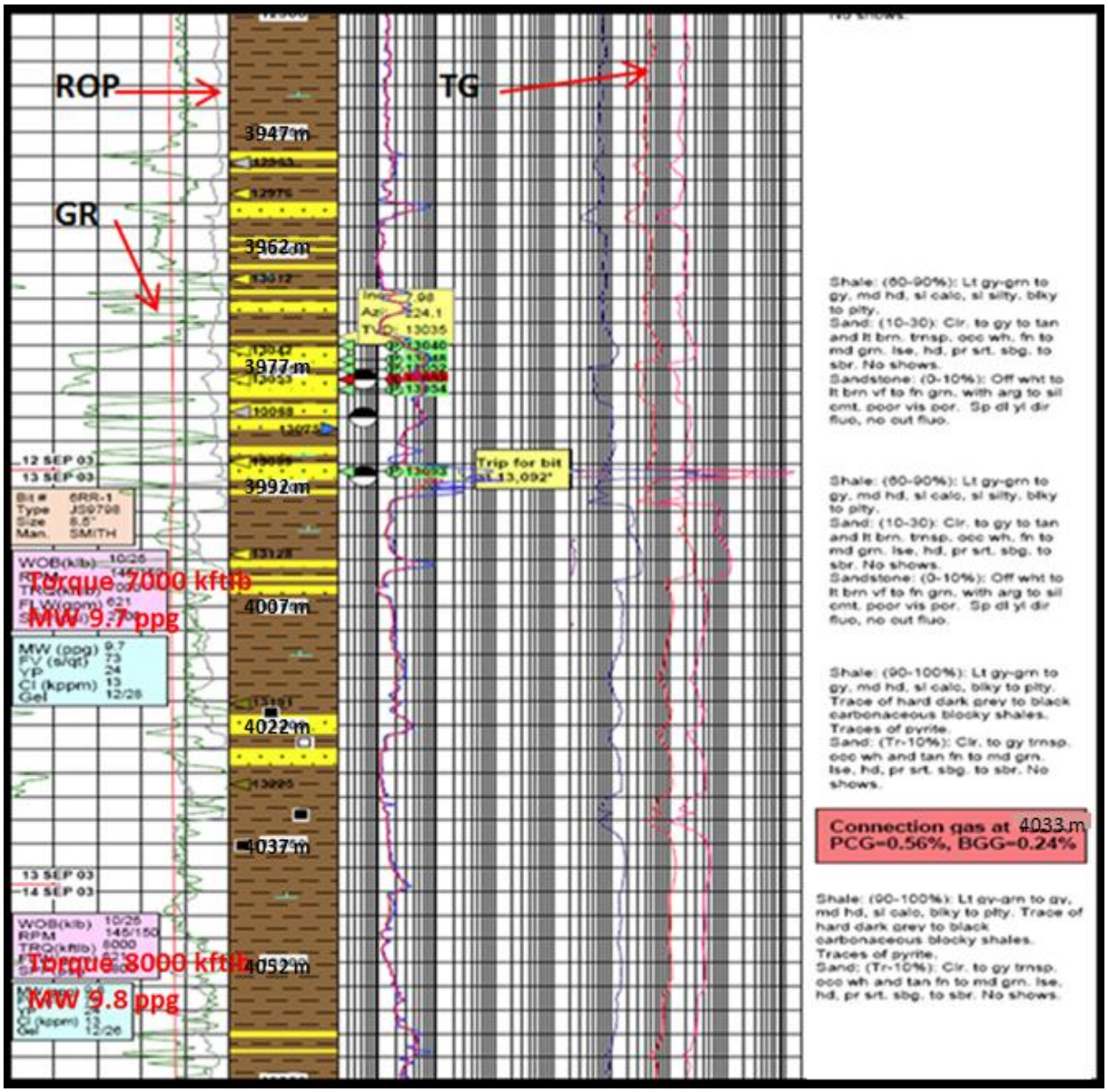

Figure 7.12. Wellsite geological log in 8-1/2" hole section for the interval 3932–4069 m.

4156 m. Mud weight was again increased to 1.17 g/cc at 4191 m, action likely necessitated as a result of gas-cut mud (Figure 7.14).

As shown in Figure 7.14, drilling continued with mud weight of 1.17 g/cc until 4239 m, where PCG and BG increased to 15.48% and 14.58%, respectively. In addition, a gain of 8 bbls was recorded in the trip tank, a clear indication that the well was flowing. The gas was circulated out through choke and mud treated to increase the weight to 1.34 g/cc. Maximum gas of 73.6% was reported while stabilizing the well. Apparently, there was another episode of gas-cut mud here: mud weight was again increased from 1.17 g/cc to 1.36 g/cc and TD was called at 4257 m.

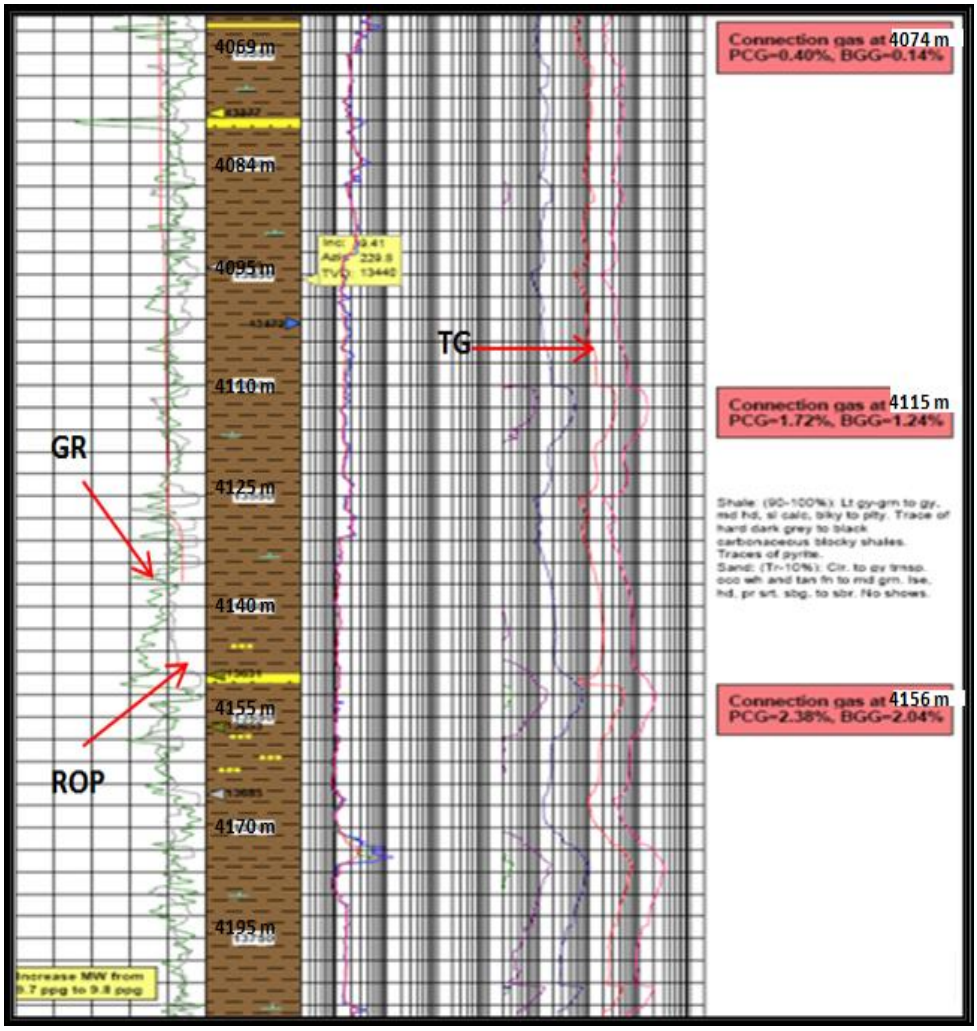

Figure 7.13. Wellsite geological log in 8-1/2" hole section for the interval 4063–4203 m.

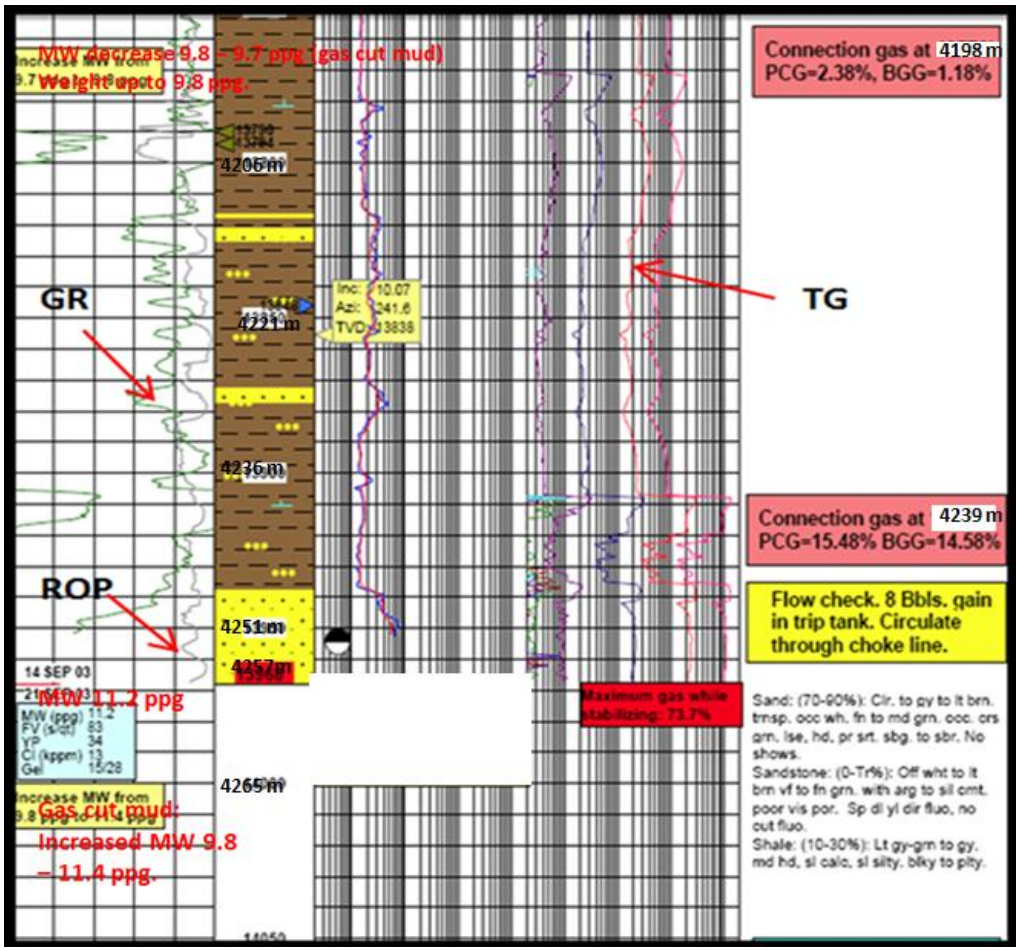

Figure 7.14. Wellsite geological log in 8-1/2" hole section for the interval 4191–4282 m.

7.3 AOE-4G1 well

In well AOE-4G1 a UBD zone is identified over the interval 750–1300 m TVDml (2036–2689 m MD) on the pressure–depth plot (Figure 6.35). In Figure 6.35 measured and predicted pore pressure track quite well, higher than the MW- an indication of UBD. For corroboration of UBD in this zone, wellsite geological logs of ROP, gas and caliper and the EOWR were used. Figures 7.15–7.18 show plots of selected zones from the wellsite geologist's report and annotations from

the EOWR. For convenience, the identified UBD zones are divided into four intervals and are presented below.

Interval 2150–2280 m

The top section of hole is relatively in-gauge for the most part; however, hole pack-off, trip gas of 12.04%, and mud losses of 20 m^3 were reported at ~2150 m (Figure 7.15). Severe hole washout is noted after pipe connection from 2240 m, through the sand interval to the bottom of the section. In general, formation gas (FG) and TG increase from top to bottom of the section. For instance, after pipe connection at 2178 m, the FG value increased from 2.2% to 4.58% towards the end of the stand. A similar trend is seen after pipe connection at 2236 m, where TG and FG increase progressively, peaking at 3.05% in the shale above the sand interval at 2260 m.

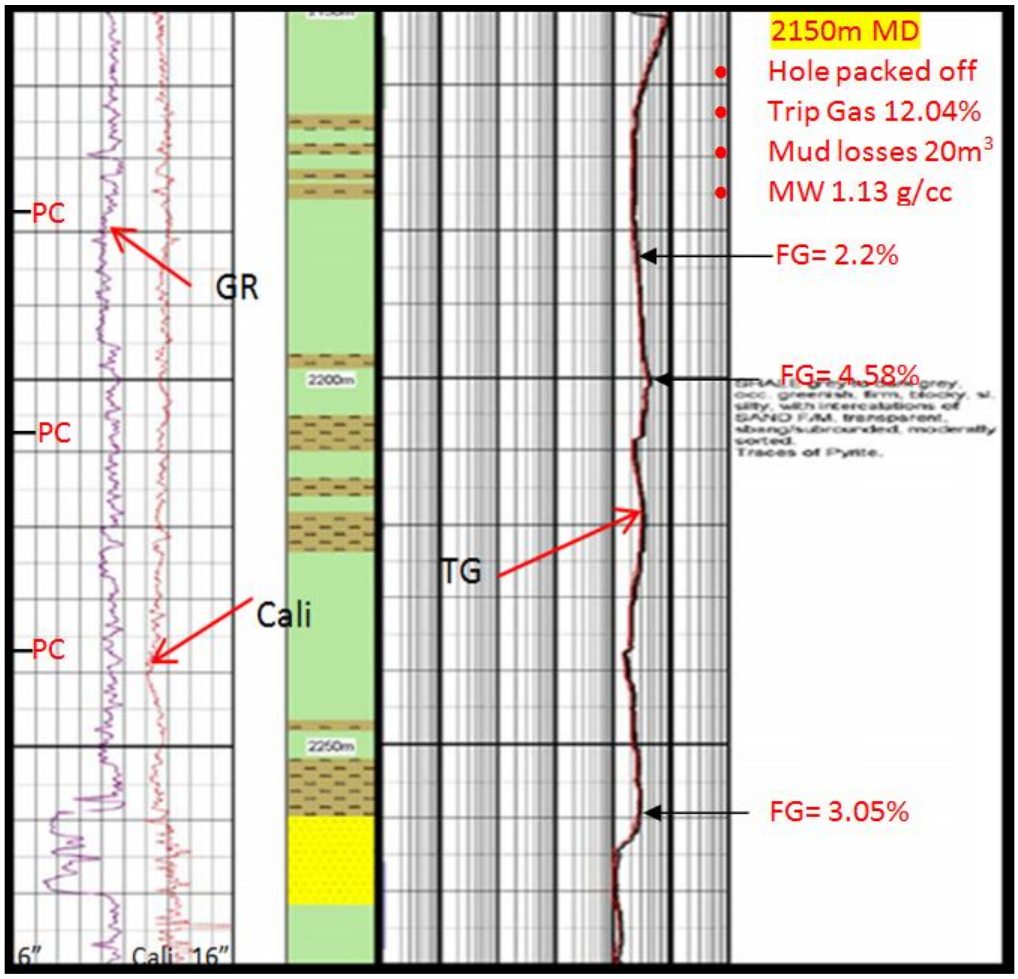

Figure 7.15. Wellsite geological log in 12-1/4" hole section for the interval 2150–2280 m.

Interval 2280–2345 m

Unlike the section above, TG and FG within this section remained fairly constant at ~1%; even in the relatively washed out zone between 2290 m and 2320 m (Figure 7.16).

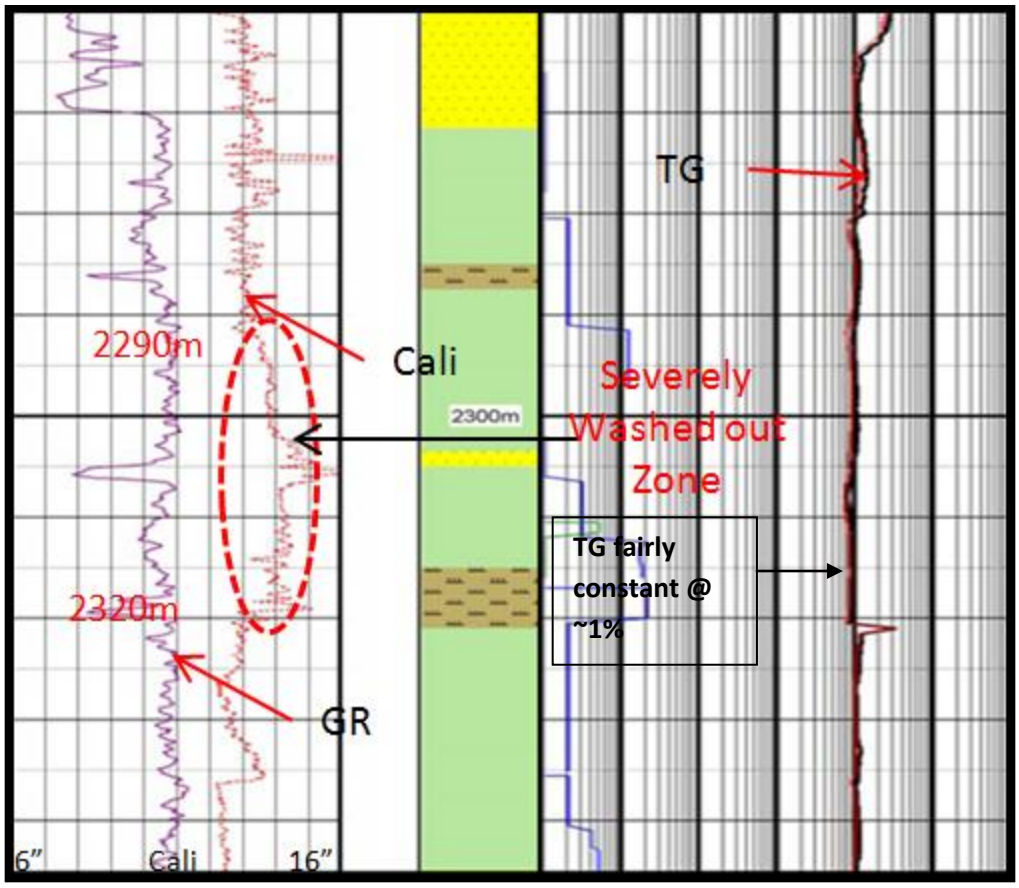

Figure 7.16. Wellsite geological log in 12-1/4" hole section for the interval 2280–2345 m.

Interval 2370–2495 m

The highest gas value (3.17%) in this section is recorded in the washed out shale between 2380 m and 2390 m (Figure 7.17). Slightly elevated gas seems to correspond to washed out zones within shale intervals.

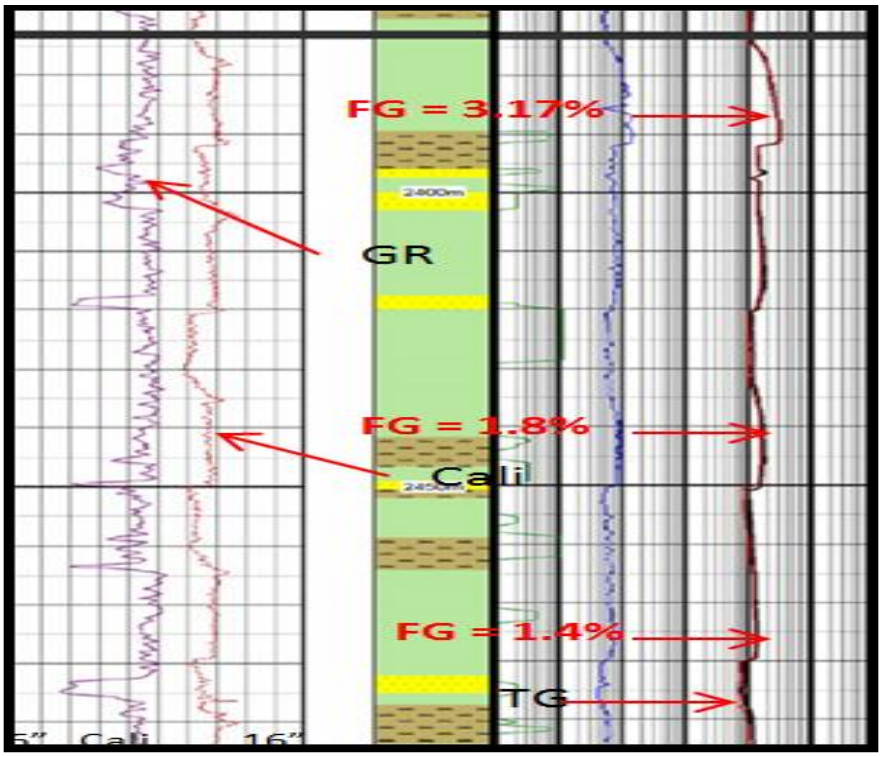

Figure 7.17. Wellsite geological log in 12-1/4" hole section for the interval 2370–2495m.

Interval 2730–2844 m

Observed gas character is similar to that observed in the interval 2150–2280 m: after pipe connection, the TG value increases towards the end of each stand drilled. For example, after pipe connection at 2734 m and at 2763 m, FG increases from 2.12% to 3.65%, then to 3.72% towards the end of each stand drilled (Figure 7.18). Also, in the interval from 2800 m to 2844 m, FG increased from 3.01% to 3.3%.

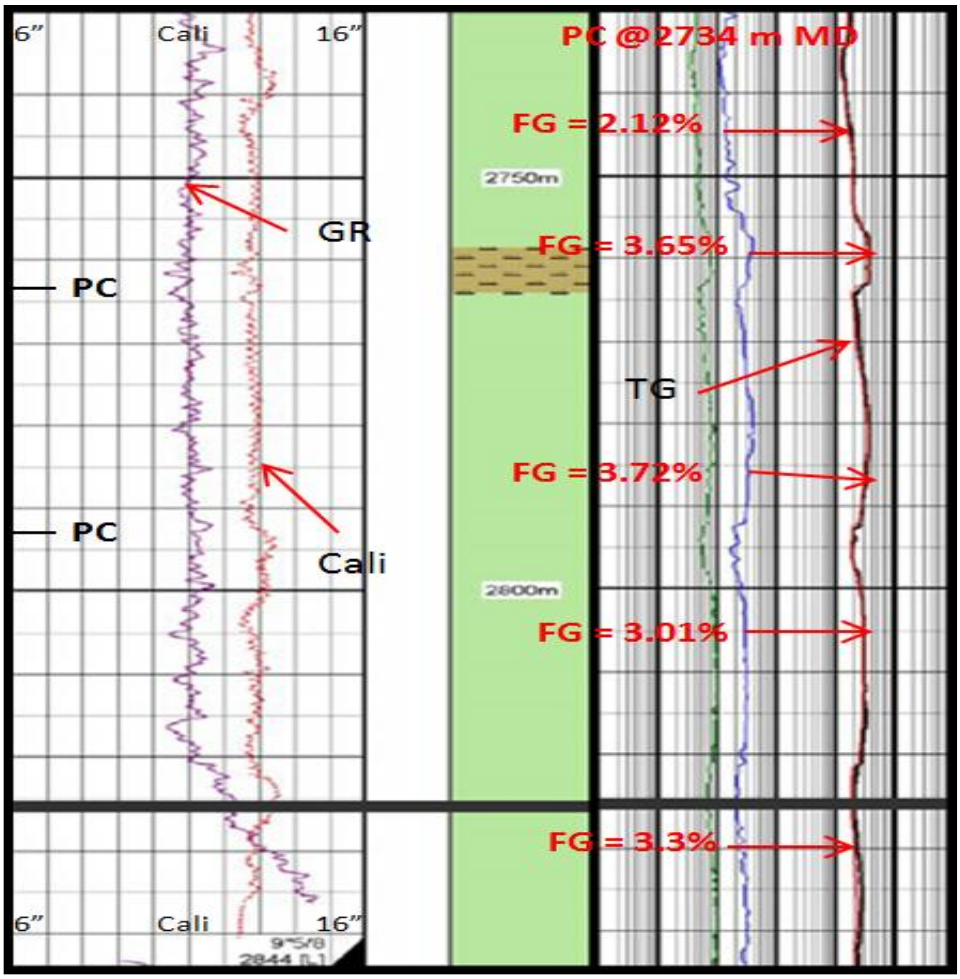

Figure 7.18. Wellsite geological log in 12-1/4" hole section for the interval 2730–2844 m.

7.4 UNE-5 well

In well UNE-05, there is a zone of UBD is apparent from 1330 m to ~2000 m TVDml (Figure 6.34), corresponding to 2176–2922 m MD. Here, measured and predicted pore pressure track quite well, so, where there are no measurements for comparison with MW, predicted pore pressure is used as a proxy. For convenience, the identified UBD zone is divided into four intervals for presentation below.

Interval 2200–2280 m

Before the pipe connection at 2245 m, BGG remained fairly constant at 2% (Figure 7.19). After pipe connection, BGG increased to 4%; peaking towards the base of the interval (13-3/8” casing shoe) with 9.8% gas peak. Though the quality of caliper log is not as great, the section of hole from 2250 m is severely washed out and has corresponding increase in gas.

This interval of hole was drilled with a mud weight of 1.22 g/cc until the section TD of 2290 m, and then the mud weight was increased to 1.24 g/cc. Partial losses were reported in the interval (Figure 15a). During wiper trip, the mud weight was further increased to 1.25 g/cc, and maximum torque of 6134 ft lb was reported.

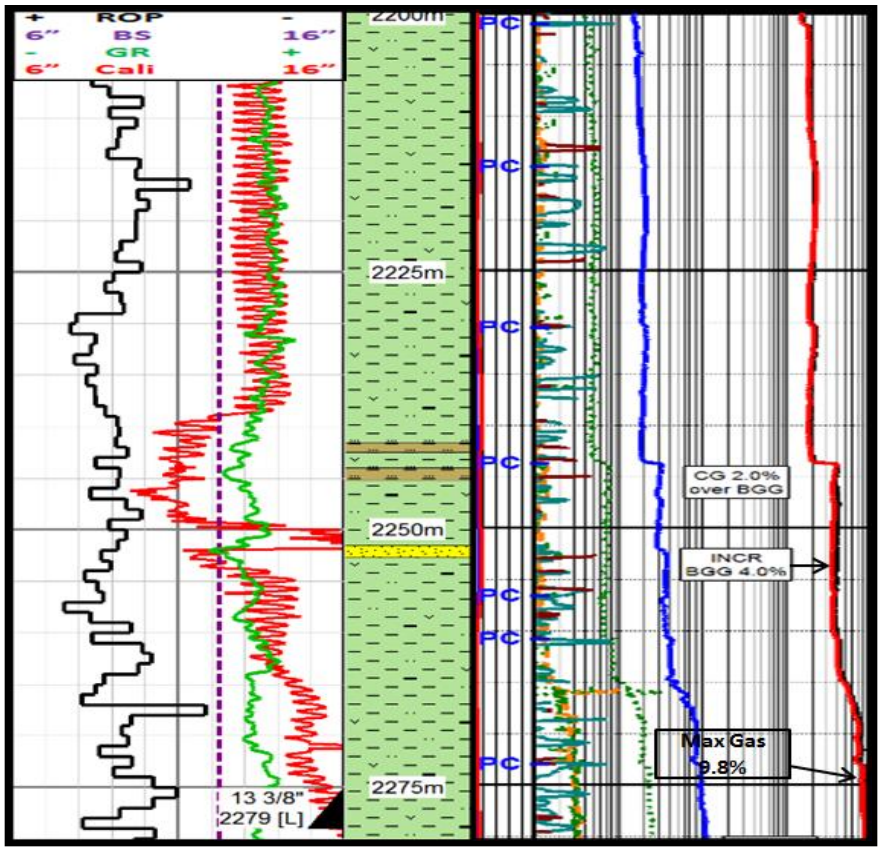

Figure 7.19. Wellsite geological logs of ROP, BS, GR, CAL, and gas character for the interval 2200–2280 m.

Interval 2375–2500 m

Although the mud weight was increased to 1.3 g/cc in this section, much higher CG of 26.3% is recorded (Figure 7.20). To counteract the high BG, the mud weight was further increased to 1.35 g/cc at 2533 m. A maximum torque of 8674 ft lb was recorded in this interval.

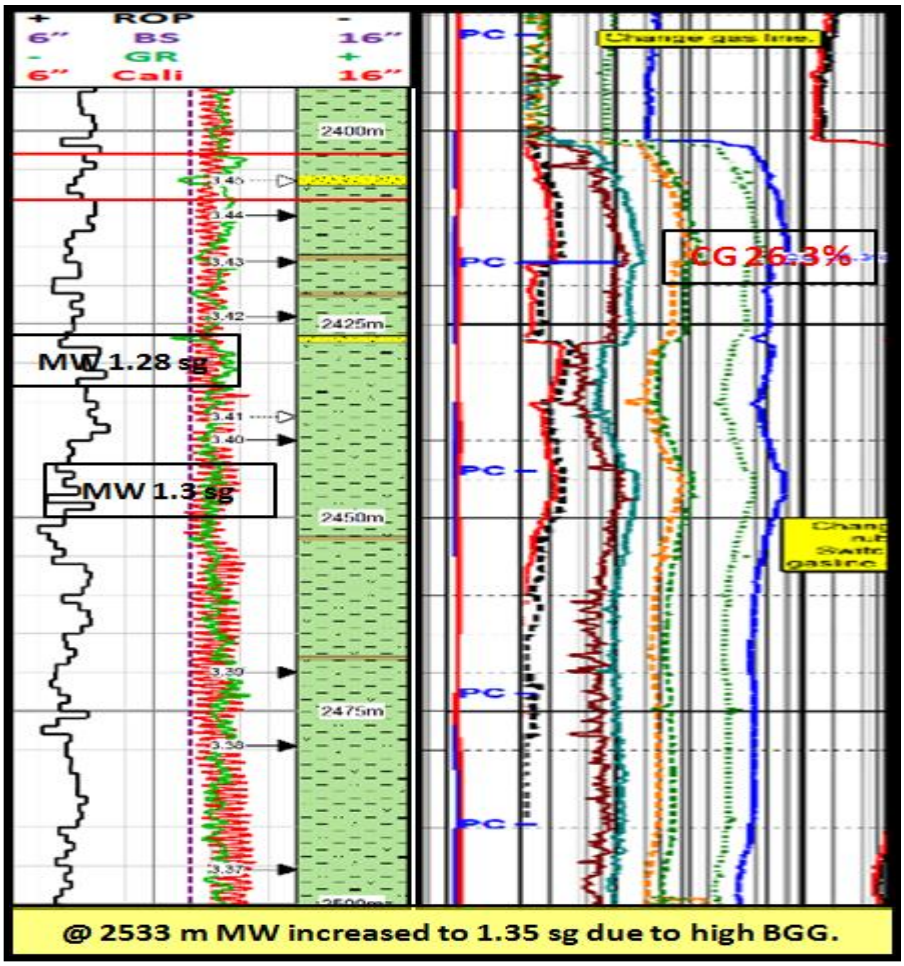

Figure 7.20. Wellsite geological logs of ROP, BS, GR, CAL, and gas character for the interval 2375–2500 m.

Interval 2550–2650 m

This section of hole continued with high level of FG (59.2%), CG 24.72%, and hole washout from 2565 m to 2590 m (Figure 7.21). Maximum torque of 10,745 ft lb was encountered in this section of hole. With a mud weight of 1.3 g/cc, a kick was picked at 2593 m with 1.7m^3 mud gain. The well was killed with 1.43 g/cc mud weight, and subsequently drilled to final section TD (12-1/4" hole) at 2539 m with a mud weight of 1.47 g/cc.

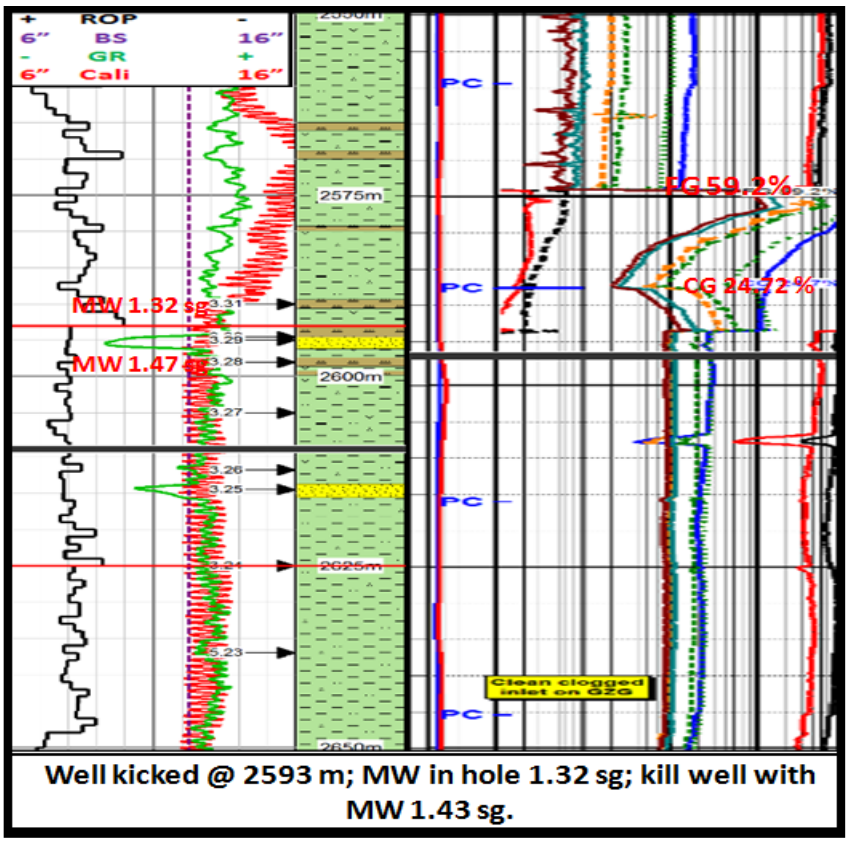

Figure 7.21. Wellsite geological logs of ROP, BS, GR, CAL, and gas character for the interval 2550–2650 m.

Interval 2865–2950 m

This section is the base of the UBD zone identified in Figure 6.34. The FG increases from ~4.2% to 16.5% towards the base of the section (Figure 7.22). Mud weight of 1.47 g/cc was used to drill to section TD at 2939 m and the 9-5/8" casing shoe was set at 2928 m.

While circulating prior to logging, and during wireline logging, kicks were picked at 2939 m with an influx of 1 m^3/hr and 0.6 m^3/hr, respectively. The well was eventually killed with mud weight of 1.51 g/cc in the first instance, and 1.57 g/cc in the second instance. The 8-1/2" hole section drilling started with a mud weight of 1.6 g/cc. The maximum recorded torque for the section was 11,203 ft lb.

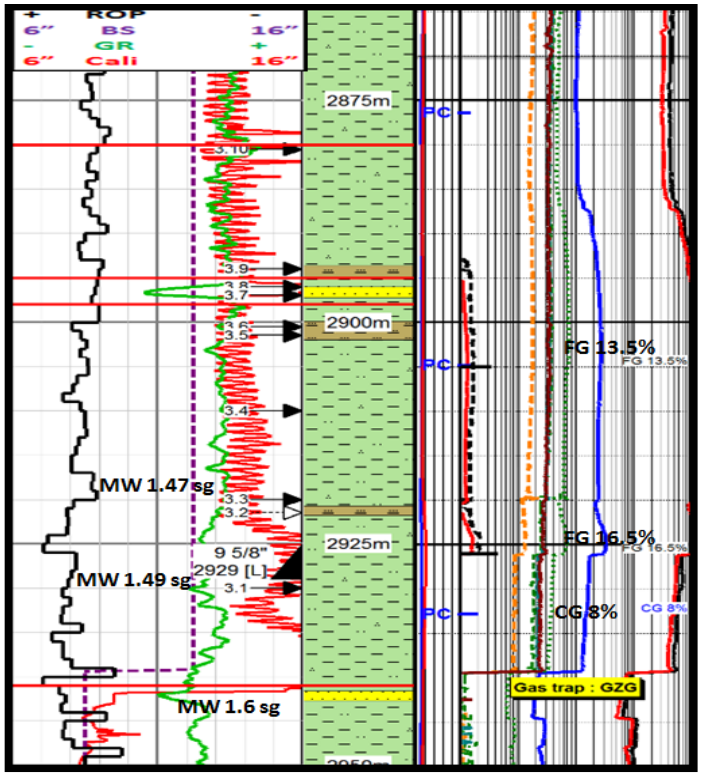

Figure 7.22. Wellsite geological logs of ROP, BS, GR, CAL, and gas character for the interval 2865–2950 m.

CHAPTER 8

Discussion, Conclusions and Suggestions for Further Work

This chapter covers the evaluation, interpretation, implications, and conclusions of the results presented in chapters 5, 6, and 7 in relation to the study objectives. The original objectives of this study were three-fold:

1. Estimation of pore pressure using density log, i.e., equivalent depth method.
2. Identification of overpressure generation mechanisms other than disequilibrium compaction, i.e., unloading mechanisms.
3. Identification of zones drilled underbalanced from pressure–depth plots with supporting evidence from drilling and mudlog data.

Most pore pressure work in the Niger Delta area (e.g., Owolabi et al., 1990; Opara & Onuoha, 2009; Ugonoh et al., 2012) uses a variety of data (sonic, density, and resistivity logs, and velocities from seismic data) for pore pressure evaluation. The widely cited mechanism for overpressure is disequilibrium compaction; however, depending on the reference depth and temperature, Cobbold et al. (2009), Opara & Onuoha (2009) and Swarbrick et al. (2011) have indicated that hydrocarbon generation and clay diagenesis are active mechanisms of overpressure generation in the Niger Delta. The results of this study have shown that the equivalent depth method using the density log, when properly calibrated with measured pore pressure data, can produce reliable pore pressure estimation down to certain depths. Although the predominant mechanism of overpressure generation is disequilibrium compaction, there are indications of

other mechanisms, especially smectite-to-illite transformation, at depths where the temperature exceeds 70°C. Finally, mudlog and drilling data validate and correlate with zones of UBD identified on pressure–depth plots.

This chapter is divided into three sections. In sections 8.1 and 8.2, wells within 80 km distance of the Charcot Fracture Zone and those at greater than 100 km distance from Charcot Fracture Zone are presented. Specifically, wells were evaluated using predicted pressure from density logs (i.e., equivalent depth method) and using cross-plots to infer the presence or absence of unloading. In addition, zones identified on pressure–depth plots with UBD were compared with drilling and mudlog data for traditional indications of UBD (i.e., gas, kick/flow, hole washout, drilling break/ROP, torque, etc.). The chapter ends in section 8.3 with the conclusions and suggestions for future work.

8.1 AIW, EIW, and NOW wells

8.1.1 Pore pressure prediction from density logs

Based on results of pore pressure prediction from density logs for wells AIW-1, AIW-2, EIW-1, and NOW-1, it is apparent that there is good correlation between measured and predicted pore pressures in the shallow section (900–2100 m TVDml) of the wells (Figures 8.1–8.4).

AIW-1

It can be observed in well AIW-1, for example, that the predicted pore pressure tracks the mud weight quite well down to the top of the early Miocene at about 900 m TVDml (Figure 8.1). In the lower sections of the well, pore pressure is either under-predicted or over-predicted by the equivalent depth method. The reason for this discrepancy may in part be due to poor lithology

discrimination within the zone, although, Bowers (2000) and Alberty (2003) have indicated that the equivalent depth method generally does not work where unloading mechanisms are active. It can also be seen from Figure 8.1 that the shale interval at 2000 to ~2080 m creates a permeability barrier (seal), preventing hydraulic communication between sands in the early Miocene.

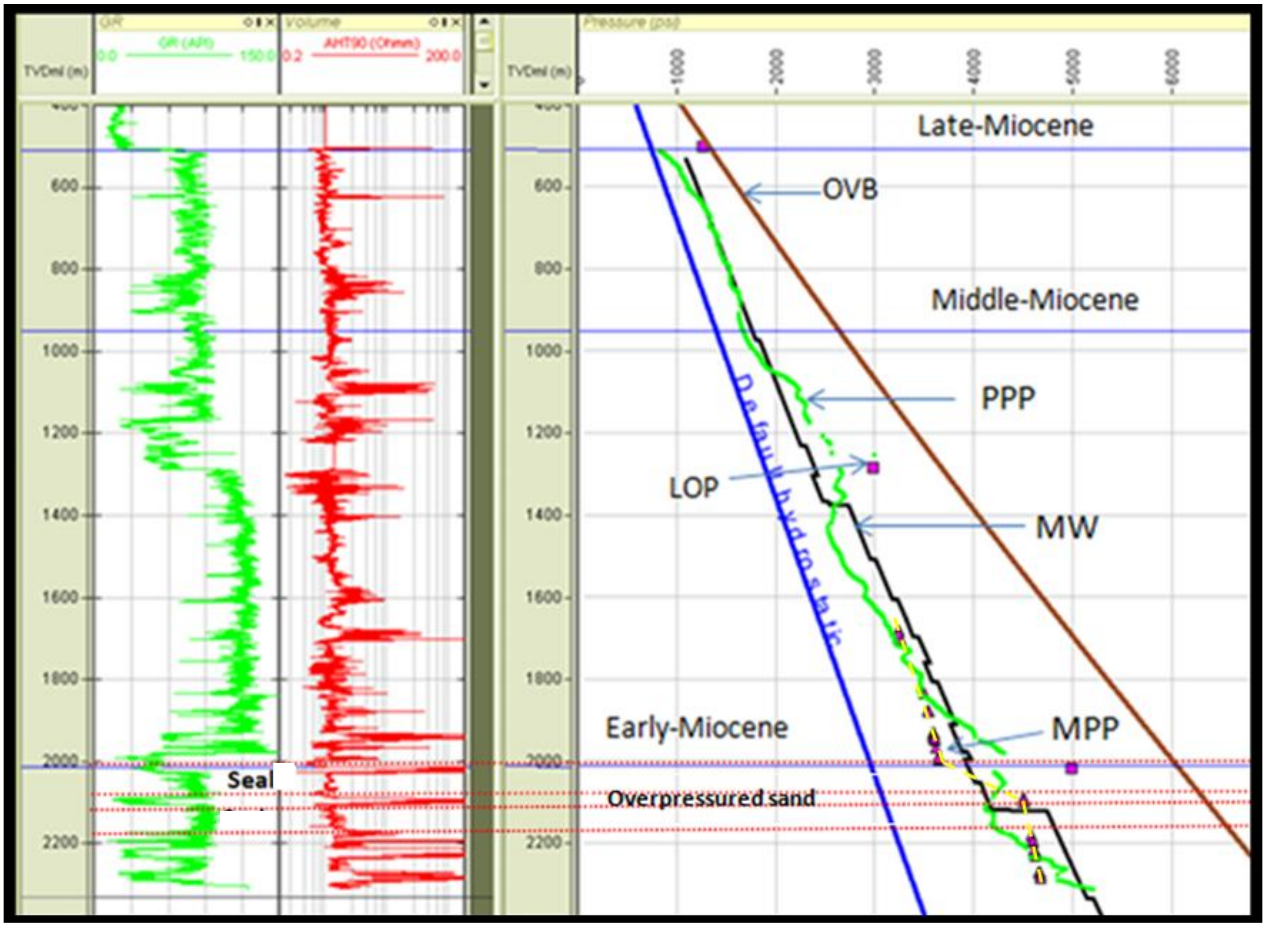

Figure 8.1. GR, resistivity, and pressure–depth plots for well AIW-1, showing a transition into higher overpressure at the base of the early Miocene.

AIW-2

In well AIW-2, the predicted pore pressure tracks the mud weight quite well down to about 2000 m depth (Figure 8.2). An apparent pressure reversal is seen in the shale interval between 2020 m

and 2220 m, and may be attributed to sandy nature of the interval. However, pressure in the underlying sandy interval is slightly over-predicted by equivalent depth method. Starting from the top of the early Miocene (~2600 m), though there are no measured pore pressure data within the interval, the predicted pore pressure increases drastically with a trend similar to the mud weight. There are pronounced velocity and resistivity log reversals within the same zone (Figure 5.10).

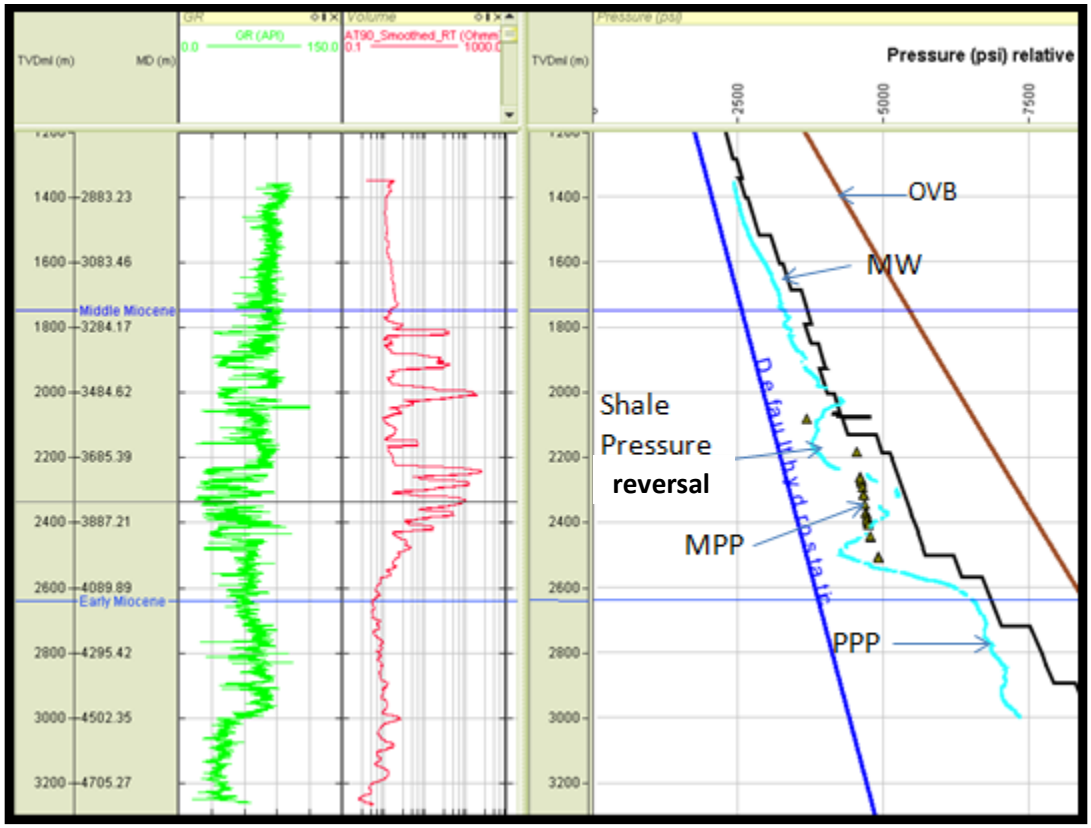

Figure 8.2. GR, resistivity and pressure–depth plots for well AIW-2. Mud weight was increased below 2600 m in response to hole conditions related to overpressure.

EIW-1

In well EIW-1, the pore pressure predicted by the equivalent depth method does a good job of tracking the measured pore pressure until ~2100 m depth; at greater depths the pore pressure is either under-predicted or over-predicted (Figure 8.3). For example, the prediction from shale density is higher than the measured pore pressures in the sands for the interval between 2215 m and 2290 m. Assuming the predicted pore pressure from shale is accurate, it can be inferred that the sand at 2215–2290 m is in all likelihood laterally drained, which is the reason why the measured pore pressure is lower than the predicted. Also in this well, the shale interval between 2310 m and 2400 m serves as a seal, preventing hydraulic communication between overlying and underlying sands. Additional overpressure due to hydrocarbon buoyancy appears to be present in the sand at 2400–2670 m because it is oil bearing (see resistivity log in Figure 8.3).

Two features are also worth noting on Figure 8.3, beginning at 2700 m. First, there is a step-wise increase in mud weight towards the lithostatic gradient, apparently in response to down hole conditions indicating increasing overpressure. Second, there are reversals on both resistivity and velocity logs. The maximum depth on the density log data is 2600 m, so no predicted pore pressure is available at greater depths for comparison with mud weight and measured pore pressure.

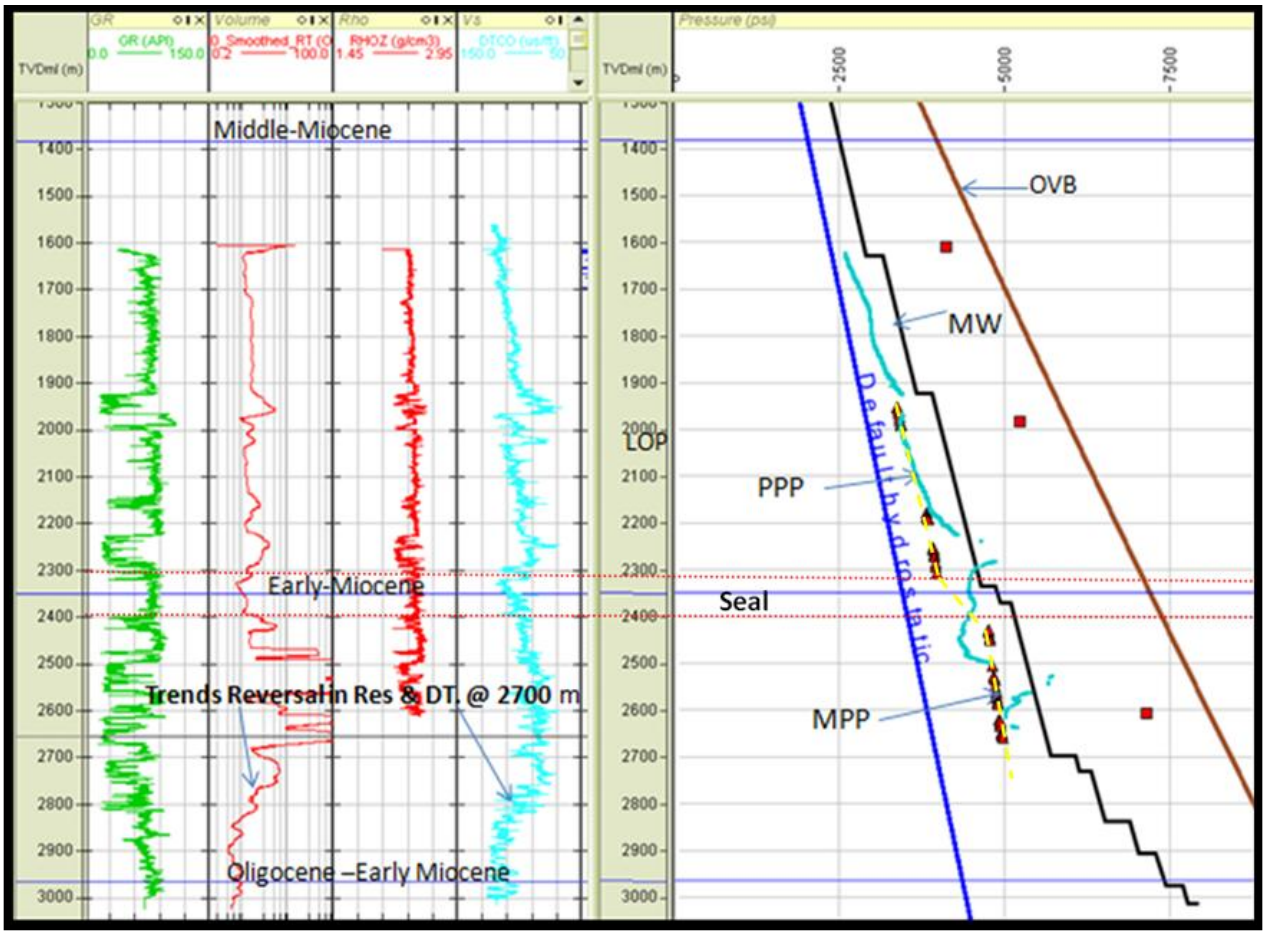

Figure 8.3. GR, resistivity, density, sonic velocity, and pressure–depth plot for well EIW-1, showing shale seal at 2300–2400 m.

NOW-1

In well NOW-1, the predicted and measured pore pressures and the mud weight track fairly well until about 2000 m depth (Figure 8.4). Below 2200 m, the predicted pore pressure is overestimated, though measured pore pressure is slightly higher than MW. This is attributed to lithology influence and/or to use other methods of pore pressure prediction within the zone.

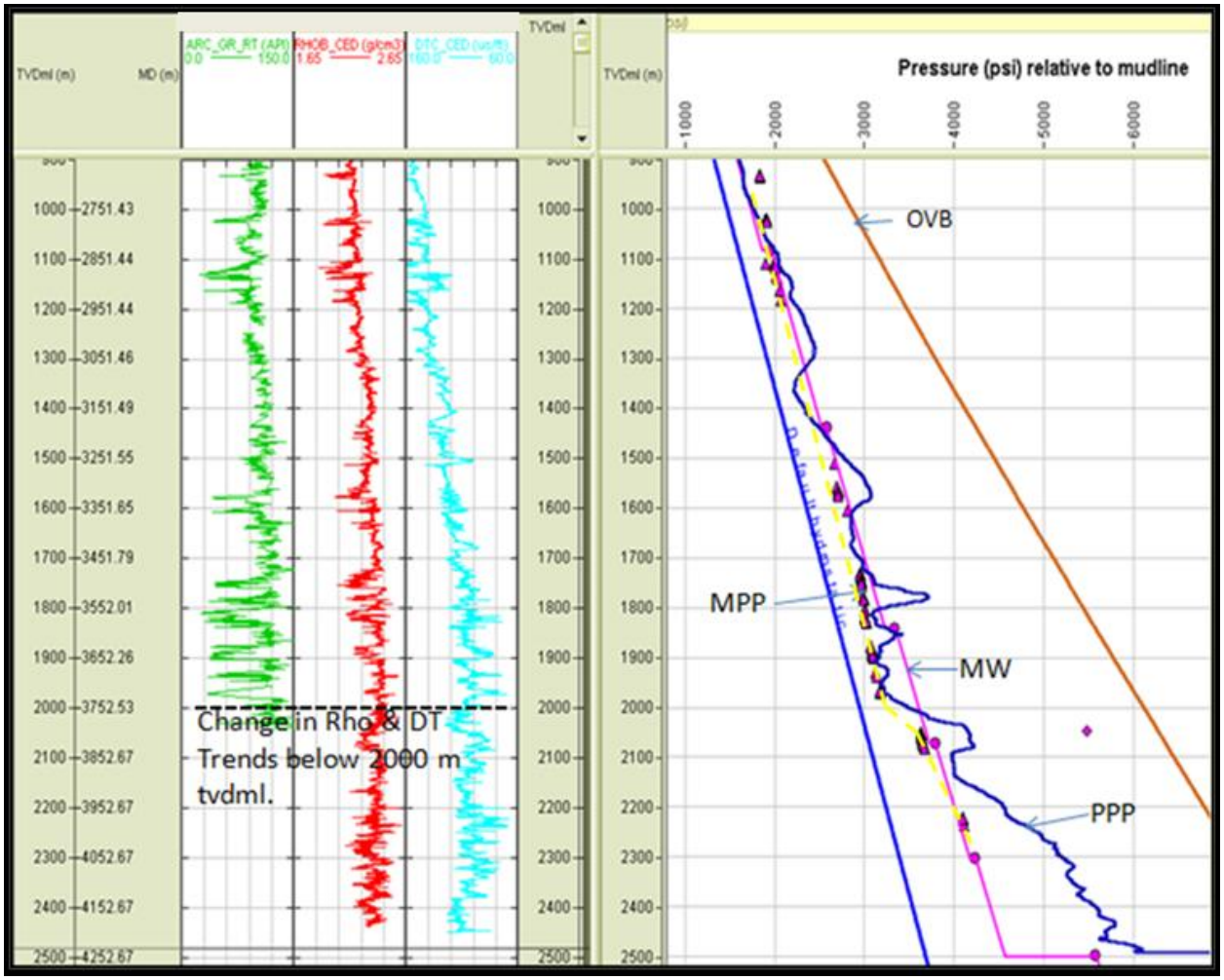

Figure 8.4. GR, density, sonic velocity, and pressure–depth plot for well NOW-1. The GR log was not run below ~2050 m depth.

8.1.2 Indications of unloading mechanisms

The second objective of this study was to determine whether mechanisms other than disequilibrium compaction, in particular smectite-to-illite transformation, contribute to overpressure in the wells studied. If water released from smectite to illite conversion is unable to escape, it will contribute to overpressure. To address this issue, discussions and interpretations of density, velocity, and resistivity logs and cross-plots are presented in this section.

Figures 5.9–5.12 show the density, velocity, and resistivity log plots for the AIW-1, AIW-2, EIW-1, and NOW-1 wells. Interpretation of these plots is based on the premise that if a reversal is seen within the same interval on density, velocity, and resistivity logs, unloading is an unlikely mechanism of overpressure generation. In such cases, the reversals can be attributed to undercompaction and/or lithology change. On the other hand, if there are reversals on sonic and resistivity logs but not on the density log, then unloading is likely to be contributing to overpressure (e.g., Bowers, 1995; Lahann, 2001; Katahara, 2003, 2006).

AIW-1

Logs in well AIW-1 show no apparent reversals. Based on the data in Figure 5.9, the dominant mechanism of overpressure generation down to 2300 m depth is disequilibrium compaction.

Figures 5.15 and 5.20 are the velocity–VES and density–VES plots for well AIW-1. Two trends are noticeable on the plots: an upper trend corresponding to data points below 2100 m, with VES reversal, higher velocity, and higher density values; and a lower trend that corresponds to depths less than 2100 m, without any reversal. Ordinarily, the upper trend in these plots would be interpreted as indications of smectite-to-illite transformation, but the temperature within the interval is rather low for smectite-to-illite transformation. Also, the plots are limited to a total depth of 2275 m – the deepest pressure measurement point available for the well.

Figure 5.30 is the cross-plot of density and sonic transit time. Based on the estimated temperature gradient of 2.92 deg C/100 m for the field, assuming there is sufficient K^+ in the system, conversion of smectite to illite should be underway by ~2400 m depth. Figure 5.30 shows that data points shift up towards the illite-rich line from about 2000 m. It can be suggested, based on the Figure 5.30 and calculated temperature that the interval from ~ 2000 m to 2300 m is more illite-rich, or less smectite-rich, but the differences are likely due to

depositional differences rather than a consequence of clay diagenesis. The predominant mechanism of overpressure generation at the depths under investigation is this well appears to be disequilibrium compaction.

AIW-2

The logs for well AIW-2 show reversals at 2600 m in density, velocity and resistivity (Figure 5.10), coinciding with a transition from low to moderately high overpressure (Figure 8.2). Assuming a temperature gradient of 2.92 deg. C /100 m, the calculated temperature of 80°C at the top of the interval is within the smectite-to-illite conversion window, and raises the possibility that the interval may be unloaded as a result of sm-ill conversion. However, reversals seen on all the three logs pose a challenge in affirmatively suggesting the presence of unloading within the interval.

The cross-plots with VES are not discussed in this section because there are no direct measurements of pore pressure below 2600 m. Figures 5.26 and 5.31 are the velocity–density and density–sonic transit time cross-plots for well AIW-2. Below about 2750 m there is a larger drop in velocity than in density relative to the shallower trend, suggestive of lithological or mineralogical variability and the temperatures in this interval are consistent with smectite-to-illite transformation. However, there is no reversal on these cross-plots that would suggest unloading has occurred from sm-ill conversion.

The preferred interpretation from all observations made so far in this well is that the predominant overpressuring mechanism is disequilibrium compaction. There is strong evidence of illitization from the density–sonic cross-plots, and the water released by this reaction would presumably have contributed to the maintenance of overpressure, but there is no specific evidence of unloading. The transition from low to moderately high overpressure is consistent

with disequilibrium compaction and a sealing layer of low permeability at a present depth of ~2500–2600 m, possibly extending to greater depths.

EIW-1

In well EIW-1, there are reversals on velocity and resistivity logs at 2800 m but the density log was not run deep enough to observe if there is a reversal at the same depth or not (Figure 5.11). The calculated temperature of 86°C for the depth would suggest that smectite–illite conversion is already in progress. Based on the logs alone, it is risky to infer or dismiss unloading in this well as a result of smectite-illite conversion.

The VES cross-plots for well EIW-1 are shown in Figures 5.17 and 5.22. The interval 2300–2350 m shows reversal of both velocity and VES (Figures 5.11, 5.17 and 8.3). The VES reversal also shows in Figure 5.22, but over the available depth range the density continues the shallow trend (Figure 5.11). Ordinarily, the velocity reversal without density reversal in the interval 2300–2350 m could be interpreted as an indication of unloading. However, the estimated temperature of ~65°C is insufficient for smectite–illite conversion and hence ruling out possibility of unloading from smectite-illite conversion. The preferred suggestion here is that, unloading is unlikely within the interval, and the difference in response between velocity and density is due to lithology difference.

The density–sonic transit time cross-plot (Figure 5.32) shows clustering of data, especially in the deeper interval, between the smectite and illite lines. The density log was limited to 2600 m depth, where the temperature is estimated to be ~80°C, which suggests that smectite–illite conversion would be under way, but the evidence for that on this cross-plot is weak. The absence of density data to correlate with the reversal on the sonic and resistivity logs at 2800 m is unfortunate, and precludes any definite conclusion about unloading. However, by

analogy with well AIW-2, the preferred interpretation must be that the dominant mechanism of overpressure generation is disequilibrium compaction. Smectite–illite transformation is taking place at depth, and may be inferred to have contributed to the maintenance of overpressure, but there is no evidence that unloading has occurred from such conversion.

NOW-1

In well NOW-1, reversals are seen on sonic and density logs at 2000 m (Figure 5.12); a resistivity log is not available for this well. Using the estimated temperature gradient of 3.58 deg C / 100 m, at 2000 m and deeper this well is within the smectite-to-illite conversion window. Considering the mud weight trend at depths below 2000 m and expected temperature for the interval, it can be said that, in all likelihood, smectite-illite transformation is contributing to overpressure at greater depth in this well. Unfortunately, wireline logs were not run deep enough to enable evaluation of the deeper intervals.

The simple nature of NOW-1 cross-plots relative to previous wells is quite striking. For example, Figures 5.18, 5.23 and 5.28 all show increase from the shallow to deep section of well and no reversal of VES is apparent. The limitation with interpretation based on these plots is that it does not reflect what happens below 2000 m. This is because the GR log which was used to discriminate shales did not log below 2000 m in this well, effectively limiting filtered data to maximum depth of 2000 m. Based on these plots, it can be said affirmatively that disequilibrium compaction is the dominant mechanism up to about 2000 m.

Figure 5.33 is the density–sonic cross-plot; the deeper interval plots closer to the illite line but there is no clear cut illite-rich trend. Based on temperature gradient of 3.58 deg C /100m calculated for the NOW wells, it is expected that sm–ill conversion would commence at about 2000 m. Pressure increases step-wise into hard overpressure at 2500 m (temperature ~90 deg C).

There is no clear evidence of unloading due to smectite-illite conversion above this depth because predicted pore pressures are unreliable without the GR log to filter shales, but there is circumstantial evidence of smectite-illite transformation below 2000 m, which would contribute to the maintenance of overpressure, and the single pressure measurement at 2500 m depth suggests that beds below that depth may be unloaded. However, we lack the necessary log data to confirm this interpretation.

8.1.3 UBD prediction

AIW-1

Results obtained by comparing predicted and measured pore pressures and mud weight (Figure 7.1) shows that intervals 2510–2835 m and 3475–3875 m were drilled underbalanced in well AIW-1. Both mudlog and drilling log data have confirmed that (Figures 7.2, 7.3, and 7.4).

Interval 2470–2580m

Figure 7.2 show plot of GR, BS, caliper, ROP, TG, and torque for the interval 2470–2580 m. The interval between 2500–2540 m (red circle) shows higher wash out compared to the other sections. This is consistent with increased torque seen in this section of hole, i.e., with more cuttings and/or cavings in hole torque has increased. Also, the TG within the interval generally increases with depth, especially in the washout intervals. Increased ROP (drilling break) recorded at 2510 m and 2534 m coupled with decreasing Dxc with depth both point to the intervals being undercompacted with overpressure due to disequilibrium compaction, and the likelihood of UBD.

Interval 2750–2860m

Observations in Figure 7.3 are similar to those made in Figure 7.2. The severity of wash out seen in the top section cannot all be attributed to UBD. Considering the fact that 13-3/8" casing was set in this part of hole at 2746 m, the associated cementing job, LOT, and other related operations can potentially contribute to hole washout state observed in the section.

However, relative to the previous interval (2470–2580 m), this section of the hole shows greater washout, in particular interval between 2790 m and 2810 m. The recorded TG in the section is still a lot higher than the background gas, and increased even further at 2810 m. The drastic increase in TG observed at 2810 m is presumably due to the cumulative effect of gas entering the hole from the upper section, which was drilled UBD, and decreasing the mud weight. In addition to the observations made above, drilling breaks in the shales, and the decreasing Dxc trend with depth are all pointers to UBD within the interval.

Interval 3480–3580m

This interval is the lower UBD zone identified on the pressure–depth plot in Figure 7.1. Though indicated as UBD zone based on pressure–depth plot data, relative to the previous zones this section shows minor hole washout (Figure 7.4). The general trend on the ROP and TG is increase with depth. The maximum ROP is seen in the shale interval at 3510–3550 m; likewise, the Dxc within the same interval shows a declining trend, suggesting undercompaction and possible overpressure. TG gradually increases from about 3510 m, and peaks between 3530m and 3542m; this is characteristic of an UBD zone. However, the torque trend decreases from top to bottom of the section, suggesting a relatively clean hole, i.e., fewer cuttings/cavings; this character is consistent with the caliper log signature.

Overall, the ROP, Dxc, torque, and TG shown on the plots are indicative of UBD and in agreement with prediction made from density pore pressure prediction in Figure 7.1.

NOW-1

17" hole: interval 2499–2621 m

A sample of the wellsite geological log in the 17" hole section for the interval 2500–2621 m is shown in Figure 7.7. The interval was drilled with mudweight of 9.0–9.1 ppg, while background gas remained steady at 1.5 %. At section TD, torque had increased by 30%. It should be noted that increased torque may not be solely due to the effect of UBD. However, within this interval, increased torque is the strongest indication of likely UBD.

12-1/4" hole: interval 2621–2896 m

In this section of hole, the torque started at 50% less than recorded at the end of 17" hole section. Despite starting the section with a mud weight of 9.3 ppg; TG increased to 5% in the shale section and peaked at 40% in the sands (Figure 7.8). By section TD at 3798 m MD, torque had increased to 8000 kftlb and mud weight was raised to 9.6 ppg.

It is apparent that, gas % and torque increased as drilling progressed from the 17" hole to the end of the 12-1/4" hole. Both the torque and especially the gas pattern seen in the 17" and 12-1/4" hole are all indicative of UBD, and corroborate pore pressure predicted from density (Figure 7.5).

8-1/2" hole: interval 3810–4257 m

In this section of hole, the CG, gas-cut mud, and mud pit gain are all pointers to the fact that the section was drilled UBD. In addition to the UBD indicators mentioned above, though secondary,

the caliper log shows severe washout in the interval 4008–4054 m (Figure 7.9). What now follows are results of gas and other drilling indicators within specific intervals.

Interval 3810–4069 m

In Figures 7.11 and 7.12, the sands at the beginning of section show relatively high TG. In the shale section between 3856 m and 3886 m, the gas trend begins to increase then remains constant. Apparently in response to increasing pore pressure downhole, mud weight was increased from 9.6 ppg to 9.8 ppg while drilling this interval.

Interval 4069–4257m

In the interval 4069–4115 m, BG decreased to 0.14% and PCG to 0.40% at 4074 m. Apparently, the increase in mud weight to 9.8 ppg from the previous interval had suppressed the gas (Figure 7.13). Subsequently, a steady increase of PCG was observed with maximum of 2.38% at 4198 m. Likewise, maximum BG of 2.05% was recorded at 4156 m. At this point gas-cut was noticed (i.e., recorded MWin of 9.8 ppg was higher than MWout of 9.7 ppg). The gas-cut mud is a strong and positive indication that within the interval the well was flowing, and the hole is underbalanced (Figure 7.13).

As shown in Figure 7.14, mud was treated and drilling continued with MW of 9.8 ppg until 4239 m where CG and BG increased drastically to 15.48% and 14.58%, respectively. In addition, a gain of 8 bbls was recorded in the trip tank. These are indications that the well was flowing and underbalanced. The gas was circulated out through choke and mud treated and weighted up to 11.2 ppg. Maximum gas of 73.6% was reported while stabilizing the well. Apparently, from the drilling reports, there was another episode of gas-cut mud here; mud was

again treated and increased from 9.8 ppg to 11.4 ppg, and the hole was then drilled to final TD at 4257 m.

Again in this section of hole, as predicted from the density log in the shales and supported by drilling data, sections of this well were drilled underbalanced.

8.2 UNE and AOE wells

A review, evaluation, and interpretation of results obtained from UNO and AOI wells is presented in this section.

8.2.1 Pore pressure prediction from density logs

UNE-4 and UNE-5

Figures 8.5 and 8.6 show the pore pressure predicted from shale density using the equivalent depth method for wells UNE-4 and UNE-5. In both wells, the pore pressure predicted from density shows a good match with the measured pore pressure down to ~800 m and 1800 m, respectively. This suggests that equivalent depth method, petrophysical based prediction methods, and seismic should work well up to 800 m and 1100 m in the respective wells.

However, in UNE-4 well, below ~800 m the density-based equivalent depth method over-predicted the pore pressure. This is an indication that the shale and the sand pressures in these zones are not in dynamic equilibrium. The exact reason is not clear but it is possible that the sands are laterally drained, so measured pore pressure is less than predicted. Assuming that NCT for the interval is accurate, another possibility is that an unloading mechanism such as sm-ill transformation has contributed to overpressure, in addition to disequilibrium compaction, causing the poor prediction from the equivalent depth method. At depths below 1800 m, the pore

pressure predicted from density shows a gradual transition into high overpressure, and correctly predicted high overpressure in the sand stringer at ~2110 m where a kick was encountered. The increase in overpressure and reduction in vertical effective stress between 1810 m and 2110 m, where pore pressure was measured, could indicate that the deeper strata have been unloaded. Alternatively, the deeper strata may have retained higher porosity due to disequilibrium compaction since they were at shallower depth, and the fact that the pore pressure predicted from the density log by the equivalent depth method matches the measured pore pressure gives support to the latter interpretation.

The pore pressure predicted from density in UNE-5 tracks the measured pore pressures quite well (Figure 6.32). Kicks were picked in this well at 1706 m and 2000 m. Judging from the step-wise increase in the mud weight profile from about 1400 m, and the depths where kicks were encountered, it is apparent that high overpressure was not anticipated. For example, drilling progressed in the well with a mud weight lower than the actual pore pressure, and as hole conditions deteriorated the mud weight was adjusted in response. High overpressure begins at 1700 m and shale pore pressure predicted from density is consistent with measured pore pressures within the zone. Essentially, density based prediction works quite well in this well, however, for verification and accuracy multiple approaches are recommended at the deeper intervals.

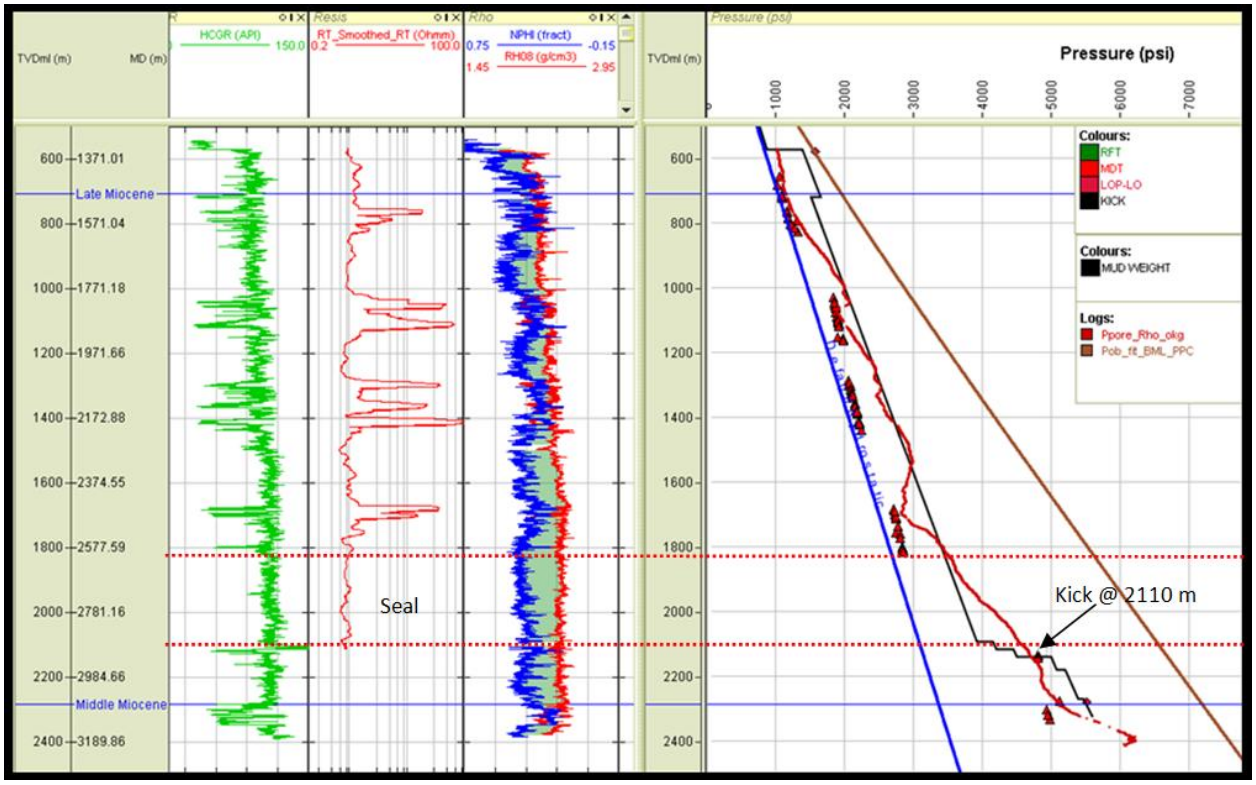

Figure 8.5. GR, resistivity, density, neutron porosity, and pressure–depth plot for well UNE-4.

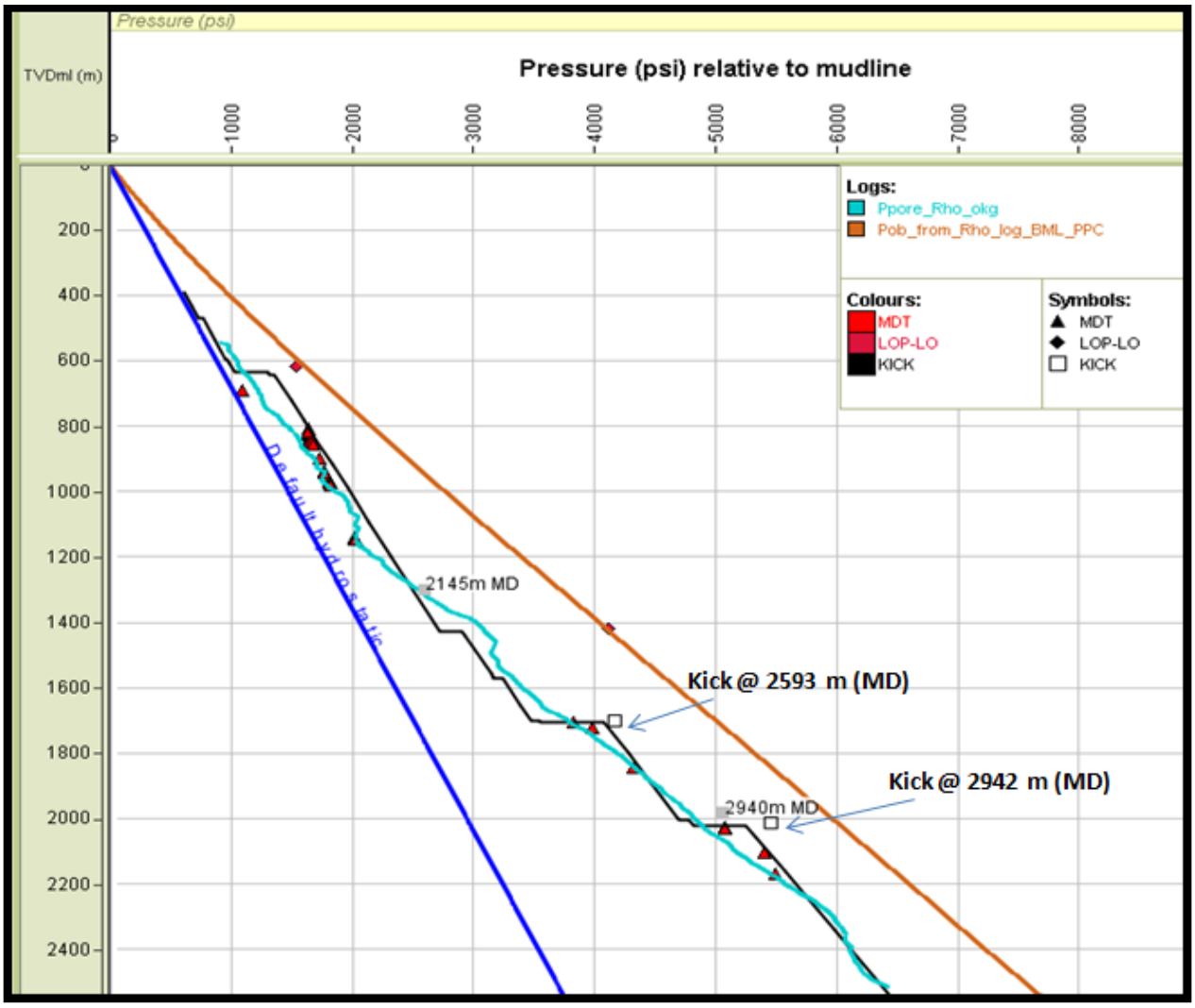

Figure 8.6. GR, shale volume and pressure–depth plot for UNE-5.

AOE-1 and AOE-4G1

Figure 8.7 is the pressure–depth plot for the AOE-1 well. The density based pore pressure predicted in shale tracks the measured pore pressure quite well down to 1800 m. The shale interval at 2485–2635 m inhibits hydraulic communication between underlying and overlying sand intervals. The sand interval at 2650–2760 m is highly overpressured. At depths below 1800

m, the density-based equivalent depth method has underestimated the pore pressure, and the underestimation is severe at depths below 2600 m.

The pressure–depth plot of well AOE-4G1 (Figure 8.8) shows that down to 1300 m the density-based equivalent depth method does a good job of predicting the pore pressure. However, below 1300 m the pore pressure is overestimated. Assuming the pore pressure predicted from density is accurate, a plausible explanation for the discrepancy between predicted and measured pore pressures is lateral drainage. Shale intervals at 1890–1955 m and 2180–2260 m are seals preventing vertical communication between adjacent sands.

In general observations from well AOE-4G1 suggest that density-based pore pressure prediction would work quite well in the shallow intervals down to about ~1300 m, but in the deeper zones, other methods, modification, or multiple approaches are considered required.

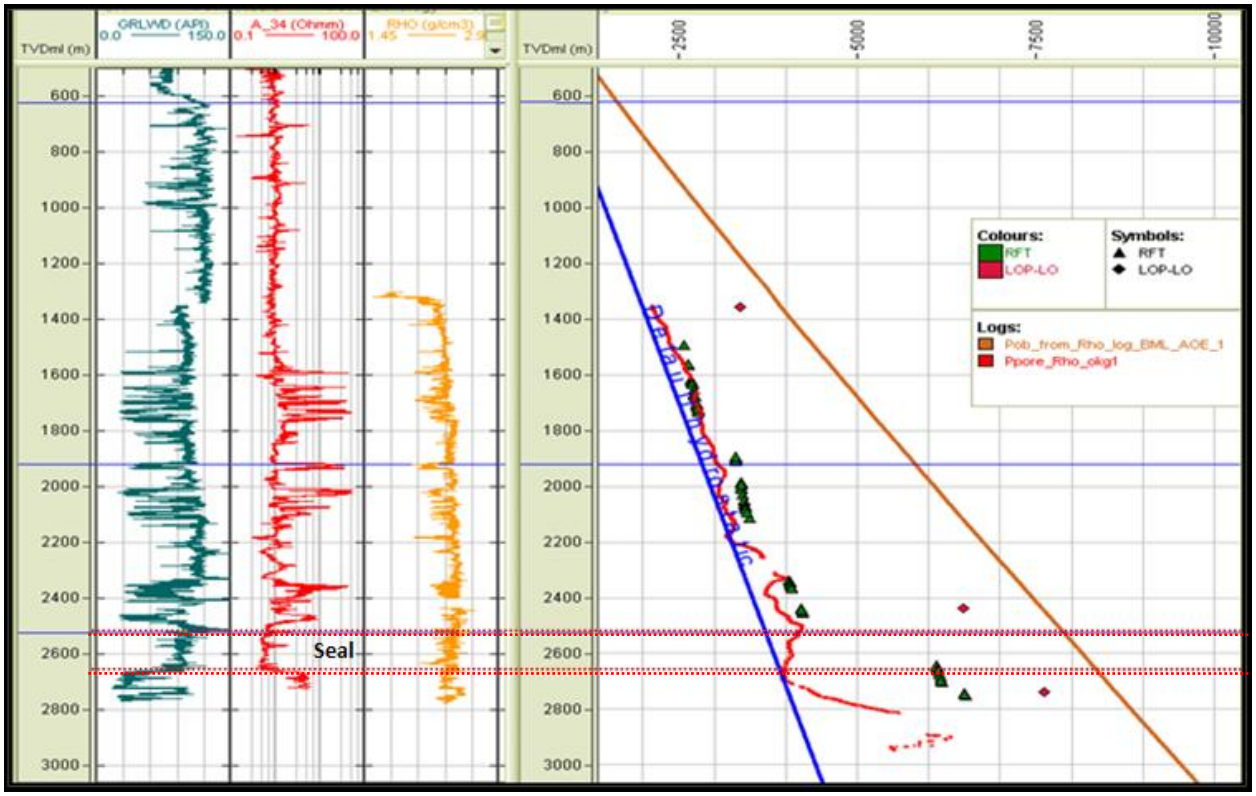

Figure 8.7. GR, resistivity, density, and pressure–depth plot for well AOE-1.

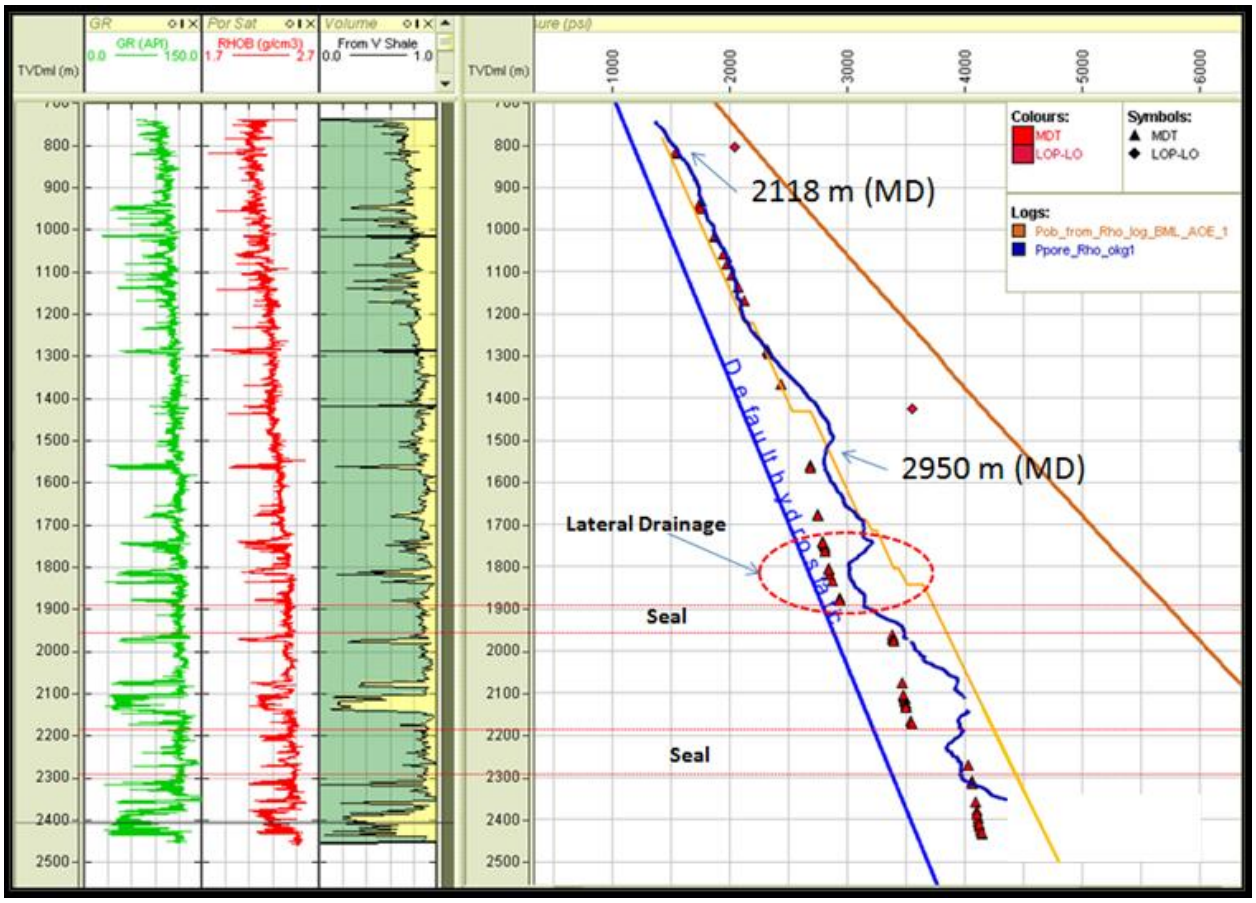

Figure 8.8. GR, resistivity, shale volume, and pressure–depth plot for well AOE-4G1.

8.2.2 Indications of unloading

Results of cross-plots presented here are used to infer whether diagenesis has occurred in these wells, and whether unloading due to sm-ill transformation has contributed to overpressure observed in the wells.

UNE-4 and UNE-5

The density, velocity, and resistivity logs for UNE-4 are shown in Figure 6.10. A reversal is seen at ~2350 m in both density and velocity, but resistivity was not logged deep enough to see the same interval. On the strength of this plot alone, it could be inferred that there is no unloading in

the interval below 2350 m because we have both density and velocity reversal so the dominant pressure mechanism is disequilibrium compaction. As seen in Figure 8.5, the shale seal at 1800–2100 m creates pressure compartments in the well.

In the logs for well UNE-5 (Figure 6.11), there is no apparent reversal, but at about 2350 m all of the logs show high readings. The observed high density, velocity, and resistivity reading are interpreted here to be due to differences in lithology, possibly with a contribution from diagenesis. There is no evidence of unloading (i.e., a velocity reversal without reversal in density) on Figure 6.11.

Figures 6.16 and 6.17 are the velocity–VES cross-plots for UNE-4 and UNE-5; VES limits the maximum depth displayed on these cross-plots, because the maximum VES depths are 2120 m and 2190 m in UNE-4 and UNE-5, respectively. The trends are consistent with loading: shallow and deeper intervals have a common trend of increasing velocity with increasing VES.

Interpretation of Figures 6.20 and 6.21, density–VES cross-plots for UNE-4 and UNE-5, are similar to that for the velocity–VES cross-plots. The general trend is increasing density with depth, except for the intervals with relatively high density which is attributed to differences in lithology.

In the velocity–density cross-plots of Figures 6.24 and 6.25, the general trend is increasing velocity with density, but at depths > 2000 m there are drastic decreases in velocity in Vp and decreases in density that take the data points along an illitization / unloading trend, not the loading trend. It appears that the shales at depths >2000 m are illitized and unloaded.

Figures 6.28 and 6.29 are the density–sonic cross-plots for wellsUNE-4 and UNE-5. The plots are used to identify whether diagenesis of smectite to illite has occurred in the system, which requires sufficient K^+ in the system and temperatures >65 deg C. The temperature gradient

calculated for UNE wells is 3.77 deg C/100m, so it is expected that smectite-to illite conversion will commence at ~1900 m. As seen in Figures 6.28 and 6.29 data points are moving from the smectite-rich trend towards the illite rich trend.

AOE-1 & AOE-4G1

The density, velocity, and resistivity logs for wells AOE-1 and AOE-4G1 are shown in Figures 6.12 and 6.13. While there are no reversals apparent in well AOE-4G1, reversals can be seen at 2500 m in well AOE-1 on all the logs, which implies that there is no unloading of the interval below 2500 m and the mechanism of overpressure is disequilibrium compaction.

The velocity–VES cross-plots for well AOE-1 (Figure 6.18) and well AOE-4G1 (Figure 6.19) are strikingly different. The trend in well AOE-4G1 is clearly that of disequilibrium compaction, where velocity increases with VES, though the plot only has data to a maximum depth of 2380 m. The general trend in well AOE-1 is increasing velocity with VES increase; however, we see reversal that tracks the general trend and intervals of unusually high velocity. The high velocity intervals are interpreted here to have resulted from differences in lithology.

Similar trends to those seen in the velocity–VES cross-plots are also seen in the density–VES cross-plots (Figures 6.22 and 6.23). Along the same lines as for the high velocities in well AOE-1, the high density is attributed to differences in lithology.

Figures 6.26 and 6.27 are the velocity–density cross-plots for wells AOE-1 and AOE-4G1. However, the classic indication of illitization and unloading, i.e., decreasing velocity with little or no change in density, is difficult to establish in these plots. In the plot for well AOE-4G1 (Figure 6.27), at depth 2100 m we see an increasing velocity with a slight drop in density.

Based on the density–sonic cross-plots in Figures 6.30 and 6.31, it is apparent that below 2250 m depth the system is illite-rich, i.e., there has been diagenetic conversion of smectite-to-

illite. The temperature gradient calculated for AOE wells is 3.56 deg C/100 m. Assuming sm-ill conversion in under way at 70 deg C, it implies that sm-ill transformation should begin at 2000 m depth.

8.2.3 UBD prediction

Two wells, UNE-5 and AOE-4G1, noted with UBD are presented in this subsection.

UNE-5

Figure 6.34 shows UBD in UNE-5 between 2176 m and 2922 m MD, with kicks picked in sand stringers at 2593 m and 2938 m MD. The main drilling and mudlog indications of UBD are the FG, BG, and PCG; because of the poor quality, the caliper log is used as a secondary indicator. It is instructive to note that in Figure 7.19, BG increased step-wise with each PC and had doubled by the end of the section; the caliper reading at the base also shows severe washout. The BG trend, CG and washout interval are all strong indicators of UBD. A similar trend is seen drilling through the long shale section (Figures 7.20–22) with recorded BG as high as 26.3% at ~2418 m MD. The kicks picked in the sand stringers at 2593 m and 2938 m MD clearly show that the surrounding shales and sand stringers are not in dynamic equilibrium.

AOE-4G1

Figure 6.35 is the pressure–depth plot for well AOE-4G1 and shows that zones between 750 m and 1300 m were drilled UBD. The gas signatures and, to a lesser extent, hole washout were the main indicators of UBD in this well. As indicated on Figure 7.15, at ~2150 m MD, hole pack off, trip gas up to 12%, FG increases with each pipe connection, and trip gas up to 12% were reported. Also, caliper reading increases in the 12-1/4” hole. All of these observations taken together are hallmarks of UBD. The over-gauged hole suggests more rock is entering the hole

than normally, and this may be due to the mud weight not being able to counterbalance the formation pressure. If appropriate intervention is not implemented, the potential for hole pack-off becomes high, and this is exactly what happened in this section of hole. Similar gas and hole washout expression to that seen in Figure 7.15 is also seen in Figure 7.18. Here, after the pipe connection at 2734 m MD, CG increased progressively from 2.12% to 3.17% with successive pipe connections.

8.3 Conclusions and future work

In this section, the main findings of the study are discussed in relation to each of the original objectives stated at the beginning of the chapter.

8.3.1Estimation of pore pressure using density log by the equivalent depth method

The effectiveness of the density log (equivalent depth method), and by extension seismic-based methods, for pore pressure prediction in shale has been demonstrated in this study with the pressure–depth plots. Although, seismic velocity data relate more directly to velocity log, there are transforms for converting density to velocity, and vice-versa; in addition, velocity data can be used with equivalent depth method. In general, this approach is quite effective and predicts pore pressure accurately anywhere between 600 m – 1200 m TVDml. Below these depths, the pore pressure is either under or overpredicted in some of the wells, and this is especially obvious when predicted pore pressures are compared with measured pore pressures on the pressure–depth plots.

8.3.2 Identification of smectite-to-illite transformation as a contributory mechanism to overpressure

Based on evidence from density, velocity, and resistivity logs; in addition to cross-plots presented in chapters 5 and 6, the following inferences can be made about overpressure generation mechanisms.

1. The main mechanism of overpressure in the shallow section is disequilibrium compaction. The shallow sections are where temperatures are < 65°C.
2. Water released from sm-ill conversion must contribute to observed overpressures in beds where the transformation is taking place, because overpressure is a transient phenomenon. The best available evidence for sm-ill transformation is on cross-plots of density against sonic transit time. Where sm-ill transformation has been responsible for reducing the vertical effective stress, a reversal on the sonic log may be observed without any reversal on the density log.
3. Deep intervals correlates to zones with temperature value of 70°C or higher. Also, shale intervals serve as permeability barriers preventing hydraulic communication between sand intervals and hence creating pressure compartments.

8.3.3 Identification of UBD from pressure–depth plots with supporting evidence from drilling and mudlog data.

Comparison of zones identified with UBD on pressure–depth plots with mudlog and drilling data shows that:

1. Gas (i.e. CG, BG, and TG) increases within zones of UBD.
2. UBD zones generally show greater hole washout on caliper log.
3. Torque generally increases while drilling through zones with UBD.

4. When available, Dxc has been useful for predicting overpressure/undercompaction and hence, depending on mud weight, possible UBD.

8.3.4 Future work

Additional and follow-up work on this study will shed more light in understanding of pressure distribution and safe drilling operation in the deepwater Niger Delta area. The list below contains suggested topics for further investigation:

1. Mineralogy, elemental (i.e., potassium and iron), and TOC analysis of shales intervals in the deep and shallow section of wells. This can be broadly divided into zones with temperature < 70 degrees C and zones with temperature >75 degrees C.
2. Specifically, zones identified as potential seals should be analysed for calcite, quartz content and porosity/permeability. This will help to discern the dominant cause of sealing (i.e., very low porosity/permeability, calcite/quartz cement and/or combination).
3. Wells with complete sets of logs (i.e., density, velocity, and resistivity) and with minimum log depth of 2800 m TVDml or more should be analysed. Since the majority of the logs used in this study terminated shallower than 2800 m; this will provide an opportunity to evaluate reasons for the drastic MW increase observed in some of the wells especially at deeper intervals.
4. Regional structural, stratigraphic and overpressure mapping studies to determine the nature of plumbing in the reservoir, i.e., charging and lateral transfer.

References

AGIP. (1980). *The wellsite geological activity in hydrocarbon exploration, Handbook.* S. Donato Milanese: Agip-Milan.

Ajakaiye, D.E. & Bally, A.W. (2002a.). Course manual and atlas of structural style on reflection profiles from the Niger Delta. *AAPG, Continuing Education Course Note Series, 41*.

Ajakaiye, D.E. & Bally, A.W. (2002b). Some structural styles on reflection profiles from offshore Niger Delta. *Search and Discovery,10031*, 1-6.

Ajienka, K., Egbon, F., & Onwuemena, U. (2009). Deep offshore fracture pressure prediction in the Niger Delta - A new approach. *SPE Paper 128339*, 1-16.

Alberty, M.W. & McLean, M.R. (2003). Emerging trend in pressure prediction. *Offshore Technology Conference, Paper 15290.*, 1-7.

Anjos, S.M.C. (1986). "Absence of clay diagenesis in Cretaceous- Tertairy marine shales, Campos Basin, Brazil". *Clays and Clay Minerals, 34*, 424-434.

Athy, L.F. (1930). Density, pororsity, and compaction of sedimentary rocks. *AAPG Bulletin, 14,*, 1-24.

Avbovbo, A. (1978). Tertiary lithostratigraphy of the Niger Delta. *AAPG Bulletin, 62*, 295-300.

Baker Hughes Corporation. (2012, March 29). Retrieved from Baker Hughes Website: http://www.bakerhughes.com/

Barker, C. (1972). Aquathermal pressuring - role of temperature in development of abnormal-pressure zones. *AAPG Bulletin, 80*, 2068-2071.

Barker, C. (1990). Calculated volume and pressure changes during the thermal cracking of oil to gas in reservoirs. *AAPG Bulletin, 72*, 1334-1359.

Beka, F.T. & Oti, M.N. (1995). The distal offshore Niger Delta: frontier prospects of a mature petroleum province. *In: Oti, M.N., & Postma, G., Geology of Deltas: Rotterdam, A.A. Balkema,*, 237-241.

Bilotti, F.D. & Shaw, J.H. (2001). Modeling the compressive toe of of the Niger Delta as a critical taper wedge (abs:). *AAPG Annual Meeting Program, 10*, A18-A19.

Bjorlykke, K. . (1998). Clay mineral diagenesis in sedimentary badins: a key to the prediction of rock properties: examples from North Sea Basin. *Clay Mineral, 33,*, 15-34.

Bjorlykke, K. & Hoeg, K. (1997). Effects of burial diagenesis on stress, compaction and fluid flow in sedimentary basins. *Marine and Petroleum Geology, 14,*, 267-276.

Bower, G.L. & Katsube, T.J. (2002). The role of shale pore structure on sensitivity of wire-line logs to overpressure. In: Huffman, A.R. & Bowers, G.L. (eds.), Pressure Regimes in Sedimentary Basins and their Prediction. *AAPG, Tulsa, Memoir 76,*, 43-60.

Bowers, G.L. (1995). Pore pressure estimation from velocity data: accounting for overpressure mechanisms besides undercompaction. *SPE Drilling and Completion, paper IADC/SPE 27488*.

Bowers, G.L. (2001). Determining an appropriate pore-pressure estimation strategy. *Offshore Technology Conference, paper OTC 13042*.

Brownfield, Michael E. & Charpentier, Ronald R. (2006). Geology and total petroleum system of the west-central coastal province (7203), West Africa. *USGS Bulletin, 2207-B*, 1-52.

Burst, J.F. (1969). Diagenesis of gulf coast clayey sediments and its possible ralation to petroleum migration. *AAPG Bulletin, 53*, 73-93.

Chapman, R. (1983). Petroleum Geology. *Elsevier, Amsterdam,*.

Cheli, Elena; Brancato, Calogero. & Vagnoux, J.P. (1995). Woodie: A tool to support overpressure detection. *SPE/IADC 29346*.

Chopra, S. & Huffman, A. (2006). Velocity determination for pore pressure prediction. *CSEG Recorder*, 29-46.

Cobbold, Peter R., Clarke, Benjamin J. & Loseth, Helge. (2009). Structural consequences of fluid overpressure and seepage forces in the outer thrust belt of the Niger Delta. *Petroleum Geoscience, 15*, 3-15.

Colton-Bradley, V.A.C. (1987). Role of pressure in smectite dehydration - effects on geopressure and smectite to illite transition. *AAPG Bulletin, 71*, 1414-1427.

Corredor, F., Shaw, J.H., & Bilotti, F. (2005). Structural styles in the deep-water fold and thrust belts of the Niger Delta. *AAPG Bulletin, 89*, 753-780.

Daines, S.R. (1982). Prediction of fracture gradient for wildcat wells. *J. Petroleum Technol., 34, 4*, 863-872.

Daniel, R. (2001). Pressure prediction for a Central Graben wildcat well, UK North Sea. *Marine and Petroleum Geology, 18*, 235-250.

Daw Robert N., Mercer, Richard F., & Myers, Donald L. (1975). Overpressure detection and control at IMP Immerk B-48 using wellsite mud gas detector. *SPWLA, Annual Symposium*.

Demaison, G. & Huizinga, B.J. (1994). Genetic classification of petroleum syatems using three factors: charge, migration, and entrapment. In: Magoon, L.B., & Dow, W.G., (eds) The Petroleum System--From Source to Trap. *AAPG Memoir, 60*, 239-248.

Dickinson, G. (1953). Geological aspects of abnormal reservoir pressure in Gulf Coast Louisiana. *AAPG Bulletin, 37,*, 410-432.

Doust, H. & Omatsola, E. (1990). Niger Delta in divergent/passive margin basins. In: J.D. Edwards and P.A. Santogrossi, eds.,. *AAPG Memoir 48*, 201-238.

Dutta. (1987).

Eaton, B. A. (1969). Fracture gradient prediction and its application in oil field operations. *J.eTechnol., petroleum 21,* , 1353-1360.

Eaton, B.A. (1975). The equation for geopressure prediction from well logs. *SPE, Pper No. 5544,*, 11p.

Ejedawe, J. (1981). Patterns of incidence of oil reserves in Niger Delta Basin. *AAPG, 65* , 1574-1585.

Ejedawe, J.E. & Okoh, S.U. (1981). Prediction of optimal depths of petroleum occurence in the Niger delta basin. *Journal of Mining Geology, 18,1*, 74-80.

Ejedawe, J.E., Coker, S.J.L., Lambert-Aikhionbare, D.O., Alofe, K.B., & Adoh, F.O. (1984). Evolution of oil-generative window and oil and gas occurrance in Tertiary Niger Delta Basin. *AAPG, 68* , 1744-1751.

Ekweozor, C.M. & Daukoru, E.M. (1994). Northern delta depobelt portion of the Akata-Agbada petroleum system, Niger Delta, Nigeria. In Magoon, L.B. & Dow, W.G. (eds) The petroleum system - from source to trap. . *AAPG Memoir, 460*, 599-613.

Ekweozor, C.M. & Okoye, N.V. (1980). Petroleum source bed evaluation of Tertiary Niger delta. *AAPG Bulletin, 64*, 1251-1259.

Evamy, B.D., Haremboure, J., Kamerling, P., Knaap, W.A., Molloy, F.A. & Rowlands, P.H. . (1978). Hydrocarbon habitat of Tertiary Niger Delta. *AAPG Bulletin, 62*, 277-298.

Evers, J.F. & Ezeanyim, R. (1983). Prediction of abnormal pressure in Wyoming sedimentary basins using wireline logs. *SPE-AIME, Meeting 11859*, 363-374.

Fertl, Walter H. & Timko, Donald J. (1971). Parametrs for identification of overpressure formation. *SPE 3223*, 125-131.

Forgotson, J. (1969). "Indication of proximity of high pressure fluid reservoir, Louisana and Texas Gulf Coast". *AAPG, 53,* , 171-173.

Frankl, E.J. & Cordry, E.A. (1967). The Niger Delta oil province-recent developments onshore and offshore. *Seventh World Petroleum Congress, Proceedings, Mexico City, Mexico, 1B*, 195-209.

Gardner, G.H.F., Gardner, L.W., & Gregory, A.R. (1974). Formation velocity and density -- the diagnostics basics for stratigraphic traps. *Geophysics, 39*, 770-780.

Geo Pressure Technology. (2011). RocDok-PressureView Training Manual.

Goulty, N.R. (2004). Mechanical compaction behaviour of natural clays and implications for pore pressure estimation. *Petroleum Geoscience*, 10, 73-79.

Goulty, N.R. (1998). Relationship between porosity and effective stress in shales. *First Break,* 16(12), 413-419.

Goulty, N.R., Ramdhan, A.M. & Jones, S.J. . (2012). Chemical compaction of mudrocks in the presence of overpressure. *Petroleum Geoscience,* 18, 471-479.

Grauls, D. & Cassignol, C. (1993). Identification of a zone of fluid pressure-induced fractures from log and seismic data - a case history. *First Break,* 11(2), 59-68.

Green, S. (2010). Rok Doc Training Manual: Pressure prediction module and pore pressure calculator.

Haack, R.C., Sundararaman, P., Diedjomahor, J.O., Xiao, H., Gant, N.J., May, E.D. & Kelsch, K. (2000). Niger Delta petroleum systems, Nigeria. In: Mello, M.R. & Katz, B.J. (eds) Petroleum system of South Atlantic margin. . *AAPG Memoir, 74*, 213-232.

Halliburton Oil Field Services. (2012, March 29). Retrieved from http://www.halliburton.com/

Han, D., Nur, A., & Morgan, D. (1986). "Effects of Porosity and Clay Content on Wave Velocities in Sandstones". *Geophysics, 51, 11*, 2093-2107.

Higgins, S., Davies, R.J. & Clarke, B. (2007). Antithetic fault linkages in a deep water fold and thrust belt. *Journal of Structural Geology, 29*, 1900-1914.

Hooper, R.J., Fitzsimmons, G.N., & Vendeville, B.C. (2002). The role of deformation in controlling deformational patterns in the south-central Niger Delta, west Africa. *Journal of Structural Geology*, 847-859.

Hospers, J. (1965). Gravity field and structures of the Niger delta, Nigeria, West Africa. *GSA Bulletin, 76*, 407-422.

Hottman, C.E. & Johnson, R.K. (1965). Estimation of formation pressure from log derived shale properties. *Journal of Petroleum Technology*, 717-722.

Hower, J., Eslinger, E.V., Hower, M.E., & Perry, E.A. (1976). Mechanism of burial metamorphism argillaceuos sediment, mineralogical, and chemical evidence. *GSA, Bulletin, 87*, 725-737.

Inyang, M.I., Ekweozor, C.M. & Pratt, L.M. (1995). Mid-Cretaceous anoxic events in southern Nigeria sedimentary basins-geochemical signatures and pertoleum potential implications. *Nigerian Association of Petroleum Explorationists, Official Programme*, 34.

Issler, D.R. & Katsube, T.J. (1994). "Effective Porosity of Shales Samples from Beaufort-Mackenzie Basin, Northern Canada"'. *in Current Research 1994-B; Geological Survey of Canada*, 19-26.

Issler, D.R. (1992). A new approach to shale compaction and stratigraphic restoration, Beaufort-Mackenzie Basin and Mackenzie Corridor, Nothern Canada. *AAPG Bulletin, 76*, 1170-1189.

Jorden, J.R. & Shirley, O.J. (1966). "Application of drilling performance data to overpressure detection". *JPT*, 1387-1394.

Kaplan, A., Lusser, C.U., & Norton, I.O. (1994). Tectonic map of the world, panel 10: Tulsa. *AAPG, scale 1:10,000,000*.

Katahara, K. (2003). Analysis of overpressure on the Gulf of Mexico shelf. *Offshore Technology Conference, Paper 15293*, 1-10.

Katahara, K. (2006). Overpressure and shale properties: stress unloading or smectite-illite transformation? *76th SEG Annual Meeting, Expanded Abstractss,*, (pp. 11520-1524).

Kulke, H. (1995). Nigeria, in H. Kulke, ed., Regional petroleum geology of the world: Part II. Africa, America, Australia and Antartica: Berlin, Gebruder Borntraeger. 143-172.

Lahann, R. (2002). Impact of smectite diagenesis on compaction modelling and compaction equilibrium. In: Huffman, A.R. & Bowers, G.L. (eds) Pressure Regimes in Sedimentary basins and their Prediction. *AAPG, Tulsa*, 61-72.

Lahann, R.W., McCarty, D.K., & Hsieh, J.C.C. (2001). Influence of clay diagenesis on shale velocity and fluid-pressure . *OTC 13046, Offshore Technology Conference*.

Lahann, R.W. & Swarbick, R.E. (2011) Overpressure generation by load transfer following shale framework weakening due to smectite diagenesis. *Geofluids, 11*, 362-375.

Lambert-Aikhionbare, D.O. & Ibe, A.C. (1984). Petroleum source-bed evaluation of the Tertiary Niger Delta: Discussion. *AAPG Bulletin, 68*, 387-394.

Lehner, P. & De Ruiter, P.A.C. (1977). Structural History of Atlantic Margin of Africa. *AAPG Bulletin, 61*, 961-981.

Lesage, M., Hall, P., Pearson, J.R.A., & Thlercelln, M.J. (1991). Pore-pressure and fracture-gradient predictions. *JPT/SPE*, 652-654.

Luo, M. & Vasseur, G. (1992). Contribution of compaction and aquathermal pressuring to geopressure and the influence of environmental conditions. *AAPG Bulletin, 76*, 1550-1559.

Magara, K. (1974). Compaction, ion filtration, and osmosis in shale and their significance in promary migration. *AAPG Bulletin, 59*, 2037-2045.

Magara, K. (1975). "Effect of Aquathermal Pressuring Effect in Gulf Coast". *AAPG Bulletin 59, 10*, 2037-2045.

Mallon, A.J. & Swarbrick, R.E. (2002). A compaction trend for non-reservoir North Sea Chalk. *Marine and Petroleum Geology, 19*, 527-539.

Mathews, M. (2004). Uncertainity - shale pore pressure from borehole resisitivity. *ARMA/NARMS Paper 04-551*.

Mathews, W.R. & Kelly, J. (1967). How to predict formation pressure and pressure gradient. *Oil and Gas Journal, 65,8*, 92-106.

Mello, Ulisses T. & Karner, Garry D. (1996). Development of sedimentary overpressure and its effect on thermal maturation: Application to the Gulf of Mexico Basin. *AAPG Bulletin, 80,9*, 1367-1396.

Merki, P. (1972). Structural Geology of the Cenozoic Niger Delta. *In: African Geology by Dessauvagie, T.F.J. & Whiteman, A.J. Eds.), Ibadan Univ. Press*, 635646.

Mouchet, J.P. & Mitchell, A. (1989). *Abnoramal Pressures While Drilling.* Elf Aquitaine, Boussens, Manual Techniques 2, 225p.

Nordgard Bolas, H.M. & Hermanrud, C. (2002). Rock stress in sedimentary basins - implications for trap integrity. In: Koestler, A.G. & Hunsdale, A. (eds), Hydrocarbon Seal Quantification. *NPF Special Publication, 11*, 17-35.

Nwachukwu, S. (1976). Approximate geothermal gradients in Niger delta sedimentary basin. *AAPG Bulletin, 60*, 1073-1077.

Nwachukwu, S.O. & Chukwurah, P.I. (1986). Oragnic matter of Agbada Formation, Niger Delta, Nigeria. *AAPG Bulletin, 70*, 48-55.

Osborne, M. & Swarbrick, R.E. (1997). Mechanisms for generating overpressure in sedimentary basins: a reevaluation. *AAPG Bulletin, 81*, 1023-1041.

Owolabi, O.O., Okpobiri, G.A. & Obomanu, I.A. (1990). Prediction of abnornal pressure in the Niger Delta Basin using well logs. *SPE 021575*, 1-15.

Pennebaker, E. (1968). Seismic data indicate depth, magnitude of abnormal pressure. *World Oil, 166, 7*, 73-78.

Peters, K.E. & Moldowan, J.M. (1993). *The biomarker guide:.* Englewood Cliffs, N.J.,: Prentice Hall, p363.

Pilkington, P. (1999). Uses of pressure and temperature data in exploration and new development in overpressure detection. Pore Pressure and Fracture Gradients. *SPE Reprint, 49*, 64-70.

Powers, M.C. (1967). Fluid realease mechanism in compacting marine mudrocks and their importance in oil exploration. *AAPB Bulletin, 51*, 1240-1254.

Raiga-Clemenceau, J., Martin, J.P. & Nicoletis, S. (1986). The concept of acoustic formation factor for more accurate porosity determination from sonic transit time data. *SPWLA 27th Symposium*, 1-14.

Ramdham, A.M. & Goulty, N.R. (2011). Overpressure and shale compaction in the Lower Kutai Basin, Indonesia - a radical reappraisal. *AAPG Bullettin, 95*, 1725-1744.

Ramdhan, A.M. & Goulty, N.R. (2010). Overpressure generating mechanisms in the Peciko Field, the Lower Kutai Basin. *Petroleum Geoscience, 16*, 367-376.

Saugy, L. & Eyer, J.A. (2003). Fifty years of exploration in the Niger Delta (West Africa). In: Halbouty, M.T. (ed.) Giant Oil and Gas Fields of the Decade 1990-1999. *AAPG Memoir, 78*, 211-226.

Schlumberger Limited. (2012, March 29). *SLB*. Retrieved from http://www.slb.com/

Seldon, B. & Flemings, P.B. (2005). Reservoir pressure and seafloor venting: Predicting trap integrity in a Gulf of Mexico deepwater turbidite minibasin. *AAPG Bulletin, 89,*, 193-209.

Short, K.C. & Stäuble, A.J. (1967). Outline of geology of Niger Delta. *AAPG Bulletin, 91*, 761-779.

Swarbrick, R.E. & Osborne, M.J. (1998). Mechanism that generate abnormal pressures: An overview. *AAPG Memoir, 70*, 13-32.

Swarbrick, R.E., Osborne, M.J. & Yardley, G.S. (2002). Comparison of overpressure magnitude resulting from the main generating mechanisms. *In: Huffman, A.R. and Bowers, G.L. (eds), Pressure Regimes in Sedimentary Basins and their Prediction: AAPG, Tulsa,*, 1-12.

Swarbrick, R.E., Osborne, M.J. & Yardley, G.S. (2002). The magnitude of overpressure from generating mechanism under realistic basin conditions. *AAPG , Memoir, 76*, 1-12.

Terzaghi, K. & Peck, R.B. (1967). *Soil Mechanics in Engineering Practice 2nd Edition.* New York. 729p: John Wiley & Sons.

Tingay, M.R.P., Hillis, R.R., Swarbrick, R.E., Morley, C.K. & Damit, A.R. (2009). Origin of overpressure and pore-pressure prediction in the Baram province, Brunei. *AAPG Bulletin, 83,*, 51-74.

Tissot, B.P. & Welte, D.H. (1984). Petroleum Formation and Occurrence. *Berlin, Springer-Verlag*, 518.

Tosaya, C.A. (1982). "Acoustical Properties of Clay Bearing Rocks". *Ph.D. Dissertation, Stanford U.*

Tuttle, Michele L.W., Charpentier, Ronald R. & Brownfield, Michael E. (1999). The Niger Delta petroleum system: Niger Delta province, Nigeria, Cameroon, and Equatorial Guinea, Africa. *USGS*.

Ugonoh, M., Anifowose, H., Ajayi, O., Sijpesteijn, C.K., Adedotun, W. & Obeta, C. (2012). Use of mud weight in appraisal and exploratory well planning - practical approach. *SPE 163002*, 1-10.

Weatherford International. (2012, March 29). Retrieved from http://www.weatherford.com/index.htm

Weber, K.J. & Daukoru, E.M. (1975). Petroleum geology of the Niger Delta:. *Proceedings of the Ninth World Petroleum Congress, volume 2, Geology: London, Applied Science Publishers, Ltd.*, 209-221.

Webster, M., O'Connor, S.A., Pindar, B. & Swarbrick, R.E. (2010). Overpressures in the Taranaki Basin: Distribution, Causes and Implications for Exploration. *Proceedings of the AAPG GTW, Singapore*.

Xiao, H., & Suppe, J.,. (1994). Origin of rollover. *AAPG Bulletin, 76*, 509-529.

Yardley, G.S. & Swarbrick, R.E. (2000). Lateral transfer: a source of additional pressure? *Marine and Petroleum Geology*, 523-538.

Yoshida, C., Ikeda, S. & Eaton, B.A. (1996). An Investigative Study of Recent Technologies Used for Prediction, Detection, and Evaluation of Abnormal Formation Pressure in North and South America. *IADC/SPE*.